Title
Fundamental Processes in Combustion of Stratified Mixtures

Author
Shi, Xian

Publication Date
2017

Peer reviewed|Thesis/dissertation

Fundamental Processes in Combustion of Stratified Mixtures

by

Xian Shi

A dissertation submitted in partial satisfaction of the

requirements for the degree of

Doctor of Philosophy

in

Engineering – Mechanical Engineering

and the Designated Emphasis

in

Computational Data Science and Technology

in the

Graduate Division

of the

University of California, Berkeley

Committee in charge:

Professor Jyh-Yuan Chen, Co-chair
Professor Robert W. Dibble, Co-chair
Professor Carlos Fernandez-Pello
Professor Fotini K. Chow

Fall 2017

Fundamental Processes in Combustion of Stratified Mixtures

Abstract

Fundamental Processes in Combustion of Stratified Mixtures

by

Xian Shi

Doctor of Philosophy in Engineering – Mechanical Engineering

with the Designated Emphasis

in

Computational Data Science and Technology

University of California, Berkeley

Professor Jyh-Yuan Chen, Co-chair

Professor Robert W. Dibble, Co-chair

Stratified combustion, combustion of fuel/air mixtures with temperature and/or mixture-composition stratification, is present in many combustion-related phenomena and applications such as forest wildfires, mining explosions, vessel ruptures, gas turbines, and reciprocating engines to name a few. A new generation of highly efficient internal combustion (IC) engines capable of satisfying stringent emission requirements, including modern direct-injection gasoline engines and gas turbines with lean premixed pre-vaporized (LPP) combustors, requires more comprehensive understanding and control of stratified combustion. Fundamentally, stratification of temperature or mixture composition affects a wide range of combustion characteristics such as flame speed, flammability, mode of combustion, instability, and others.

This dissertation aims to identify, analyze and evaluate fundamental processes in the combustion of stratified mixtures, using theoretical analysis and advanced numerical simulation tools. ASURF-Parallel, a transient numerical solver of compressible reacting flow, is developed on the basis of the original A-SURF and exploited for stratified combustion simulations. A domain-decomposition parallelization scheme using Message Passing Interface (MPI) is developed and implemented in ASURF-Parallel to speed up the otherwise time-consuming numerical simulations. A significant speedup with the speed-up factor up to 10 is achieved on lab-scale servers.

Effects of stratification on flame speeds, lean flammability limit, and modes of combustion are numerically investigated and studied. For flame speeds, laminar flame speeds of stratified flames propagating from rich mixtures to lean mixtures are generally faster than those of the corresponding homogeneous flames, primarily due to the preferential diffusion of lighter species and radicals such as H_2, H and OH, i.e., the chemical effect. The degree of enhancement in flame speeds can be correlated to the degree of stratification, leading to the development of a transient local stratification level (LSL) model which is able to determine the stratified flame speeds incorporating both chemical effect and memory effect. For lean flammability limits, the extension introduced by stratification is very weak due to reduced overall reactivity and reduced degree of stratification. For modes of combustion, different modes can be realized by specific reactivity gradients, regardless of the sources of such gradients. Pressure waves introduced by ignition in a closed chamber can also lead to different modes of reaction front propagation and end-gas combustion. A transient reactivity gradient method is proposed to identify the onset of detonation.

Dedicated to those who rode along on this incredible journey
Thanks for your company, support and love

Contents

Contents **ii**

List of Figures **iv**

List of Tables **xi**

Nomenclature **xii**

1 Introduction **1**
1.1 Background and motivation 1
1.2 Fundamental combustion characteristics 6
1.3 Structure of this dissertation 16
1.4 Dissertation contributions 19

2 ASURF-Parallel **20**
2.1 Adaptive Simulation of Unsteady Reactive Flow (A-SURF) 20
2.2 Domain decomposition parallelization 23

3 Flame Speed **32**
3.1 Literature review 32
3.2 Flame characteristics 36
3.3 Hydrogen/air stratified flames 41
3.4 Hydrocarbon/air stratified flames 58
3.5 Stratified flame speed model 74

4 Lean Flammability Limit **96**
4.1 Definition of flammability limit 96
4.2 Hydrogen/air lean stratified flames 97
4.3 Methane/air lean stratified flames 98

5 Modes of Combustion **103**
5.1 Zeld'ovich reactivity gradient theory 103
5.2 Combustion modes of stratified mixtures 105

5.3 Modes of reaction front propagation and end-gas combustion 117

6 Concluding Remarks **137**
6.1 Conclusions 137
6.2 Future work 138

A Plasma Assisted Combustion **140**
A.1 Background and motivation 140
A.2 Code modification 142

B Chemical Kinetic Models **146**
B.1 A 16-species reduced model of methane combustion 146
B.2 A 24-species reduced model of propane combustion 147
B.3 A 32-species reduced model of n-heptane combustion 147

References **151**

List of Figures

1.1 Human development index, total primary energy demand per capita, population and GDP per capita of selected countries, 1995–2008 (Arto et al., 2016). 2
1.2 Global comparison of passenger car efficiency standards, 2000–2025 (Miller and Façanha, 2014). 3
1.3 Energy demand varies by sector, 2015, 2025, 2040 (ExxonMobil, 2017). 4
1.4 LLNL energy flow chart: the estimated U.S. energy consumption in 2016. 5
1.5 Ideal flame configuration 1 – Stationary flame. 8
1.6 Ideal flame configuration 2 – Moving flame propagating from an open end towards a closed end (wall). 10
1.7 Ideal flame configuration 3 – Moving flame propagating from a closed end (wall) towards an open end. 11
1.8 The Rayleigh line and the Hugoniot curve (Lee, 2008). 14
1.9 The tangency or Chapman-Jouguet solutions (Lee, 2008). 15
1.10 ZND model of detonation structure (Lee, 2008). 16
1.11 Numerical results of a detonation wave: hydrogen/air mixture, $\phi = 1$, $T_0 = 1000$ K, $P_0 = 4$ atm; (a) heat release rate, temperature, pressure, and density; (b) mole fraction of H_2, O_2, H_2O, H, and OH. 17

2.1 Profiling diagram of the original serial A-SURF. 25
2.2 Schematic of the domain-decomposition splitting scheme. 25
2.3 Scaling test on Firebrand: (a) Strong scaling test; (b) weak scaling test with regard to grid space. 29
2.4 Scaling test on Hopper: (a) Strong scaling test; (b) weak scaling test with regard to time. 29
2.5 Profiling diagram of ASURF-Parallel on Firebrand; Case (a) and (b) used the same number of processors and the same simulation time, while Case (b) has 5 times more grid cells compared to that of Case (a). 30

3.1 (a) Equivalence ratio of unburnt mixture (ϕ_u) and equivalence ratio at flame front (ϕ_f), and (b) their differences, of methane/air homogeneous flames. 37
3.2 Fuel consumption speed integration with different cutoff integral limits with regard to maximum heat release rate. 38

3.3 Equivalence ratio and temperature profiles of (a) a homogeneous flame and (b) a rich–to–lean stratified methane/air flame, $\phi_f = 0.97$. 41
3.4 Schematic of stratification thickness calculation in the rich–to–lean stratified flame propagating from $\phi_u = 1.6$ to $\phi_u = 0.6$. 42
3.5 Schematic of stratified flame propagating in 1-D planar coordinate. 43
3.6 Fuel consumption speeds with 0% cutoff and 5% cutoff of SF and HF, when SF propagates from $\phi_f = 2.0$ to $\phi_f = 0.5$, $d_s = 0.1$ cm, with equal diffusivity assumption. 45
3.7 (a) Heat release rate and temperature, (b) major species mole fraction and (c) thermal and species normalized diffusion speeds profiles of SF and HF at $\phi_f = 1.2$, when SF propagates from $\phi_f = 2.0$ to $\phi_f = 0.5$, $d_s = 0.1$ cm, with equal diffusivity assumption. 46
3.8 Flame front propagation speeds, fluid expansion speeds and respective differences between SF and HF, when SF propagates from $\phi_f = 2.0$ to $\phi_f = 0.5$, $d_s = 0.1$ cm, with equal diffusivity assumption. 47
3.9 Fluid velocity profiles when SF propagates from $\phi_f = 2.0$ to $\phi_f = 0.5$, $d_s = 0.1$ cm, with equal diffusivity assumption. 48
3.10 Fuel consumption speeds with 0% cutoff and 5% cutoff of SF and HF, when SF propagates from $\phi_f = 0.5$ to $\phi_f = 2.0$, $d_s = 0.1$ cm, with equal diffusivity assumption. 49
3.11 Flame front propagation speeds and fluid expansion speeds of SF and HF, when SF propagates from $\phi_f = 0.5$ to $\phi_f = 2.0$, $d_s = 0.1$ cm, with equal diffusivity assumption. 50
3.12 Fuel consumption speeds with 0% cutoff and 5% cutoff of SF and HF, when SF propagates from $\phi_f = 1.6$ to $\phi_f = 0.4$, $d_s = 0.1$ cm, with mixture-average diffusivity assumption. 51
3.13 (a) Heat release rate and temperature, (b) major species mole fraction and (c) thermal and species normalized diffusion speeds profiles of SF and HF at $\phi_f = 1.0$, when SF propagates from $\phi_f = 1.6$ to $\phi_f = 0.4$, $d_s = 0.1$ cm, with mixture-average diffusivity assumption. 52
3.14 Flame front propagation speeds and fluid expansion speeds of SF and HF, when SF propagates from $\phi_f = 1.6$ to $\phi_f = 0.4$, $d_s = 0.1$ cm, with mixture-average diffusivity assumption. 53
3.15 Fuel consumption speeds with 0% cutoff and 5% cutoff of SF and HF, when SF propagates from $\phi_f = 0.4$ to $\phi_f = 1.6$, $d_s = 0.1$ cm, with mixture-average diffusivity assumption. 54
3.16 Flame front propagation speeds and fluid expansion speeds of SF and HF, when SF propagates from $\phi_f = 0.4$ to $\phi_f = 1.6$, $d_s = 0.1$ cm, with mixture-average diffusivity assumption. 55
3.17 (a) Fuel consumption speeds and (b) flame front propagation speeds of SF at different stratification thicknesses and corresponding HF, when SF propagates from $\phi_f = 2.0$ to $\phi_f = 0.5$, with equal diffusivity assumption. 56

3.18 (a) Fuel consumption speeds and (b) flame front propagation speeds of SF at different stratification thicknesses and corresponding HF, when SF propagates from $\phi_f = 1.6$ to $\phi_f = 0.4$, with mixture-average diffusivity assumption. 57
3.19 Fuel consumption speeds of the rich–to–lean stratified flames and the corresponding homogeneous flames. 61
3.20 Percentage differences between fuel consumption speeds of the rich–to–lean stratified flames and the corresponding homogeneous flames. 62
3.21 Heat release rates and fuel consumption rates in methane/air stratified and homogeneous flames, at $\phi_f = 1.41$. 63
3.22 Temperature, mole fractions of reactants and products in methane/air stratified and homogeneous flames, at $\phi_f = 1.41$. 63
3.23 Mole fractions of intermediate species and radicals in methane/air stratified and homogeneous flames, at $\phi_f = 1.41$. 64
3.24 Difference between absolute heat release rates of reaction steps in methane/air stratified and homogeneous flames, at $\phi_f = 1.41$. 65
3.25 Heat release rates and fuel consumption rates in propane/air stratified and homogeneous flames, at $\phi_f = 1.42$. 66
3.26 Temperature, mole fractions of reactants and products in propane/air stratified and homogeneous flames, at $\phi_f = 1.42$. 66
3.27 Mole fractions of intermediate species and radicals in propane/air stratified and homogeneous flames, at $\phi_f = 1.42$. 67
3.28 Difference between absolute heat release rates of reaction steps in propane/air stratified and homogeneous flames, at $\phi_f = 1.42$. 68
3.29 Difference between absolute heat release rates of reaction steps in n-heptane/air stratified and homogeneous flames, at $\phi_f = 1.44$. 69
3.30 Flame front propagation speeds of the rich–to–lean stratified flames and the corresponding homogeneous flames. 70
3.31 Percentage differences between flame front propagation speeds of the rich–to–lean stratified flames and the corresponding homogeneous flames. 71
3.32 Mole fraction of molecular hydrogen on the unburnt side of flame front, for both the rich–to–lean stratified flames and the corresponding homogeneous flames. . . 72
3.33 Enhancement of laminar flame speeds with hydrogen addition for methane, propane and n-heptane homogeneous flames; $X_{H2,unburnt}$ represents mole fraction of hydrogen in initial homogeneous unburnt mixtures. 73
3.34 H/C ratio at flame front of the rich–to–lean stratified flames and the corresponding homogeneous flames. 74
3.35 Fuel consumption speeds of SF propagating into lean mixtures and corresponding HF. 76
3.36 Fuel consumption speeds of SF propagating into rich mixtures and corresponding HF. 77
3.37 Heat release rate and temperature profiles of the 1.6–0.6 SF and HF, $\phi_f = 0.97$. 78
3.38 Reactant and product profiles of the 1.6–0.6 SF and HF, $\phi_f = 0.97$. 79

3.39 Major intermediate species and radical profiles of the 1.6–0.6 SF and HF, $\phi_f = 0.97$. 80
3.40 Production rate profiles H_2, H and OH, of the 1.6–0.6 SF and HF, $\phi_f = 0.97$. . . 80
3.41 Fuel consumption speeds of the 1.6–0.6 SF and HF with different assumptions of unity Lewis number: (a) $Le = 1$, (b) $Le_{H_2,H_2O,H,OH} = 1$, (c) $Le_{H_2,H_2O} = 1$, (d) no unity-Le assumption. 81
3.42 (a) Fuel consumption speeds of the 1.6–0.6 SF and HF, and (b) the respective differences between SF and HF, with different diffusivity of H_2. 82
3.43 (a) Fuel consumption speeds of the 1.6–0.6 SF and HF, and (b) the respective differences between SF and HF, with different diffusivity of H_2O. 83
3.44 Fuel consumption speeds of the 1.6–0.6 SF with different stratification thicknesses and HF. 84
3.45 Fuel consumption speeds of the 1.0–0.6 SF with different stratification thicknesses and HF. 85
3.46 Departure of fuel consumption speeds of stratified flames compared to homogeneous flames based on instantaneous equivalence ratio gradients at flame front: (a) $\phi_u = 0.8$, (b) $\phi_u = 1.0$, (c) $\phi_u = 1.2$. 86
3.47 Correlation: difference between flame speeds of SF and HF, versus difference between mole fractions of H_2 on the unburnt side of SF and HF flame fronts. . . 87
3.48 Control volume analysis of Local Stratification Level (LSL): (a) stratified flame propagation along negative equivalence ratio gradient, e.g., from rich to lean; (b) stratified flame propagation along positive equivalence ratio gradient, e.g., from lean to rich. 89
3.49 Increases of laminar flame speeds with hydrogen addition to methane/air mixtures. 90
3.50 (a) Mole fraction of H_2 on the unburnt side of flame front, of the 1.6–0.6 SF, HF and the 0.6–1.6 SF. (b) Transfer function of equivalence ratio gradient based on $X^u_{H_2,f}$ in HF. 91
3.51 LSL model assessment – three stratification cases are tested: (a) rich–to–lean, $d_s = O(0.05$ cm), (b) rich–to–lean, $d_s = O(0.1$ cm), (c) rich–to–lean, $d_s = O(1$ cm). The results are presented versus time, from top to bottom: 1) equivalence ratio at flame front, 2) equivalence ratio gradient at flame front, 3) fuel consumption speeds of model, Quasi-HF and simulation results, and 4) percentage errors of model v.s. simulation and Quasi-HF v.s. simulation. 92
3.52 LSL model assessment – three stratification cases are tested: (a) lean–to–rich, (b) rich–lean–rich, (c) arbitrary equivalence ratio profile. The results are plotted against time, from top to bottom: 1) equivalence ratio at flame front, 2) equivalence ratio gradient at flame front, 3) fuel consumption speeds of model, Quasi-HF and simulation results, and 4) percentage errors of model v.s. simulation and Quasi-HF v.s. simulation. 93
3.53 Local stratification level model assessment of the rich–to–lean stratified flame, $d_s = O(0.1$ cm). The results are plotted against local equivalence ratio. 94

4.1 (a) Major species mole fraction and (b) heat release rate and major exothermic reaction rate profiles of SF and HF at $\phi_f = 0.356$, when SF propagates from $\phi_u = 1.0$ to $\phi_u = 0.4$, $d_s = 0.1$ cm, with mixture-average diffusivity assumption. 99
4.2 (a) Major species mole fraction and (b) heat release rate and major exothermic reaction rate profiles of HF at $\phi_f = 0.356$ and SF at $\phi_f = 0.346$, when SF propagates from ϕ_u 1.0 to 0.2, $d_s = 0.1$ cm, with mixture-average diffusivity assumption. 100
4.3 Equivalence ratio profiles of 1.6–0.0 and 1.0–0.0 SF at $\phi_f = 0.5$. 101
4.4 Equivalence ratio at flame front during the propagation of 1.6–0.0 and 1.0–0.0 stratified flames from $\phi_f = 0.5$ to 0.0. 102

5.1 Numerical schematic in 1-D spherical coordinate with initial equivalence ratio (or temperature) profile. Note the initial gradient within 5 mm layer is not to scale. 106
5.2 Computed ignition delay time of stoichiometric H_2/CO/air mixtures at different temperatures, P = 50 atm. 107
5.3 Computed ignition delay time of H_2/CO/air mixtures at 1000 K and different equivalence ratios, P = 50 atm. 108
5.4 Development of a supersonic autoignitive deflagration and thermal explosion, $\xi = 1$ with a negative equivalence ratio gradient: (a) Initial condition of equivalence ratio; (b) Temperature; (c) Pressure; (d) Velocity. Time sequence (μs): 1 - 2101, 2 - 2102, 3 - 2103, 4 - 2104, 5 - 2105. 109
5.5 Development of a developing detonation and thermal explosion, $\xi = 3$ with a negative equivalence ratio gradient: (a) Initial condition of equivalence ratio; (b) Temperature; (c) Pressure; (d) Velocity. Time sequence (μs): 1 - 2096, 2 - 2098, 3 - 2100, 4 - 2102, 5 - 2104. 110
5.6 Development of a deflagration to detonation transition and thermal explosion, $\xi = 10$ with a negative equivalence ratio gradient: (a) Initial condition of equivalence ratio; (b) Temperature; (c) Pressure; (d) Velocity. Time sequence (μs): 1 - 2070, 2 - 2080, 3 - 2090, 4 - 2098, 5 - 2100, 6 - 2101, 7 - 2102, 8 - 2103, 9 - 2104, 10 - 2105. 111
5.7 Development of a deflagration to detonation transition and thermal explosion, $\xi = 10$ with a negative temperature gradient: (a) Initial condition of equivalence ratio; (b) Temperature; (c) Pressure; (d) Velocity. Time sequence (μs): 1 - 2070, 2 - 2080, 3 - 2090, 4 - 2098, 5 - 2100, 6 - 2101, 7 - 2102, 8 - 2103, 9 - 2104, 10 - 2105. 113
5.8 Development of a deflagration to detonation transition and thermal explosion, $\xi = 10$ with a negative temperature gradient and a negative equivalence ratio: (a) Initial condition of equivalence ratio; (b) Temperature; (c) Pressure; (d) Velocity. Time sequence (μs): 1 - 2070, 2 - 2080, 3 - 2090, 4 - 2098, 5 - 2100, 6 - 2101, 7 - 2102, 8 - 2103, 9 - 2104, 10 - 2105. 114

5.9 Development of a deflagration to detonation transition and thermal explosion, $\xi = 10$ with a positive temperature gradient and a negative equivalence ratio: (a) Initial condition of equivalence ratio; (b) Temperature; (c) Pressure; (d) Velocity. Time sequence (μs): 1 - 2070, 2 - 2080, 3 - 2090, 4 - 2098, 5 - 2100, 6 - 2101, 7 - 2102, 8 - 2103, 9 - 2104, 10 - 2105. 115
5.10 Ignition delay time of H_2/CO/air mixtures (50% H_2 and 50% CO by volume) at different temperature and equivalence ratio, P = 50 atm. 116
5.11 Schematic of the 1-D planar closed chamber. 119
5.12 Schematic of simulation setups with different ignition locations and chamber sizes, with down arrows indicating the location of ignition. 120
5.13 Development of deflagration to end-gas detonation, Setup 1, T_0 = 940 K, a) temperature b) pressure c) fluid velocity. The time sequence of number-labeled profiles: 1-1196.0 μs, 2-1198.0 μs, 3-1200.0 μs, 4-1202.0 μs, 5-1204.0 μs, 6-1206.0 μs, 7-1208.0 μs, 8-1210.0 μs 122
5.14 Temporal evolution of reaction front, Setup 1, $T_0 = 940$ K 123
5.15 Temporal evolution of end-cell gas temperature and pressure, Setup 1, $T_0 = 940$ K 123
5.16 Development of deflagration to detonation transition, Setup 1, T_0 = 990 K, a) temperature b) pressure c) fluid velocity. The time sequence of number-labeled profiles: 1-50.0 μs, 2-65.0 μs, 3-80.0 μs, 4-85.0 μs, 5-90.0 μs, 6-95.0 μs, 7-100.0 μs, 8-105.0 μs 124
5.17 Temporal evolution of reaction front, Setup 1, $T_0 = 990$ K 125
5.18 Temporal evolution of end-cell gas temperature and pressure, Setup 1, $T_0 = 990$ K 125
5.19 Development of deflagration to detonation transition, Setup 2, T_0 = 980 K, a) temperature b) pressure c) fluid velocity. The time sequence of number-labeled profiles: 1-95.0 μs, 2-100.0 μs, 3-104.0 μs, 4-108.0 μs, 5-112.0 μs, 6-116.0 μs, 7-132.0 μs, 8-135.0 μs 127
5.20 Onset of deflagration to detonation transition on the right side of ignition, Setup 2, $T_0 = 980$ K, a) temperature b) pressure. The time sequence of number-labeled profiles: 1-5.0 μs, 2-40.0 μs, 3-60.0 μs, 4-80.0 μs, 5-90.0 μs, 6-100.0 μs 129
5.21 Temporal evolution of reaction fronts, Setup 2, $T_0 = 980$ K 130
5.22 Regime diagram for modes of overall combustion, in terms of ν_b and T_0 131
5.23 Regime diagram for modes of reaction front propagation and end-gas combustion, based on the Zeld'ovich theory 133
5.24 Onset of Deflagration to Detonation Transition, Setup 1, $T_0 = 990$ K, a) temperature b) pressure c) ignition delay (d) reactivity gradient dimensionless number. The time sequence of number-labeled profiles: 1-40.0 μs, 2-50.0 μs, 3-60.0 μs, 4-70.0 μs, 5-75.0 μs, 6-80.0 μs 134
5.25 Ignition delay times of stoichiometric hydrogen/air mixtures under various initial temperatures and pressures from SENKIN 135

A.1 Schematic of plasma assisted combustion and applications (Ju and Sun, 2015). . 141

A.2 Schematic of major enhancement pathways of plasma assisted combustion (Ju and Sun, 2015). 142

B.1 Laminar flame speeds of homogeneous methane/air flames at 300 K, 1 atm. . . . 147
B.2 Comparison between numerical results of mole fraction profiles of H2, H and OH at different equivalence ratios, with GRI3.0 model and the 16-species reduced model. 148
B.3 Laminar flame speeds of homogeneous propane/air flames at 300 K, 1 atm. . . . 149
B.4 Laminar flame speeds of homogeneous n-heptane/air flames at 300 K, 1 atm. . . 150

List of Tables

1.1 Flame speeds and characteristic velocities of three different one-dimensional flames. 11
1.2 Flammability limits of fuel-air mixtures at standard conditions (% of fuel by volume in mixture) (Zabetakis, 1965; McAllister et al., 2011). 12

5.1 Parameters of numerical simulation setups 120
5.2 Modes of reaction front propagation and end-gas combustion under initial pressure 4 atm and over a range of initial temperatures 850-1050 K 126

Nomenclature

Abbreviations

Le	Lewis number
A-SURF	Adaptive Simulation of Unsteady Reactive Flow
AMR	Adaptive mesh refinement
CJ	Chapman-Jouguet
CPM	Coarse particle method
DDT	Deflagration to detonation transition
DISI	Direct injection spark ignition
EEDF	Electron energy distribution function
HDI	Human Development Index
HF	Homogeneous flame
IC	Internal combustion
ICE	Internal combustion engine
IPCC	Intergovernmental Panel on Climate Change
LFL	Lean flammability limit
LIF	Laser induced fluorescence
LLNL	Lawrence Livermore National Laboratory
LPP	Lean premixed pre-vaporized
MPI	Message Passing Interface
NERSC	National Energy Research Scientific Computing Center

ODE Ordinary differential equation

PDE Partial differential equation

QSSA Quasi steady-state approximation

RCM Rapid compression machine

RFL Rich flammability limit

RTP Reactant to product

RTR Reactant to reactant

SF Stratified flame

TPED Total primary energy demand

TSA Target Search Algorithm

UN United Nations

UNDP United Nations Development Programme

Greek Symbols

δ Local Stratification Level (LSL)

δ_f Local Stratification Level (LSL) at flame front

$\dot{\omega}_F$ Fuel production rate

$\dot{\omega}_k$ Production rate of species k

λ Mixture thermal conductivity

μ Mixture viscosity

μ_k Mobility of species k

∇ Gradient operator

ν_b Volumetric ratio between burnt and total mixtures

ν_{elas} Elastic collision frequency of electrons

Φ Viscous dissipation

ϕ_b Equivalence ratio of burnt mixture

ϕ_f Equivalence ratio at flame front

ϕ_f^b Equivalence ratio at flame front on burnt side

ϕ_f^u Equivalence ratio at flame front on unburnt side

ϕ_u Equivalence ratio of unburnt mixture

ρ Density

ρ_0 Unburnt gas density (Fristrom, 1965)

ρ_b Density of burnt mixture

ρ_c Charge density

ρ_f Density of mixture at flame front

ρ_u Density of unburnt mixture

σ Standard deviation

τ Viscous stress

τ_e Excitation time

τ_i Ignition delay time

ε Excitation dimensionless number

ε_0 Vacuum permittivity

ξ Reactivity gradient dimensionless number

ξ_l Lower bound of ξ

ξ_u Upper bound of ξ

Roman Symbols

$\bar{M}$ Mean molecular weight of mixture

ΔH_i Enthalpy of formation of chemical reaction i

$\dot{m}$ Mass flow rate (Fristrom, 1965)

$\dot{q}$ Specific heat release rate

$\dot{Q}_{elas}$ Energy transfer due to elastic collisions of electrons

$\dot{Q}_{elec}$	Energy transfer due to electron generation
$\dot{Q}_e$	Energy transfer between electrons and neutral gases
$\dot{Q}_{inel}$	Energy transfer due to inelastic collisions of electrons
$\dot{r}_i$	Reaction rate of chemical reaction i
$\hat{V}'_k$	Normalized diffusion speed of species k
$\hat{V}'_T$	Normalized thermal diffusion speed
$\mathbf{E}$	Electric field
$\mathbf{U}$	Vector of independent variables (governing equation)
$\mathbf{V_E}$	Electric potential
$\mathcal{C}$	convection term (LSL model)
$\mathcal{D}$	diffusion term (LSL model)
$\mathcal{R}$	reaction term (LSL model)
$\tilde{q}$	Heat addition rate
$\tilde{q}_m$	Ignition power
$\tilde{S}_d$	Density-weighted displacement speed
a	Sound speed
a_0	Inlet cross-section area (Fristrom, 1965)
a_r	Flame front cross-section area (Fristrom, 1965)
C_F	scale constant (LSL model)
c_p	Specific heat capacity at constant pressure
c_v	Specific heat capacity at constant volume
$C_\mathcal{C}$	convection constant (LSL model)
$C_\mathcal{D}$	diffusion constant (LSL model)
$C_\mathcal{R}$	reaction constant (LSL model)
C_{grad}	gradient constant (LSL model)

$c_{p,e}$	Specific heat capacity of electrons at constant pressure
C_{rlx}	relaxation constant (LSL model)
$c_{v,e}$	Specific heat capacity of electrons at constant volume
D	Mixture diffusivity
d_f	Flame thickness
D_k	Mass diffusivity of species k
d_s	Stratification thickness
D_T	Thermal diffusivity
E	Total energy
F	Convection term (governing equation)
F_v	Diffusion term (governing equation)
h_k	Enthalpy of species k
k_B	Boltzmann constant
L	Chamber size
m	Mass
m_e	Electron mass
n_e	Mole of electrons
N_p	Nubmer of processors
P	Pressure
P_0	Initial pressure
q	Heat flux (governing equation)
R_u	Universal gas constant
r_i	Radius of ignition kernel
S_c	Fuel consumption speed
S_d	Flame displacement speed

S_d^u	Displacement speed relative to unburnt mixture
S_f	Flame front propagation speed
S_L^0	Laminar flame speed (unstretched, relative to unburnt mixture)
S_R	Chemical source term (governing equation)
S_{CJ}	Chapman-Jouguet speed
S_{exp}	Fluid expansion speed
T	Temperature
t	Time
T_0	Initial temperature
T_b	Temperature of burnt mixture
T_e	Electron temperature
T_g	Gas temperature
T_u	Temperature of unburnt mixture
T_c	Critical ignition temperature
T_f	Adiabatic flame temperature
U	Fluid velocity
u	Fluid velocity (governing equation)
u_b	Fluid velocity of burnt mixture
u_f	Fluid velocity at flame front
u_p	Reaction front propagation speed relative to unburnt gas
u_u	Fluid velocity of unburnt mixture
V_k'	Diffusion velocity of species k
v_0^*	Burning velocity (Fristrom, 1965)
v_0	Inlet gas velocity (Fristrom, 1965)
$V_{d,k}$	Drift velocity of species k

x	Spatial coordinate
X_F^b	Mole fraction of fuel species in burnt mixture
X_F^u	Mole fraction of fuel species in unburnt mixture
x_c	Cell size
X_F	Mole fraction of fuel species
X_k	Mole fraction of species k
x_i	Ignition location
Y_F^b	Mass fraction of fuel species in burnt mixture
Y_F^u	Mass fraction of fuel species in unburnt mixture
Y_F	Mass fraction of fuel species
Y_k	Mass fraction of species k

Acknowledgments

Being able to attend the most prestigious public university in the world is a life-changing gift. As a graduate student at Cal, I enjoyed Yosemite, Tahoe, and Golden Gate as much as everyone else did. More importantly, I learned a tremendous amount of knowledge and skills from many world-class minds here at Berkeley. Many great individuals have offered me their guidance, encouragement and support, which I am truly grateful for.

I would like to express my most sincere gratitude to my research advisors Professor Jyh-Yuan Chen and Professor Robert Dibble. Their motivation, enthusiasm, patience and continuous support for my study and research consist of the strong foundation for what I have accomplished so far. Things that I greatly appreciate from them are simply too many to list thoroughly. To name a few, I thank Professor Chen for teaching me how to become a passionate researcher who thinks logically and critically, for guiding me patiently through many research difficulties and adversities, and making every comment and correction on my paper manuscripts. I thank Professor Dibble, for admitting me to Berkeley, for bringing me to the scientific world outside Berkeley, and for every small or big, relevant or "irrelevant", but always inspiring conversation about science and life. Besides, I am honored to know and learn from many other brilliant professors and researchers on campus: I took classes from Professor Carlos Fernandez-Pello and Professor Tina Chow; both have served on my qualifying exam committee and dissertation committee. I benefited a lot from taking their classes and invaluable feedback regarding my qualifying presentation and this dissertation. Professor Pello also taught me his teaching art while I was his teaching assistant. Moreover, I thank Professor Tarek Zohdi for saving me from the hopeless scheduling of qualifying exam by agreeing on serving as the fourth committee member. Outside Berkeley, I would like to thank Professor Zheng Chen at Peking Unversity for allowing me to use A-SURF for my dissertation study, and thank Professor Wai K. Chang at Massachusetts Institute of Technology for the helpful discussions on experimental stratified flame studies.

I have spent at least half of my graduate school time in Hesse Hall. I will not survive without my fellow lab mates: Benjamin Wolk, Tiernan Casey, Daniel Pineda, Yulin Chen, Je Ir Ryu, Charles Scudiere, Alex Frank, Yumin Huang, Chenkun Zheng and Sirui Fu from Combustion Modeling Lab, David Vuilleumier, Miguel Sierra Aznar and Tim Sennott from Combustion Analysis Lab, Dan Murphy, James Urban and Maria Thomsen-Solis from Combustion and Fire Processes Laboratory, Ravi Singh, Jim Oreluk, Wenyu Li and Zhenyuan Liu from Professor Micheal Frenklach's lab, and visiting students and scholars Timo Lipkowicz, Yongliang Xie, Ziyang Zhang, Fredrik Grøvdal and Tao Chen. It has been an awesome research community: during my first two years, senior students were always willing to help me get involved in research activities. Peers in my year took classes together and helped each other through homework and projects. Different ideas and opinions were being exchanged on a very frequent basis, and I can always find myself being inspired by various conversations. The collaborative and friendly environment where everyone can be others' hand and resource made my research journey very joyful.

Sometimes research can be tedious and frustrating. Thus I am also extremely grateful for my friends outside campus, from whom I knew from very young to whom I met at Berkeley. Every time when I felt depressed or discouraged, I was always able to find comforts in a fun hangout, in a warm phone call, or in a welcomed getaway. My life would have been considerably harder without the friendships and I love every one of them.

I cannot thank my parents enough, the best parents in the world. I cannot imagine myself being the man I am right now without their love and support. They showed me the way to becoming a kind, responsible, confident and capable person by being the perfect examples, giving me a sweet home and always standing behind me. Other family members have also contributed in many ways showing their support of me chasing my dreams and broadening my horizon. And of course, my girlfriend Longxia has always been by my side during my ups and downs in the past four years. Her unending patience, company and encouragement were what made this dissertation possible in the end.

Lastly, I would like to pay a special tribute to my grandfather, who passed away while I was working on this dissertation. He is a hero to the family, as he grew up from poor, overcame a lot of obstacles and carried the entire family on his shoulders. To me, he was a cool, thoughtful and like-to-spoil grandfather. I can still remember the old time when he took me out on his bike and bought me my favorite ice cream. He makes me feel special in all I do with his endless love. Grandpa, I am sorry that I did not get a chance to say goodbye. Please rest in peace and you will be remembered and missed every day. I hope I have made you proud and will continue to do so.

Chapter 1

Introduction

1.1 Background and motivation

1.1.1 Energy for the present and future

A stable and adequate access to energy has been an indispensable component of the social, economic and cultural growth of human societies throughout the history. For example, about two hundred years ago, easy access to coal or wood fuel propelled the popularity of steam power, while the substitution of coke for charcoal greatly lowered the fuel cost for pig iron and wrought iron production (Landes, 2003). Since then, an abundance of fossil energy combined with modern agriculture and governance has fueled the Industrial Revolution and enabled human beings to live longer, healthier, and more comfortable lives. Generally speaking, countries with cheaper energy access and greater energy use boast higher levels of human development. In order to quantify the levels of human development, United Nations Development Programme (UNDP) published the Human Development Index (HDI), an overall measure of average achievement in the following key dimensions: a long and healthy life, being knowledgeable and a decent standard of living (UNDP, 2017). Figure 1.1 shows the relation between the total primary energy demand (TPED) per capita and the HDI of a selected group of countries (Arto et al., 2016). While in most highly developed countries (where TPED is bigger than 100 GJ/year per capita), TPED and HDI were not very strongly correlated, changes in the energy use translate into changes in the degree of human development in most developing countries. As global population will continuously increase from around 7.4 billion today to nearly 10 billion by 2050, with most growth coming from developing countries (UN, 2017), energy will inevitably remain as a central theme for the human development blueprint in the foreseeable future.

The Paris Agreement on climate change is one of many indicative signals embracing a brand-new era of the energy landscape. Thousands of researchers have reached the conclusion that climate change is happening, an immediate threat to mankind's survival and sustainable development. One of the biggest contributors to climate change is energy-related

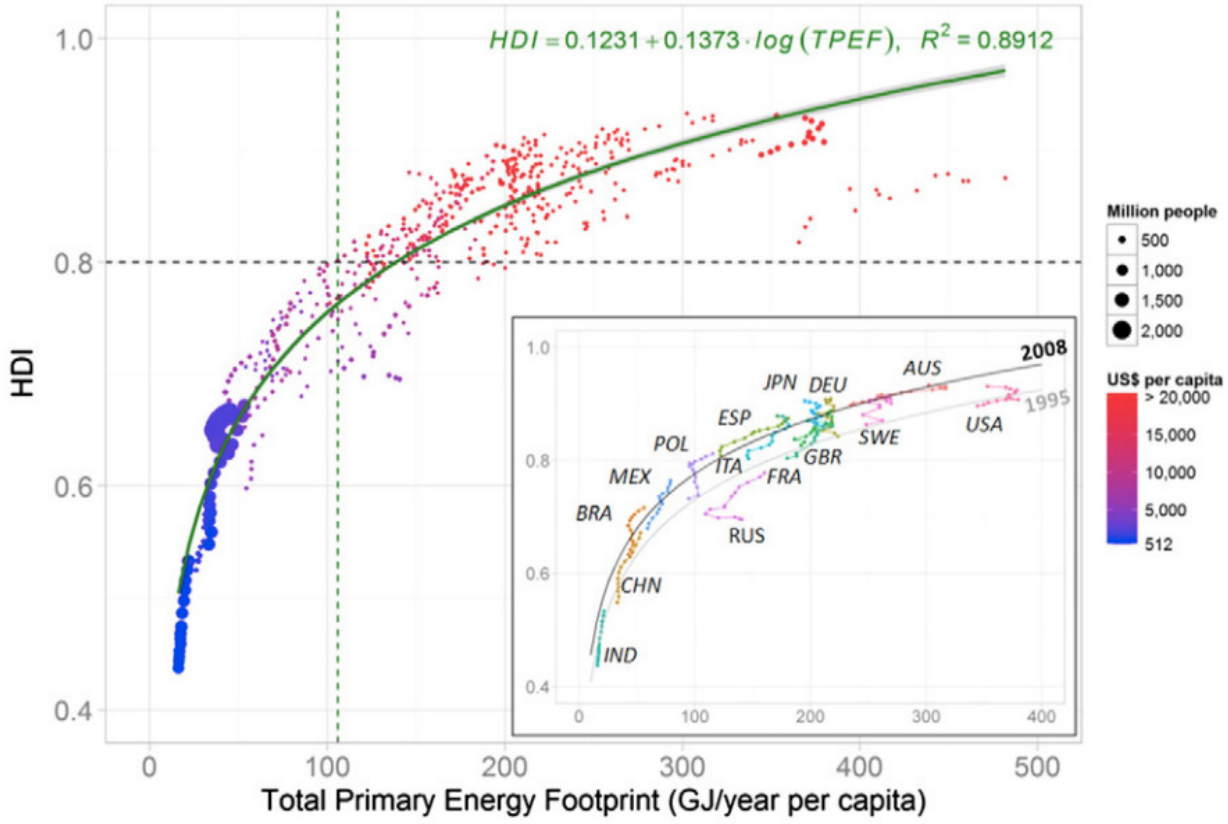

Figure 1.1: Human development index, total primary energy demand per capita, population and GDP per capita of selected countries, 1995–2008 (Arto et al., 2016).

greenhouse gas emissions. CO_2 emissions have increased by about 90% from 1970 to 2011, with fossil fuel combustion and industrial processes contributing 78% of the total increase (IPCC, 2014). Moreover, air pollution and the corresponding health impacts have become an urgent issue in most developing countries, such as China and India, particularly in urban areas with high levels of motorized transport activities. Figure 1.2 shows the passenger car efficiency standards in terms of CO_2 emissions in different countries, including both past performances and future targets. A universal trend is observed, as all the mentioned countries and organizations demand substantial emission reductions in the years to come.

While recognizing the dilemma between the significance of energy for human development and the problems associated with climate change, it is also worth noticing that the world is rapidly changing and so are energy needs. Traditional demand centres such as heavy industries are being overtaken by fast-growing emerging markets such as high-tech companies. The energy mix is shifting, driven by technological improvements and environmental concerns (BP, 2017). The consequent task for the industry is to adopt new policies, strategies and infrastructures, to meet those changing energy needs. In conclusion, growing

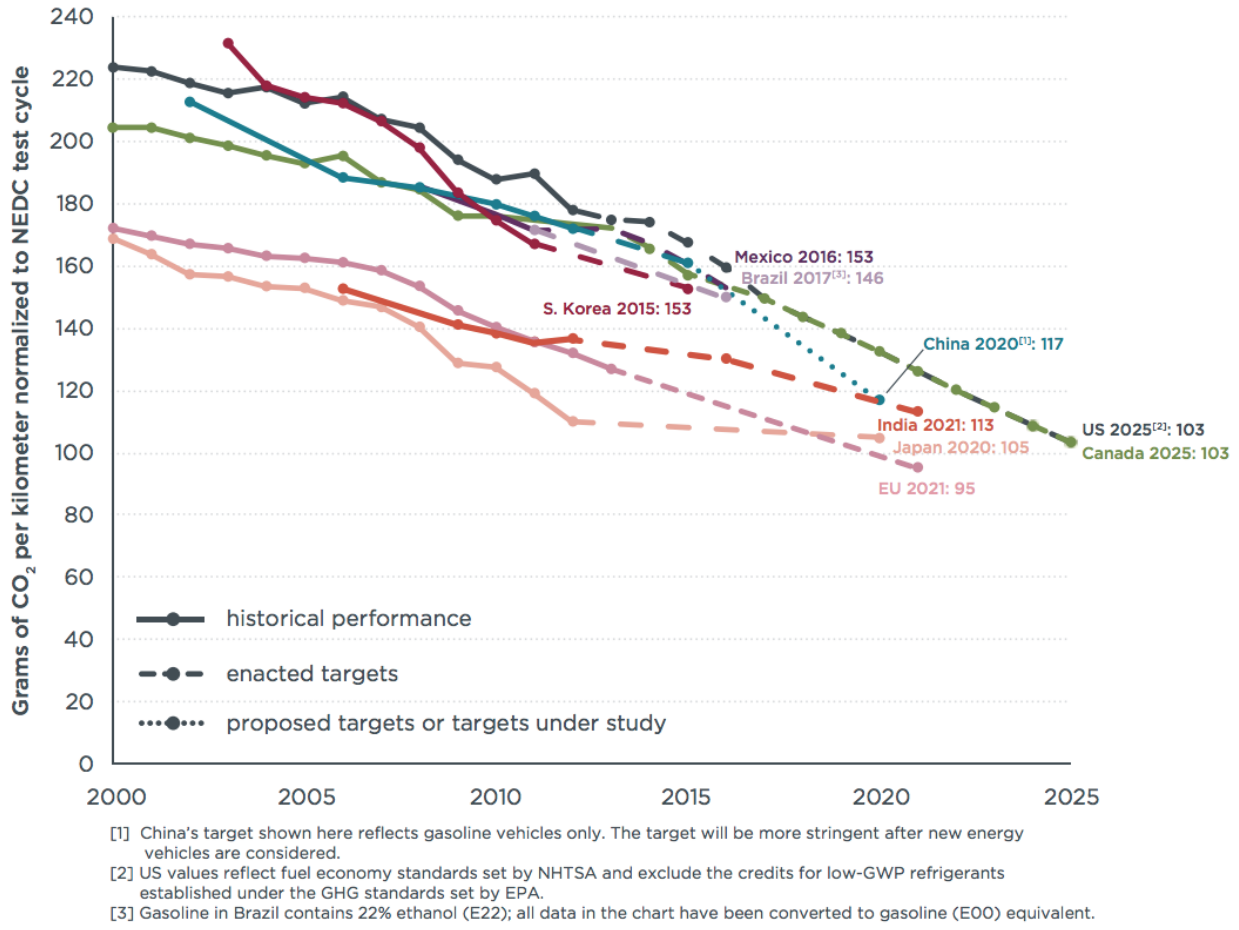

Figure 1.2: Global comparison of passenger car efficiency standards, 2000–2025 (Miller and Façanha, 2014).

population, rising demands and competitions for resources, and needs for migrating climate change has brought the energy sector many unprecedented challenges.

1.1.2 The role of combustion

The rise of human beings and human civilization cannot be imagined without combustion. From heating and cooking of food, to material processing and power production, combustion has contributed to almost every aspect of human society. Many pieces of emerging evidence indicate that combustion plays a central role in the modern world energy landscape and will continue to be a dominant factor for at least the next century. Figure 1.3 shows the energy demand distribution for different sectors, including data from 2015 and predictions for 2025 and 2040 (ExxonMobil, 2017). Coal, gas and oil continue to be the three dominant energy sources for basic human activities and services. Over 80% of total electricity generation

comes from power plants where many different kinds fuels are being burnt. Energy demand for transportation and industrial applications are and will be dominated by combustion processes of liquid fuels.

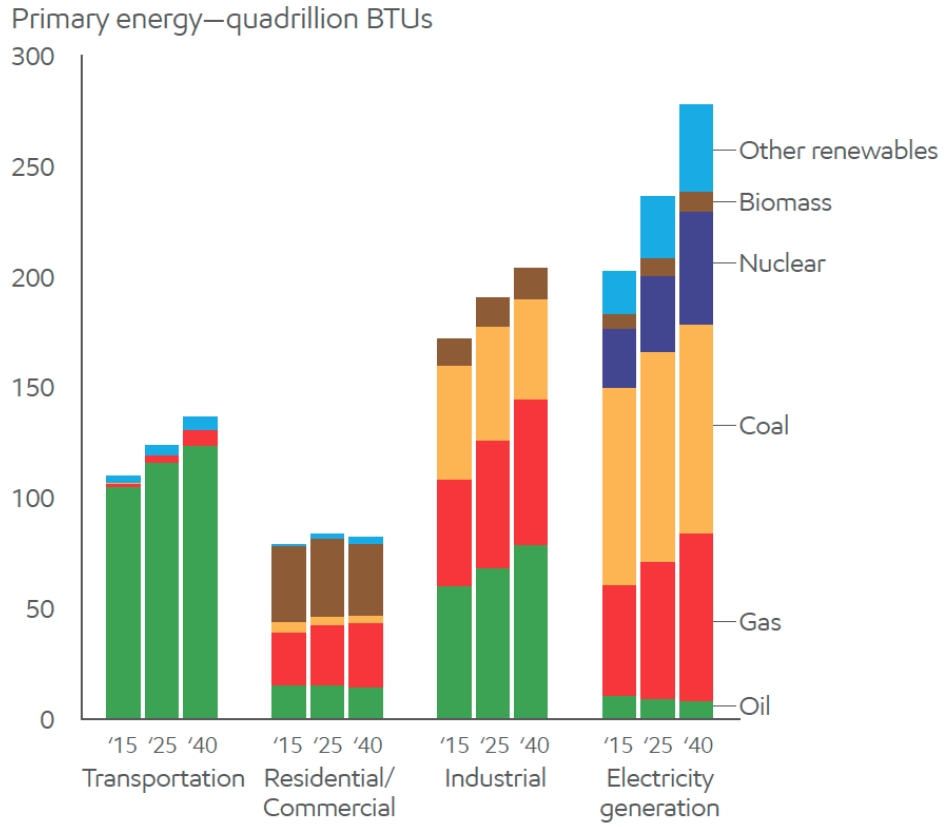

Figure 1.3: Energy demand varies by sector, 2015, 2025, 2040 (ExxonMobil, 2017).

The famous "energy flow chart" (the estimated U.S. energy consumption in 2016 published Lawrence Livermore National Laboratory (LLNL), as shown in Fig. 1.4) reveals that the overall energy use efficiency is strikingly low (overall about 30%). Not only does the traditional combustion of fossil fuels have lots of potentials to achieve a better efficiency, electricity utilization is also quite far away from the optimal. This observation made the arguable trend of electrification including electrical vehicles an unwise decision, as not much of an efficiency gain can be achieved from a energy-life-cycle standpoint. Another interesting fact according to the flow chart is that the total percentage of renewable energy used in the US barely reached 10%.

Therefore, although technologies of sustainable energy offer a seemingly bright future, continuous improvement on the efficiency of current practical combustion devices and on the magnitude of emission reduction remains a necessary step in order to solve those immediate issues and ensure a smooth transition to the renewable energy era.

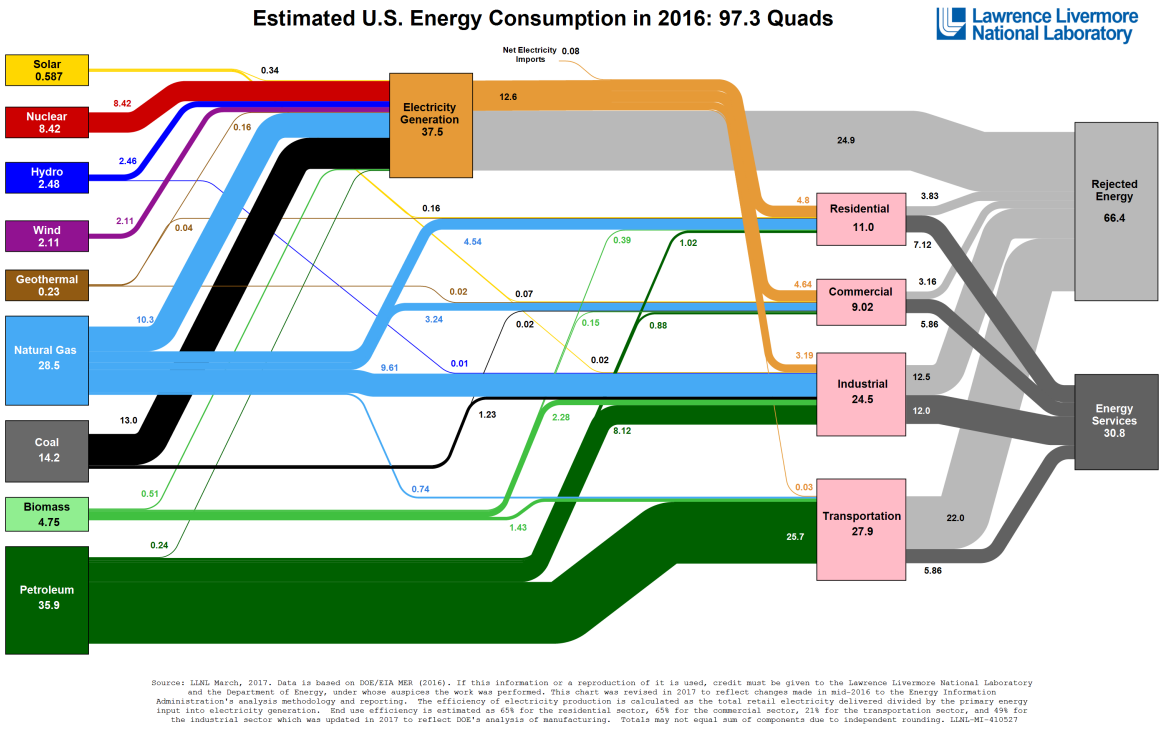

Figure 1.4: LLNL energy flow chart: the estimated U.S. energy consumption in 2016.

1.1.3 Combustion of stratified mixtures

Stratified combustion exists in a wide range of practical combustion phenomena and industrial applications, from forest wildfires (Gill et al., 2013), mine gas and vessel ruptures (Phillips, 1965; Newman, 1984), to gas turbines and reciprocating engines (Sjöberg and Dec, 2006; Reitz, 2013; Ax and Meier, 2016). A new generation of highly efficient internal combustion engines capable of satisfying stringent emission requirements, including modern direct-injection gasoline engines and gas turbines with lean premixed pre-vaporized (LPP) combustors, requires more comprehensive understanding and control of stratified combustion (Lipatnikov, 2017). Fundamentally, stratification of temperature or mixture composition affects a wide range of combustion characteristics such as flame speed, flammability, ignition, mode of combustion, and instability. For example, in gas turbines, oscillations in equivalence ratio may trigger thermo-acoustic instabilities in the combustion chamber, which can deteriorate the turbine performance or even cause severe physical damages (Candel, 2002). In contrast, stratified combustion in direct injection spark ignition (DISI) internal combustion engines (ICE) has been an effective technique to improve fuel efficiency and reduce emissions (Alkidas, 2007; Park et al., 2012). In more recent years, a new engine knock mode, super knock, started to appear in downsized, low-speed and high-boost modern engines (Wang et al., 2015). Different from traditional knock (Liu et al., 2013), super knock can damage engine components catastrophically due to extremely high peak pressure with severe oscil-

lations, and possible in-cylinder detonation formations. The occurrence of super knock is believed to be the results of in-cylinder inhomogeneity, i.e., either hot spots, hot surfaces, or lubricant oil droplets (Wang et al., 2017). Therefore, it is of practical significance as well as fundamental interest to understand combustion of stratified mixtures.

1.2 Fundamental combustion characteristics

1.2.1 Flame speed

Flame speed is the most important property of a combustible mixture. Understanding flame speeds not only reveals a significant amount of fundamental knowledge regarding the underlying physics during combustion processes, but also provides guidance towards design and performance optimization of almost all combustion practical devices. An emphasis on laminar flame speed is given in this section. For those who are interested in turbulent flames and the associated flame propagation speeds, please refer to many insightful discussions in Poinsot and Veynante (2005).

Classical definition of laminar flame speed

There are several different descriptions of laminar flame speed S_L^0. For example, Linnett (1953) defined the laminar flame speed as the linear velocity of the flame front normal to itself relative to the unburnt mixture. An important deduction from this definition is that for an ideal one-dimensional flame in an infinite planar geometry, if the flame front is stationary, the speed of incoming unburnt mixture at infinity is equal to the defined laminar flame speed. Another definition was also given as the volume of unburnt gas consumed per unit time divided by the area of the flame front in which that volume is consumed. Based on this definition, Fristrom (1965) considered an ideal stream tube where unburnt gas enters the tube from the inlet and burnt gas exits from the outlet, while the flame is steadily established inside the tube. Laminar flame speed (referred as burning velocity in the original paper) is thereby defined as

$$v_0^* = \frac{\dot{m}}{\rho_0}\frac{1}{a_r} = \frac{\dot{m}}{\rho_0 a_0}\frac{a_0}{a_r} = v_0\frac{a_0}{a_r}, \tag{1.1}$$

where v_0^* is the defined laminar flame speed; $\dot{m}$ is mass flow rate; ρ_0 is unburnt gas density; v_0 is the inlet gas velocity; a_0 and a_r are the inlet cross-section area and flame front cross-section area respectively. If the steam tube is assumed with a uniform cross section, the laminar flame speed is equal to inlet gas velocity. This definition indicated that the laminar flame speed is independent of flame front and depends only on the state of the inlet unburnt gas (pressure, temperature and mixture composition).

Such a definition seems fairly straightforward in ideal flames (planar, stationary and adiabatic) but may not be practical in real flame studies (stretched, stratified, nonadiabatic, etc.). Therefore, various alternatives have been proposed in order to evaluate laminar flame

speeds at most convenience. These alternatives, in turn, help define additional mathematical formulation of S_L^0.

Fuel consumption speed, S_c

Laminar flame speeds can be determined through the profile of flame properties across flame reaction zone, such as temperature variation and species distribution (Law, 2006). This consideration is mostly adopted in numerical simulations, as relevant scalars could be impossible to measure experimentally. For example, regarding the consumption of fuel species across the flame, fuel consumption speed can be defined (Poinsot et al., 1992; Varea et al., 2015). For a simple stationary one-dimensional flame shown in Figure 1.5, continuity equation and conversation of fuel species mass fraction can be written as

$$\frac{d}{dx}(\rho u) = 0, \qquad \rho u = \rho_u u_u, \tag{1.2}$$

where ρ_u is unburnt mixture density and u_u is the fluid velocity of unburnt mixture. And

$$\rho u \frac{dY_F}{dx} = \frac{d}{dx}\left(\rho D \frac{dY_F}{dx}\right) + \dot{\omega}_F, \tag{1.3}$$

where Y_F is fuel species mass fraction, D is diffusivity and $\dot{\omega}_F$ is the fuel species production rate. Integrate Equation 1.3 from unburnt mixture side (negative infinity) to burnt mixture side (positive infinity):

$$-\rho_u u_u (Y_F^u - Y_F^b) = \cancelto{0}{\rho D \frac{dY_F}{dx}\Big|_{-\infty}^{+\infty}} + \int_{-\infty}^{+\infty} \dot{\omega}_F dx, \tag{1.4}$$

where Y_F^u, Y_F^b are the fuel species mass fraction in the unburnt and burnt mixture. The limits of the integral represent unburnt and burnt homogeneous mixture, where $dY_F/dx = 0$. Therefore the first term on the RHS of Equation 1.4 is zero. Since

$$S_c = S_L^0 = u_u \tag{1.5}$$

for this specific flame, the fuel consumption speed is then derived as:

$$S_c = -\frac{1}{\rho_u (Y_F^u - Y_F^b)} \int_{-\infty}^{+\infty} \dot{\omega}_F dx. \tag{1.6}$$

Note that this definition is not always perfect in practice. For example, in stratified flames, Y_F^b is not well-defined as the burnt gas is stratified. Even for homogeneous flames, uncertainty exists in Y_F^b as the burnt gas composition of propagating flames can deviate from the corresponding equilibrium composition (Wu et al., 2014). Therefore, Y_F^u is sometimes used instead of $Y_F^u - Y_F^b$ to enable reasonable comparison between different flames.

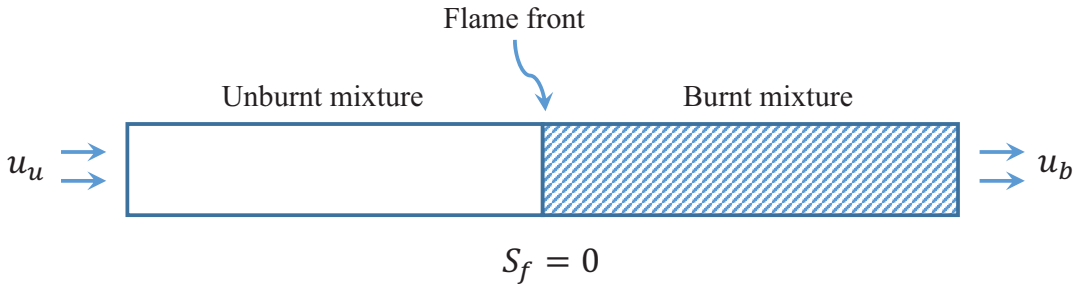

Figure 1.5: Ideal flame configuration 1 – Stationary flame.

In addition, as fuel species is not only consumed around the flame front but also continuously reacting in the burnt gas due to finite rates of chemistry, the integral limits used in Equation 1.6 will determine the scope of fuel consumption speed. For homogeneous flames, the limits can range from negative to positive infinity. However, for stratified flames, the same infinity integral limits would include fuel consumption from burnt gases of various equivalence ratios, causing ambiguity when compared to the corresponding homogeneous flames with the same equivalence ratio at flame front. Therefore, different integral limits can be applied to distinguish local and global fuel consumption speeds. For example, both 0% and 5% cutoff integral limits were applied in Shi et al. (2016). While 0% cutoff represents the integral over the entire domain, 5% means that the integral will be conducted only over the domain where local heat release rate exceeds 5% of the maximum heat release rate. In this way, 5% cutoff fuel consumption speed is considered as the local fuel consumption speed and therefore represent local flame characteristics.

Flame front propagation speed, S_f

In experimental studies, laminar flames can be directly characterized by a global behavior of the flame, as the absolute propagation speed of flame front is often used. The flame front is usually represented by certain measurable scalars, such as maximum density gradient in Schlieren technique (Hu et al., 2009) and concentration of certain species measured by laser induced fluorescence (LIF) technique (Vagelopoulos et al., 2005).

Flame displacement speed, S_d

According to Giannakopoulos et al. (2015), flame displacement speed, defined as the speed of a scalar (temperature, fuel mass fraction, etc.) iso-surface (flame front) relative to local fluid velocity, is used to represent the motion of the flame. The kinematic expression for one-dimensional flame displacement speed is defined as

$$S_d = S_f - u_f \tag{1.7}$$

where S_f is the absolute flame front propagation speed and u_f is the local fluid velocity at flame front. Note that this flame displacement speed is not equal to the classical definition of laminar flame speed, as different fluid velocities are considered. In classical definition of laminar flame speeds, the velocity of unburnt mixture u_u is used, while local fluid velocity at flame front u_f is used in flame displacement speed. u_u and u_f are essentially different due to variations in density.

For a meaningful comparison between displacement speeds at different locations, i.e., $S_f - u$, Giannakopoulos et al. (2015) proposed the density-weighted displacement speed. In one-dimensional flame reference frame, continuity equation can be written as

$$\rho(S_f - u) = \rho_f(S_f - u_f). \tag{1.8}$$

Therefore the density-weighted displacement speed can be defined as

$$\tilde{S}_d = \frac{\rho_f}{\rho} S_d. \tag{1.9}$$

Then the flame displacement speed relative to unburnt mixture,

$$S_d^u = \frac{\rho_f}{\rho_u} S_d, \tag{1.10}$$

can be now directly compared to the laminar flame speed S_L^0.

Relations among flame speeds in different flame configurations

Three one-dimensional and adiabatic flames are analyzed in this section, in order to elaborate relations among S_L^0, S_c, S_f, S_d, u_u, u_f and u_b. While S_L^0 and S_c are regarded as scalars, all other variables are considered with their directions. Since the theoretical derivation of S_c does not depend on flame configurations, S_c is assumed to be equal to S_L^0. In Figure 1.5, the stationary flame is given. We have already known that

$$S_c = S_L^0 = u_u, \qquad S_f = 0,$$

according to the classical definition of laminar flame speed. Apply the continuity equation at the flame front and the burnt mixture with respect to the unburnt mixture,

$$u_f = \frac{\rho_u}{\rho_f} u_u = \frac{\rho_u}{\rho_f} S_L^0, \tag{1.11}$$

$$u_b = \frac{\rho_u}{\rho_b} u_u = \frac{\rho_u}{\rho_b} S_L^0. \tag{1.12}$$

Then the flame displacement speed is

$$S_d = S_f - u_f = -\frac{\rho_u}{\rho_f} S_L^0. \tag{1.13}$$

The second type of flame is a moving flame propagating from an open end towards a closed end, as shown in Figure 1.6. Due to confinement,

$$u_u = 0, \qquad S_f = -S_L^0,$$

as the flame propagates towards the wall. Apply continuity equation in flame reference frame,

$$\rho_u(0 - S_f) = \rho_f(u_f - S_f), \qquad u_f = \left(\frac{\rho_u}{\rho_f} - 1\right) S_L^0, \tag{1.14}$$

$$\rho_u(0 - S_f) = \rho_b(u_b - S_f), \qquad u_b = \left(\frac{\rho_u}{\rho_b} - 1\right) S_L^0. \tag{1.15}$$

Note that the flame front propagation speed is towards the wall while the fluid is leaving the wall. Therefore the flame displacement speed is

$$S_d = S_f - u_f = -\frac{\rho_u}{\rho_f} S_L^0. \tag{1.16}$$

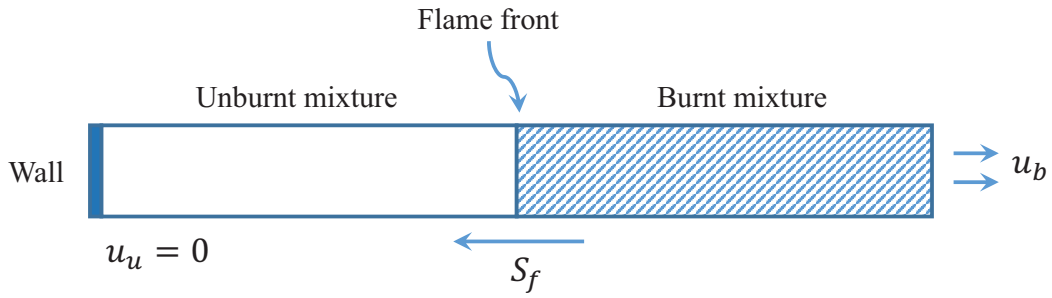

Figure 1.6: Ideal flame configuration 2 – Moving flame propagating from an open end towards a closed end (wall).

The third type of flame is a moving flame propagating from a closed end towards an open end, as shown in Figure 1.7. Due to confinement and dilatation,

$$u_b = 0, \qquad S_f = \frac{\rho_u}{\rho_b} S_L^0.$$

Again apply continuity equation in flame reference frame,

$$\rho_b(0 - S_f) = \rho_f(u_f - S_f), \qquad u_f = \left(\frac{\rho_u}{\rho_b} - \frac{\rho_u}{\rho_f}\right) S_L^0, \tag{1.17}$$

$$\rho_b(0 - S_f) = \rho_u(u_u - S_f), \qquad u_u = \left(\frac{\rho_u}{\rho_b} - 1\right) S_L^0. \tag{1.18}$$

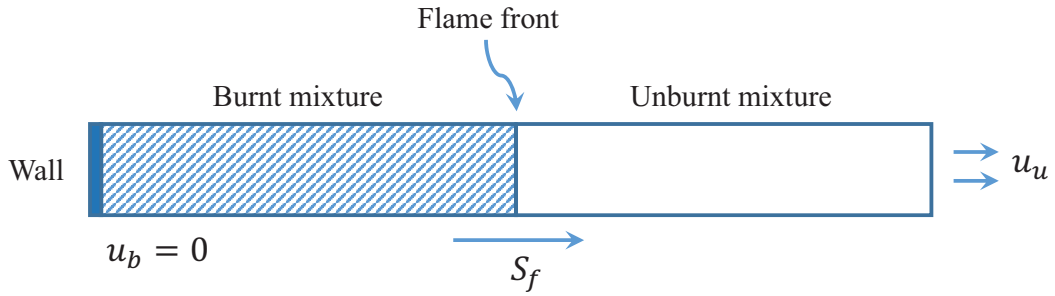

Figure 1.7: Ideal flame configuration 3 – Moving flame propagating from a closed end (wall) towards an open end.

The flame displacement speed is

$$S_d = S_f - u_f = \frac{\rho_u}{\rho_f} S_L^0. \tag{1.19}$$

Results from the above analysis are summarized in Table 1.1. Note that while flame front propagation speeds and fluid velocities are completely different among three different flames, the magnitude of flame displacement speed S_d is always equal to the laminar flame speed weighted by densities of local and unburnt mixtures. S_c is always equal to S_L^0 by definition. Therefore, S_d and S_c are most consistent and should be primarily used for flame studies.

Table 1.1: Flame speeds and characteristic velocities of three different one-dimensional flames.

	S_c	S_f	S_d	u_u	u_f	u_b
Flame 1	S_L^0	0	$-\frac{\rho_u}{\rho_f} S_L^0$	S_L^0	$\frac{\rho_u}{\rho_f} S_L^0$	$\frac{\rho_u}{\rho_b} S_L^0$
Flame 2	S_L^0	$-S_L^0$	$-\frac{\rho_u}{\rho_f} S_L^0$	0	$\left(\frac{\rho_u}{\rho_f} - 1\right) S_L^0$	$\left(\frac{\rho_u}{\rho_b} - 1\right) S_L^0$
Flame 3	S_L^0	$\frac{\rho_u}{\rho_b} S_L^0$	$\frac{\rho_u}{\rho_f} S_L^0$	$\left(\frac{\rho_u}{\rho_b} - 1\right) S_L^0$	$\left(\frac{\rho_u}{\rho_b} - \frac{\rho_u}{\rho_f}\right) S_L^0$	0

Complexity on flame speed

Besides the above complication of multiple definitions, flames in real applications are even harder to deal with in terms of the determination of laminar flame speeds. The complexity mainly comes from the following aspects:

- Discrepancies in the determination of flame front location.
- Stretched flames, such as opposed jet flames and spherical flames.
- Stratified flames, whose unburnt and burnt mixtures are no longer homogeneous.
- Turbulent flames, whose flame speeds are mostly enhanced compared to the corresponding laminar flames, due to increased transport processes of heat and mass by small-scale turbulence, and increased surface area due to wrinkling of the flame by large turbulent eddies (McAllister et al., 2011).

Therefore, consistency in the definition of laminar flame speeds is critical for meaningful and reasonable comparison among different flames.

1.2.2 Flammability limit

A combustible mixture normally consists of three main components: fuel, oxidizer, and diluent. If one of these three components has a critically higher concentration than those of the other two, the mixture will eventually become incombustible. The flammability limit is thereby defined by the boundary mixture composition, where a slight change will results in the mixture being either combustible or incombustible (Coward and Jones, 1952). A quantitative knowledge of flammability limit is of importance for assessment of fire hazards, as well as the system performance of lean or near-limit combustion applications, such as lean-burn IC engines and ultra-lean gas turbines (Law, 2006).

Speaking of fuel and air mixtures in most practical combustion applications, there are clearly two limits, lean flammability limit (LFL) and rich flammability limit (RFL), corresponding to scenarios of excess air and excess fuel respectively. Standardized determination of these limits were proposed and conducted by U.S. Bureau of Mines, using a vertically oriented tube. A mixture is regarded flammable if the flame is able to be ignited at the bottom of the tube and propagate to the top (Zabetakis, 1965). These two limits of some common fuels are shown in Table 1.2.

Table 1.2: Flammability limits of fuel-air mixtures at standard conditions (% of fuel by volume in mixture) (Zabetakis, 1965; McAllister et al., 2011).

Fuel	LFL	RFL
Hydrogen (H_2)	4.0	75.0
Carbon monoxide (CO)	12.5	74.0
Methane (CH_4)	5.0	15.0
Ethane (C_2H_6)	3.0	12.4
Ethanol (C_2H_6O)	3.3	19.0

Experimental determinations of flammability limits are often biased by system limitations and condition fluctuations, such as unexpected wall or radiation heat losses and pressure or temperature perturbations. In contrast, theoretical analysis of flammability limits offers a much clearer picture of the underlying physical processes related to flammability. There have been two mechanisms, aiming to illustrate flammability limit as a fundamental concept. From an energy-balance point of view, heat addition from the ignition along with heat release from initial chemical reactions are competing with heat loss processes. If the total heat loss is strong enough to prevent the local mixture from reaching the critical ignition temperature, the mixture will fail to burn. Alternatively, from a chemical-kinetic point of view, the chain branching reactions are competing with the chain termination reactions. If the chain termination reactions are strong enough to prevent radical pools from building up in a runaway manner, the combustion process will not anchor. Similar to flame speed, a clear definition of flammability limit is crucial in parametric studies of relevant parameters, including stratification. A detailed discussion on various experimental measurement and numerical explorations of flammability limits is given in Chap. 4.

1.2.3 Modes of combustion

One can easily tell the difference between a candle flame and a bomb explosion: One is peaceful and gentle, the other is violent and catastrophic. Such a difference infers that different modes of combustion processes are possible. Upon ignition of combustible mixtures, a reaction front wave is created. Across the reaction front, reactants are transformed into products, while the chemical energy of reactants is transformed into chemical, thermal and kinetic energy of products. The thermodynamic and gas-dynamic states of reactants and products are dramatically different due to the energy release. The consequent gradient fields of these states across the reaction front, in turn, sustain the propagation of the reaction front itself (Lee, 2008).There are two types of such self-sustained propagation modes of reaction front: deflagration and detonation.

Deflagration is driven by the diffusion of heat and mass. The transport of heat and active radical species from the reaction zone and burnt products to the reactants sustain the chemical reactions and heat release. Therefore, the propagation velocity of deflagration is associated with the characteristic diffusivity of the mixture. In contrast, the occurrence of detonation propagation results from the compression heating from a shock wave. The thermodynamic states (pressure and temperature) of reactants are brought up by the shock wave to initiate the chemical reactions, while the consequent heat release supports the shock wave propagating downstream. Therefore, the propagation velocity of detonation is closely related to that of the shock wave, i.e., the local sound speed. A transition from the deflagration mode to the detonation mode is referred to as deflagration to detonation transition (DDT).

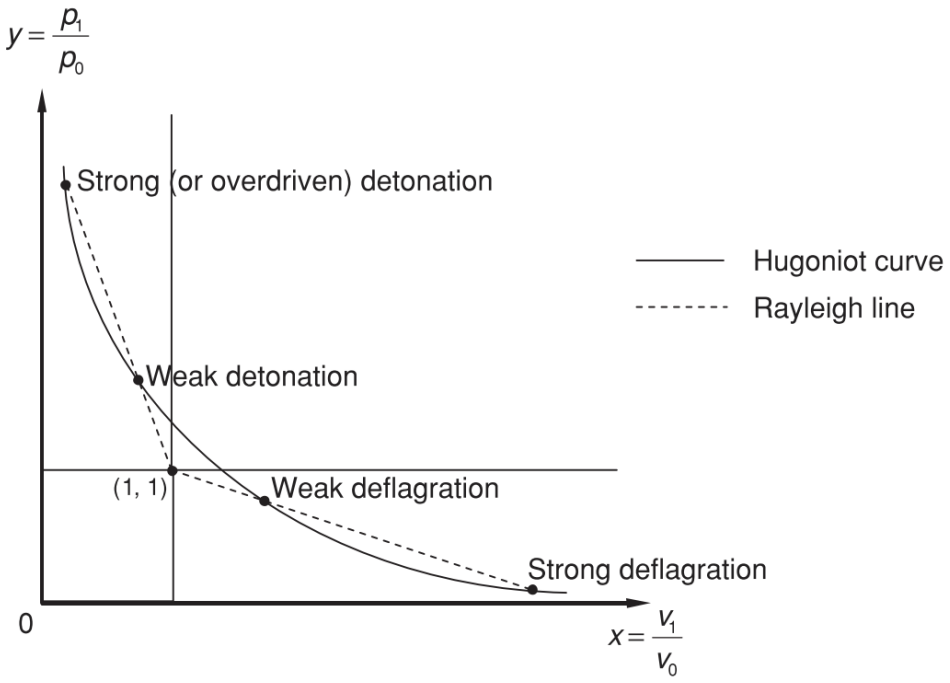

Figure 1.8: The Rayleigh line and the Hugoniot curve (Lee, 2008).

Rankine–Hugoniot conditions and Chapman–Jouguet solutions

A quantitative theory regarding thermodynamic and gas-dynamic states of reactants and products in different combustion modes was formulated by Chapman (1899) and Jouguet (1905). For a one-dimensional reaction front in the coordinate system that is moving with the reaction front, there are four basic equations, i.e., the conservation equations of mass, momentum, energy, as well as the equation of state. The first three conservation equations are called the Rankine–Hugoniot conditions (Rankine, 1870). In order to solve this system of equations, a Rayleigh line is constructed based on mass, momentum conversations and the equation of state, while a Hugoniot curve (Hugoniot, 1888) is constructed upon the energy conservation. In Fig. 1.8, two Rayleigh lines and the Hugoniot curve are drawn in the axis system of x (the ratio of the specific volume of product over that of reactant) and y (the ratio of the pressure of product over that of reactant). The intercepts between the Rayleigh lines and the Hugoniot represent solutions for possible combustion modes. All the deflagration modes are located in the lower right corner of this diagram while detonations are at upper left.

When the Rayleigh lines are tangent to the Hugoniot curve, the Chapman–Jouguet (CJ) solutions are achieved, as shown in Fig. 1.9. The argument about CJ solutions was that there existed a minimum-velocity, or minimum-entropy detonation velocity that corresponds to the unique propagation velocity observed in detonation experiments.

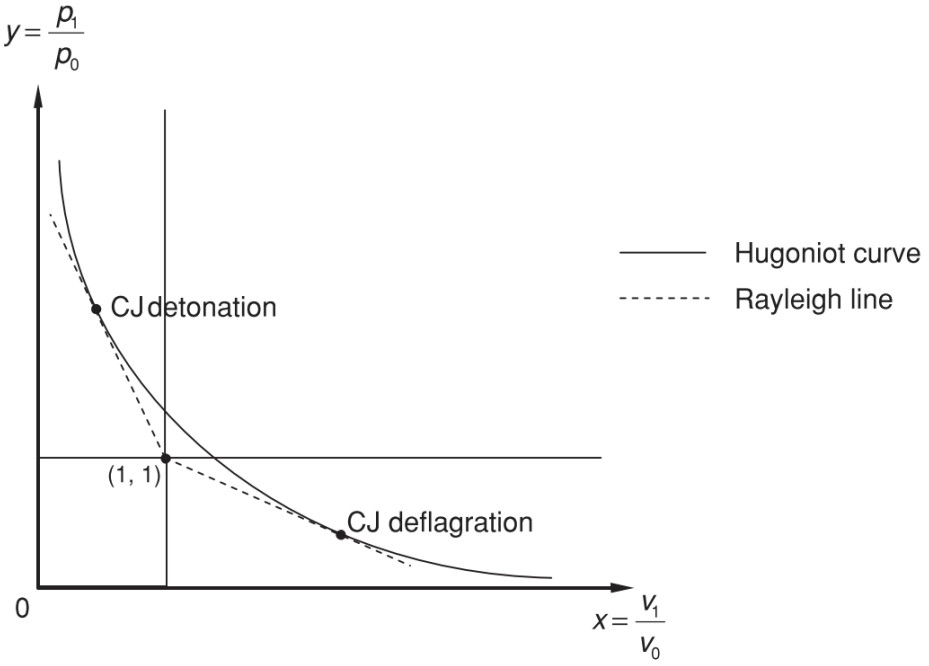

Figure 1.9: The tangency or Chapman-Jouguet solutions (Lee, 2008).

Detonation structure

Based on the gas-dynamic theory of detonation, the downstream states of detonations (as well as shocks and deflagrations) can be directly analyzed based on the upstream states and the conservation equations across the front. However, the detailed structure of the transition from upstream to downstream is not yet specified. Therefore, in order to describe this transition zone, a model for the structure of the detonation wave must be defined (Lee, 2008). The model of detonation structure is formally credited to Zeldovich (1940), von Neumaa (1942), and Döring (1943), while the model is generally referred to as the ZND model.

A sketch of the ZND model is shown in Fig. 1.10. The ZND model consists of four zones from right to left: reactant, reaction, induction and product zones. In the induction zone, due to the adiabatic compression of the leading shock, temperature, pressure and density of the induction zone are higher than those of the reactant zone. As a result, active radical species are produced through thermal dissociation of fuel molecules. In the following reaction zone, the amount of radicals is sufficient so that chain branching reactions kick off and convert reactants to products. The associated energy release leads to a further rise in temperature and a corresponding drop in pressure and density. A front thrust is consequently generated to support the shock propagation. Therefore, apart from the CJ theory, the ZND model describes both the ignition and the driving mechanisms for the detonation propagation.

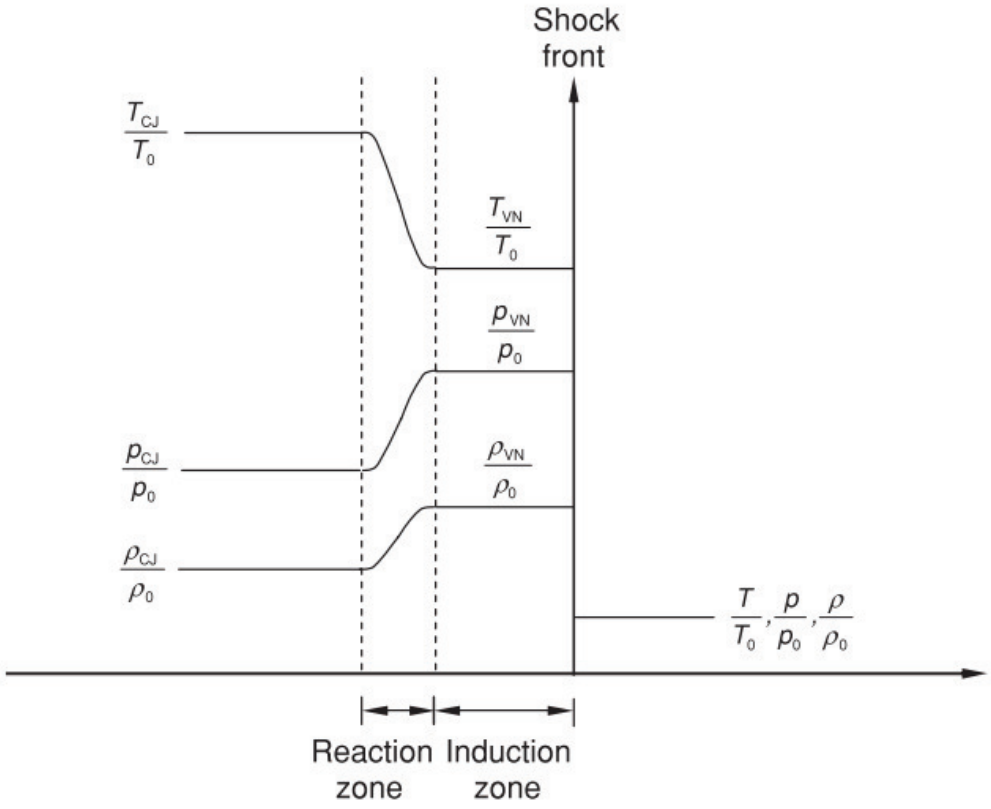

Figure 1.10: ZND model of detonation structure (Lee, 2008).

Numerical simulation results from ASURF-Parallel are shown in Fig. 1.11. A multi-species chemical kinetic model with finite reaction rates is considered in the simulation. A detonation wave is triggered in a stoichiometric hydrogen/air mixture at 1000 K and 4 atm. More details regarding the numerical simulations are given in Chap. 4. The results in Fig. 1.11 (a) matches with the ZND model quantitatively. Moreover, the distributions of reactants, products and intermediate radicals are also resolved as shown in Fig. 1.11 (b). For more in-depth discussions on the detonation phenomenon, please refer to Lee (2008).

1.3 Structure of this dissertation

This dissertation aims to identify, analyze and evaluate fundamental processes in the combustion of stratified mixtures, using theoretical analysis and advanced numerical simulation tools. The content is organized in the following order:

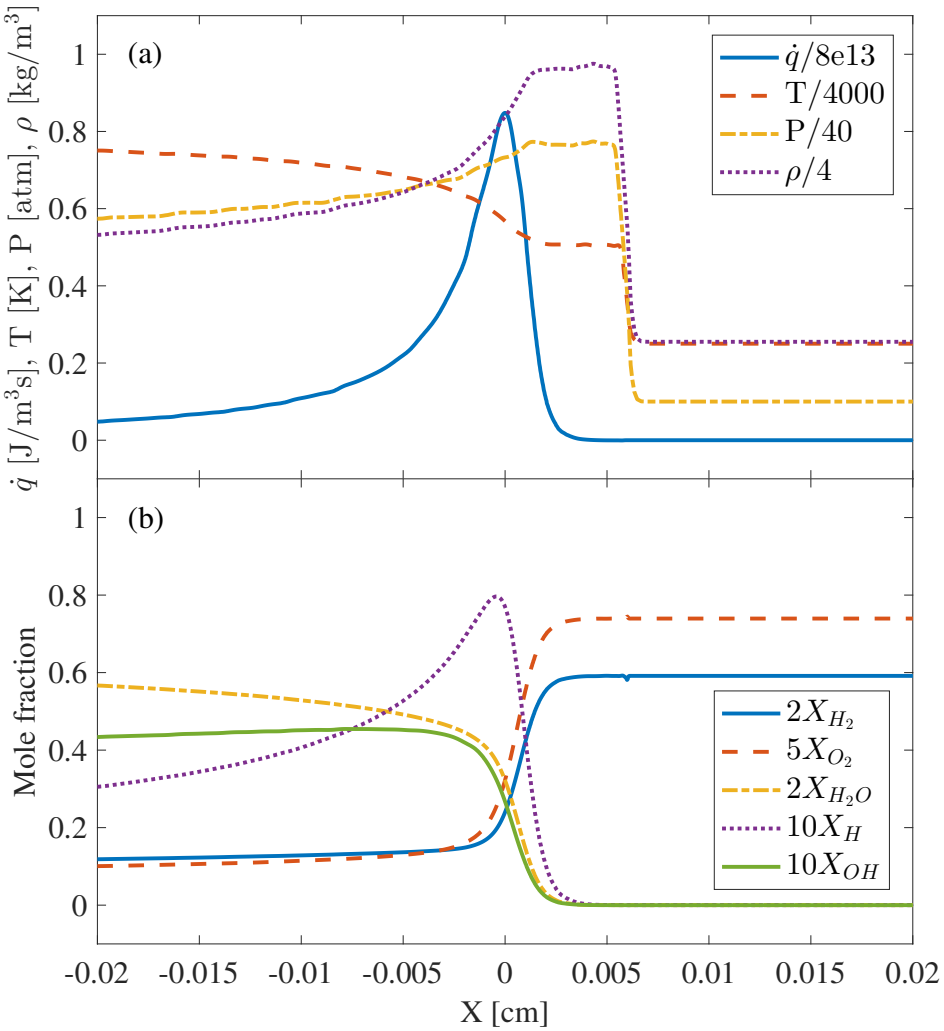

Figure 1.11: Numerical results of a detonation wave: hydrogen/air mixture, $\phi = 1$, $T_0 = 1000$ K, $P_0 = 4$ atm; (a) heat release rate, temperature, pressure, and density; (b) mole fraction of H_2, O_2, H_2O, H, and OH.

1. The first chapter begins with many pieces of evidence showing the present and future world energy paradigm and the substantial role of combustion. Fundamental combustion characteristics, including flame speeds, flammability limits and modes of combustion, are then introduced, aiming to facilitate further discussions in the context of stratified combustion. Both the structure of this dissertation and its contributions are given at the end of this chapter.

2. The second chapter provides a detailed description of the numerical simulation tool ASURF-Parallel. The governing conservation equations, the transport and chemistry models, and the numerical schemes and methods are discussed. The development

details of parallelization and performance evaluation are then illustrated.

3. The third chapter discusses the effect of stratification on flame speeds. An in-depth literature review of the past studies is given first. As consistency in characterizing flame properties of stratified and homogeneous flames is crucial, all the relevant flame characteristics are clearly defined and illustrated. A case study on hydrogen/air flames with mixture composition stratification is presented, followed by discussions on methane, propane and n-heptane flames. Based on what has been learned from the above analysis, a local stratification level model which describes the instantaneous flame speed difference between stratified and homogeneous flames is proposed and tested.

4. The fourth chapter discusses the effect of stratification on lean flammability limits. The potential of lean flammability limit extension due to mixture composition stratification is discussed by analyzing two study cases: hydrogen/air lean stratified flames compared to a reference "at-limit" homogeneous flame, and methane/air stratified flames with different stratification configurations.

5. The fifth chapter discusses the effect of stratification on modes of combustion. The classical Zeld'ovich reactivity gradient theory is first discussed in a relatively detailed way as it provides the theoretical relation between gas dynamics and chemical kinetics. Ignition pockets containing gradients of temperature, equivalence ratio, and the combination of the two are studied and different modes of combustion are observed. The corresponding results can be well explained by the Zeld'ovich theory. A study case with a more practical setup is then performed, where an energy-deposit ignition is employed in a finite-length closed chamber. Different modes of the reaction front propagation introduced by the ignition and the end-gas combustion are observed, based on which a transient reactivity gradient method is proposed to identify the onset of detonation transition locally.

6. The sixth chapter concludes with key findings from Chaps. 3–5 and discusses possible improvements of the current studies as well as alternative future research directions regarding stratified combustion.

7. The first appendix contains the details of a continued code development based on ASURF-Parallel. The goal is to make the numerical solver capable of simulating plasma assisted combustion. Special adjustments regarding electron- and ion-related chemistry and transport are elaborated first with detailed implementation procedures, followed by preliminary simulation examples. The second appendix provides validation of three reduced chemical kinetic models for methane, propane, and n-heptane combustion, respectively.

1.4 Dissertation contributions

Contributions of the work presented in this dissertation to the development of advanced numerical solvers and the increased understanding of combustion of stratified mixtures include:

- Successful implementation of parallelization on an existing serial numerical solver. The resulting parallel version of the solver can be efficiently run on lab-scale servers, i.e., with the number of processors ranging from 10 to 100. As there are many robust and well-validated, but serial solvers in the numerical combustion community, the successful experience of this parallelization development effort can benefit whom wants to perform a similar code modification.
- Detailed and in-depth investigations are performed towards the effect of stratification on flame speeds, lean flammability and modes of combustion. On one hand, an increased understanding of the fundamental processes in combustion of stratified mixtures is achieved. On the other hand, the analysis logic and methodologies are robust and can be extended to other types of combustion-related studies.
- Two models, i.e., stratified flame speed model and transient reactivity gradient model, are proposed and tested based on the results of numerical simulations. To the best of the author's knowledge, the stratified flame speed model is the first model that is capable of predicting the stratified flame speeds using global stratification parameters in a wide range of mixture compositions. The model development efforts bridge the fundamental understanding (seemingly irrelevant) of stratified combustion to the practical use (relevant) of such knowledge.

Chapter 2

ASURF-Parallel

ASURF-Parallel (Shi et al., 2017a), a parallel version of the Adaptive Simulation of Unsteady Reacting Flow (Chen et al., 2009; Chen, 2010) written in FORTRAN, is used to perform transient simulations of combustion of stratified mixtures and those of the corresponding homogeneous mixtures. The original A-SURF has been extensively used and validated by many researchers investigating various combustion-related problems (Chen, 2010, 2011; Dai and Chen, 2015; Varea et al., 2015; Pan et al., 2016b). The unsteady compressible Navier-Stokes equations for a multi-species reactive mixture in one-dimensional coordinates are solved. Dynamically and locally adaptive mesh refinement (AMR) is applied to resolve various types of reaction fronts and mixture layers of interests. A domain-decomposition parallelization approach using Message Passing Interface (MPI) is implemented to speed up the calculation.

In this chapter, details regarding the original A-SURF are first given. The parallelization development process is then elaborated and the corresponding performance improvement is evaluated.

2.1 Adaptive Simulation of Unsteady Reactive Flow (A-SURF)

The governing conservation equations, transport and chemistry models, and numerical schemes and methods of the original A-SURF are briefly discussed in this section. For more concrete details including formulation in cylindrical and spherical coordinates, and vigorous code validation, please refer to Chen (2009).

Governing conservation equations

A compact form of the governing equations in a rectangular coordinate is shown as below

$$\frac{\partial \mathbf{U}}{\partial t} + \frac{\partial F(\mathbf{U})}{\partial x} = \frac{\partial F_v(\mathbf{U})}{\partial x} + S_R(\mathbf{U}), \tag{2.1}$$

where the four vectors $\mathbf{U}$, $F(\mathbf{U})$, $F_v(\mathbf{U})$, $S_R(\mathbf{U})$, i.e., unsteady term, convection term, diffusion term, chemical source term, are defined as:

$$\begin{aligned}
\mathbf{U} &= \begin{pmatrix} \rho Y_1 \\ \rho Y_2 \\ \vdots \\ \rho Y_N \\ \rho u \\ E \end{pmatrix}, \qquad F(\mathbf{U}) = \begin{pmatrix} \rho u Y_1 \\ \rho u Y_2 \\ \vdots \\ \rho u Y_N \\ \rho u^2 + P \\ (E+P)u \end{pmatrix}, \\
F_v(\mathbf{U}) &= \begin{pmatrix} -\rho u Y_1 V_1' \\ -\rho u Y_2 V_2' \\ \vdots \\ -\rho u Y_N V_N' \\ \tau \\ q + \Phi \end{pmatrix}, \qquad S_R(\mathbf{U}) = \begin{pmatrix} \dot{\omega}_1 \\ \dot{\omega}_2 \\ \vdots \\ \dot{\omega}_N \\ 0 \\ 0 \end{pmatrix}.
\end{aligned} \tag{2.2}$$

In total, N+2 equations are solved including conversation equations of N species, momentum, and energy. In the species conservation equations, N is the total number of species, ρ is the mixture density, and Y_k, V_k', $\dot{\omega}_k$ are the mass fraction, diffusion velocity and production rate of species k, respectively. In the momentum equation, P is the hydro-static pressure and τ is the viscous stress,

$$\tau = \frac{4}{3}\mu \frac{\partial u}{\partial x}, \tag{2.3}$$

where μ is the mixture viscosity. In the energy equation, E is the total energy,

$$E = -P + \frac{\rho u^2}{2} + \rho \sum_{k=1}^{N} (Y_k h_k), \tag{2.4}$$

where h_k is the enthalpy of species k. q is heat flux while Φ is the viscous dissipation,

$$q = \lambda \frac{\partial T}{\partial x} - \rho \sum_{k=1}^{N} (Y_k h_k V_k'), \tag{2.5}$$

$$\Phi = u \frac{\partial \tau}{\partial x} + \frac{4}{3}\mu \left(\frac{\partial u}{\partial x} \right)^2, \tag{2.6}$$

where λ is the mixture thermal conductivity.

Transport and chemistry models

The gas mixture is assumed to behave as a Newtonian fluid. Therefore, the diffusion processes of mass, momentum and energy are modeled according to Fick's law of diffusion, Stokes law of friction, and Fourier's law of heat conduction, respectively. For a multi-species mixture system, mass diffusion processes are not as straightforward as a single-species gas. A system of diffusion equations needs to be solved in order to evaluate the diffusivity and the corresponding diffusion velocity of each species simultaneously. In the original A-SURF, a mixture-average diffusivity model (Kee et al., Sandia National Laboratories, Livermore, CA, USA, 1983) is employed, with a corresponding mass-weighted correction velocity model to ensure mass conservation. In ASURF-Parallel, a multi-component diffusivity model (Dixon-Lewis, 1968) is developed and added. The thermal diffusion phenomenon (Soret effect) is considered in both diffusivity models with the evaluation of thermal diffusion coefficients. All the associated transport properties are calculated through the TRANSPORT package (Kee et al., Sandia National Laboratories, Livermore, CA, USA, 1986) with input files containing fundamental transport and thermodynamic data of each species.

For the chemical system, the production rate of each species can be specified through associated chemical reactions. In ASURF-Parallel, the production rate is evaluated according to the law of mass action, while the reaction rate for each elementary reaction is modeled using the empirical Arrhenius law. The rate parameters are calculated through the CHEMKIN package (Kee et al., Sandia National Laboratories, Livermore, CA, USA, 1989) with an input file of chemical kinetic models (elements, species, and reactions are specified in a CHEMKIN-readable format).

Numerical schemes and methods

Finite volume method is employed as the discretization scheme, where integral quantities are evaluated over a control volume representing the domain of interest, instead of derivative quantities at a discretized point (finite difference method).

For the overall time integration, fraction-step procedures are used. The basic idea is that the stiff chemistry source terms are taken away from the transport terms such as diffusion and convection. In this way, a set of ordinary differential equations (ODEs), i.e., the homogeneous reacting system, and a set of partial differential equations (PDEs), i.e., the non-reacting and transport-only system, can be solved separately using appropriate numerical solvers. Both the first-order and second-order schemes are implemented in ASURF-Parallel. In the first-order method, PDEs are solved first, whose solutions are used as the input for the ODEs. Both PDEs and ODEs are solved for one entire time step. In the second-order method, i.e., Strang splitting (Strang, 1968), PDEs are solved first for only half of the time step. ODEs are then solved for one time step, followed by PEDs being solved for the another half time step.

For the reacting ODE system, explicit method, point-implicit method (Bussing and Mur-

man, 1988), and implicit VODE method (Brown et al., 1989) are available in ASURF-Parallel. All of these methods are of the first-order accuracy with regard to time. For the non-reacting PDE system, first-order Euler method, and second-order and third-order Runge-Kutta methods are used for the time integration. Regarding detailed spatial discretization, the MUSCL-Hancock (Van Leer, 1984) and central difference schemes, both of second-order accuracy with regard to space, are employed to evaluate the convection and diffusion terms.

2.2 Domain decomposition parallelization

This section is based on the final class report of *CS C267 / E C233 Applications of Parallel Computers*, Spring 2015, University of California, Berkeley. Discussions with Professor James Demmel on potential parallelization schemes and teamwork inputs from Charles Scudiere are acknowledged.

Introduction

Despite the wide use of the original serial A-SURF, it maintains its originally developed serial implementations of numerical schemes. Running the solver on certain problems, such as ignitions and deflagration to detonation transition (DDT), is slow with the necessarily small time steps (micro/nanoseconds) and micro space discretization (micro/millimeters). The performance issue becomes a serious problem with large chemistry kinetic models normally consisting of hundreds of species and thousands of elementary reactions, with the numerical intensity increasing exponentially on the order of $O(N^2)$, as N is the number of species. To achieve a simultaneously high-fidelity and high-performance of these sparse matrix numerical simulations utilizing modern multi-thread and multi-core computational structures, parallelized numerical solvers are expected. No existing parallelization has been implemented/reported on A-SURF yet.

In this section, detailed profiling analysis of the serial code performance was first conducted to identify its potential for parallelization. Accordingly, different parallelization implementations were attempted and their suitability for A-SURF was illustrated. A final parallelization scheme based on MPI was implemented and the final parallel version of this solver was tested on both an in-house server (Firebrand) and a computational server system (Hopper) at National Energy Research Scientific Computing Center (NERSC). The scaling and profiling results were then discussed. All the analysis and tests are based on simulation cases of hydrogen/air flames.

Profiling of Serial A-SURF

The solver is executed as the following simplified steps:

1. Initialize all the variables
2. Time advancing loop starts
3. Apply adaptive mesh refinement (AMR)
4. Output certain time-sensitive variables
5. Solve ODEs (chemistry); Update corresponding states
6. Solve PDEs (transport); Update corresponding states
7. Check if time reaches the preset end time: if yes, go to step 8; otherwise go to step 3
8. Time advancing loop ends; Output summary

A common simulation case of A-SURF will require thousands of time steps, making initialization and summary output time-wise negligible. Clearly, parallelizing the time advancing loop will most likely improve the solver performance. Within one time step, detailed profiling analysis was performed, as shown in Fig. 2.1. ODE solver contains chemical reaction rate calculation (Rate Cal.) and state updates, while PDE solver contains diffusion term calculation (Diff.), convection term calculation (Conv.) and state updates. According to the diagram, ODE and PDE solvers approximately split the total time. Therefore, parallelizing both ODEs and PDEs is necessary to achieve an overall performance improvement.

Attempted Parallelization Implementations

MPI

The serial implementation of the code performed a regular data logging between time steps. To parallelize this code, synchronization and uniformity of the information were required. We addressed this issue by dedicating ONE node to logging/writing files. To accomplish this task, all of the files which wrote an output were modified using ONE processor rank based condition test.

Load balancing was primarily handled by the splitting scheme used. We decomposed the domain between the processors based on their rank with regard to the number of grid cells, in both ODE and PDE solvers. The domain-decomposition splitting scheme is illustrated in Fig. 2.2. Since the update of one grid cell depends on its adjacent cells, each processor updates its own set of subdomain, based on both center cells inside the subdomain and additional boundary cells which ensure the updating correctness of the fringe of center cells. These boundary cells are abandoned after MPI_GATHER is called. The updated data set is then broadcast to every processor to start a new time step.

This step went through several iterations, with progressively improved performance:

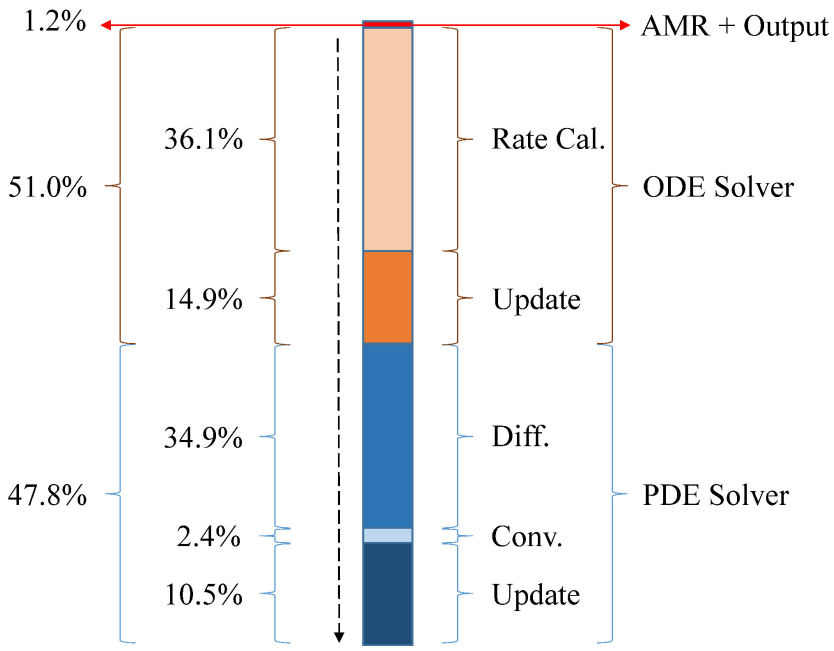

Figure 2.1: Profiling diagram of the original serial A-SURF.

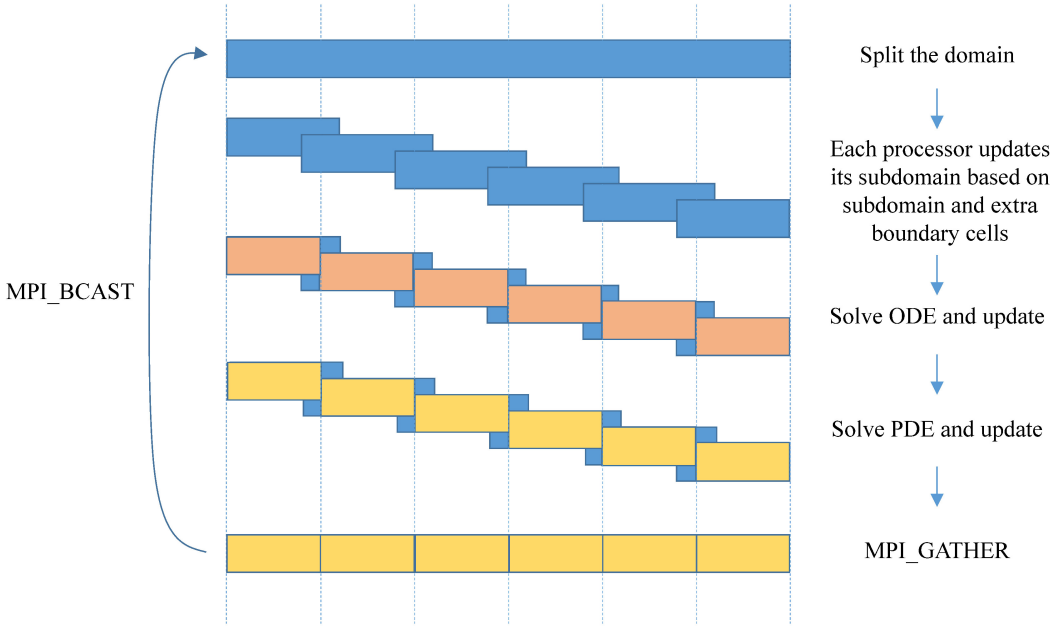

Figure 2.2: Schematic of the domain-decomposition splitting scheme.

- Initial with no Message Passing
- Passing of individual variables with Gather-Broadcast-Send
- Passing of individual variables with Gather-Broadcast
- Integration of ODE and PDE Send into unified Gather-Broadcast operation
- Pack and unpack of sending variables
- Consideration of alternatives

For a first step in the parallelization, each of the processors ran the serial code in unison and error checks were performed. This required finding and overcoming several compiler and execution challenges.

In the initial individual variables iteration, we chose the Gather-Broadcast-Send approach to pass each of the multidimensional state variables associated with the grid used in the code. Although this method was effective in communicating, we profiled and noticed message passing was using a significant percentage of the time and hurting overall performance.

Further successful improvements in performance were applied with further load balancing considerations of the unevenly divisible work loads. As the GATHER routines require equality of the size of data sent from each node, we chose to move operations to the gather master node. Although the work on the master was increased slightly, this allowed for the removal of a send operation that would otherwise be necessary for the gathering section of the code.

Since the ODE and PDE solvers were implemented such that the routines could run independently, the solvers handled their own message passing. For the next improvement in communication, we implemented a unified state variable update. To execute this, we aligned the work each processor performed at each time step at the end of each time step in the overarching solver routine, effectively cutting the send operations necessary in half.

In consideration of reducing the message overhead, weighing bandwidth, latency and MPI data transmission overhead, we implemented a further optimization to combine each of the SEND and GATHER operations performed on each variable. This improvement forged the two message sending operations into a single transmission. This algorithm, therefore, utilized the high bandwidth, and generated even better speed when the latency was significantly longer. The cost to do this optimization was for the processors to perform a pack and unpack sequence. With profiling of the resultant code, we found the costs associated with packing the data in a buffer for a single send operation was significantly outweighed by the reduction in the overall time savings from the reduction in message passing. Our estimates of the performance improvement were on the order of 100-500% in the variety of cases considered.

We also considered the use of the MPI_ALLGATHER routine for each processor's chunk of processed data. In making the decision, we weighed the saleability of this algorithm over

the Gather-Broadcast algorithm. Although the ALLGATHER routine requires a small send and a large receive per processor, reducing the necessary bandwidth, the performance hit in the number of sends required made this option undesirable. With the number of send operations of the Gather-Broadcast scaling as $O(N_p)$ and the MPI_ALLGATHER Routine scaling as $O(N_p^2)$, where N_p is the number of processors, we decided to keep the Gather-Broadcast due to the reduced send operations.

In a further iteration of parallelization optimization, calls to the MPI routines were minimized with the use of global FORTRAN COMMON variables. Following profiling and noting the number of calls to several of the functions, in the hundreds of thousands for even small times, we moved to remove MPI calls altogether in these routines.

Although it is known that global variables are usually to be avoided for code clarity, creating the global variables, in this case, were justified by the significant performance increase. Initialization of these variables was performed in the primary initialization step and values carried through and utilized through out the parallelization implementation. For example, for the commonly used values from calls to MPI_COMM_RANK and MPI_COMM_SIZE alone, performance was enhanced by over 10% in the cases considered.

OpenMP

Encouraged by the successful experience of MPI implementation, we attempted to further implement OpenMP. We followed the same strategy of file handling and loading balancing, wishing to update the shared domain with multiple threads. One advantage of OpenMP compared to MPI is that the splitting scheme can be automatically taken care by default OpenMP calls. The attempted implementation details can be simply summarized:

- Initialization of OpenMP
- Parallelization on variable updating loops by directly calling OpenMP DO

However, certain obstacles arose. One basic condition of OpenMP was to declare variables as shared or private. While we clearly knew that all the variables which were passed by MPI implementation should be declared as shared, we had a very hard time distinguishing other variables. Most of them were intermediate global single variables defined in the original serial code. On one end, if one variable was declared shared but used in updating every grid cell, the racing condition is inevitable. On the other end, if all other variables were declared as private, it defeats the purpose of OpenMP as it would just act like a "fake MPI". Another issue which happened in our attempt was that declaring a large amount of variable as private led to stack overflow. Therefore, we gave up on parallelizing such loops with heavy data dependency on intermediate global single variables.

Unfortunately, most of the loops in the code exploited such variables. Implementation of OpenMP on other simple loops did not gain significant performance improvement. Therefore, OpenMP is not used in the final version of parallel A-SURF.

SIMD

The system architecture of our local server is Intel(R) EM64T (x86_64) system, with Intel(R) Xeon(TM) processors. Intel(R) Fortran Compiler automatically optimizes with streaming SIMD Extensions 3 (SSE3) instruction support. Therefore, for the scaling test on the local server as well as further code application in Intel systems and processors, SIMD was enabled. Vectorization and loop unrolling were also automatically utilized with various compiler flags.

Results and Discussions

Scaling tests were performed on two platforms: Firebrand (in-house local server) and Hopper. Firebrand has Intel(R) EM64T (x86_64) system, with two Intel(R) 8-core hyper-threading Xeon(TM) processors. The total available threads are 32. Hopper has over thousands of compute nodes. Each compute node has two AMD Opetaron 6172 12-core processors.

Scaling tests on Firebrand

On Firebrand, both strong scaling and space-wise weak scaling were tested. For the weak scaling, the total number of grid cells increased with increasing number of processors. Maximum thread number used was 24. The results are shown in Fig. 2.3. Both ODE and PDE time scaled reasonably well in both strong and weak scaling tests, while the total time fell behind due to communication overhead.

Scaling tests on Hopper

On Hopper, both strong scaling and time-wise weak scaling were tested. For the weak scaling, total simulation times increased with increasing number of processors. Maximum processor number used was 32. The results are shown in Fig. 2.4. While the strong scaling test still showed promising results, weak scaling performance dropped significantly with a larger number of processors. Besides communication overhead, dynamically AMR also affects time-wise weak scaling. Physically, with longer simulation time would more fuel be burned, creating more temperature gradients. As a result, AMR added slightly more cells in the calculation domain, which made the simulation time even longer.

We did not go up to even larger number of processors on Hopper, as the communication overhead has almost dominated the total time according to the strong scaling results. Profiling results of next session demonstrated the existence of communication overhead.

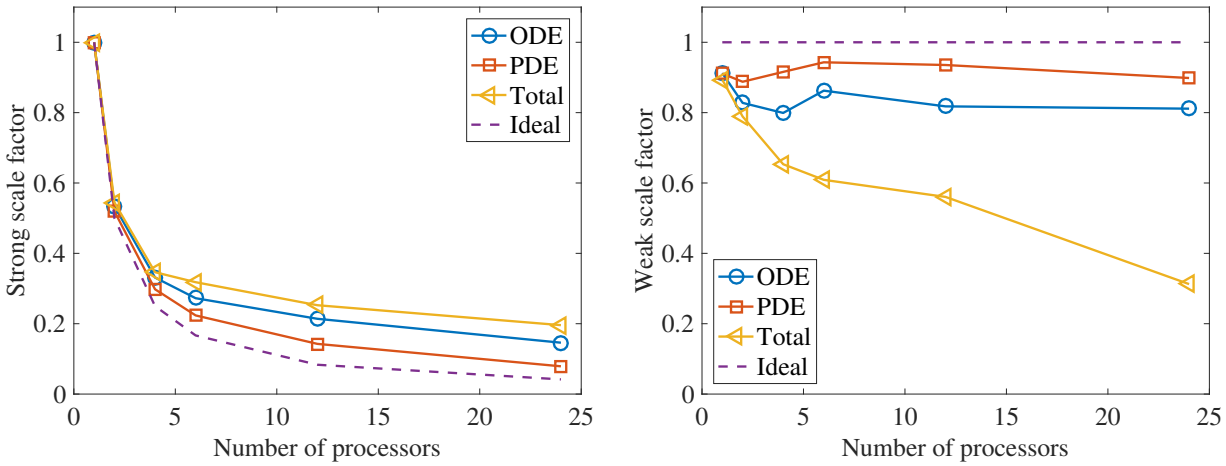

(a) (b)

Figure 2.3: Scaling test on Firebrand: (a) Strong scaling test; (b) weak scaling test with regard to grid space.

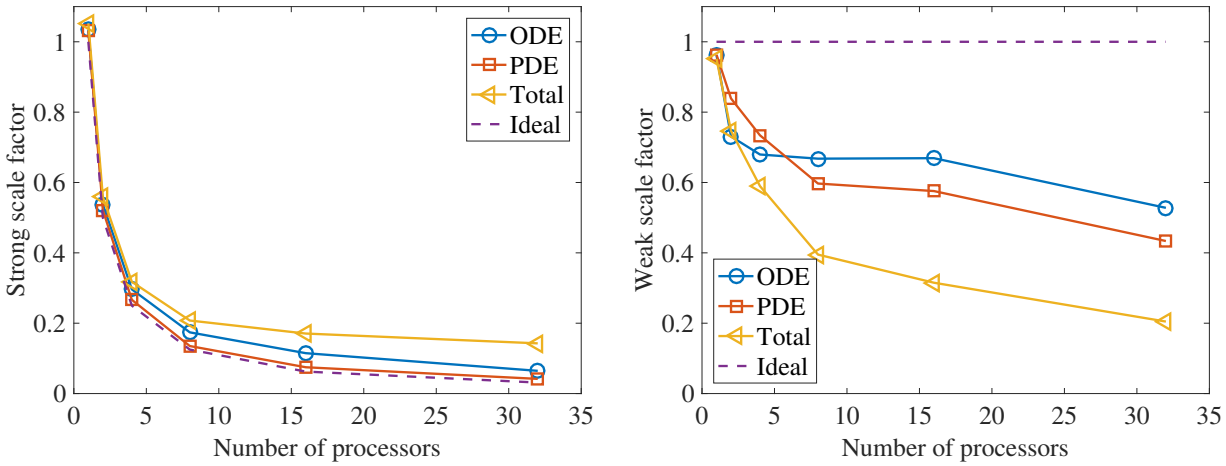

(a) (b)

Figure 2.4: Scaling test on Hopper: (a) Strong scaling test; (b) weak scaling test with regard to time.

Profiling of Parallel A-SURF

Profiling of parallel A-SURF was conducted, where MPI operation time profiling is included. MPI operation contains MPI_GATHER (GAT.), MPI_BCAST (BCA.) and data pack/unpack (P/UP). The profiling results of two different cases are shown in Fig. 2.5. More interestingly, different from both strong and weak scaling tests, these two profiling tests shared the same number of processors and simulation time but a different number of grid cells. From the diagram, we can see that Case (b) with the larger number of grid cells

actually has a smaller fraction of MPI operation time out of the total time. The results actually indicated that the bandwidth of message passing was relatively large compared to messages passed between processors in A-SURF. As we increased the number of grid cells, the communication time remained the same as a same amount of processors involved. In the meanwhile, all ODE, PDE and AMR scaled up with a larger number of grid cells. Therefore it resulted in a smaller MPI fraction in case of larger number of grid cells.

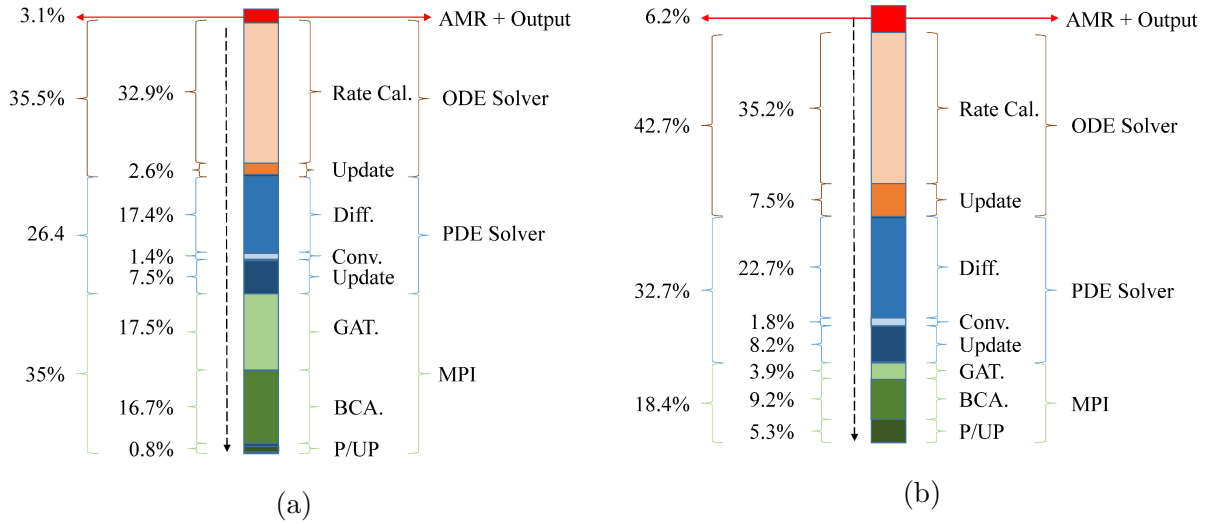

Figure 2.5: Profiling diagram of ASURF-Parallel on Firebrand; Case (a) and (b) used the same number of processors and the same simulation time, while Case (b) has 5 times more grid cells compared to that of Case (a).

Summary and Future Work

Domain-decomposition parallelization was successfully implemented on A-SURF. A list of tasks accomplished was provided as followed:

- Conducted a detailed profiling of the serial code, pointing out parallel potentials;
- Attempted different parallelization with detailed consideration and analysis;
- Implemented a final and successful parallelization scheme using MPI;
- Performed strong and weak scaling tests on different platforms, showing promising performance;
- Conducted two detailed profiling of the parallel code.
- Examined the effect of changing the number of processors, number of grid cells and simulation time, with corresponding scaling and profiling tests.

- Overall, a significant speedup, with the speed-up factor up to 10, is achieved.

There are certain aspects of future work to be considered:

- Parallelism on I/O and AMR, in which way MPI operations between time steps can be avoided;
- More advanced load balancing scheme is expected, as the current version depends on the number of grid cells only;
- Clean up certain intermediate global variables or convert them into local variables, to enable effective OpenMP implementation.

Chapter 3

Flame Speed

In this chapter, the effect of mixture composition stratification on laminar flame speeds of stratified fuel/air mixtures is numerically investigated and studied. First, a comprehensive literature review of the past and current research efforts of stratified flame speeds is given and discussed. Then, flame characteristics used to describe stratified and homogeneous flames are defined and illustrated. For specific case studies, stratified hydrogen/air flames are investigated first, followed by three hydrocarbon/air flames, i.e., methane, propane, and n-heptane. Finally, a stratified flame speed model for methane/air mixtures is proposed, developed and tested.

3.1 Literature review

After a stratified mixture is successfully ignited, a flame will be established and propagate through the stratified mixture. Such mixtures exist in a wide range of industrial applications, such as DISI engines. Flame propagation speeds of in-cylinder stratified fuel/air mixtures can differ from those of homogeneous mixtures based on local and instantaneous equivalence ratios. How fast the stratified flame propagates compared to the corresponding homogeneous flames is a key question to answer as to the determination of combustion duration and emissions. Both practically and fundamentally is the difference between laminar flame speeds of stratified and homogeneous mixtures neither well understood nor quantified.

There are two typical types of stratified flames: stratified flames propagating perpendicular to the mixture stratification layer, or along the layer. The first type of stratified flames is often investigated with a detailed discussion on the structure of tribrachial triple flames (Chung, 2007; Im and Chen, 1999; Guo et al., 2005), as a diffusion flame branch is created along the stoichiometric mixture fraction line. In comparison, the second type of stratified flames, when the propagation of stratified flames occurs along the mixture stratification layer, only has the premixed flame branch. It is relatively complicated as flame characteristics are mostly transient and change in time due to flame passing through differ-

ent local mixture compositions across the stratification layer. This chapter focuses on the latter stratified flames, which propagate along the mixture stratification layer.

There have been extensive experimental, theoretical and numerical research on stratified flames propagating along mixture stratification layer. Researchers have experimentally observed that stratified flames propagated at different speeds compared to homogeneous flames. Karim and Tsang (1975) used a circular pipe filled with two mixtures separated by a plate, where a stratified mixture was formed after removing the separation plate. They found that the flame speeds of a rich–to–stoichiometric methane/air stratified flames were close to the corresponding quasi-homogeneous flame speeds, while the stoichiometric–to–lean stratified flame were about 30% faster than the corresponding homogeneous flames. Girard et al. (1979) adopted the soap bubble method and studied a laminar hemispherical flame in a rich–to–lean mixtures. The mixture stratification was created by filling a soap bubble with a richer mixture while the rest of the vessel was filled with lean mixtures. The flame was initiated at the center of the bubble by a spark plug. Both hydrogen and propane were tested. When the radius of the bubble increased, an increase in the burning velocity was indicated according to a reduced combustion time, defined by the time reaching the maximum pressure. Badr and Karim (1984) performed a similar experimental investigation and extended Karim and Tsang's conclusion: stratified flames propagating from mixtures with higher flame speeds to those with lower speeds, e.g., stoichiometric to either lean or rich, were faster than the corresponding homogeneous flames, while stratified flames with opposite directions were close to homogeneous flames. Moreover, the observed stratified flame speeds can be correlated to the homogeneous flame speeds corresponding to fuel concentrations at the ignition point and concentration gradients. However, the correlation was case-specific and valid only under simple stratification cases, where stratification does not change its direction. Ra and Cheng (2001) revisited the soap bubble idea. The stratification was created by placing a small spherical soap bubble containing near-stoichiometry methane/air mixtures, in the center of the vessel containing lean mixtures. The bubble was ignited by a laser beam. Both the time history of pressure and the growth of the flame kernel radius using high-speed Schlieren technique were recorded. A "back-support" effect was observed, as an increase in the burning velocity was found during the step layer compared to the corresponding homogeneous flames. They found that for a given lean mixture, the initial burning velocity enhancement in the transition increases as the richer mixture equivalence ratio increases. Kang and Kyritsis (2005, 2007) studied a similar stratified flame of methane/air mixtures in a novel burner that allowed accurate control of mixture stratification using convective-diffusive balance of two fresh methane/air mixture streams. They found that from stoichiometric to either leaner or richer, the stratified flame velocities are higher than the homogeneous flames. Furthermore, the increase in flame speed was more prominent when the flame approached the flammability limits and encountered higher equivalence ratio gradients. Balusamy et al. (2014) performed stratified flame experiments of propane/air in a constant volume chamber, where a rich mixture was ignited and the corresponding flame propagated into lean mixtures. The flame propagation in the lean mixtures was found back-supported by the ignition in richer

conditions, as the flame benefited from the rich composition of the burnt gas compared to that of lean homogeneous flames.

Despite the fruitful observations from experimental studies, there still remain critical questions which cannot be fully resolved by experiments:

1. In a stratified flame, both thermal and mass diffusion processes are different from those in the corresponding homogeneous flames. Experimental evaluation of each process cannot be conducted exclusively thus their comparative impacts on laminar flame speeds of stratified flames were yet understood.

2. Specific experimental setups, including propagation directions and boundary conditions, might introduce additional effects or biases. For example, for flames propagating vertically upwards, the hot burned gases are more buoyant and tend to propagate faster relative to the flame and thereby assist the convective mass transfer of active species ahead of the flame.

3. Flame stretch and curvature undermine the accuracy of measured flame speeds. For example, in Balusamy et al. (2014), due to the initial mixture preparation and ignition setup, an oval contour of the flame front was developed instead of an ideal sphere. Consequently, tracking flame front propagation and extrapolation of the unstretched laminar flame speed are problematic.

4. Discrepancy exists between stoichiometry of unburnt mixture and mixtures at flame front, due to preferential diffusion of lighter species. As some lighter but important chemical species and radicals, e.g., H, H_2, diffuse much faster than other species, mixture composition at the flame front can be quite different from that of the corresponding unburnt mixture. Therefore, the structure of a pre-defined stratified mixture based on unburnt mixtures might change during the course of stratified flame propagation.

In order to compensate the above experimental limitations, theoretical and numerical studies with idealized setups are conducted to reduce the problem complexity and help identify dominant processes which are responsible for the differences between stratified and homogeneous flames. In terms of theoretical analysis of stratified flames, Mikolaitis (1984) performed an asymptotic analysis using exponential scaling of premixed flame propagation with thermal and concentration gradients. The results were restricted to the scenario where the flame preheat zone thickness is very thin and smaller than the length scale of initial temperature or concentration variations. Under this restriction, the author concluded that the flame propagation can be simply determined by the local values of temperature and mixture composition from the initial conditions. As the author pointed out in the paper, such an exponentially thin flame is not of practical significance for most applications. For this reason, Bissett and Reuss (1986) adopted a similar approach and obtained a slowly-varying flame with the usual algebraic distance scaling for the flame. They demonstrated

that the burning rate of the slowly-varying flame propagating through a region of varying temperature or mixture composition is different from that of corresponding homogeneous flames. In recent years, Kang and Kyritsis (2005, 2009) analyzed their experimental results and performed a corresponding asymptotic analysis. Their conclusions were very similar to that of Bissett and Reuss (1986) and they pioneered the development of stratified flame speed model. Two different models were proposed: 1) An integrated measure Q model was proposed in (Kang and Kyritsis, 2005), where Q is the product of the average equivalence ratio gradient times the ratio of the average over the local value of equivalence ratio. A critical value $Q_0 = 0.018$ mm^{-1} is used to determine whether a stratified flame starts to deviate from its corresponding homogeneous flames. 2) A theoretical model was further proposed (Kang and Kyritsis, 2009) on the basis of the hypothesis that stratified flames differ from homogeneous flames due to the effect of cumulative heat support from burnt gas. The model predicted quantitatively well with their experimental results of stoichiometric–to–lean or lean–to–leaner stratified flames but not rich flames.

Much understanding of stratified flames and the underlying physical processes has also been achieved through numerical simulation investigations. Cruz et al. (2000) performed 1-D unsteady simulations of laminar stratified methane/air flames. They concluded that the propagation of lean–to–rich stratified flames is influenced mainly by heat from burned gases, i.e., thermal effect. For rich–to–lean stratified flames, the propagation is dominated by production and consumption of molecular hydrogen in the rich burnt gas, i.e., chemical effect. However, although the differences between temperature and species distributions at the flame front of stratified flames and of homogeneous flames were reported, an analysis with adequate details about how these diffusion processes compete was not given. Zhou and Hochgreb (2013) conducted numerical simulations of methane/air counterflow stagnation flames and confirmed that methane/air stratified flames are primarily dominated by the diffusion of heat under lean conditions, and diffusion of H_2 under rich conditions. In contrast, Zhang and Abraham (2016) investigated planar stratified methane/air flames. They confirmed that additional diffusion of heat and active species had made rich–to–lean stratified flames faster than corresponding homogeneous flames. More importantly, they studied comparative effect of thermal and species diffusion by considering equal-diffusivity transport model and concluded that species diffusion is more important in increasing flame speeds of stratified mixtures.

This chapter focuses on transient numerical simulations of one-dimensional planar flames of stratified and homogeneous mixtures. Compared to previous studies, features of the following presented research include:

1. Flame characteristics of both stratified and homogeneous mixtures, including equivalence ratios and laminar flame speeds, are clearly defined

2. Different fuels were studied with detailed chemical kinetic models and consideration of preferential diffusion processes

3. Different setups of stratification were investigated and a stratified flame speed model covering both rich and lean mixtures was developed and tested

3.2 Flame characteristics

Flame characteristics in stratified mixtures are not as well-defined as those in homogeneous mixtures due to the composition variation across the flame zone (Cruz et al., 2000). In order to make meaningful comparisons between stratified and homogeneous flames, several flame characteristics are specifically defined and explained in the following.

Flame front

Flame front is defined by the location of maximum heat release rate, if not specified otherwise.

Equivalence ratio

The conventional definition of equivalence ratio, i.e., the ratio of the fuel/air ratio to the stoichiometric fuel/air ratio, is suitable for unburnt mixtures where fuel and air are unanimously defined. However, this definition is not applicable to the instantaneous mixtures within the flame zone due to two issues. First, fuel and oxidizer may have reacted into intermediate species so that the equivalence ratio can no longer be calculated based on fuel and air only. Second, differential diffusion of species alters the mixture compositions across the flame zone. Note that both issues exist in both stratified and homogeneous flames. For a homogeneous flame, its equivalence ratio can be uniquely defined using the unburnt mixture. In contrast, stratified flames are more complicated in the absence of a unique unburnt mixture.

In this study, the reference equivalence ratio is defined on the basis of the element composition of fuel/air systems:

$$\phi = \frac{X_H + 4X_C}{2X_O}, \tag{3.1}$$

where X_H, X_C and X_O denote the mole fractions of elements H, C and O respectively. Figure 3.1 shows the computed equivalence ratios of a series of methane/air homogeneous flames with the unburnt temperature at 300 K and pressure at 1 atm. Each point represents one specific homogeneous flame and ϕ_u refers to the equivalence ratio calculated based on the element composition of the unburnt mixture while ϕ_f is based on the element composition at flame front. The location of maximum heat release rate is referred to as the flame front. The difference between ϕ_u and ϕ_f is shown in the lower part of the figure. Due to differential diffusion, ϕ_u and ϕ_f can differ up to 0.04 in methane/air homogeneous flames under ambient conditions. For consistent comparisons between stratified and homogeneous flames, Equation (3.1) will be used for computing the equivalence ratios.

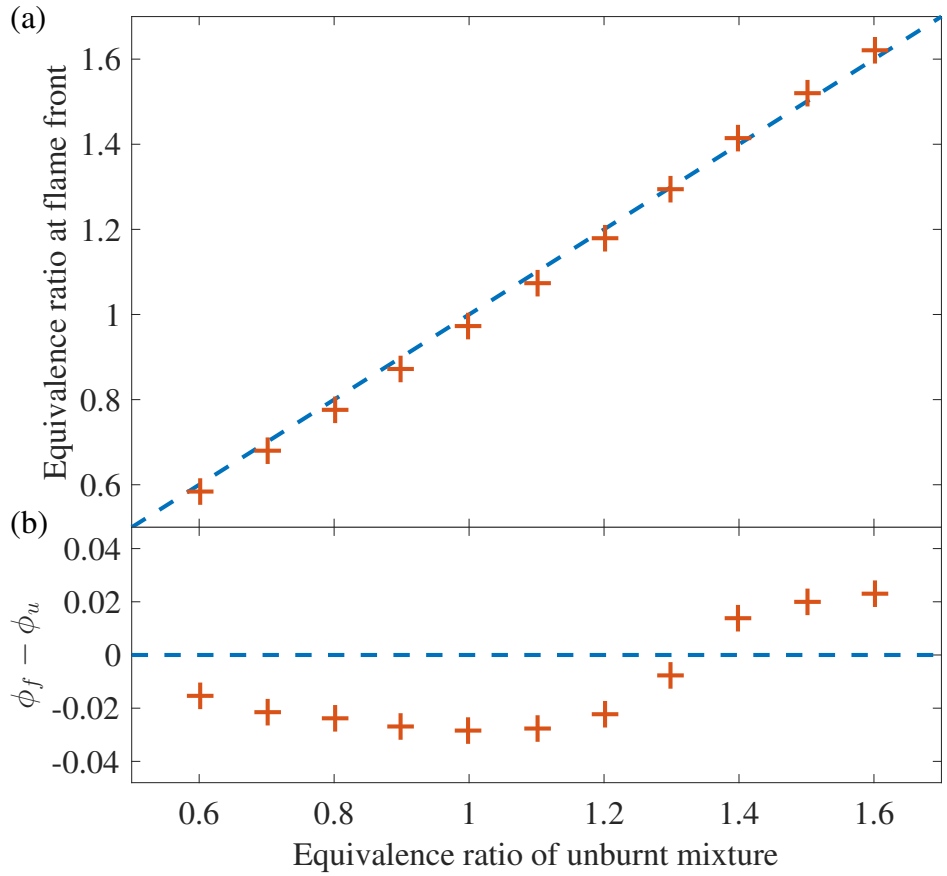

Figure 3.1: (a) Equivalence ratio of unburnt mixture (ϕ_u) and equivalence ratio at flame front (ϕ_f), and (b) their differences, of methane/air homogeneous flames.

Laminar flame speed

Both fuel consumption speed and flame front propagation speed are used. For the detailed descriptions of these two speeds, please refer to Chapter 1, Section 1.2. Fuel consumption speed will be calculated as below:

$$S_c = -\frac{1}{\rho_u Y_F^u} \int \dot{\omega}_F dx, \tag{3.2}$$

where Y_F^u is the mass fraction of fuel species in the unburnt gas; ρ_u is the unburnt gas density and $\dot{\omega}_F$ is the fuel production rate. Theoretically, $Y_F^u - Y_F^b$ may be used in Eq. 1.6 instead of Y_F^u, especially for rich mixture flames (Poinsot and Veynante, 2005). However, in stratified flames, Y_F^b is not well-defined as the burnt gas is stratified. Even for homogeneous flames, uncertainty exists in Y_F^b as the burnt gas composition of propagating flames can deviate from the corresponding equilibrium composition (Wu et al., 2014). Therefore, Y_F^u is used for both stratified and homogeneous flames.

Different integral limits are applied to distinguish between local and global fuel consumption speeds. In Fig. 3.2, both 0% and 5% cutoff integral limits are illustrated. While 0% cutoff represents the integral over the entire domain, 5% means that the integral will be conducted only over the domain where local heat release rate exceeds 5% of the maximum heat release rate. In this way, 5% cutoff fuel consumption speed is considered as the local fuel consumption speed and therefore represents local flame characteristics.

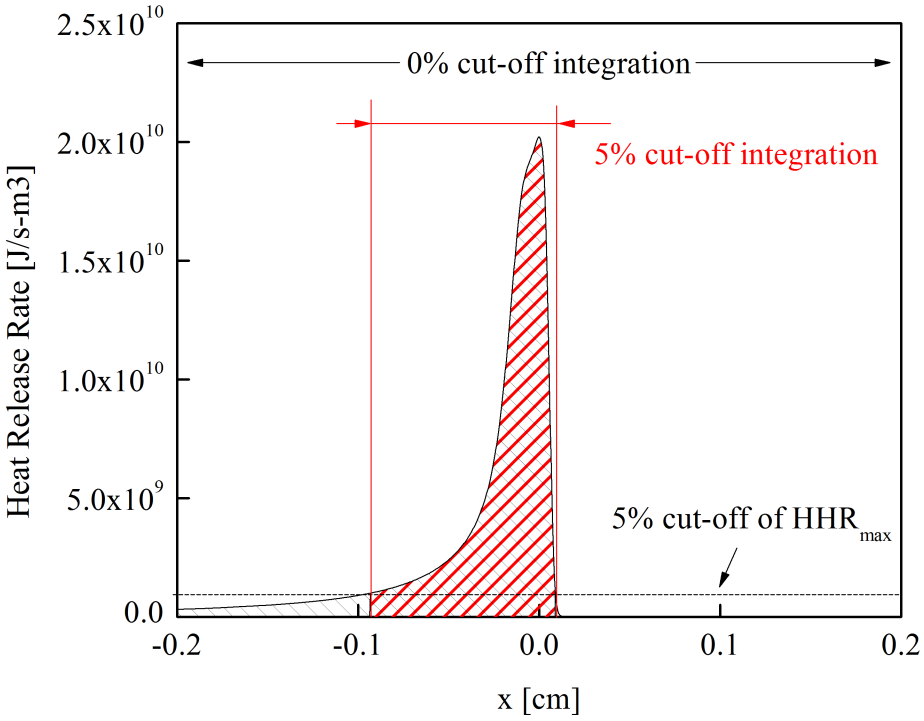

Figure 3.2: Fuel consumption speed integration with different cutoff integral limits with regard to maximum heat release rate.

Flame front propagation speed, S_f, is defined as the physical moving speed of the flame front in the calculation domain. Note that S_f can be directly measured from experiments and is related to S_L^0. In homogeneous flames, the relation between S_f and S_L^0 can be expressed as

$$S_f = \frac{\rho_u}{\rho_b} S_L^0, \tag{3.3}$$

Similar to Y_F^b, ρ_b is not well-defined in stratified flames as well as propagating homogeneous flames. Therefore S_L^0 cannot be unambiguously derived from the above relation.

Fluid expansion speed, S_{exp}

Propagation of flame front is resulted from not only the burning velocity that flame propagates into unburnt mixture, but also the expansion of burnt gas due to additional heat release. It is useful to define burnt gas expansion speed for assessing the fluid expansion effect on the flame front propagation speed. In order to formulate this speed definition, each computational cell is regarded as a single 1-D control mass, which can only expand or shrink but not exchange mass with neighbor cells. The cell size changing rate represents the gas expansion due to heat release. Therefore, the sum of the size changing rates of all cells, from closed end to flame front, will represent the total burnt gas expansion. If the burnt gas heat release and consequential expansion differ between SF and HF, the corresponding differences will be observed in fluid expansion speeds as well as flame front propagation speeds. To calculate the cell size changing rate, mass conservation is applied to each single 1-D cell:

$$d(\rho x_c) = 0, \tag{3.4}$$

where x_c stands for the cell size. Taking the derivative of the above equation with respect to time yields:

$$\frac{dx_c}{dt} = -\frac{x_c}{\rho}\frac{d\rho}{dt}. \tag{3.5}$$

Based on ideal gas law with constant pressure, density changing rate can be written as temperature changing rate. Molecular weight of the mixture is assumed unchanged as burnt gas composition has approximately reached equilibrium. As temperature increase is related to heat release, temperature changing rate can be further expressed as a function of local heat release rate, density and specific heat. Therefore, the size expansion rate can be eventually written as

$$\frac{dx_c}{dt} = \frac{x_c}{T}\frac{dT}{dt} = \frac{x_c}{\rho c_p T}\frac{dq}{dt} = \frac{x_c \dot{q}}{\rho c_p T}, \tag{3.6}$$

The fluid expansion speed is then determined by integrating the expansion rate of all grid cells up to the location of flame front.

$$S_{exp} = \int_0^{x_f} \frac{\dot{q}}{\rho c_p T} dx, \tag{3.7}$$

where x_f stands for the location of flame front. Numerically it can be also expressed as

$$S_{exp} = \sum^{f} \frac{x_c \dot{q}}{\rho c_p T}. \tag{3.8}$$

Normalized diffusion Speed, $\hat{V}_k'$

In order to quantify the thermal and chemical effects introduced by the burnt gas of stratified flames, thermal and species normalized diffusion speeds are defined as following:

$$\hat{V}_T' = -D_T \frac{d \ln T}{dx}, \qquad D_T = \frac{\lambda}{\rho c_p} \tag{3.9}$$

$$\hat{V}_k' = -D_k \frac{d \ln Y_k}{dx}, \tag{3.10}$$

where D_T is thermal diffusivity and D_k is mass diffusivity of species k. These quantities are used in the energy and species conservation equations and represent how fast heat and chemical species diffuse relative to fluid velocity. Normalized diffusion speed is thereby defined as diffusion velocity relative to the lab frame, i.e., diffusion velocity plus local fluid velocity. Thermal or chemical effects on local flame characteristics will exist only if heat or mass diffusion on the basis of fluid velocity are fast enough to catch up the propagation of flame front.

Flame thickness, stratification gradient and thickness

Figure 3.3 presents the computed temperature and equivalence ratio profiles of both (a) a homogeneous flame and (b) a stratified flame, where $x = 0$ denotes the location of the flame front. The region $x > 0$ corresponds to the unburnt mixture. For the homogeneous flame, ϕ_u is 1.00. For the stratified flame, the flame experiences an equivalence ratio change from $\phi_u = 1.6$ to 0.6. At the flame front of this particular moment, the equivalence ratio, ϕ_f, of both flames is 0.97. As seen in Fig. 3.3, these two flames have similar temperature profiles. In Fig. 3.3(b), the stratified flame experiences a decreasing profile of equivalence ratio as it propagates from a rich mixture into a lean mixture. The flame thickness can be calculated on the basis of temperatures by the following equation (Law and Sung, 2000),

$$d_f = \frac{T_b - T_u}{\left|\frac{dT}{dx}\right|_{max}}. \tag{3.11}$$

Based on d_f, the instantaneous equivalence ratio gradient at the flame front can be approximated by

$$\frac{d\phi}{dx} = \frac{\phi_f^b - \phi_f^u}{d_f}, \tag{3.12}$$

where ϕ_f^u and ϕ_f^b denote the equivalence ratios at the boundaries of flame zone. As d_f changes with flame dynamics, equivalence ratio gradient at flame front is a transient property of a propagating flame and it can be evaluated instantaneously. The equivalence ratio gradient at flame front is used to describe the instantaneous stratification conditions when the flame front passes through the stratification layer and therefore a key parameter in stratified flame speed models.

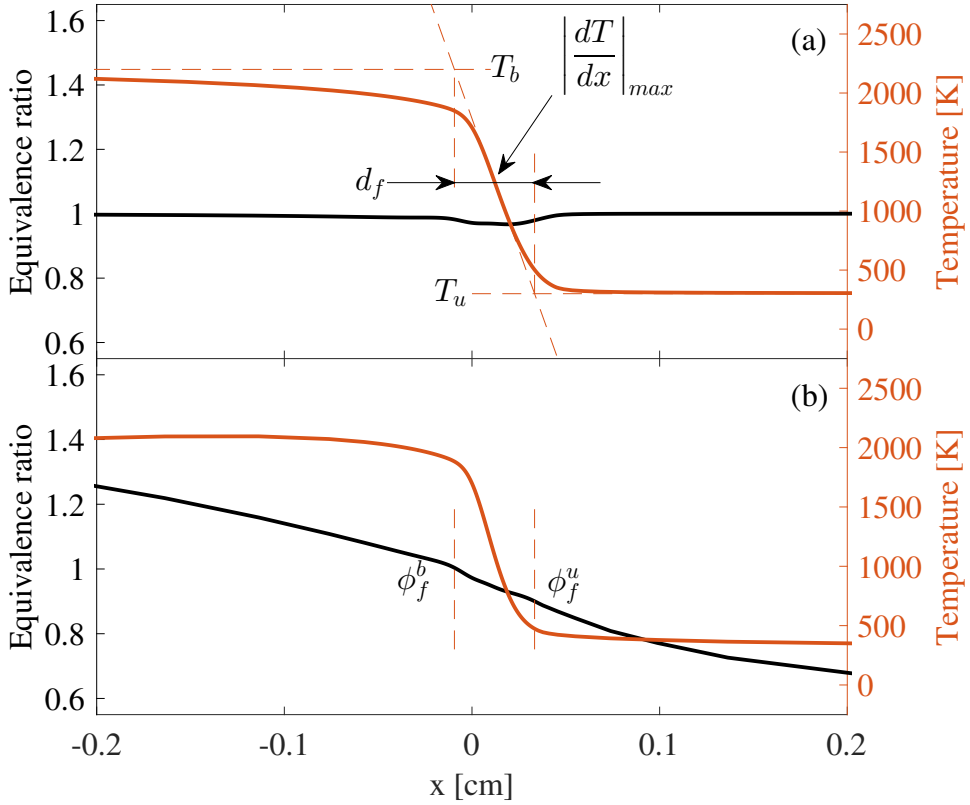

Figure 3.3: Equivalence ratio and temperature profiles of (a) a homogeneous flame and (b) a rich–to–lean stratified methane/air flame, $\phi_f = 0.97$.

To quantify the degree of initial stratification in different stratified configurations, stratification thickness d_s is defined as

$$d_s = \frac{|\phi_2 - \phi_1|}{\left|\frac{d\phi}{dx}\right|_{u,max}}. \tag{3.13}$$

In the case of stratified flames propagating from unburnt mixture ϕ_1 to ϕ_2. d_s is calculated when the flame front in stratified flames reaches the stratification layer as shown in Fig. 3.4. Therefore d_s is based on equivalence ratio of unburnt mixtures and least affected by differential diffusion.

3.3 Hydrogen/air stratified flames

This section is based on the paper published in *Combustion and Flame* (Shi et al., 2016).

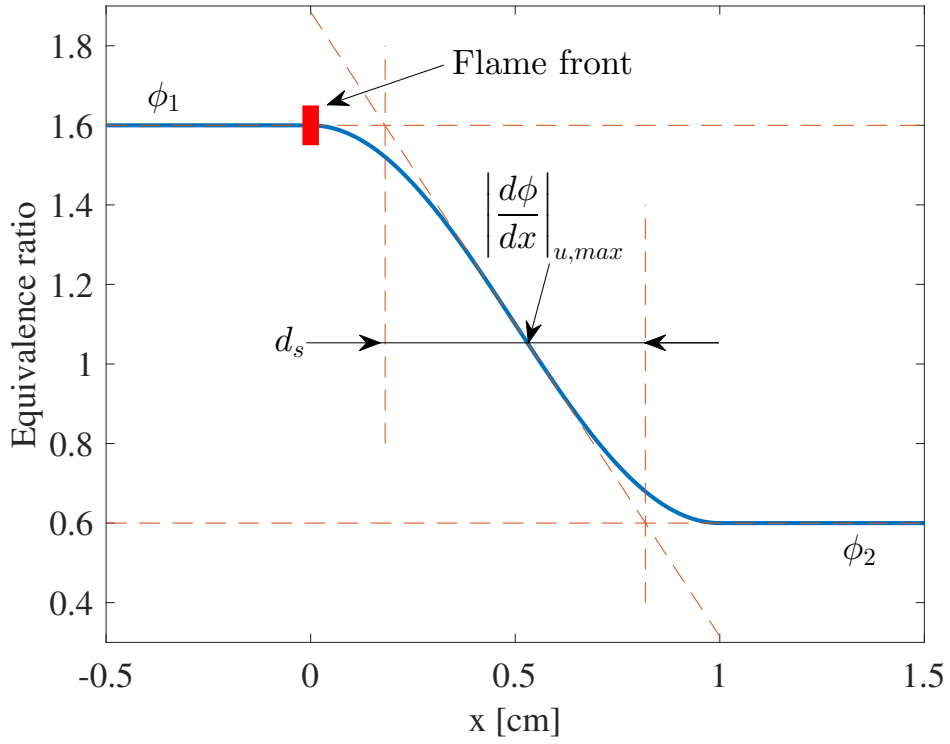

Figure 3.4: Schematic of stratification thickness calculation in the rich–to–lean stratified flame propagating from $\phi_u = 1.6$ to $\phi_u = 0.6$.

Introduction

As one of the fundamental combustible mixtures, hydrogen/air flame generates intermediate radicals, which appear in almost all hydrocarbon flames. Therefore a thorough understanding of hydrogen/air flames is essentially important to establish the first picture of fuel stratification concept.

The objective of this section is to understand how hydrogen/air stratified flame behaves differently in comparison to homogeneous flames. More specifically, the following questions are to be answered:

1. What is the detailed mechanism that stratification introduces thermal effect or chemical effect, if any, leading to variation of flame characteristics between stratified flames and homogeneous flames?

2. What is the role of differential diffusion of chemical species in stratified flames? Is it related to the chemical effect?

3. How do flame characteristics respond to different degrees of stratification?

To answer these questions, fuel consumption speed, as well as flame front propagation speed, are used to quantify the differences between stratified and homogeneous flames. Two transport models with equal diffusivity and mixture-average diffusivity assumptions respectively are considered and analyzed.

Numerical model and setup

The present numerical model represents hydrogen/air flame propagation in one-dimensional (1-D) planar coordinate with one end closed and the other open, as sketched in Fig. 3.5. The flame is initialized at the closed end and propagates toward the open end. Stratification is introduced by specifying a step change in the initial equivalence ratio profile. The simulated condition is analogous to constant-volume bomb experiments where ignition occurs in the center and flame propagates outwardly (Kuznetsov et al., 2012), or to tube experiments where flame propagates in a pipe from its closed bottom to the open end (Dahoe, 2005).

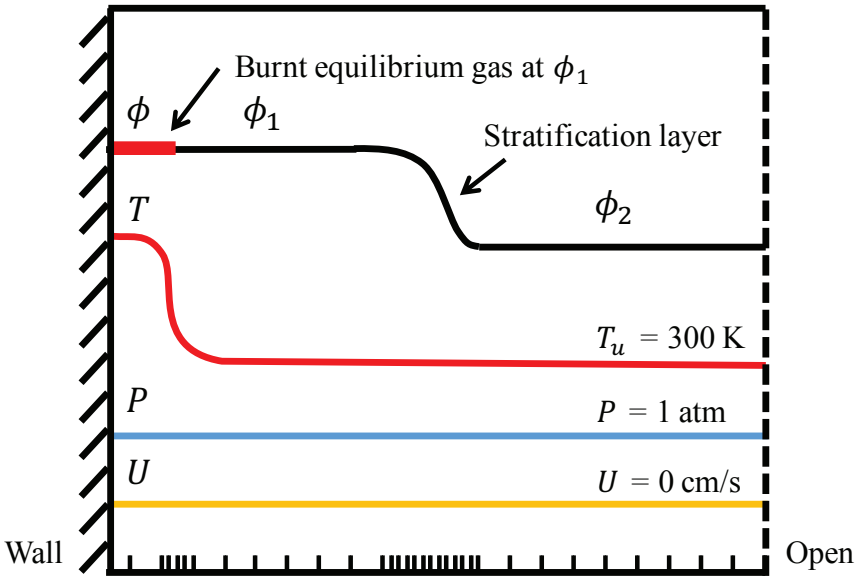

Figure 3.5: Schematic of stratified flame propagating in 1-D planar coordinate.

The numerical simulation is carried out by ASURF-Parallel. A 9-species detailed chemistry mechanism of hydrogen/air mixture (Burke et al., 2012) is used. For this study of stratified flames, three major modifications have been made: 1) application of transport model with equal diffusivity assumption, 2) specification of the initial equivalence ratio profile through a step change and 3) additional AMR based on local equivalence ratio gradient. All the cases reported here were conducted in a 50 planar cm domain. The initial temperature is 300 K while pressure is 1 atm. The reflective boundary condition is applied at the

first grid point to simulate the closed end, while transmissive boundary condition at the last grid point to simulate open end. The time step is specified by a fixed CFL number of 0.25.

The flame is initialized by imposing burnt gas composition and temperature profiles from CHEMKIN PREMIX (Kee et al., Sandia National Laboratories, Livermore, CA, USA, 1985) to the grid points on the left side so that the flame can be established with relatively small time duration and the initial unsteadiness is minimized. The step change in equivalence ratio is placed a certain distance away from the initial flame so that the flame will achieve a steady state when it reaches the stratification. The step itself is specified by a sharp change between ϕ_1 and ϕ_2 across several grid points, as shown in Fig. 3.5. Stratification thickness in all cases demonstrated in this study is of the order of 0.1 cm if not specified otherwise.

Results and discussion

In piston engines, fuel stratification is created by fuel injection into the combustion chamber. Ignition is often initiated in a rich mixture, creating stratified flames propagating from rich to lean ambient mixtures. Therefore, rich–to–lean stratified flame is the most common stratified flame in practical applications and thus the primary focus in understanding stratified flames. Other stratification cases are also considered in this study as theoretical references.

Equal diffusivity results (Le = 1)

In this section, equal diffusivity is assumed: mass diffusivity of all chemical species are set to the thermal diffusivity, i.e. Lewis number is set to one ($Le = 1$). Thermal diffusivity is calculated on the basis of local mixture properties. This assumption is a useful tool to separate thermal and chemical effects when studying stratified flames, as it suppresses differential diffusion and examines whether thermal effect itself will lead to any difference between SF and HF. As differential diffusion is excluded, ϕ_f is equal to ϕ_u in homogeneous flames.

Figure 3.6 compares fuel consumption speed results calculated with both 0% and 5% cutoffs, of both stratified flames (SF) and homogeneous flames (HF). The stratified flame is propagating from a homogeneous charge of equivalence ratio 2.0 (rich) to that of 0.5 (lean) through the step change. Note that the fuel consumption speeds based on 0% cutoff peak at $\phi_f = 1.0$, and some certain differences are observed between SF and HF. In contrast, the 5% cutoff results peak at $\phi_f = 1.3$ and collapse on top of each other, indicating that there is no difference in local fuel consumption between SF and HF.

To interpret these results, detailed flame characteristics near flame front such as temperature and species distributions are investigated. Figure 3.7 shows the heat release rate, temperature, species mole fraction and their corresponding diffusion speeds profiles of SF and HF when $\phi_f = 1.2$. The position at $x = 0$ represents the location of the flame front. Thus the region of $x < 0$ represents burnt gas near the flame and the other side is unburnt. In Fig. 3.7(a), heat release rate profiles are identical between SF and HF, which agree with

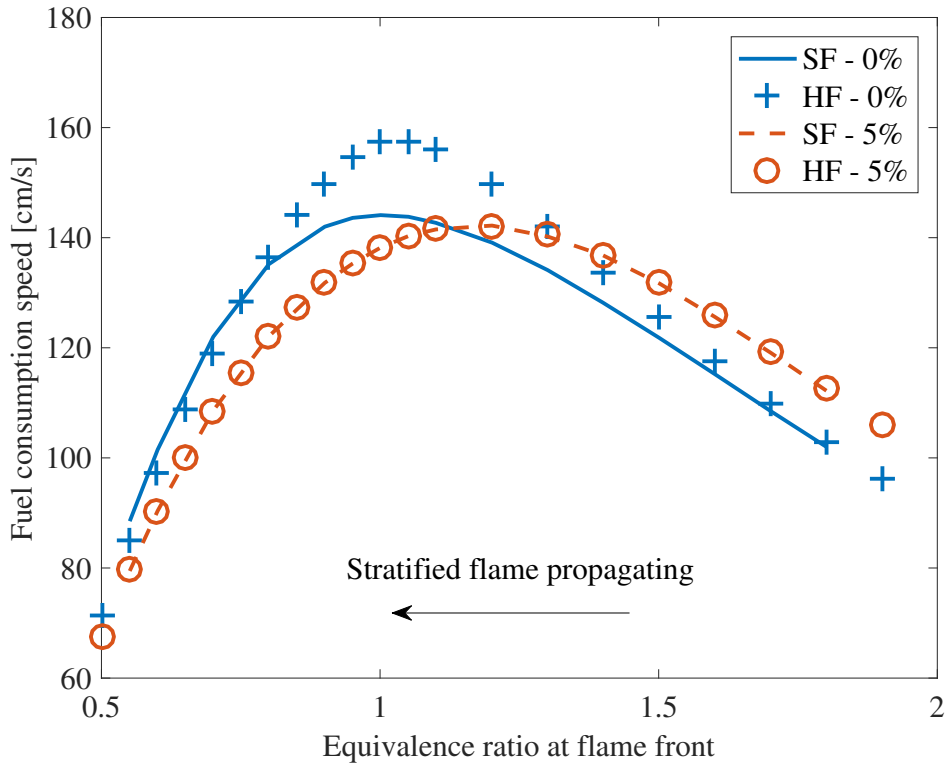

Figure 3.6: Fuel consumption speeds with 0% cutoff and 5% cutoff of SF and HF, when SF propagates from $\phi_f = 2.0$ to $\phi_f = 0.5$, $d_s = 0.1$ cm, with equal diffusivity assumption.

the 5% S_c results. The temperature in the burnt gas of SF seems to be slightly lower than that of HF as SF propagates from richer mixture with lower adiabatic flame temperature. In Fig. 3.7(b), more H and H_2 but less OH are found in the burnt gas of SF than HF, while they are almost identical near the flame front. These temperature and species differences agree with previous results reported in Cruz et al. (2000), but certainly do not lead to changes in local flame characteristics as heat release and 5% S_c results are identical between SF and HF. If diffusion of heat and species in the burnt gas are not fast enough to catch up with the propagation of flame front, there will be no effect introduced by these differences. Figure 3.7(c) shows the absolute thermal and species diffusion speeds compared to S_f, the flame front propagation speed. The thermal diffusion speed, labelled as T, is found much slower than S_f, indicating heat diffusion is much slower than flame front propagation. Therefore, extra heat diffusion due to the difference in burnt gas temperature between SF and HF is not able to influence local fuel consumption. In comparison, species diffusion speeds are also overall slower than S_f except that H and OH diffusion is faster than S_f in the region near the flame front. However, in the same region, H and OH mole fraction profiles are identical between SF and HF as shown in Fig. 3.7(b). Therefore, the difference in species distribution is also not able to influence local fuel consumption. In short, with equal diffusivity assumption, the above analysis reveals that neither thermal effect nor chemical effect impacts local

fuel consumption.

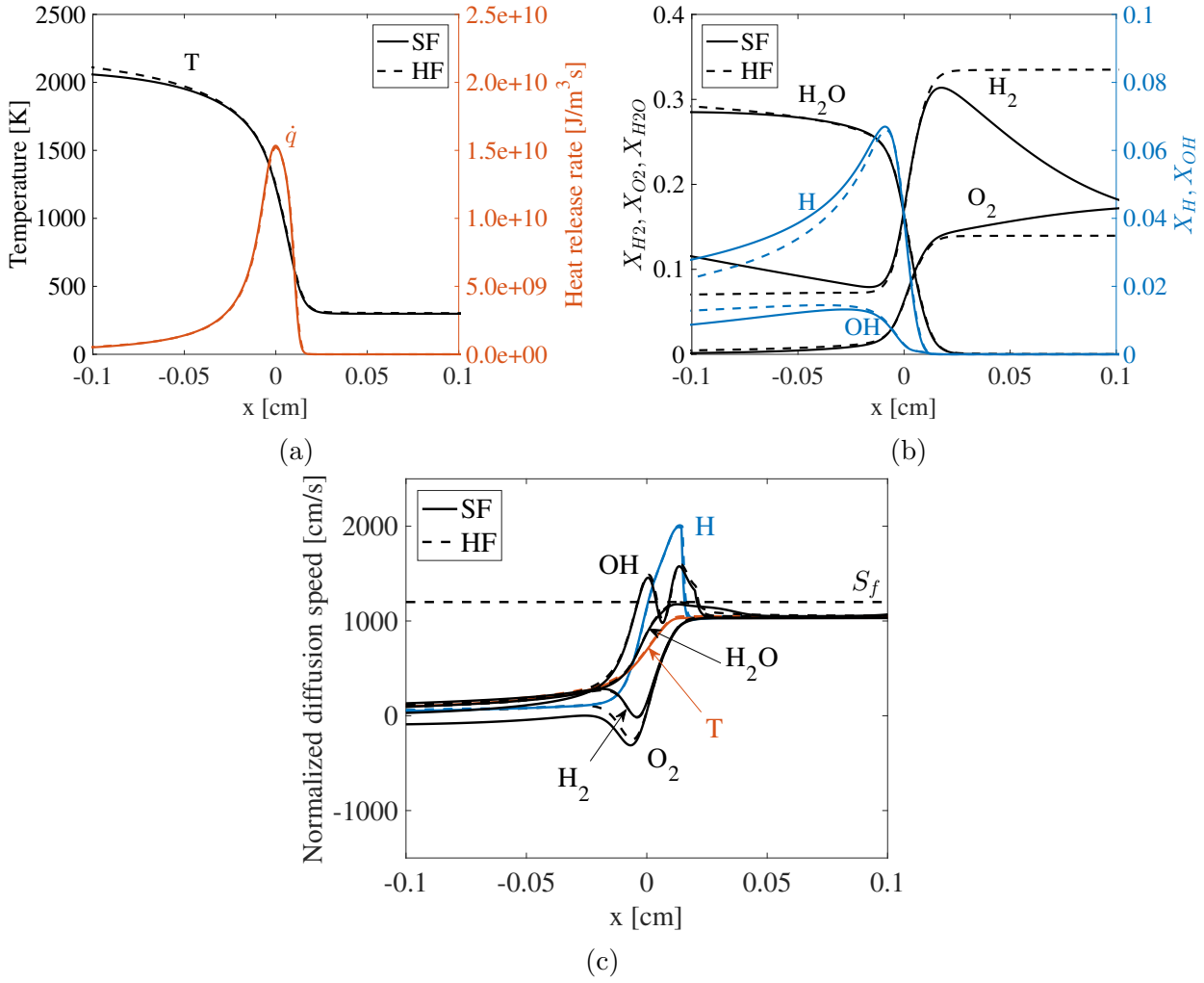

Figure 3.7: (a) Heat release rate and temperature, (b) major species mole fraction and (c) thermal and species normalized diffusion speeds profiles of SF and HF at $\phi_f = 1.2$, when SF propagates from $\phi_f = 2.0$ to $\phi_f = 0.5$, $d_s = 0.1$ cm, with equal diffusivity assumption.

The difference observed in the 0% cutoff results is due to additional fuel consumption in the burnt gas dominated by burnt gas temperature, since chemical reactions do not completely finish and continue to happen after the flame has passed through. As SF propagates firstly from rich to stoichiometry, the burnt gas of SF has lower adiabatic temperature than that of HF. Therefore, less fuel per unit mixture is consumed, which makes less contribution to the overall 0% fuel consumption speed of SF. When SF continues to propagate from stoichiometry to lean, higher burnt gas temperature is achieved. As a result, the gap between SF and HF results starts to decrease and eventually SF catches up with HF. This explains

the trend that 0% cutoff S_c of SF is firstly slower than that of HF but later able to catch up with HF.

Figure 3.8 compares the flame front propagation speeds and fluid expansion speeds of both SF and HF, and shows their respective differences ($\Delta S|_{SF-HF} = S|_{SF} - S|_{HF}$). For both flame front propagation speeds and fluid expansion speeds, the same trends are observed: the results of SF are firstly lower than those of HF and then higher, similar to 0% S_c results. However, the differences in S_{exp} between SF and HF, $\Delta S_{exp}|_{SF-HF}$, are smaller than the differences in S_b between SF and HF, $\Delta S_b|_{SF-HF}$. Since local fuel consumption of SF and HF are identical, there must be additional effects besides burnt gas expansion that are responsible for the relatively large difference between S_f.

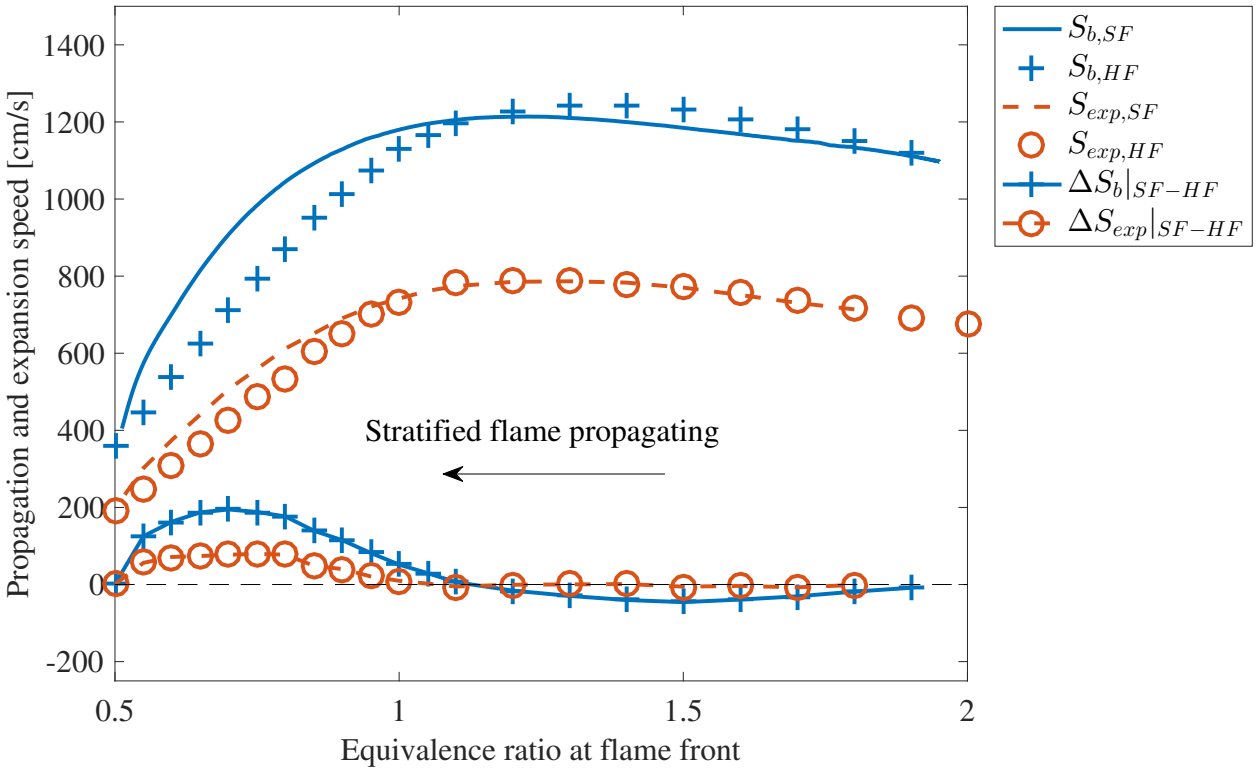

Figure 3.8: Flame front propagation speeds, fluid expansion speeds and respective differences between SF and HF, when SF propagates from $\phi_f = 2.0$ to $\phi_f = 0.5$, $d_s = 0.1$ cm, with equal diffusivity assumption.

Figure 3.9 presents the velocity profiles of SF at several different time steps, where x-axis stands for the spatial location of the 1D domain and y-axis is the corresponding fluid velocity. The sharp change of each curve is indicative of the flame front location. When the flame is located outside the stratification ($\phi_f = 0.5$ or 2.0), burnt gas reaches steady state as the fluid velocity from the closed end to the flame is almost zero. However, when SF propagates through the stratification, the burnt gas velocities deviate from zero. For

example, at $\phi_f = 1.7$ when the flame propagates from $\phi_f = 2.0$ to 1.3, while the unburnt gas in front of the flame front holds relatively slower speed, the flame front itself accelerates. As a result, not only is the unburnt gas further pushed away by the flame front, the burnt gas is also compressed towards the closed end, resulting in slightly negative fluid velocities as shown by the fluid velocity profile at $\phi_f = 1.7$ in Fig. 3.9. The flame front propagation speed is consequently smaller compared to that if the burnt gas is still. In comparison, when the flame propagates in the later part of stratification from ϕ_f 1.3 to 0.5, unburnt gas in front of the flame front still holds a higher speed while flame front itself has already slowed down. As a result, a contraction effect is created around: Instead of remaining still near the closed end, burnt gases are attracted towards the flame. As a result, burnt gases now have positive fluid velocities, as shown by in $\phi_f = 0.9$ results in Fig. 3.9. The fluid velocity at the flame front is then increased, leading to an elevated flame front propagation speed. This hydrodynamic effect due to fluid continuity is caused by the variation of flame front propagation speeds across stratified charges with different equivalence ratios, which is only observed in stratified flames but not homogeneous flames. In short, this additional hydrodynamic effect also contributes to the difference in S_f between SF and HF.

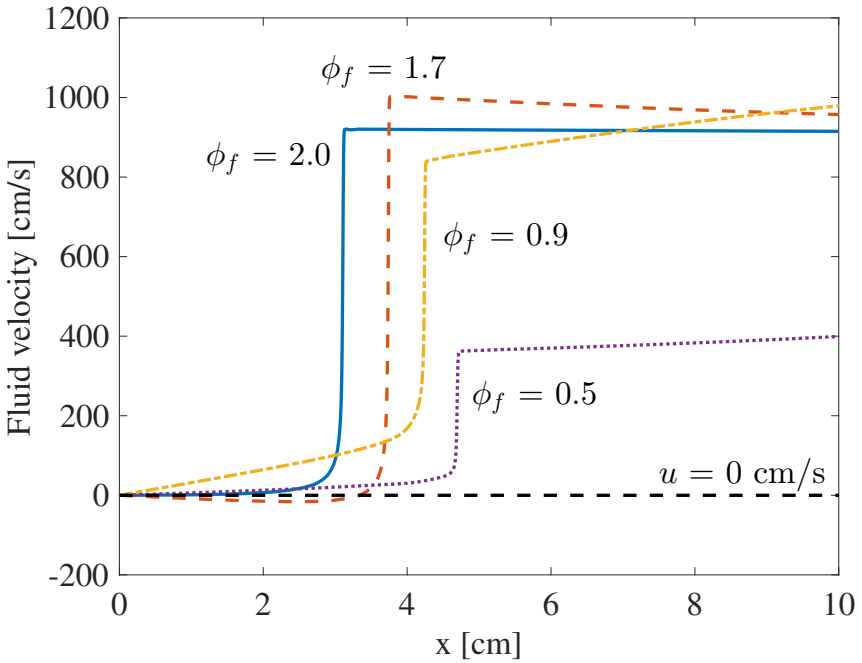

Figure 3.9: Fluid velocity profiles when SF propagates from $\phi_f = 2.0$ to $\phi_f = 0.5$, $d_s = 0.1$ cm, with equal diffusivity assumption.

For lean–to–rich stratification case, where SF propagates from $\phi_f = 0.5$ to $\phi_f = 2.0$, the comparison of fuel consumption speeds and flame front propagation speeds are shown in Fig. 3.10 and Fig. 3.11 respectively. In Fig. 3.10, while 5% cutoff results are still identical, 0% result of SF is firstly lower and then higher than that of HF, as the burnt gas temperature

of SF is still lower and then higher compared to that of HF. In Fig. 3.11, both S_{exp} and S_f of SF are lower and then higher than those of HF, while the additional hydrodynamic effect due to fluid continuity is still present as $\Delta S_{exp}|_{SF-HF}$ does not match $\Delta S_b|_{SF-HF}$. Therefore, the same rationale and analysis are still valid in this opposite stratification case.

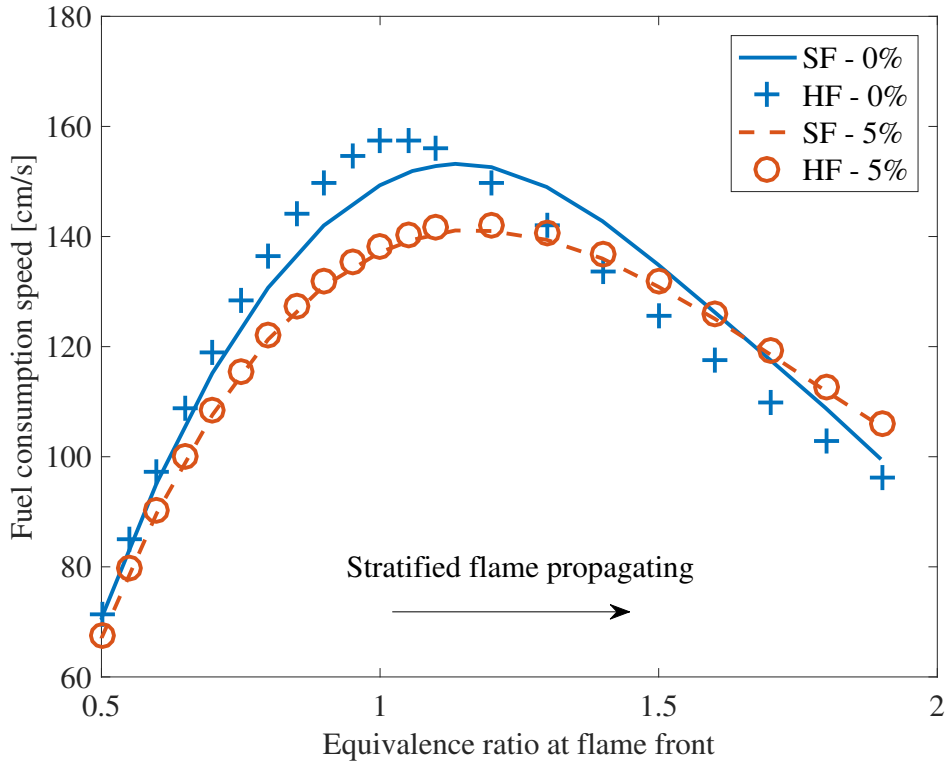

Figure 3.10: Fuel consumption speeds with 0% cutoff and 5% cutoff of SF and HF, when SF propagates from $\phi_f = 0.5$ to $\phi_f = 2.0$, $d_s = 0.1$ cm, with equal diffusivity assumption.

Mixture-average diffusivity results

Results with mixture-average diffusivity assumption are presented in this section. Each species has its own mass diffusivity which depends on temperature and the thermal differential diffusion (the Soret effect). Therefore, the Lewis number is not fixed: each species has its own Lewis number which changes at different positions in the flame. Due to preferential diffusion, lighter species, such as H, H_2, diffuse faster compared to heavier species. A similar set of numerical simulations as that with equal diffusivity assumption are investigated: the stratified flame propagates from a unburnt charge of equivalence ratio 2.0 to that of 0.5 through the step change, as well as the opposite stratification case. Note that ϕ_u is no longer equal to ϕ_f due to preferential diffusion. In terms of ϕ_f, the stratified flame is actually propagating from $\phi_f = 1.6$ to 0.4.

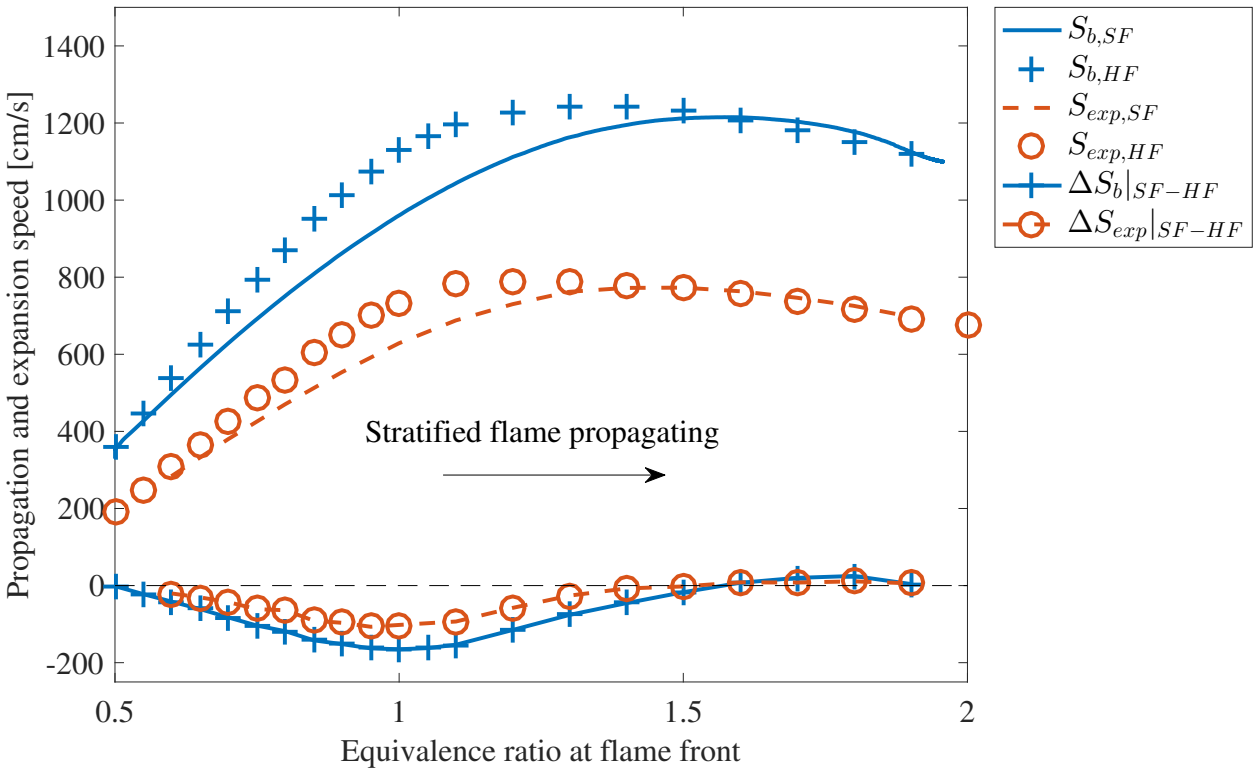

Figure 3.11: Flame front propagation speeds and fluid expansion speeds of SF and HF, when SF propagates from $\phi_f = 0.5$ to $\phi_f = 2.0$, $d_s = 0.1$ cm, with equal diffusivity assumption.

Figure 3.12 compares fuel consumption speed results calculated with both 0% and 5% cutoffs of SF and HF. Unlike the equal diffusivity results, both 0% cutoff and 5% cutoff results differ between SF and HF. More specifically, 5% S_c of SF is overall faster than that of HF across the entire stratification.

Detailed flame characteristics of SF and HF at $\phi_f = 1.0$ are investigated as shown in Fig. 3.13. In Fig. 3.13(a), heat release rates near the flame front of SF are higher than those of HF, indicating that local fuel consumption of SF is larger than that of HF. The temperature and species mole fraction profiles in Fig. 3.13(a) and 3.13(b) show similar results as those in the case with equal diffusivity assumption: burnt gas temperature of SF is lower than that of HF. More H and H_2 and less OH are found in the burnt gas of SF than HF, while they are almost identical near the flame front. In Fig. 3.13(c), diffusion speed profiles are presented and significant differences arise compared to the corresponding case with equal diffusivity assumption: while thermal diffusion speed is still much lower than S_f, diffusion of H is able to catch up with the flame front propagation over a wide range across the flame front. Moreover, within the same range, H mole fraction in SF is notably higher than that of HF. Therefore compared to equal diffusivity case, H radical in burnt gas of SF will influence local fuel consumption speeds, referred as the chemical effect. In this rich–

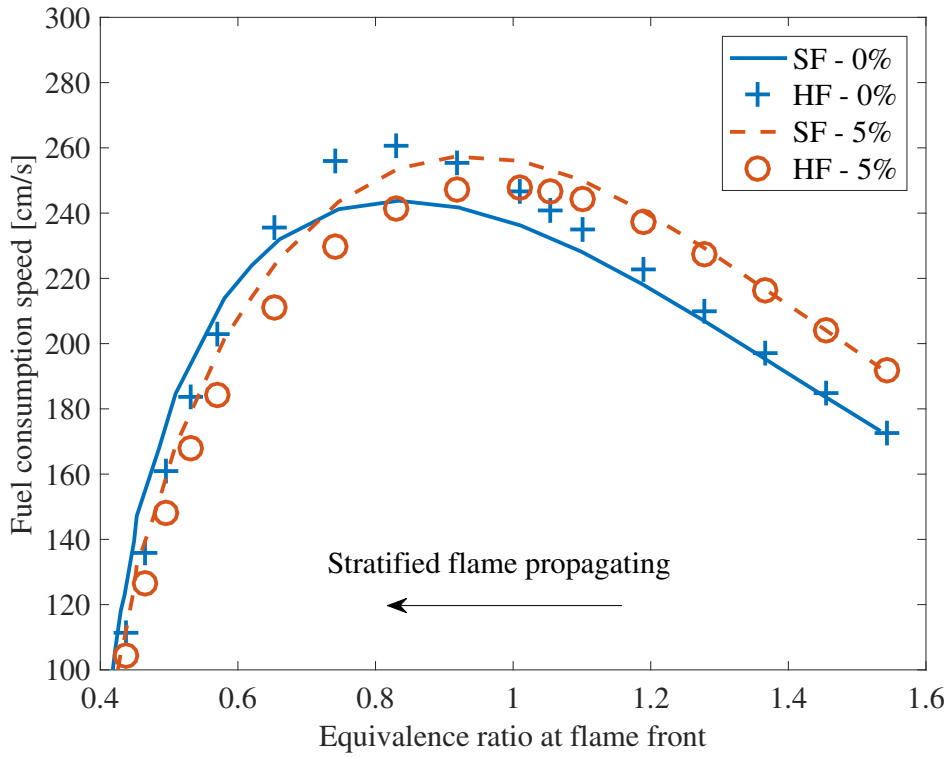

Figure 3.12: Fuel consumption speeds with 0% cutoff and 5% cutoff of SF and HF, when SF propagates from $\phi_f = 1.6$ to $\phi_f = 0.4$, $d_s = 0.1$ cm, with mixture-average diffusivity assumption.

to–lean stratified flame, more H radicals are generated in burnt gas of SF compared to HF. As a result, more H radicals will diffuse into the stratified flame and thus enhance the local chain-branching reactions, leading to enhancement of local flame speed near the flame front. This local chemical effect agrees with the 5% S_c results as SF is always faster than that HF. Therefore, the chemical effect is observed and has its impact on local flame characteristics with mixture-average diffusivity assumption, while thermal effect still does not exist. This observation is different from the conclusion drawn on methane/air stratified flames in Cruz et al. (2000). As burnt gas fuel consumption is still dominated by burnt gas temperature, 0% cutoff results still follow the similar trend as seen in the corresponding equal diffusivity case.

Figure 3.14 compares the flame front propagation speeds and fluid expansion speeds of SF and HF, and shows their differences. Compared to equal diffusivity case, the difference in S_{exp} between SF and HF, $\Delta S_{exp}|_{SF-HF}$, is almost zero. Recall that with equal diffusivity assumption, fluid expansion effect results from heat release in the burnt gas and the difference between SF and HF is due to different burnt gas compositions. In comparison with mixture-average diffusivity assumption, additional H radicals in stratified flames are more likely to diffuse towards the region of the flame front due to preferential diffusion. As a result, the

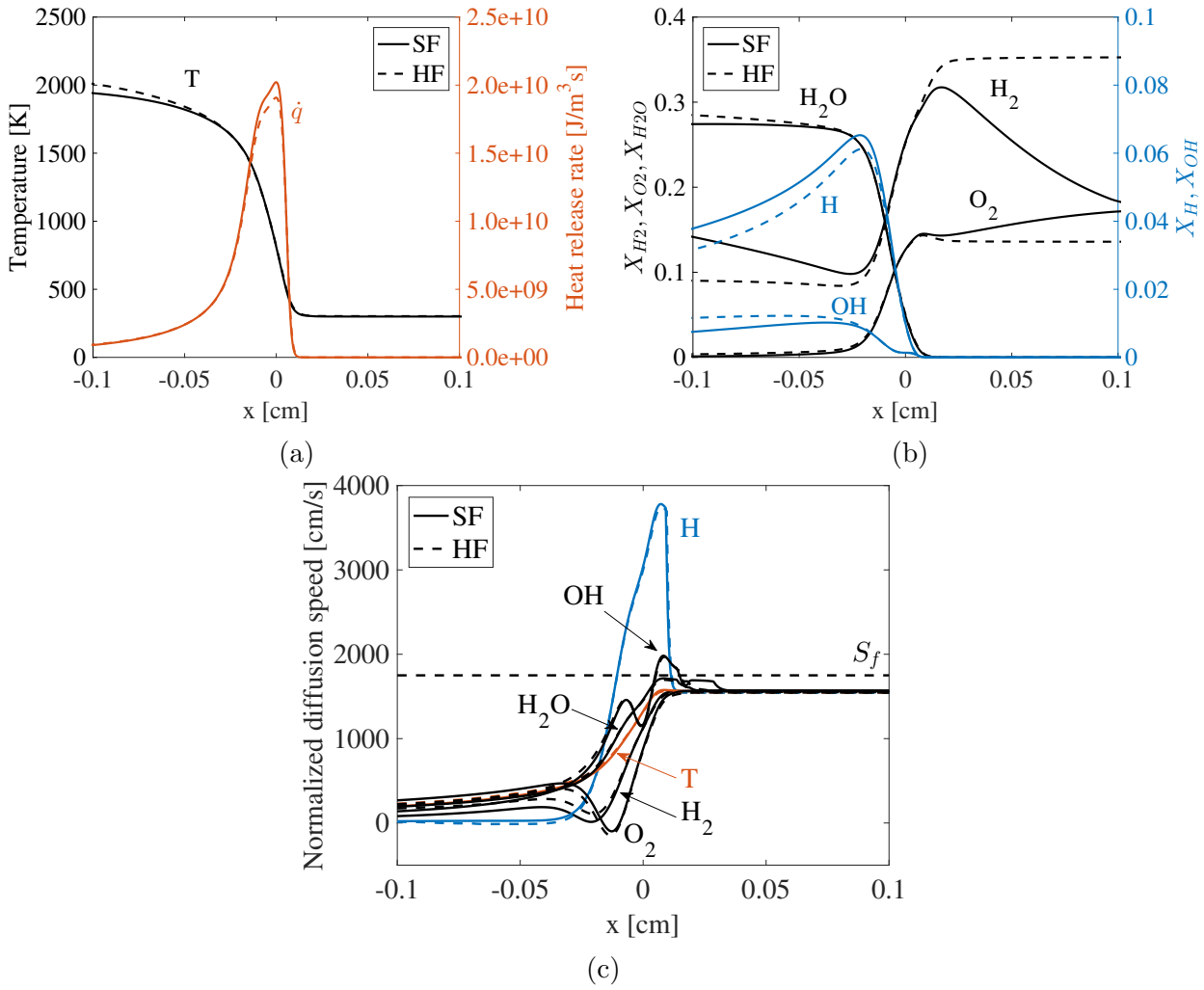

Figure 3.13: (a) Heat release rate and temperature, (b) major species mole fraction and (c) thermal and species normalized diffusion speeds profiles of SF and HF at $\phi_f = 1.0$, when SF propagates from $\phi_f = 1.6$ to $\phi_f = 0.4$, $d_s = 0.1$ cm, with mixture-average diffusivity assumption.

difference in burnt gas heat release between SF and HF as well as its contribution to flame front propagation speeds on flame front propagation speed becomes insignificant. As the flame is still burning at different speeds with different equivalence ratios, the hydrodynamic effect of fluid continuity is still present in SF. Therefore, the difference in S_f resulted from the chemical effect on local flame speeds and the hydrodynamic effect due to fluid continuity. In Fig. 3.14, during the initial rich region, S_f of SF is found slightly slower than HF due to the hydrodynamic effect. Afterwards, S_f of SF is overall faster than that of HF across the rest of the stratification due to faster local flame speeds.

The flame speed results of the opposite stratification case, where SF propagates from

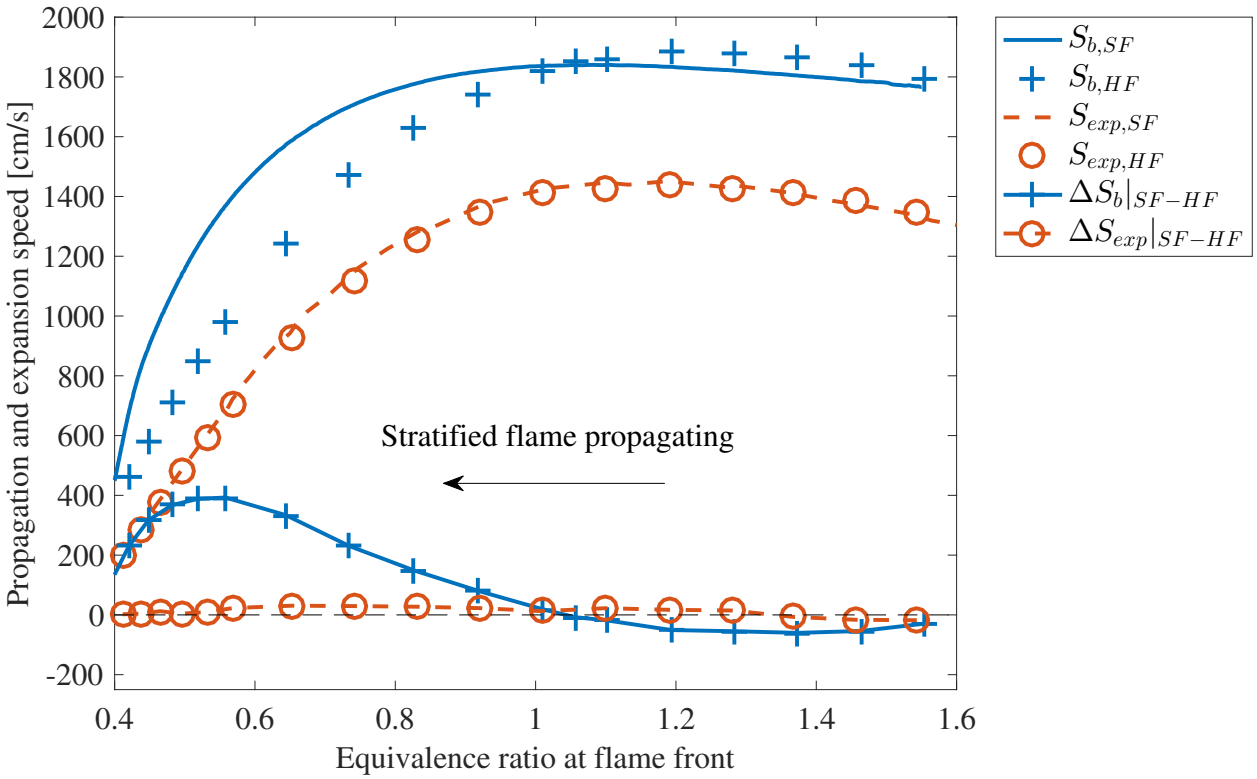

Figure 3.14: Flame front propagation speeds and fluid expansion speeds of SF and HF, when SF propagates from $\phi_f = 1.6$ to $\phi_f = 0.4$, $d_s = 0.1$ cm, with mixture-average diffusivity assumption.

$\phi_f = 0.4$ to $\phi_f = 1.6$, are also investigated: As seen in Fig. 3.15, 5% S_c of SF is overall lower than that of HF, as fewer radicals diffuse into the local flame front of SF. 0% S_c of SF shows the trend of lower to higher than HF due to burnt gas temperature. In Fig. 3.16, while $\Delta S_{exp}|_{SF-HF}$ is still negligible, S_f of SF is overall slower than that of HF across most of the stratification due to slower local flame speeds of SF, and slightly faster in the rich region due to hydrodynamic effect. Therefore, results from both stratification cases can be understood with the analysis of 5% S_c, 0% S_c, species and fluid velocity profiles.

Effect of stratification thickness

Stratified flames with different stratification thicknesses, ranging from the order of flame thickness to relatively large distance (approximately 20 times larger than the flame thickness), are compared to homogeneous flames, with both equal and mixture-average diffusivity assumptions. Figure 3.17 shows the effect of stratification thickness on 5% S_c and S_f for the stratified flame propagating from $\phi_f = 2.0$ to $\phi_f = 0.5$ with equal diffusivity assumption. While no difference is observed between 5% S_c of SF and HF when $d_s = 0.1$ cm and $d_s = 1$ cm, SF with $d_s = 0.04$ cm is overall slightly faster than HF, similar to previous mixture-

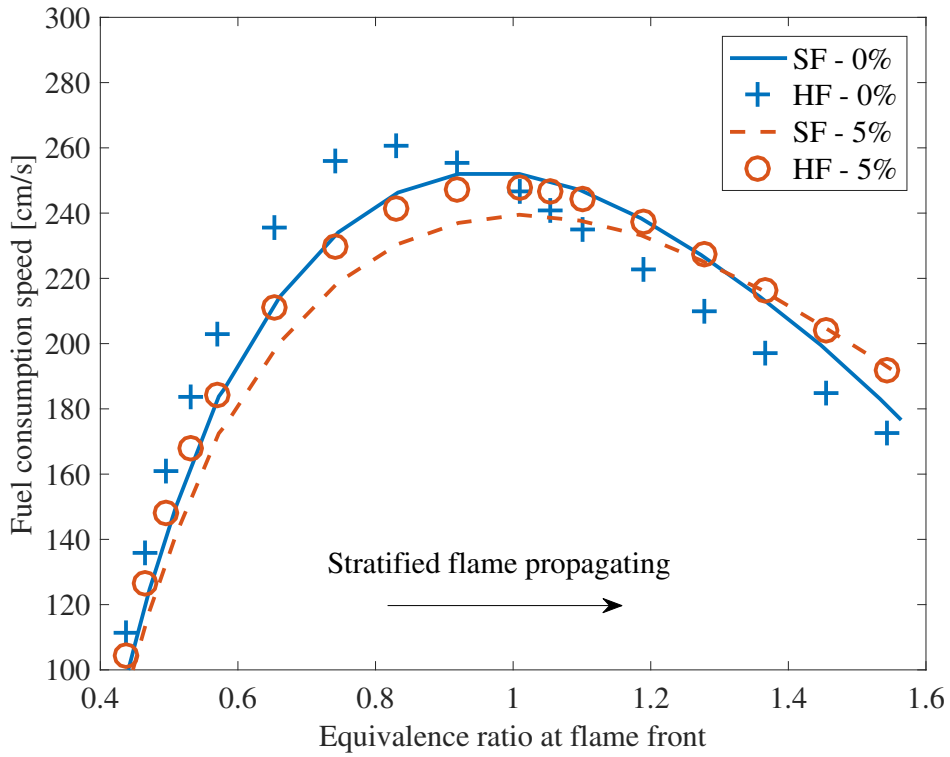

Figure 3.15: Fuel consumption speeds with 0% cutoff and 5% cutoff of SF and HF, when SF propagates from $\phi_f = 0.4$ to $\phi_f = 1.6$, $d_s = 0.1$ cm, with mixture-average diffusivity assumption.

average diffusivity results. Therefore, when d_s is reduced to the order of flame thickness, a weak chemical effect is observed even with equal diffusivity assumption. S_f of SF at different d_s are always different from HF due to hydrodynamics effects. With increasing d_s, the difference between S_f of SF and HF decreases.

Figure 3.18 shows the influence of stratification thickness on 5% S_c and S_f for the stratified flame propagating from $\phi_f = 1.6$ to $\phi_f = 0.4$ with mixture-average diffusivity assumption. Both S_c and S_f of SF with different d_s are different from those of HF. When d_s is 0.04 cm, both S_c and S_f results show considerably large differences between SF and HF. As d_s increases, both S_c and S_f of SF approach their corresponding results of HF. For local fuel consumption speeds, larger stratification thickness reduces the difference between burnt gas composition of SF and HF. As a result, less difference in burnt gas heat release between SF and HF is achieved. The local chemical effect is therefore suppressed leading to a smaller difference in S_c between SF and HF. For flame front propagation speeds, larger stratification thickness reduces the magnitude of fluid velocity variation so that the hydrodynamic effect due to continuity is also decreased. As both local chemical and hydrodynamic effects are weakened, the difference in S_f between SF and HF becomes smaller. In conclusion, with increasing stratification thickness, both local chemical and hydrodynamic effects decrease.

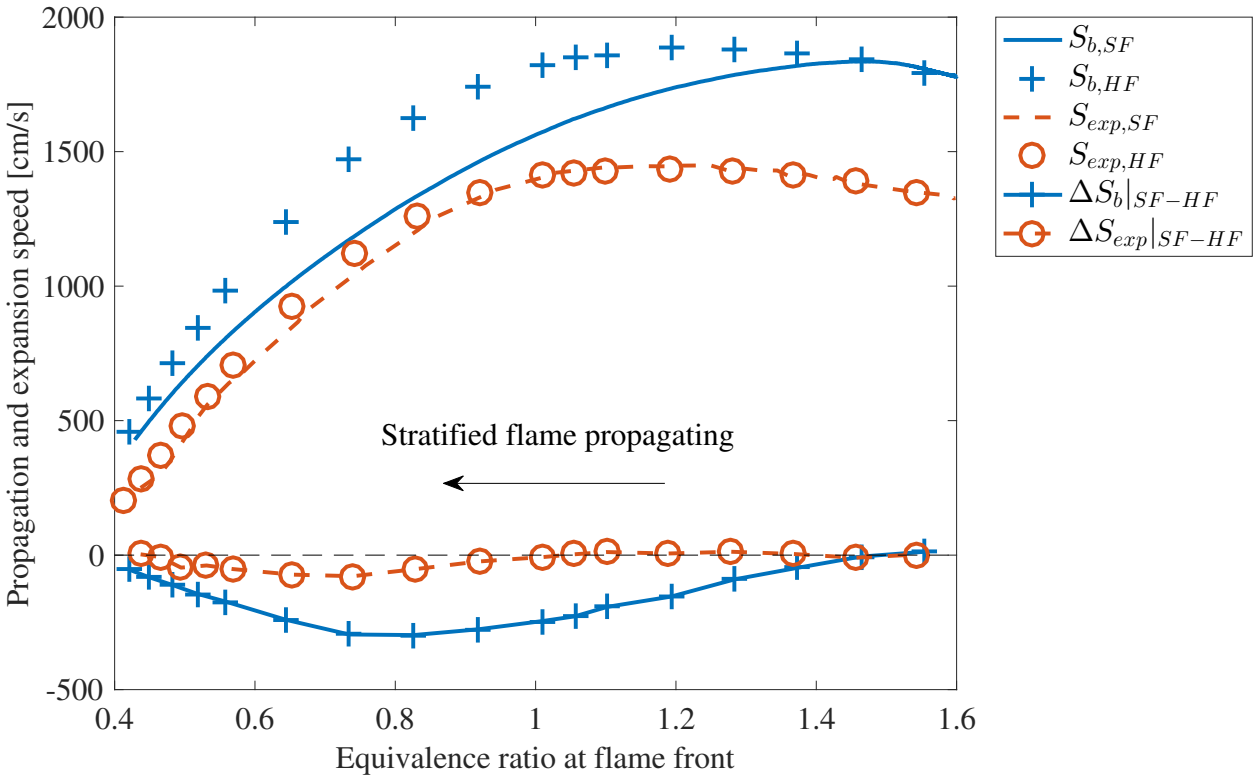

Figure 3.16: Flame front propagation speeds and fluid expansion speeds of SF and HF, when SF propagates from $\phi_f = 0.4$ to $\phi_f = 1.6$, $d_s = 0.1$ cm, with mixture-average diffusivity assumption.

Summary

In addition to the comparison of 0% fuel consumption speeds and flame front propagation speeds, new insights of how stratification influences laminar flame speed are gained by analyzing local fuel consumption, burnt gas expansion, diffusion speeds of heat and species and hydrodynamic effect due to fluid velocity variation. The following specific conclusions have been reached from the observations and analysis:

- With equal diffusivity assumption, as 5% cutoff fuel consumption speeds are identical between SF and HF when stratification thickness is larger than flame thickness, neither thermal effect nor chemical effect is seen locally near flame front. When stratification thickness reduces to the order of flame thickness, a weak chemical effect due to the different level of H radical in burnt gases is observed even with equal diffusivity assumption. As burnt gas continues to react after the flame has passed through, the difference between 0% cutoff fuel consumption speeds results from burnt gas fuel consumption dominated by burnt gas temperature. The difference between flame front propagation speeds are caused by fluid expansion due to burnt gas heat release as well

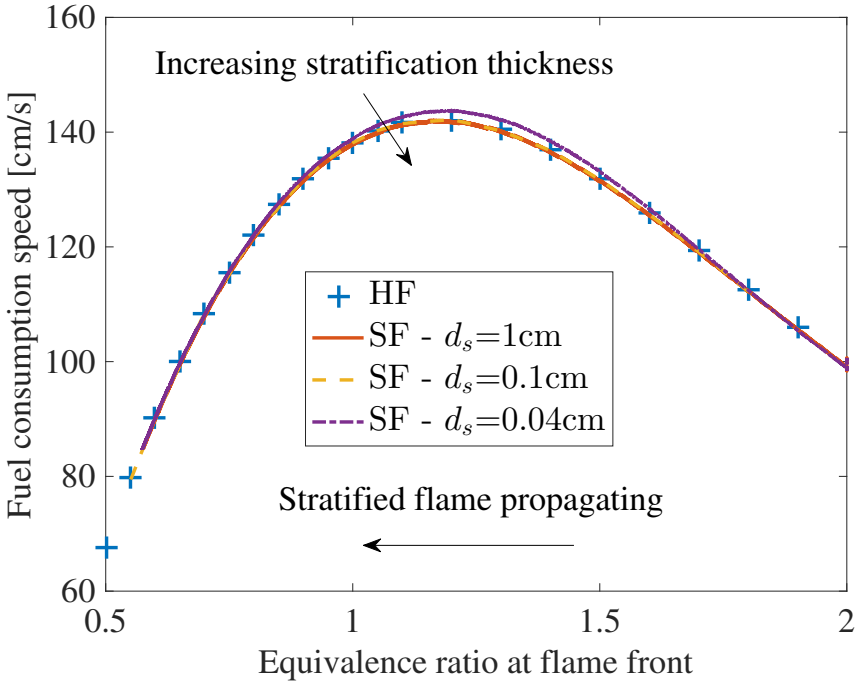

(a)

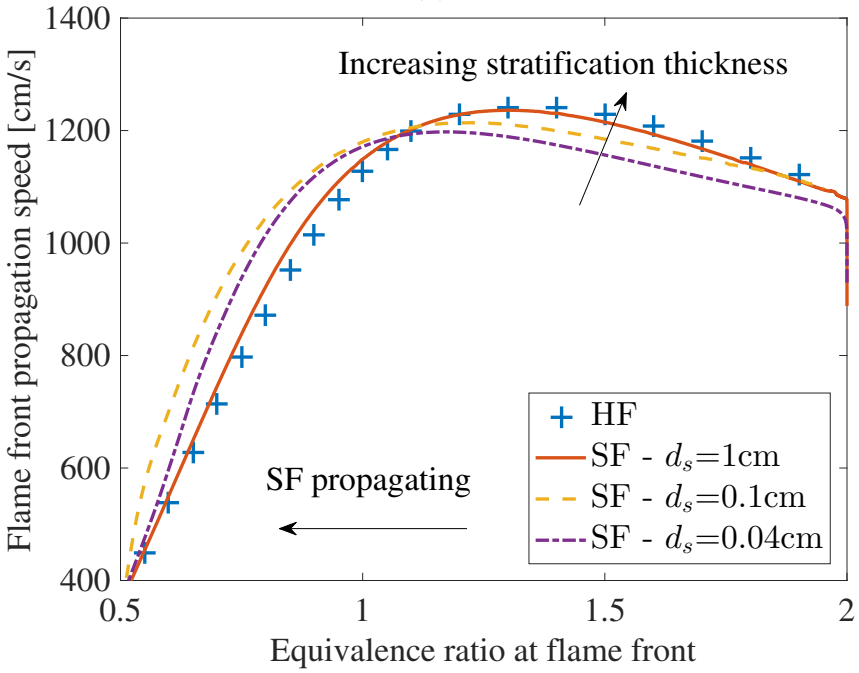

(b)

Figure 3.17: (a) Fuel consumption speeds and (b) flame front propagation speeds of SF at different stratification thicknesses and corresponding HF, when SF propagates from $\phi_f = 2.0$ to $\phi_f = 0.5$, with equal diffusivity assumption.

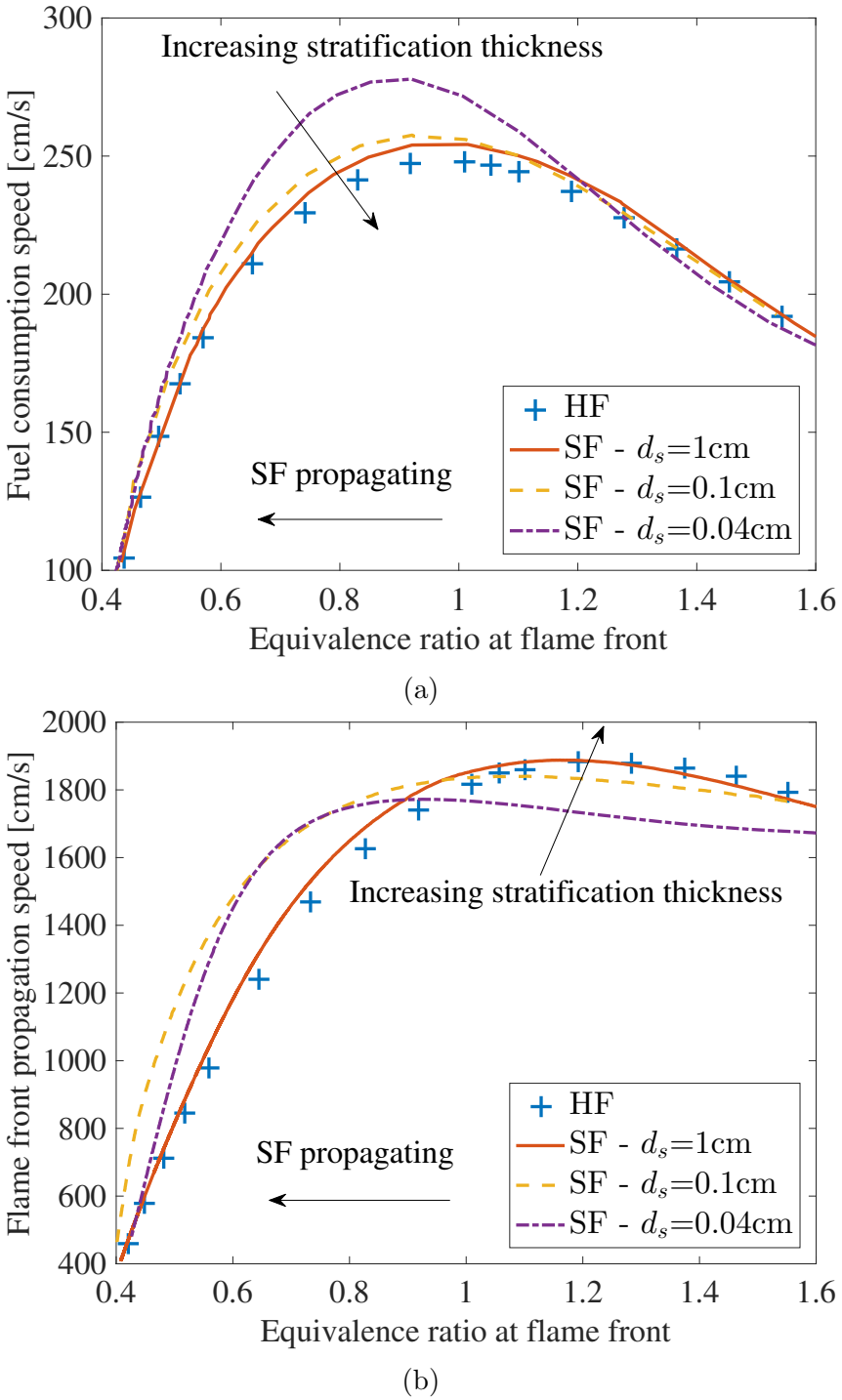

Figure 3.18: (a) Fuel consumption speeds and (b) flame front propagation speeds of SF at different stratification thicknesses and corresponding HF, when SF propagates from $\phi_f = 1.6$ to $\phi_f = 0.4$, with mixture-average diffusivity assumption.

as the hydrodynamic effect due to fluid continuity.

- With mixture-average diffusivity assumption, the chemical effect due to the different level of H radicals in burnt gas is observed in stratified flames as 5% cutoff fuel consumption speed of rich–to–lean SF is overall faster than the corresponding HF. The chemical effect is further enhanced by preferential diffusion of H radical. lean–to–rich SF is respectively slower than HF. 0% cutoff fuel consumption speeds are still influenced by burnt gas fuel consumption. As additional H radicals generated from burnt gas fuel consumption in SF diffuse from the burnt gas into the flame region, the difference in burnt gas heat release between SF and HF becomes insignificant. The difference between flame front propagation speeds thereby results from the difference between local flame speeds due to chemical effect in addition to the hydrodynamic effect due to fluid continuity.

- Two transport models respond differently to different stratification thicknesses: with equal diffusivity assumption, a weak chemical effect is observed only when stratification thickness is reduced to the order of flame thickness. In comparison, with mixture average diffusivity assumption, the chemical effect is observed in a wider range of stratification thicknesses up to 1cm, as preferential diffusion of H radical further enhances the chemical effect. Overall, increasing stratification thickness leads to decreased gradients in burnt gas compositions as well as a decrease in the changing rate of flame front propagation speeds. Thus both local chemical and hydrodynamic effects are reduced.

Using the same methodology, different fuel/air mixtures can be investigated. Different results are expected due to differences in transport, chemistry and mass diffusivity of reactants and radicals.

3.4 Hydrocarbon/air stratified flames

This section is based on the paper published in *Combustion and Flame* (Shi et al., 2017a).

Introduction

As a continuous endeavor of the above hydrogen study, this numerical study compares stratified flames of three different hydrocarbon fuels, i.e., methane, propane and n-heptane, in a quantitative manner. Specifically, the study focuses on rich–to–lean stratified flames and aims to answer:

1. How different are flame properties, such as temperature and species distributions as well as chemical reaction pathways, between stratified and homogeneous flames of different hydrocarbon fuels?

2. Does the trend, that rich–to–lean stratified flames are faster than homogeneous flames, still hold for larger hydrocarbon fuels? If not, what is the corresponding dominant process responsible for the opposite trend?

Numerical simulations of methane, propane and n-heptane/air stratified flames are performed and compared to their corresponding homogeneous flames. For one to one comparison, consistency in characterizing flame properties between stratified and homogeneous flames is crucial, e.g., flame front location, reference equivalence ratio and flame speed. Therefore, in this study, all the investigated and relevant flame characteristics are consistently defined and illustrated in the section of Flame Characteristics in this chapter. Since stratified flames propagate through varying mixture compositions, the Lewis number of deficient reactant may affect flame stability. As all the simulations are one-dimensional and conducted in a planar geometry, the potential flame instability introduced by curvature is not captured.

Numerical model and setup

A similar numerical setup compared to that in the above hydrogen study is used in this study. All the cases were conducted in a 1-D domain of 20 cm under initial temperature and pressure of 300 K and 1 atm. A 9-level AMR scheme is applied with $\Delta x_{max} = 0.2$ cm and $\Delta x_{min} = 4$ μm. As a result, the flame front where major heat release occurs is revolved by approximately 250 grids. The time step is 1 ns. Only planar simulations are conducted and hence all the results reported are stretch free. The stratification thickness is of the order of 0.1 cm, approximately the same order of flame thickness.

For methane/air flames, a 16-species reduced chemical kinetic mechanism was developed from a short version of GRI3.0 (Smith et al., 1999) without NO_X chemistry. For propane/air flames, a 24-species reduced mechanism was developed from a 70-species detailed mechanism (Qin et al., 2000). For n-heptane/air flames, a 32-species reduced mechanism was developed from a 65-species skeletal mechanism (Smallbone et al., 2009). All the reduced mechanisms were developed using in-house Computer Assisted Reduction Mechanism (CARM) software (Chen, 1988), including directed relation graph (DRG) method and target search algorithm (TSA). The computed flame speeds of homogeneous flames agree well with experimental data in the literature and the comparisons are included in Appendix B. A further validation of n-heptane reduced chemistry against detailed chemistry is provided as well.

Results and discussion

In this section, rich–to–lean stratified flames, propagating from a unburnt mixture of $\phi_u =$ 1.60 to 0.60, are compared to their corresponding homogeneous flames, at the same equivalence ratio at flame front ϕ_f. Both fuel consumption speeds with 5% cutoff integration limits and flame front propagation speeds are compared. Note that stratified flame is essentially

unsteady, as the flame front passes through mixtures with varying compositions. Therefore, the equivalence ratio of upstream burnt gas is no longer the same as that at flame front. The arbitrary burnt gas composition will result in enhanced/reduced diffusion processes between burnt gas and flame front compared to homogeneous flames, especially of intermediate lighter species such as molecular hydrogen. Therefore, the local flame behaviors and laminar flame speeds of stratified flames are different from those of homogeneous flames. Detailed analyses of temperature, species and reaction heat release around the flame front are conducted to explain the trends and identify contributions from diffusion processes and chemical reaction pathways.

Comparison among fuel consumption speeds

Figure 3.19 presents the fuel consumption speeds of SF and HF for all three hydrocarbon fuels. Fuel consumption speeds S_c are plotted against equivalence ratio at flame front ϕ_f. Transient stratified flames are represented by the solid lines, while the reference homogeneous flames are shown in terms of symbols. The stratified flame first started with the same S_c as that of the homogeneous mixture at rich end $\phi_f \approx 1.6$, then deviated from homogeneous flames throughout its propagation inside the stratification layer, and gradually converged to the lean end $\phi_f \approx 0.6$. For methane/air, the overall trend is that S_c of the rich–to–lean SF are enhanced compared to those of HF across the entire stratification layer, which agreed with some previous studies (Cruz et al., 2000). However, for propane and n-heptane, while the enhancement on S_c of SF is found on the lean side, an opposite trend is observed on the rich side. The percentage differences between S_c of SF and HF with regard to HF are calculated and presented in Fig. 3.20. From $\phi_f \approx 1.6$ to 1.3, negative percentages for propane and n-heptane are observed, indicating decreases in S_c of SF. In order to understand this unexpected behavior of propane and n-heptane SFs, detailed flame properties are analyzed $\phi_f \approx 1.40$, where the maximum discrepancy occurs.

For reference, methane/air mixture is first analyzed. For the homogeneous mixture of $\phi_u = 1.40$, ϕ_f is equal to 1.41. Figure 3.21 shows the profiles of computed fuel consumption rates (negative values of fuel production rates) and heat release rates, where $x = 0$ is the location of the flame front. Both peak heat release rate and fuel consumption rate of SF are larger than those of HF. The location of peak fuel consumption is also located very close to the flame front. Figures 3.22 and 3.23 compare the computed temperature, reactant, product as well as intermediate species profiles of both SF and HF. In Figure 3.22, the temperature at the flame front is about 1800 K. On the unburnt side ($x > 0$), the decreasing profile of CH_4 seen in the SF is indicative of that the flame propagates towards a leaner mixture. A higher level of H_2O is found in the unburnt mixture of SF, which exhibits the same trend as temperature: the unburnt temperature of SF near the flame front is notably higher (about 150 K) than that of HF. Similarly, in Figure 3.23, higher levels of H_2 and CO are also found in the unburnt mixture of SF. As there is no discernible heat release in the preheat zone of SF ($x > 0.025$ cm) thus no local formation of products, these species (H_2O, H_2, CO)

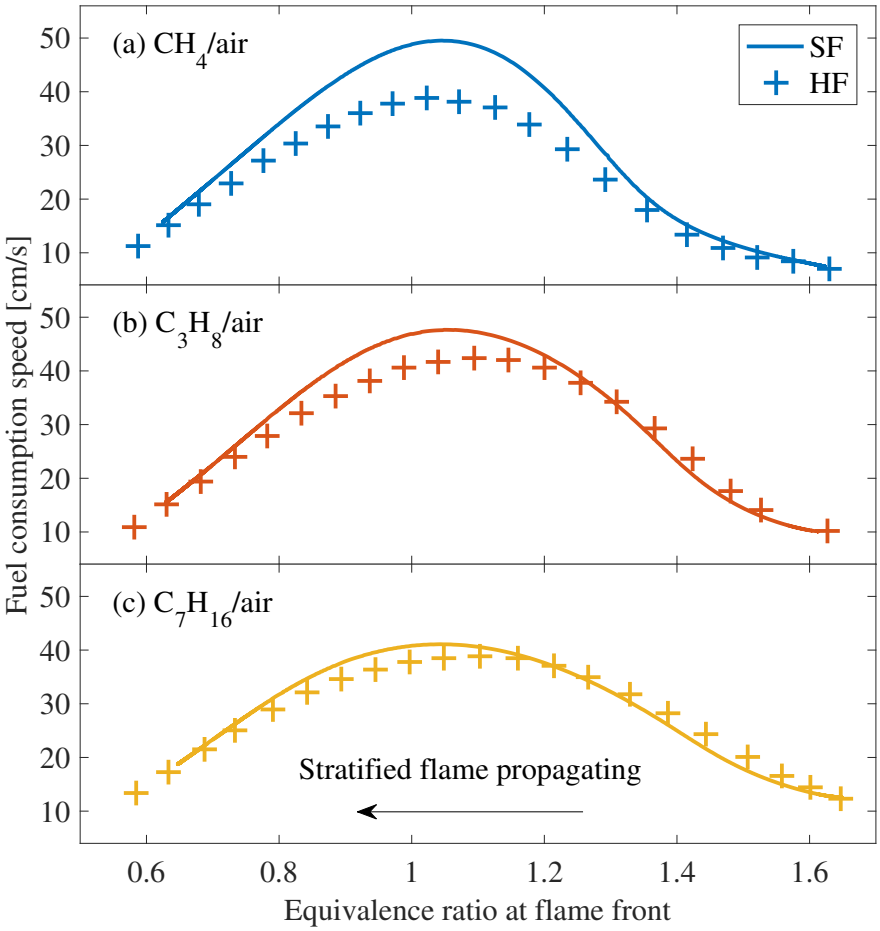

Figure 3.19: Fuel consumption speeds of the rich–to–lean stratified flames and the corresponding homogeneous flames.

must have diffused from the flame front or burnt gas into the unburnt mixture. A higher temperature of the unburnt mixture is achieved due to high enthalpy carried by these species. In Figure 3.23, more H and OH radicals are found near the flame front in SF than HF, which agree with the observation of higher heat release rate and fuel consumption rate in SF. This enhancement in radical pool resulted from preferential diffusion of molecular hydrogen and was referred to as the chemical effect of SF from previous studies (Cruz et al., 2000). Note that the burnt gas temperature of SF is lower than that of HF in Fig. 3.22, which should have led to a decreased unburnt gas temperature of SF due to reduced thermal diffusion. However, the unburnt gas temperature of SF is higher due to enhanced radical and product diffusion, therefore, the impact of chemical effect is dominant compared to thermal effect (Shi et al., 2016). Although not presented in this section, the results around $\phi_f = 1$ where the enhancement is most prominent show that substantially more hydrogen (almost twice as much), water as well as consequent higher unburnt gas temperature were observed in the

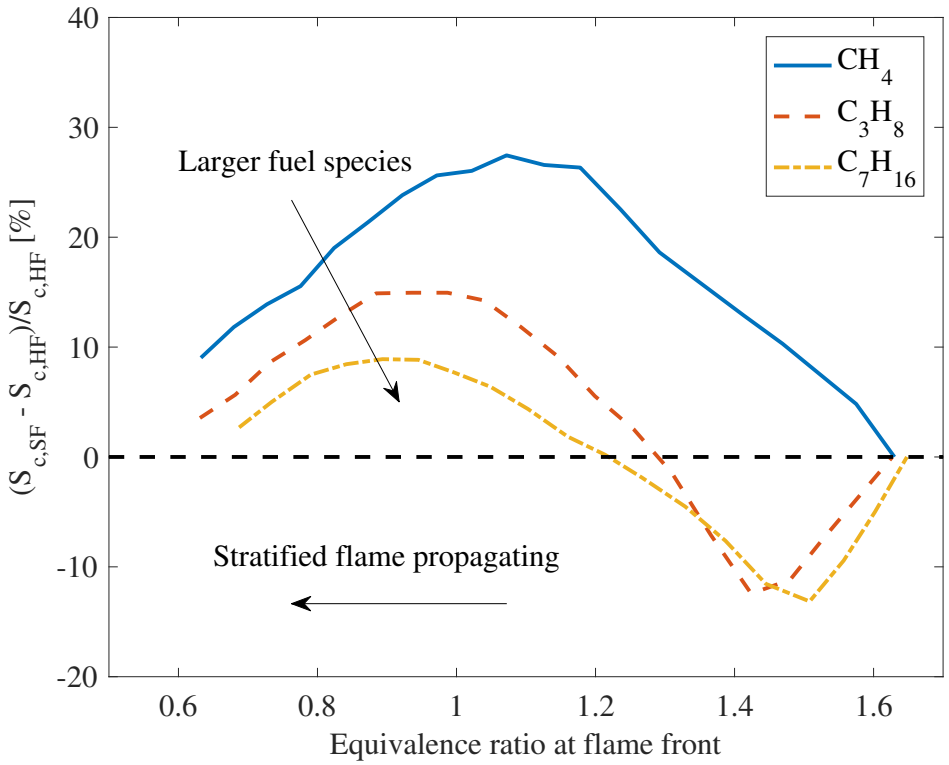

Figure 3.20: Percentage differences between fuel consumption speeds of the rich–to–lean stratified flames and the corresponding homogeneous flames.

stratified flame. This observation confirmed the dominance of chemical effect. In all, fuel consumption speeds of SF are higher than those of HF for methane/air mixtures, due to enhanced radical pool at the flame front and increased unburnt mixture temperature.

Another evidence of the chemical effect is revealed by the reaction heat release analysis. Figure 3.24 shows the differences between heat release rates of each reaction in methane/air SF and HF, plotted against reaction index number. The reaction heat release rate is calculated as the integration of heat release of one particular reaction over the entire calculation domain divided by the domain length. A positive value means that this reaction releases/absorbs more heat in SF than that in HF. Reactions A-G substantially releases/absorbs more heat in SF than that in HF and indicated that the overall heat release behavior in SF is more active compared to HF. All major reactions are associated with radicals (H and OH) or reactive intermediate species (H_2, CO and CH_3) that are formed more in SF.

A similar analysis is conducted for propane/air HF and SF. Detailed flame properties are analyzed at $\phi_f = 1.42$ (corresponding to HF with the unburnt mixture of $\phi_u = 1.40$). As propane/air flames at $\phi_f = 1.42$ have higher flame speeds ($\sim$23 cm/s) compared to methane/air flames ($\sim$13 cm/s), both profiles of heat release rates and fuel consumption

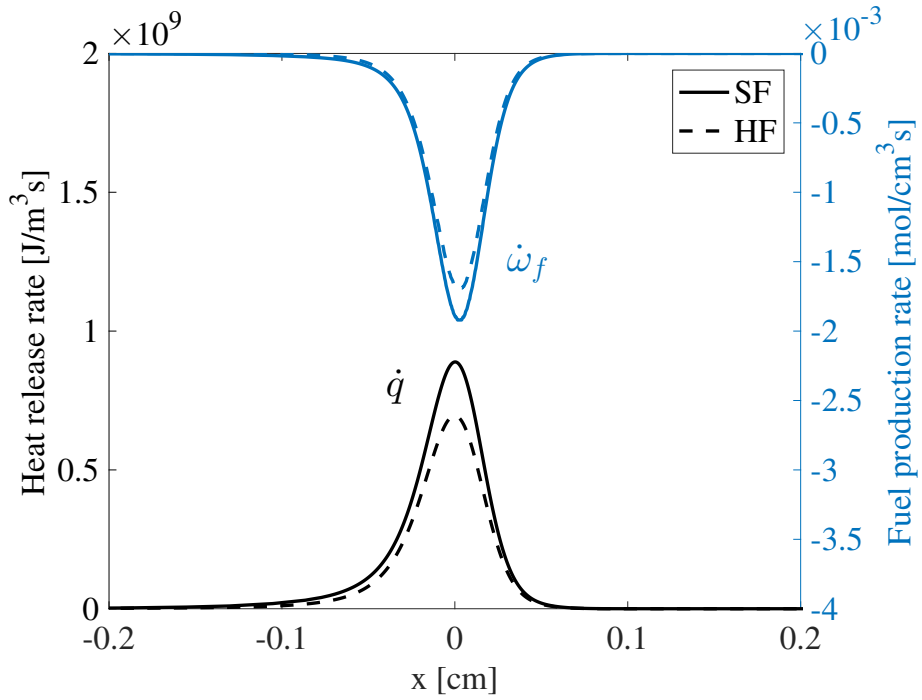

Figure 3.21: Heat release rates and fuel consumption rates in methane/air stratified and homogeneous flames, at $\phi_f = 1.41$.

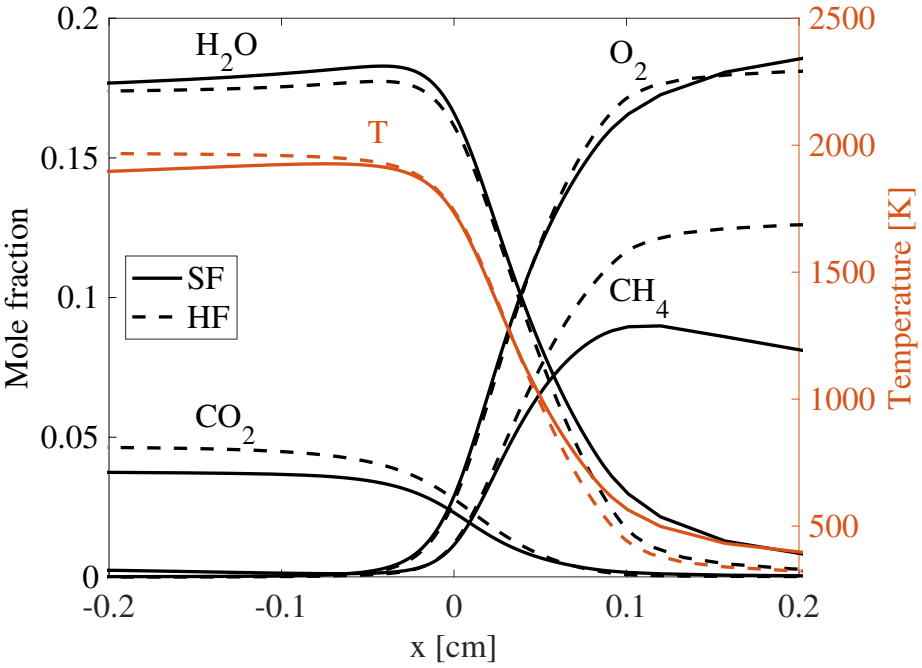

Figure 3.22: Temperature, mole fractions of reactants and products in methane/air stratified and homogeneous flames, at $\phi_f = 1.41$.

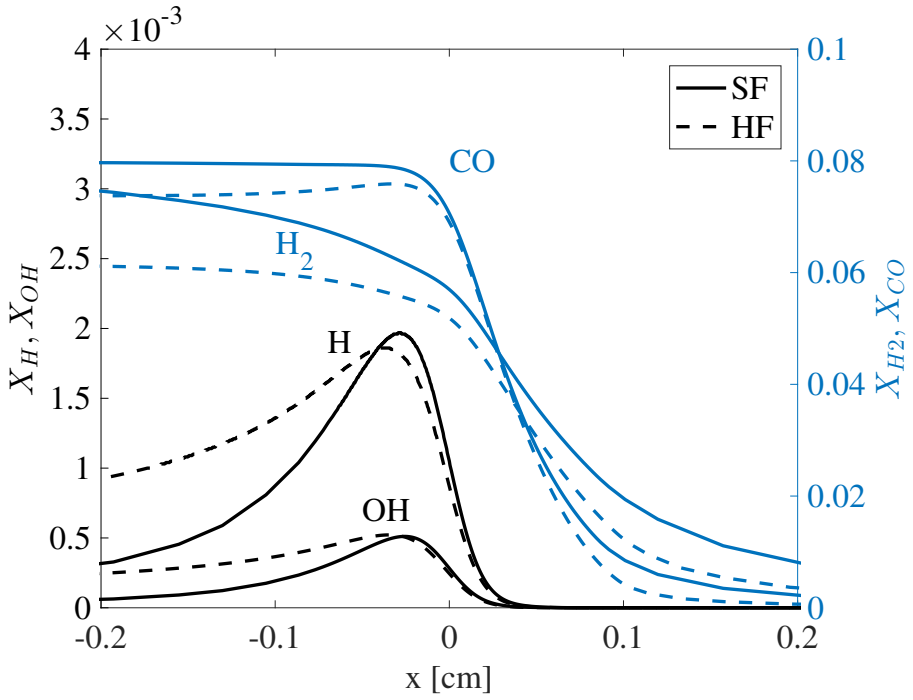

Figure 3.23: Mole fractions of intermediate species and radicals in methane/air stratified and homogeneous flames, at $\phi_f = 1.41$.

rates of propane/air flames shown in Fig. 3.25 are thinner compared to methane/air flames. In Fig. 3.25, while the peak fuel consumption rate of SF is clearly smaller than that of HF, heat release rates of both flames are almost identical. Although the peak heat release rate of SF is smaller than HF, the total heat release rate of SF is still slightly higher than HF since SF releases more heat on the burnt side of the peak location. The peak locations of heat release rate and fuel consumption rate no longer coincide, showing that major fuel consumption occurs on the unburnt side of major heat release. As fuel decomposition reaction steps in propane/air flames have lower activation temperatures compared to methane/air flames, fuel consumption peaks at a lower temperature, about 1400 K.

Temperature and major species profiles in Fig. 3.26 show similar trends as those of methane/air flames. The unburnt mixture of SF has higher temperatures than HF. As a result, fuel consumption of SF occurs slightly earlier than HF in Fig. 3.25, while mole fraction of C_3H_8 decreases earlier as well in Figure 3.26. For radical distributions in Fig. 3.27, while mole fractions of CO and H_2 are still higher in SF similar to methane, mole fractions of H and OH near the flame front of propane SF are lower than those of HF, opposite to methane. Therefore, a reduced level fuel consumption rate and S_c is expected for SF due to a reduced pool of key radicals.

In the reaction heat release analysis shown in Fig. 3.28, Reaction A, recombination of H and CH_3, and Reaction B, wet route of CO oxidation, release more heat in SF than

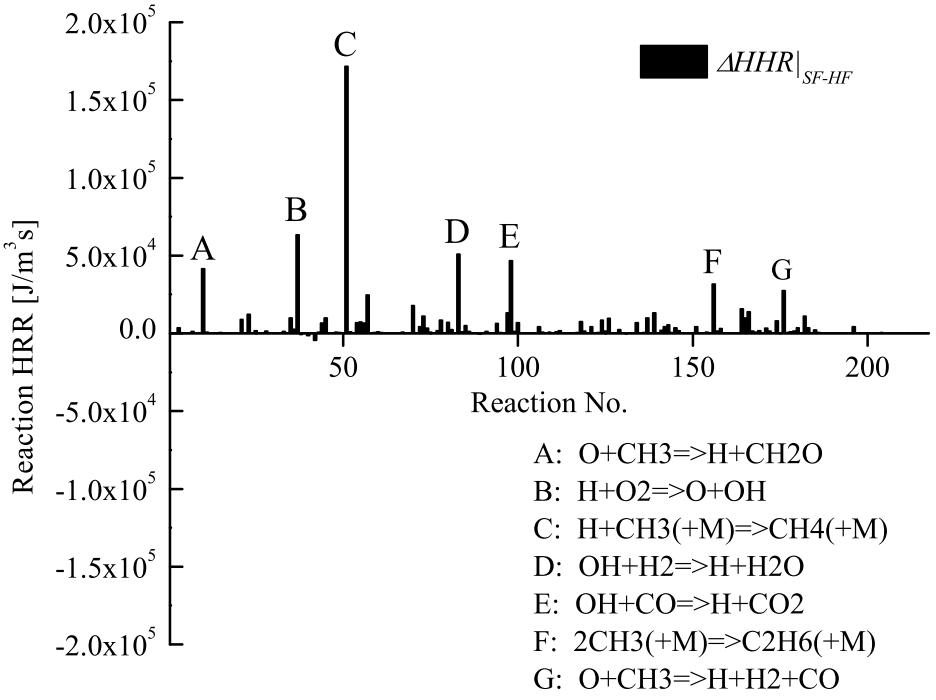

Figure 3.24: Difference between absolute heat release rates of reaction steps in methane/air stratified and homogeneous flames, at $\phi_f = 1.41$.

HF and they consume more H and OH radicals respectively. In contrast, there are fewer reactions of radical production in propane/air SF compared to methane/air SF. Therefore, in propane/air SF, intermediate hydrocarbon species generated from richer mixtures consume radicals in the burnt gas, leading to decreased levels of these key radicals and consequently reduced fuel consumption rate of SF. These intermediate hydrocarbon species are mainly seen in rich flames of larger hydrocarbon fuels. The enhancement in fuel consumption speed seen in methane/air SF is thereby suppressed.

Due to the nature of complicated chemical pathways for larger hydrocarbon fuels, the heat release not only comes from reactions related to fuel decomposition around flame front, but also the reactions between small hydrocarbon molecules and reactive radicals on the burnt side of the flame front. In stratified flames of propane/air mixtures, the heat release is enhanced through the latter reactions so that radicals are consumed on the burnt side and not as available for fuel decomposition compared to HF. Although S_c is reduced in SF, the total heat release rate of SF is still slightly higher indicated by Fig. 3.28.

The computed n-heptane/air flames exhibit a very similar trend as propane/air flames. Therefore, only the heat release reaction pathway analysis is provided for n-heptane/air flames. For unburnt mixture $\phi_u = 1.40$ of n-heptane/air mixtures, ϕ_f is equal to 1.44. In

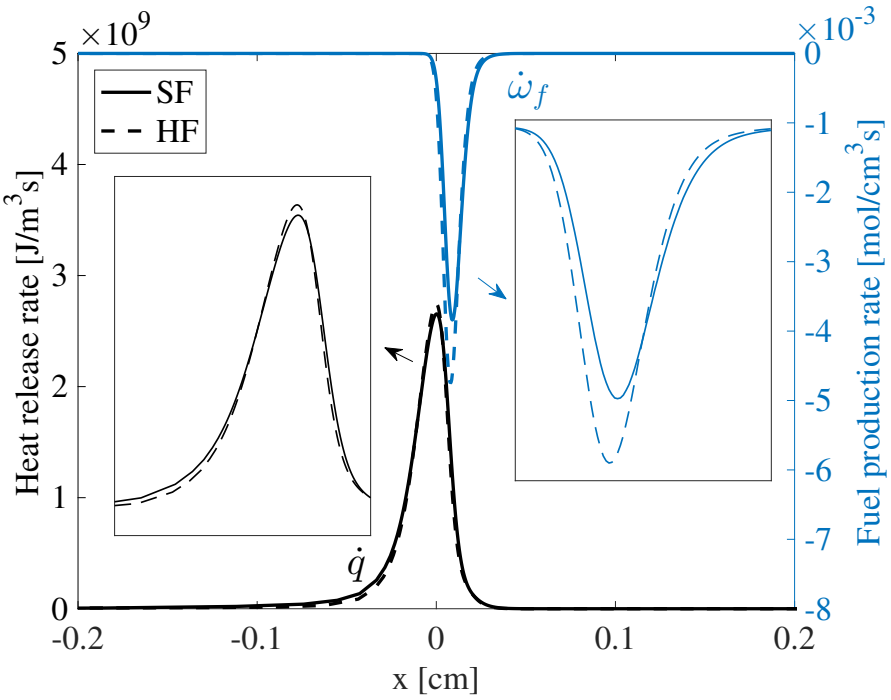

Figure 3.25: Heat release rates and fuel consumption rates in propane/air stratified and homogeneous flames, at $\phi_f = 1.42$.

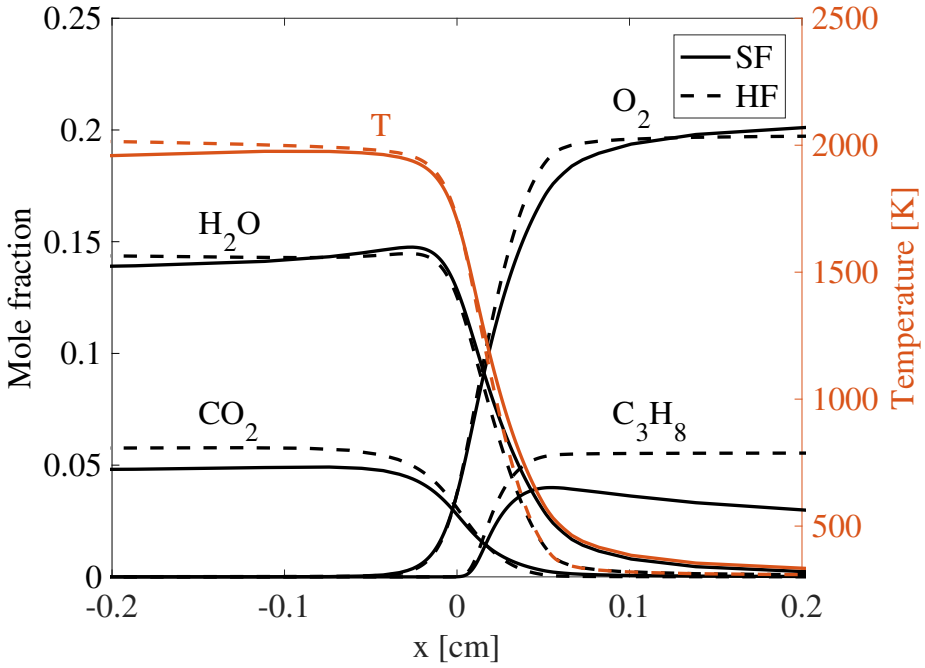

Figure 3.26: Temperature, mole fractions of reactants and products in propane/air stratified and homogeneous flames, at $\phi_f = 1.42$.

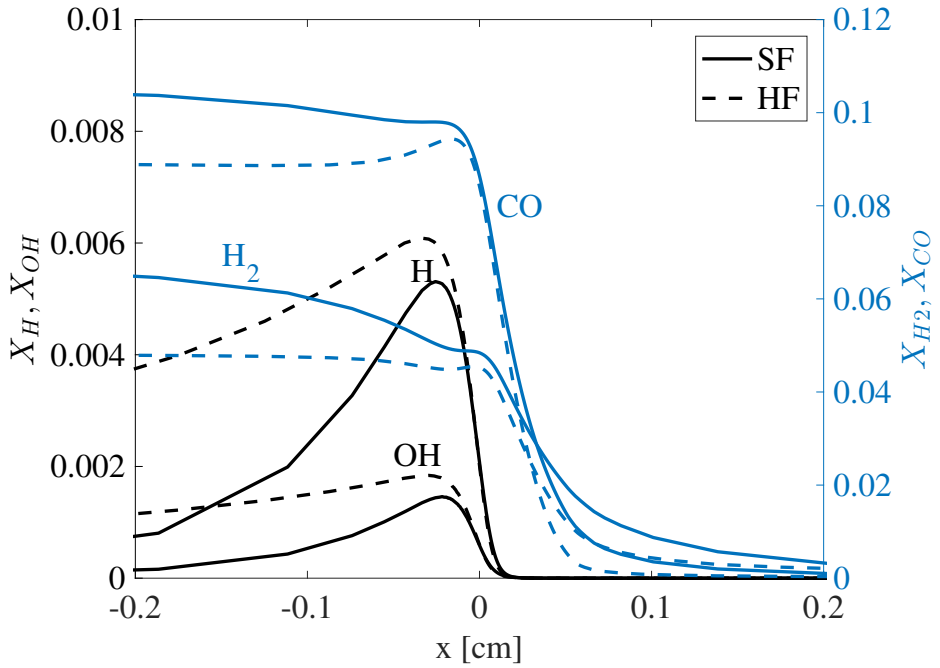

Figure 3.27: Mole fractions of intermediate species and radicals in propane/air stratified and homogeneous flames, at $\phi_f = 1.42$.

Figure 3.29, besides Reaction A and C which appear in propane/air flame analysis, Reaction B and D which involve in CH_2O and CH_2CO consuming H release more heat are found more active in SF than HF. Small intermediate hydrocarbon species such as CH_2O and CH_2CO remain in the burnt gas composition of richer mixtures and react with available radicals. It again indicates that the enhancement in fuel consumption speed is suppressed as radicals are consumed by the intermediate species of richer mixtures. The total heat release rate is still higher in SF, similar to propane.

Comparison among flame front propagation speeds

Comparisons of the computed flame front propagation speeds S_f are presented in Fig. 3.30 and 3.31. Different from the fuel consumption speed, the flame front propagation speed represents the local heat release behavior as well as the expansion of burnt gas. Moreover, the flame front propagation speed can be experimentally measured, facilitating comparisons between numerical results and experimental observations. For all three fuels, S_f of SF are consistently faster than those of HF throughout the entire stratification layer. The trends in S_f are consistent with those in S_c between SF and HF of all three fuels on the lean side, due to preferential diffusion of molecular hydrogen, i.e. chemical effect. In contrast, S_f of SF on the rich sides are also enhanced compared to HF, different from the S_c results of propane and n-heptane. Recall that although the fuel consumption speeds are reduced, the total heat release rates are still faster in rich SF of propane and n-heptane compared to their

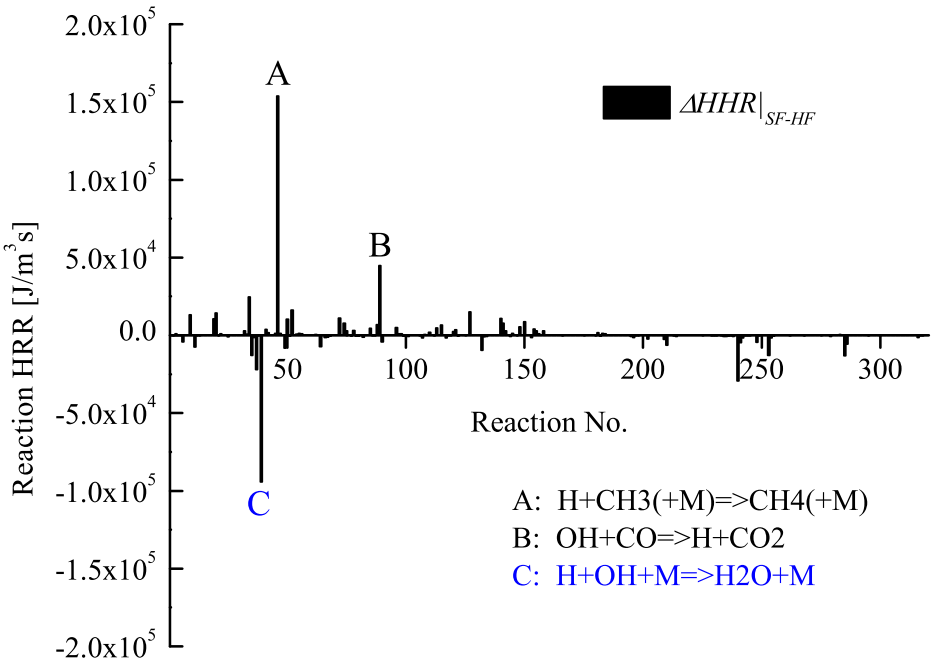

Figure 3.28: Difference between absolute heat release rates of reaction steps in propane/air stratified and homogeneous flames, at $\phi_f = 1.42$.

corresponding HF. According to the previous hydrogen stratified flame study, the transient expansion of burnt gas can introduce hydrodynamic effect, which changes the local velocity field thus influencing the flame front propagation speeds. When the flame front accelerates, propagating from rich to stoichiometric mixtures, not only is the unburnt gas further pushed away by the flame front, the burnt gas is also compressed towards the closed end, resulting in slightly negative fluid velocities. The flame front propagation speed tends to decrease due to consequent negative velocity field of burnt gases near the wall and vice versa. For SFs of three fuels in this study, the magnitude of flame acceleration/declaration is much smaller compared to hydrogen/air SF, as the velocity field of burnt gas remains negligibly small during the stratified flame propagation. Therefore, the hydrodynamic effect is negligible compared to the enhanced heat release due to chemical effect.

Effect of intermediate molecular hydrogen and its preferential diffusion

Despite the discrepancy between the results of S_c and S_f when comparing SF and HF on the rich side, a similar trend was shown when comparing different fuel species. In both Fig. 3.20 and Fig. 3.31, the percentage difference between SF and HF decreases in the sequence of methane, propane and n-heptane. Recall that all three stratified flames have about the same stratification thickness. Therefore, the reduced trend on impacts of stratification with larger fuel species should be related to specific fuel properties.

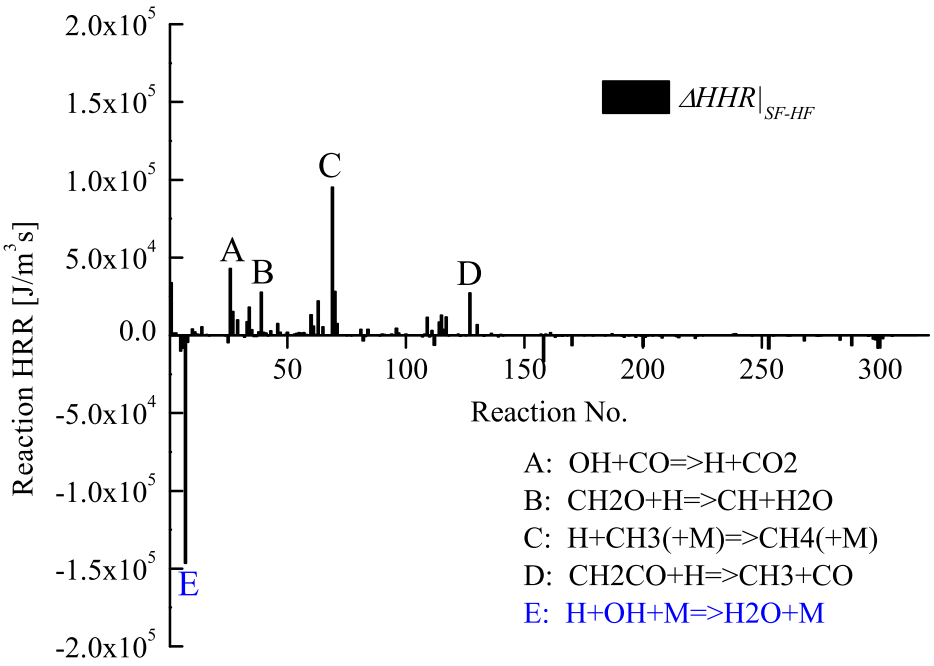

Figure 3.29: Difference between absolute heat release rates of reaction steps in n-heptane/air stratified and homogeneous flames, at $\phi_f = 1.44$.

According to the previous analysis, the enhancement in fuel consumption speeds of stratified mixtures results from the chemical effect, where lighter species such as H_2 diffuse ahead of the flame front. Figure 3.32 plots the mole fraction of molecular hydrogen (H_2) on the unburnt side of the flame front (half flame thickness from the flame front into the unburnt mixture) against equivalence ratio at flame front. The rich–to–lean stratified flame and the corresponding homogeneous flames are shown in terms of lines and symbols respectively. For homogeneous flames of all three fuels, little amount of hydrogen was produced under lean conditions. On the rich side, methane/air flames produced the most amount of hydrogen, followed by propane and n-heptane in part due to their lower H/C ratio of fuel molecule. As larger fuel tends to produce less intermediate molecular hydrogen under rich conditions, the corresponding stratified flames contain less hydrogen in the burnt gas to assist the local heat release. As a result, the enhancement in fuel consumption speeds of propane and n-heptane are not as strong as methane.

Although the amount of intermediate hydrogen produced in rich mixtures has been found to decrease in mixtures of larger fuel species, it does not necessarily indicate that the enhancement in fuel consumption speeds scales with hydrogen since combustion chemistry is different. Figure 3.33 quantifies the enhancement of homogeneous laminar flame speeds due to hydrogen addition for all three fuels. The computed results come from simulations of homogeneous mixtures with different amount of initial hydrogen addition. Lean ($\phi_u = 0.7$), stoichiometric ($\phi_u = 1.0$) and rich ($\phi_u = 1.3$) conditions are all tested. For each condition,

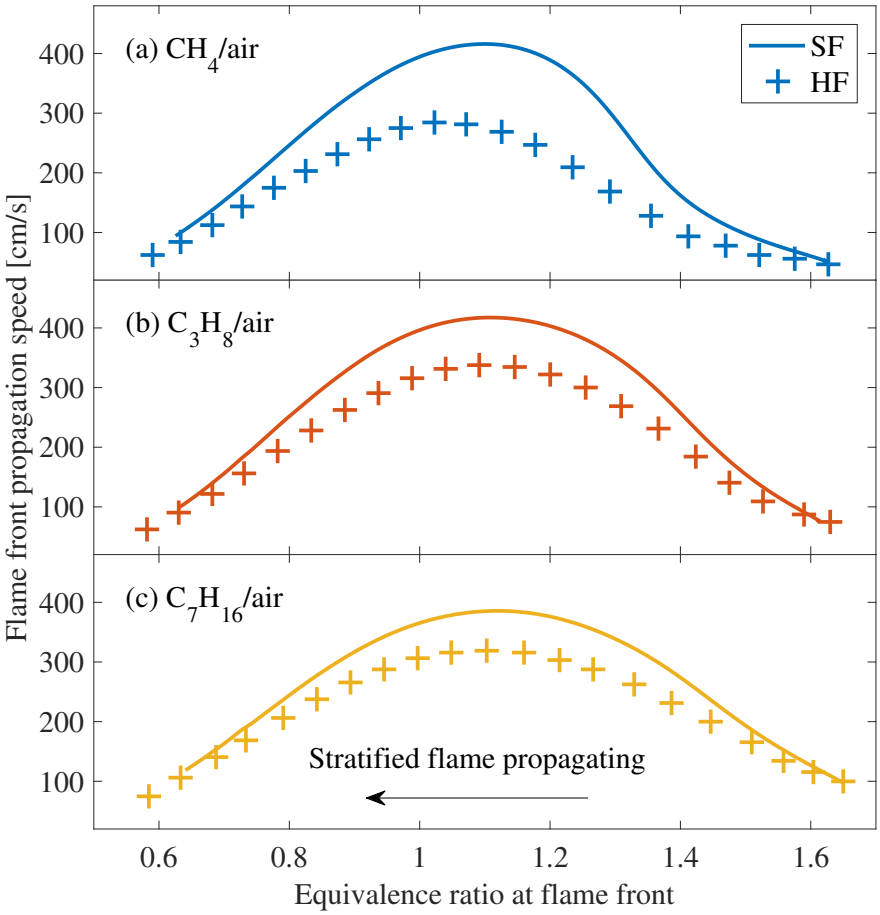

Figure 3.30: Flame front propagation speeds of the rich–to–lean stratified flames and the corresponding homogeneous flames.

hydrogen is added to the initial unburnt mixture and the overall equivalence ratio of the unburnt mixture based on element composition (Eq.3.1) is kept constant. The enhancement is evaluated by comparing laminar flame speeds of hydrogen-added and hydrogen-free mixtures. The enhancement percentage is plotted against the mole fraction of hydrogen in the initial unburnt mixture. According to Fig. 3.33, for the same amount of hydrogen addition, the enhancement is found to be stronger in methane compared to propane and n-heptane, for all investigated initial mixture compositions.

Therefore, Figure 3.32 and 3.33 together indicate that for fuels with a high H/C ratio such as methane, more intermediate hydrogen are being generated from its rich mixtures. In a rich–to–lean stratified flame, due to preferential diffusion of hydrogen, this enhanced level of hydrogen molecules assisted the local heat release, leading to an even more enhanced laminar flame speed compared to the corresponding homogeneous flames.

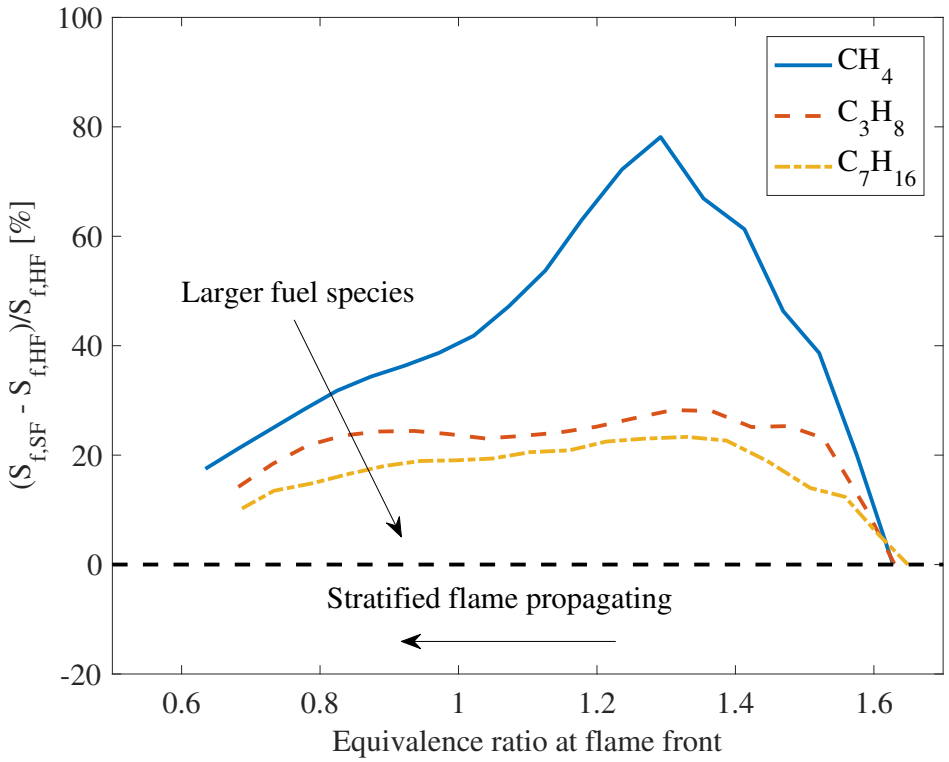

Figure 3.31: Percentage differences between flame front propagation speeds of the rich–to–lean stratified flames and the corresponding homogeneous flames.

Identification of mixture properties for stratified flames

Although equivalence ratio at flame front ϕ_f is able to evaluate the overall stoichiometry, the ratio between hydrogen and carbon elements can still vary. For rich–to–lean SF, the enhanced level of H_2 and H_2O increased the amount of hydrogen element at flame front. As a result, the mixture composition of stratified flame is not exactly the same as that of the corresponding homogeneous flame even with equal ϕ_f. Moreover, the mixture composition of stratified flames with different stratification thicknesses may also vary from each other. Therefore, equivalence ratio at the flame front is inadequate to identify the exact mixture composition of stratified flames.

Figure 3.34 plots the ratio of hydrogen and carbon elements of SF and HF for all three fuels. The observed trend is consistent compared to the results of S_f in Fig. 3.31. This result further confirms that the enhanced flame front propagation speeds of rich–to–lean stratified flames result from the chemical effect due to preferential diffusion of molecular hydrogen. For model development purpose, the H/C ratio combined with equivalence ratio at flame front may be used together to identify specific stratified flames.

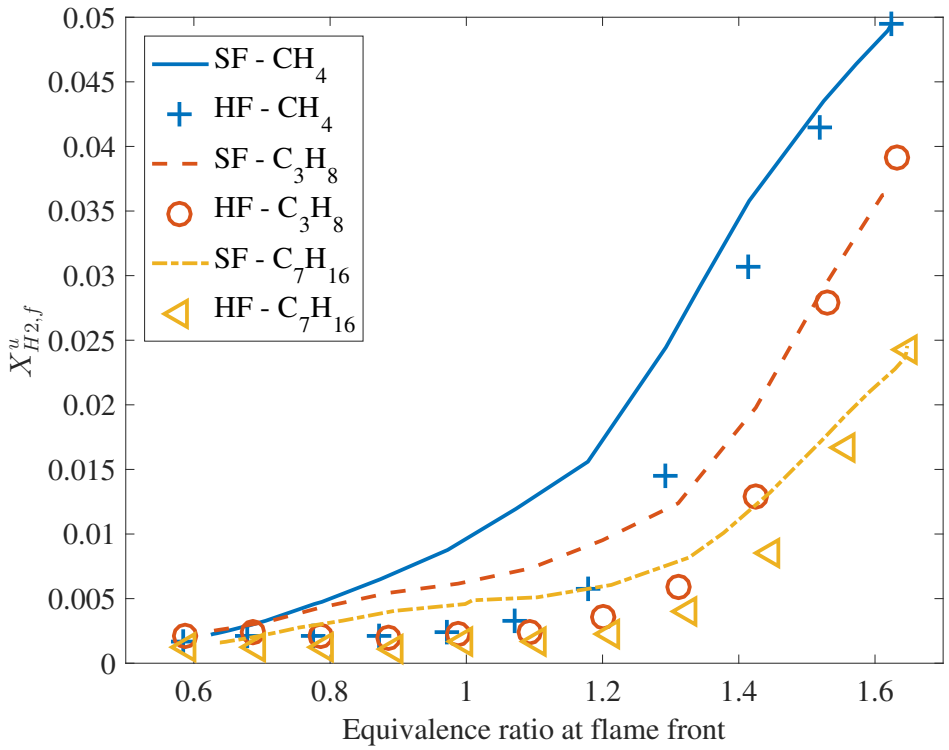

Figure 3.32: Mole fraction of molecular hydrogen on the unburnt side of flame front, for both the rich–to–lean stratified flames and the corresponding homogeneous flames.

Summary

Computed rich–to–lean stratified flames of three different hydrocarbon fuels are compared to their corresponding homogeneous flames in terms of fuel consumption speeds and flame front propagation speeds. The following conclusions are drawn:

1. For fuel consumption speeds, the stratified flame of methane/air is overall faster than homogeneous flames, due to the enhanced chemical activities by more radicals from burnt products of rich mixtures. In comparison, the rich–to–lean stratified flames of both propane/air and *n*-heptane/air flames have slightly lower fuel consumption speeds compared to those of homogeneous flames on the rich side. As reactive radicals such as H and OH react with intermediate hydrocarbon species in rich burnt gases, the overall fuel consumption rates of stratified flames are reduced due to lack of radicals at flame front.

2. For flame front propagation speeds, the stratified flames of all three hydrocarbon fuels are found faster than their corresponding homogeneous flames. For methane/air stratified flames, the enhancement of flame front propagation speeds resulted from the chemical effect - preferential diffusion of molecular hydrogen. For propane and

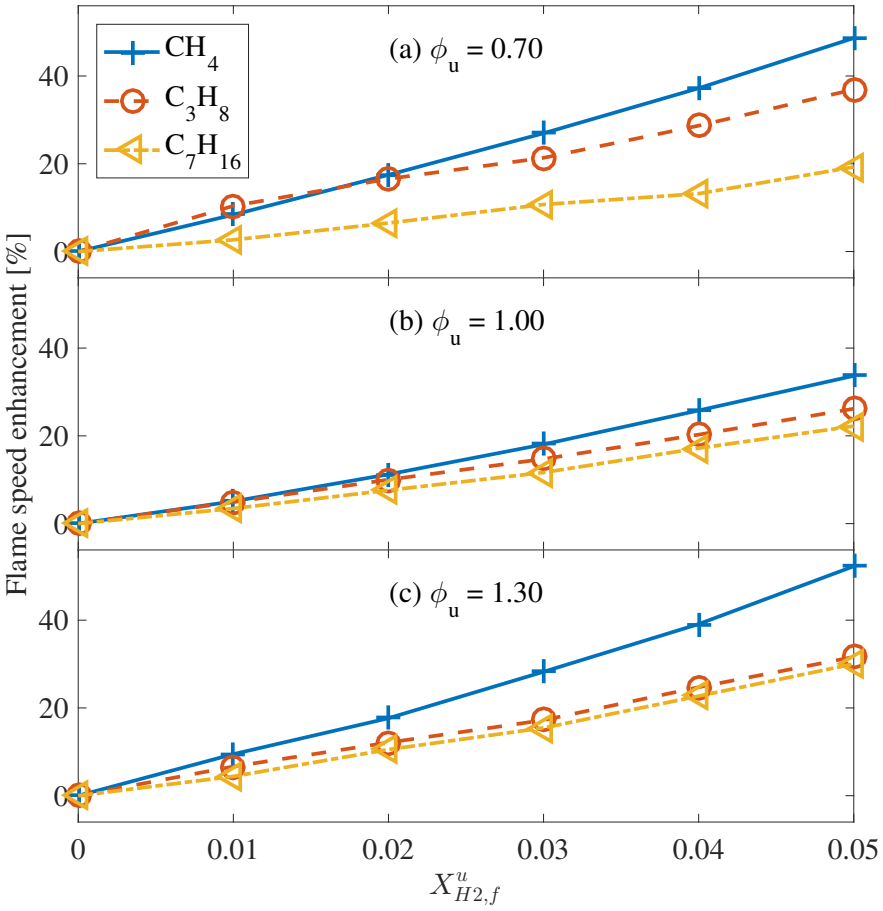

Figure 3.33: Enhancement of laminar flame speeds with hydrogen addition for methane, propane and n-heptane homogeneous flames; $X_{H2,unburnt}$ represents mole fraction of hydrogen in initial homogeneous unburnt mixtures.

n-heptane, while the enhancement on the lean side consistently resulted from chemical effect, the enhancement on the rich side resulted from enhanced total heat release rate for those reactions between intermediate species from burnt gas and key radicals (H, OH) release more heat on the burnt side of the flame front. The hydrodynamic effect is found unimportant for stratified flames of these three fuels.

3. For both fuel consumption speeds and flame front propagation speeds, stronger enhancement of stratified laminar flame speeds is observed in methane/air mixtures. More intermediate hydrogen is generated in the rich mixtures of methane, while the corresponding enhancement on laminar flame speeds due to the same amount of hydrogen addition is also stronger in methane/air mixtures.

4. Equivalence ratio at flame front is insufficient to define a specific stratified flame as the amount of carbon and hydrogen elements can still vary. The H/C ratio along with

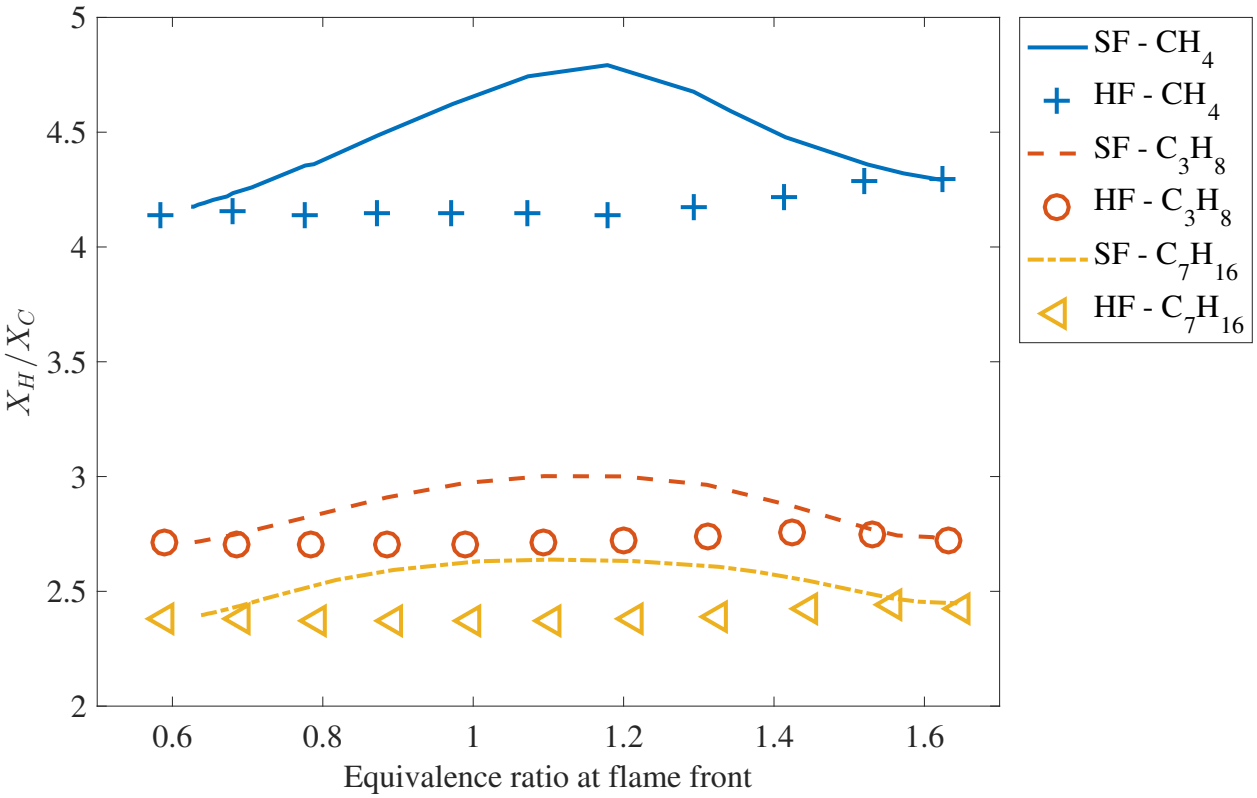

Figure 3.34: H/C ratio at flame front of the rich–to–lean stratified flames and the corresponding homogeneous flames.

equivalence ratio at the flame front may be used to provide an improved identification of the exact mixture composition of stratified flames.

3.5 Stratified flame speed model

This section is based on the paper published in *Combustion and Flame* (Shi and Chen, 2017).

3.5.1 Introduction

The thermal and chemical effects have been carefully investigated in the above two sections for stratified flames of various fuel species. The role of preferential diffusion has been confirmed to play an important role in the departure of stratified flames from the corresponding homogeneous flames. The next question is how the stratified flame speeds can be modeled with the consideration of preferential diffusion. An accurate prediction of stratified flame speeds can benefit experiment interpretation and turbulent combustion modeling by developing more comprehensive flame speed look-up tables with consideration of fuel stratification.

This section examines the effect of preferential diffusion on the enhancement of flame speed with a detailed quantitative analysis, including a sensitivity study of transport properties. Furthermore, to the best of the author's knowledge, there does not exist a stratified flame speed model that takes into account of differential diffusion and covers a wide range of conditions, both rich and lean. In order to improve current understanding of stratified flames and to facilitate development of stratified flame speed models, this section

1. presents detailed one-dimensional stratified flame numerical results of methane/air flames with mixture-average diffusivity model and validated reduced chemical kinetic model;
2. discusses various stratification configurations of stratified methane/air flames;
3. conducts a sensitivity study of diffusivities to identify the root cause for the difference between laminar flame speeds of stratified and homogeneous mixtures;
4. proposes a transient local stratification level (LSL) model incorporating both the effect of preferential diffusion and the memory effect.

Stratified and homogeneous flame simulation results are presented in the sequence of 1) detailed comparisons among various stratification configurations, 2) a sensitivity analysis of transport properties and 3) the LSL model including model approach, development and assessment.

Numerical model and setup

A similar numerical setup as shown in Fig. 3.5 is used in this study. The length of the entire calculation domain is 20 cm. Reflective boundary condition (wall) is imposed on the left end, while zero-gradient boundary condition (open) is imposed on the right. A 7-level adaptive mesh refinement scheme is implemented with the minimum grid size 4 μm to resolve both the flame front and the stratification layer. The initial temperature, pressure and fluid velocity fields of unburnt gases are set to 300 K, 1 atm, and 0 cm/s respectively. For all the stratified flame cases investigated in this study, the stratification thickness is kept on the order of 0.1cm if not specified otherwise. Cases are run with a range of stratification thicknesses, which are either on the same order of or larger than the flame thickness. These runs intend to simulate stratified flames in the wrinkled flame regime, which is observed in many practical devices, such as a direct injection IC engine. The stratification in such an engine is mainly dominated by the turbulence smallest length which is normally larger than the flame thickness.

The 16-species reduced chemical kinetic model was used for methane/air stratified and homogeneous flames. Detailed validation of the reduced chemical kinetic model can be found in Appendix B.

Results and discussion

Comparison between stratified and homogeneous flames

A series of SF is first compared to their corresponding HF. Figure 3.35 presents the computed fuel consumption speeds of five SF propagating from unburnt mixtures of $\phi_u = 1.6, 1.4, 1.2, 1.0, 0.8$ into an unburnt mixture of $\phi_u = 0.6$, and the corresponding HF. The computed flame speeds are plotted against equivalence ratio at flame front ϕ_f. Similarly, Figure 3.36 shows the results of five SF propagating from unburnt mixtures of $\phi_u = 0.6, 0.8, 1.0, 1.2, 1.4$ into an unburnt mixture of $\phi_u = 1.6$ as well as HF. The stratification thicknesses of all the SF cases shown in Fig. 3.35 and Fig. 3.36 are on the order of 0.1 cm. While fuel consumption speeds of most SF cases are very close to those of HF for lean–to–rich SF, the rich–to–lean SF, e.g., 1.6–0.6 and 1.4–0.6 SF, show significant departures from HF, with up to 30% increase in fuel consumption speeds.

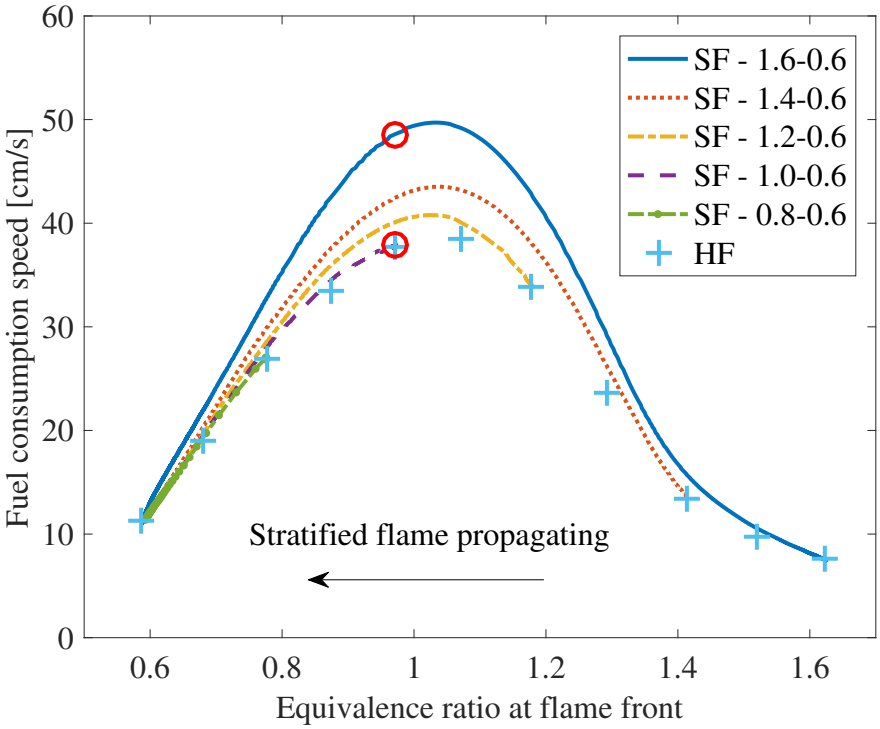

Figure 3.35: Fuel consumption speeds of SF propagating into lean mixtures and corresponding HF.

To reveal the underlying physics causing such large departures, detailed flame property profiles of the 1.6–0.6 SF and HF at $\phi_f = 0.97$ (marked by circles in Fig. 3.35) are analyzed, where a significant difference in fuel consumption speeds is observed ($S_{c,HF} = 37.8$ cm/s, $S_{c,SF} = 48.5$ cm/s). Figure 3.37 compares the computed profiles of heat release rate and temperature in the flame front frame of reference, where $x = 0$ denotes the flame front location, with the unburnt mixture on the right and the burnt mixture on the left. As seen

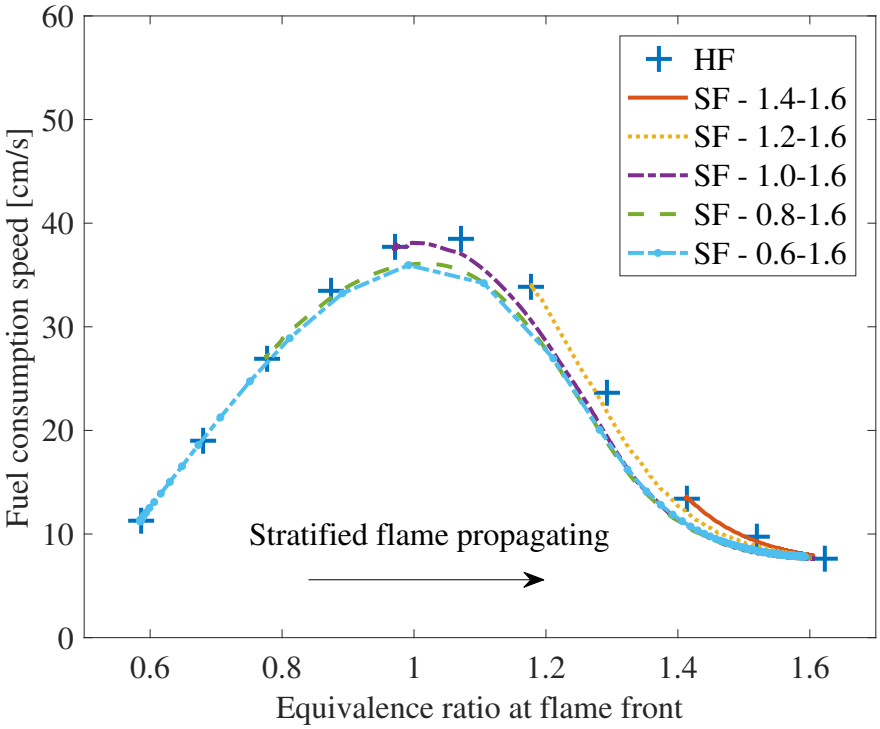

Figure 3.36: Fuel consumption speeds of SF propagating into rich mixtures and corresponding HF.

in the figure, the heat release rate of SF is significantly higher (∼60%) than that of HF near the flame front, which is consistent with the observed flame speed enhancement. In terms of temperature, SF and HF are very similar: on the burnt side, the temperature of SF is slightly higher than that of HF due to a higher heat release rate. For the region $x > 0.04$ cm, the unburnt temperature of SF is seen higher than that of HF by approximately 50 K. Since there is negligible heat release in the unburnt mixture of SF, the temperature rise is caused by transport processes, i.e., either heat diffusion or mass diffusion carrying extra enthalpy.

Figure 3.38 shows the profiles of reactants CH_4, O_2 and products H_2O, CO_2 for both SF and HF. The decreasing profile of CH_4 in the unburnt mixture of SF ($x > 0.04$ cm) is indicative of that SF propagates into a leaner mixture. On the burnt side ($x < 0$), SF has much more H_2O but less CO_2. On the unburnt side, SF also has more H_2O, similar to the temperature profile comparison. Since H_2O has a smaller molecular mass compared to other major product species, preferential diffusion of H_2O leads to more H_2O diffusing into the unburnt mixture. Figure 3.39 compares the profiles of intermediate species CO, H_2 and radical H, OH, while Figure 3.40 compares the production rates of H_2, H and OH. The production rate profile of CO is very similar to that of H_2, thus not shown. Relative to the HF, all these species have higher concentrations near the flame front in SF, as well as higher production rates. In particular, the concentration of H_2 in SF is much higher than HF, not

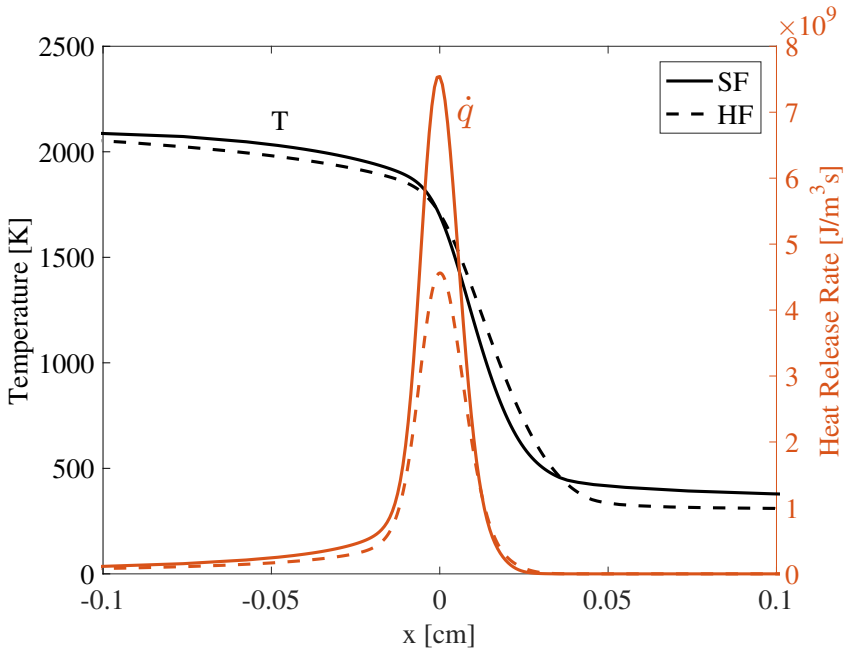

Figure 3.37: Heat release rate and temperature profiles of the 1.6–0.6 SF and HF, $\phi_f = 0.97$.

only near the flame front, but also on both burnt and unburnt sides. As the SF propagates from rich mixtures, excess fuel decomposes and produces extra H_2 in the burnt products. As an extremely light species with small molecular mass, H_2 is able to diffuse much faster than most other species as well as the flame front propagation. Consequently, the extra H_2 in the rich burnt products diffuses into the flame front as well as the unburnt mixture. The enhanced level of H_2 not only boosts flame speed by producing more H and OH radicals as indicated in Fig.3.40, but also increases the temperature of unburnt mixtures and generates even more H_2. This also explains that SF produces more H_2O but not CO_2 compared to HF. To summarize, the increase in flame speeds of rich–to–lean SF is found closely related to the preferential diffusion of lighter species, such as H_2O and H_2.

Sensitivity study of transport properties

Although the detailed analysis of flame properties has revealed the key differences between SF and HF, the relative contributions from various transport processes, such as heat transfer, mass diffusion of different species, need to be clarified. To evaluate the relative importance of these transport processes, a sensitivity study of thermal and mass diffusivities on the computed flame speeds is conducted. Figure 3.41 compares the fuel consumption speeds of the 1.6–0.6 SF and HF under four different scenarios of transport properties. In Fig. 3.41(a), the assumption of unity Lewis number (unity-Le) is made for all species, i.e., the diffusivity of every species is set equal to the thermal diffusivity of the bulk fluid. The computed flame speeds of HF drop by approximately 30% compared to those without the assumption

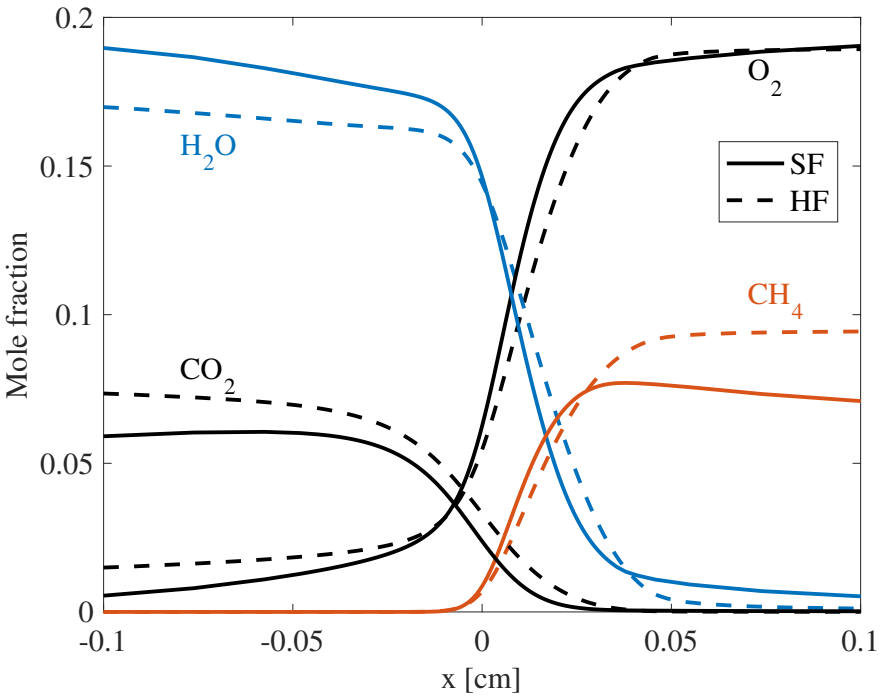

Figure 3.38: Reactant and product profiles of the 1.6–0.6 SF and HF, $\phi_f = 0.97$.

of unity Lewis number, i.e., the results in Fig. 3.41(d). Furthermore, the computed flame speeds of SF and HF are very close to each other with the maximum difference less than 5%. Since the effect of differential diffusion is eliminated by the unity-Le assumption, the differences between SF and HF are caused by both heat and mass diffusion. Through the stratification layer, the instantaneous adiabatic flame temperature varies according to the varying mixture composition at the flame front, so do the distributions of intermediate species and radicals. Therefore, SF flame front still experiences either back- or front-support heat and mass diffusion (Kang and Kyritsis, 2007; Cruz et al., 2000). However, the unity-Le result suggests that the effect of heat and mass diffusion processes without differential diffusion is very weak in the methane SF.

If the unity-Le assumption is only applied to lighter species H_2, H_2O, H and OH, the computed results shown in Fig. 3.41(b) are only slightly different from those in Fig. 3.41(a). In Fig. 3.41(c), the unity-Le assumption is made only to H_2 and H_2O. A significant increase in the computed flame speeds is observed in both SF and HF, while a clear difference between SF and HF appears. These results imply that the preferential diffusion of radicals H and OH not only plays an important role in HF, but also contributes to the enhancement observed in SF. Compared to Fig. 3.41(c), the HF results without the unity-Le assumption in Fig. 3.41(d) are almost identical; however, an even larger difference between SF and HF is observed. To summarize, the enhancement of flame speeds in SF mainly comes from the preferential diffusion of lighter immediate species and radicals.

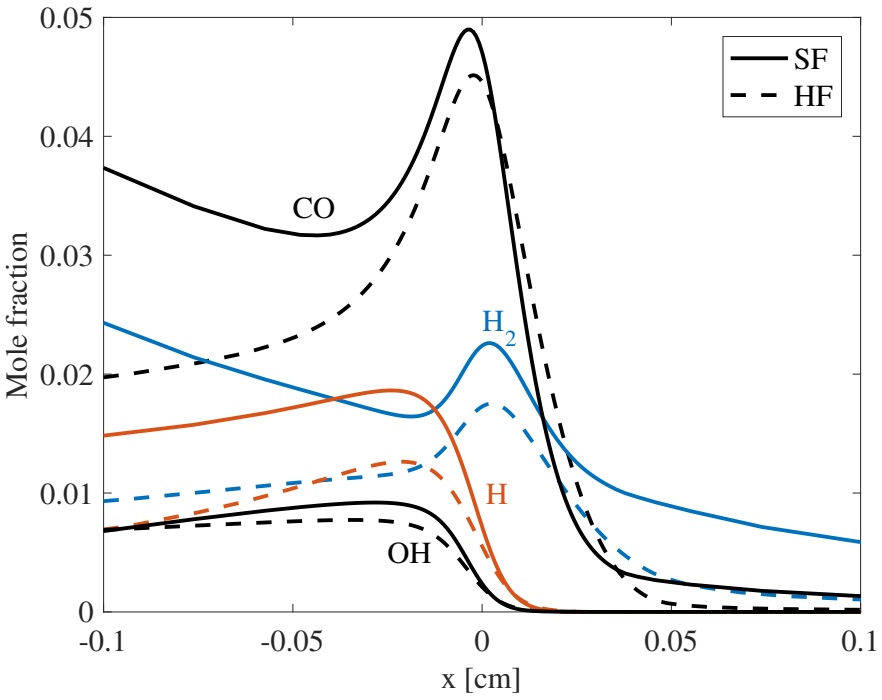

Figure 3.39: Major intermediate species and radical profiles of the 1.6–0.6 SF and HF, $\phi_f = 0.97$.

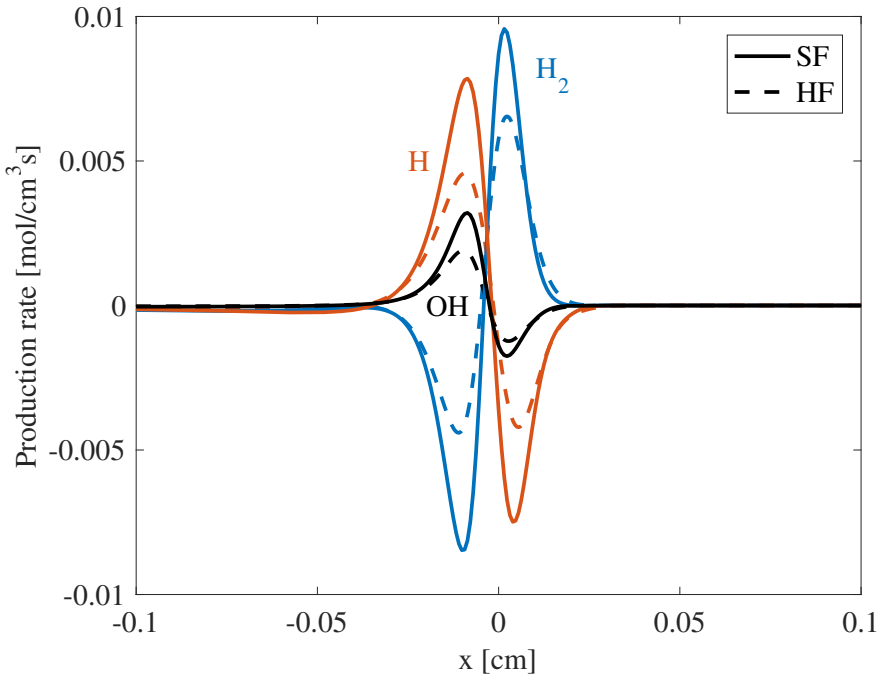

Figure 3.40: Production rate profiles H_2, H and OH, of the 1.6–0.6 SF and HF, $\phi_f = 0.97$.

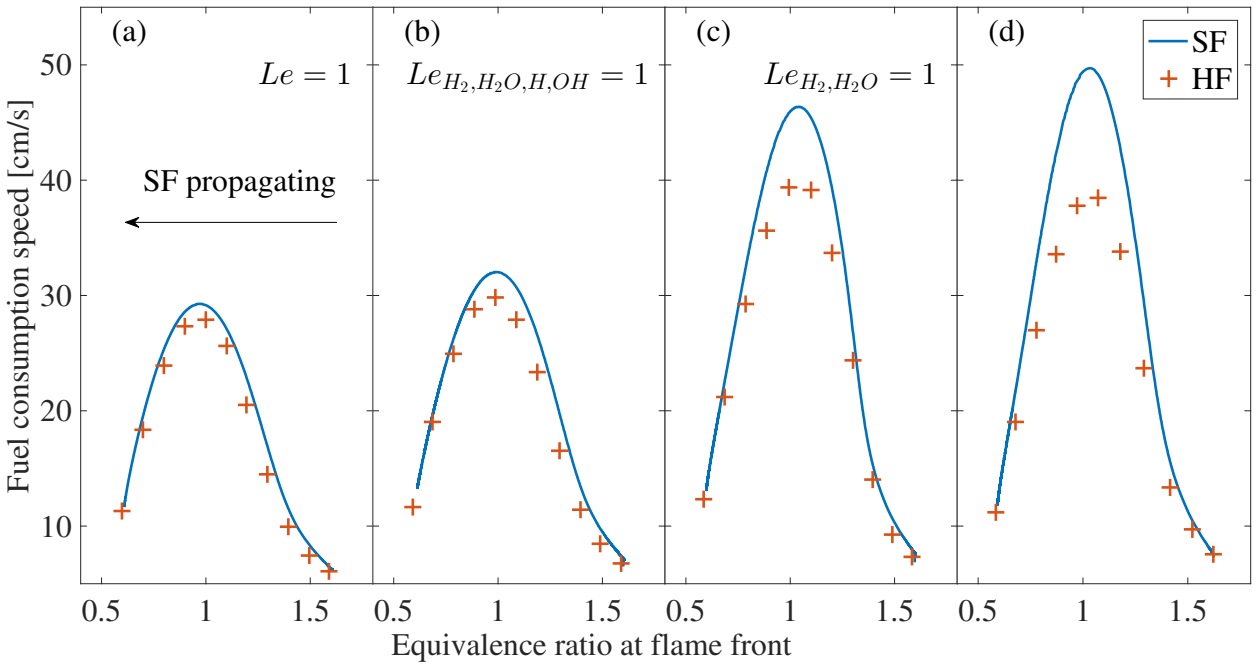

Figure 3.41: Fuel consumption speeds of the 1.6–0.6 SF and HF with different assumptions of unity Lewis number: (a) $Le = 1$, (b) $Le_{H_2,H_2O,H,OH} = 1$, (c) $Le_{H_2,H_2O} = 1$, (d) no unity-Le assumption.

As H_2 and H_2O in SF are capable of diffusing preferentially into unburnt mixtures and causing an increase in unburnt temperature, the reaction rates, as well as flame temperatures, may increase correspondingly. Numerical experiments are conducted with enhanced or reduced diffusivities of H_2 and H_2O by 50%. Figure 3.42 shows the sensitivity of computed results with respect to the diffusivity of H_2. While the flame speeds of HF with three different diffusivity values are almost the same, the differences between SF and HF increase with enhanced H_2 diffusivity. This is expected as more H_2 diffuse from the burnt zone toward the flame front leading to an enhanced reactivity of the flame front by producing more radicals. In comparison, Figure 3.43 shows the corresponding results when the diffusivity of H_2O is altered. With higher diffusivity value of H_2O, the difference between SF and HF reduces implying that preferential diffusion of H_2O decreases the reactivity of SF. By comparing the detailed flame profiles, slightly higher unburnt temperature, more H_2O but slower chemical kinetics are observed in the unburnt mixture near the flame front with a higher H_2O diffusivity. Therefore, the dilution/quenching effect introduced by H_2O outplays its enthalpy-carrying benefit.

In conclusion, the preferential diffusion of H_2 along with radicals H and OH is found to play an influential factor in stratified flames. Unlike short-lived radicals H and OH, a noticeable amount of H_2 can be produced from rich methane/air flames. On one hand, H_2 as a very reactive species, produces key chain-branching radicals, such as H and OH,

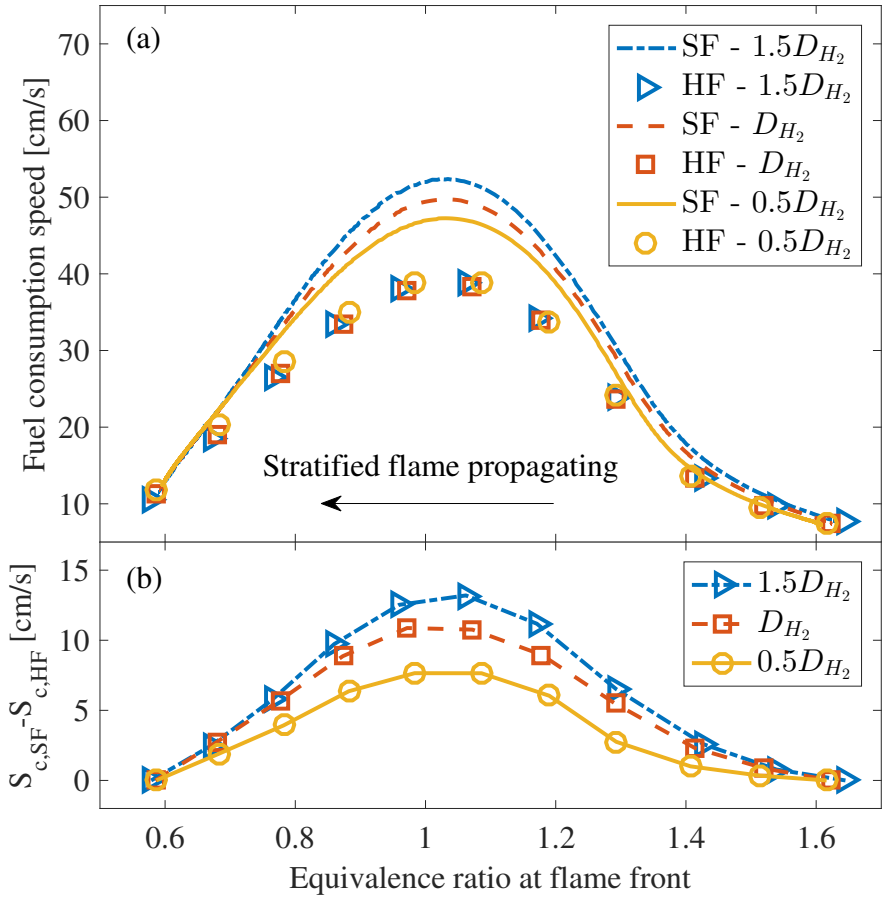

Figure 3.42: (a) Fuel consumption speeds of the 1.6–0.6 SF and HF, and (b) the respective differences between SF and HF, with different diffusivity of H_2.

leading to higher heat release rates and consequent higher flame speeds. On the other hand, extra H_2 diffuses from the burnt zone into the unburnt mixture and increases the unburnt temperature, which also results in higher reaction rates.

The methodology of this sensitivity study can be applied to heavier fuel species or different diluent scenarios. As shown in the previous study, rich flames of heavier fuel species, such as propane and *n*-heptane, have more complicated chemical pathways than those of methane. In particular, some small intermediate hydrocarbon molecules also play a role in causing the differences between flame speeds of SF and HF. Therefore, sensitivity studies under such scenarios need to include a wider range of species and radicals.

Effect of stratification thickness and equivalence ratio gradient

Although the main cause of SF to differ from HF is tied to preferential diffusion, correlations between the degree of stratification and departure of SF from HF are needed for development

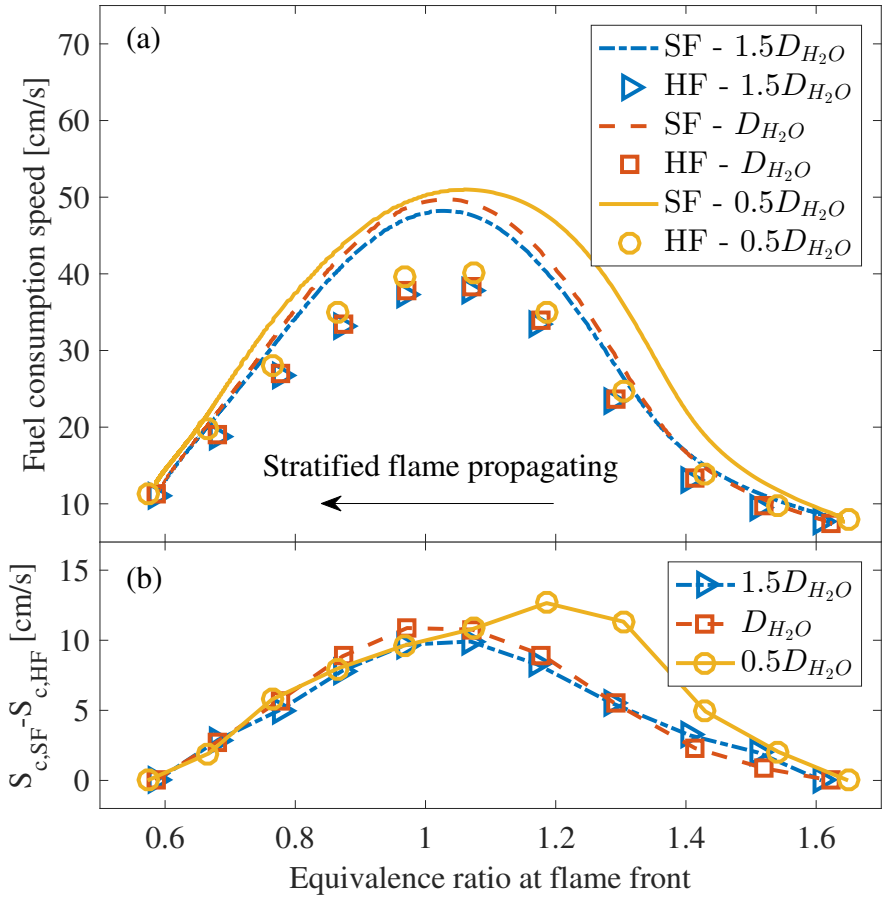

Figure 3.43: (a) Fuel consumption speeds of the 1.6–0.6 SF and HF, and (b) the respective differences between SF and HF, with different diffusivity of H_2O.

of stratified flame speed models. To this end, several cases of SF with different initial stratification thicknesses, determined by Eq. 3.13, are computed. Figure 3.44 shows the results of three 1.6–0.6 SF compared to HF. As expected, a stratification layer with a smaller thickness results in a larger gradient of H_2 in the burnt products leading to stronger enhancement in SF, up to 50% increase in the d_s =O(0.05 cm) case. In comparison, Figure 3.45 shows the results of three 1.0–0.6 SF compared to HF. As the stoichiometric methane/air flame does not produce as much hydrogen in the burnt products, even with the smallest stratification thickness, the enhancement in SF is noticeable but insignificant. Therefore, the difference in the flame speeds between SF and HF depends on the degrees of stratification as well as the availability of H_2 in burnt gases.

Besides the initial stratification thickness, the instantaneous equivalence ratio gradients at the flame front, calculated by Eq. 3.12, is also a useful parameter to correlate the differences between SF and HF when the SF burns through the stratified layer. Figure 3.46 shows the results of stratified flames at $\phi_u = 0.8$, 1.0 and 1.2 from different initial stratification

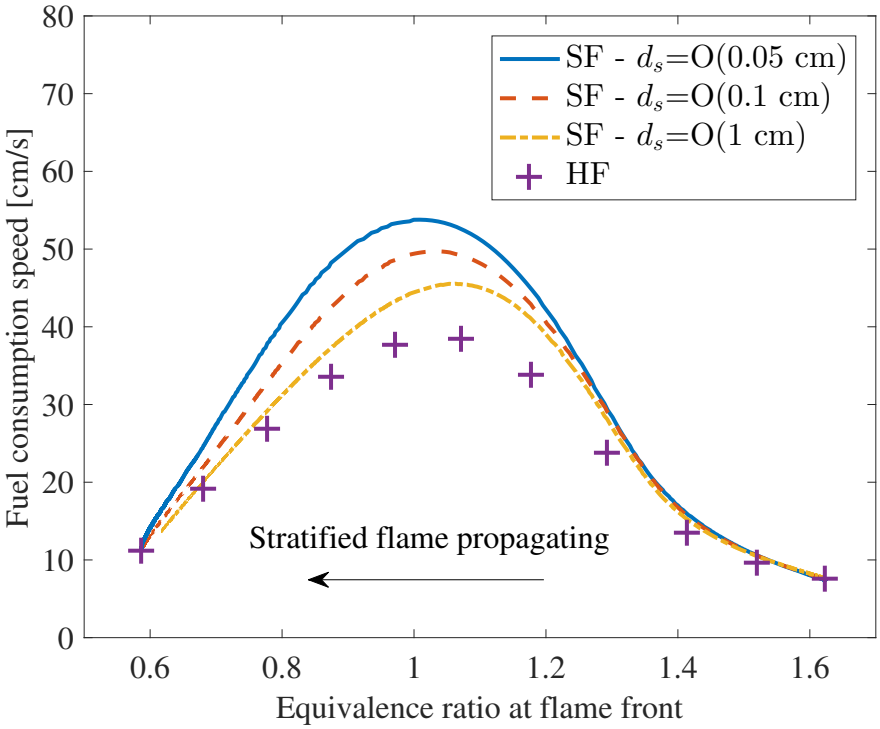

Figure 3.44: Fuel consumption speeds of the 1.6–0.6 SF with different stratification thicknesses and HF.

setups. The points are taken from the simulations presented in Fig. 3.35 and Fig. 3.36, as well as simulations of same configurations but with different stratification thicknesses. A positive correlation can be seen between the instantaneous equivalence ratio gradient and the difference between SF and HF. The deviation from a linear line shows that the instantaneous equivalence ratio alone is insufficient to describe the flame speed mainly due to the memory effect. In addition, all the stratified flames simulated so far are ideal and monotonic cases, where the flame monotonically propagates from one mixture into another. A simple correlation may not hold for more complicated and non-monotonic stratified flame configurations. For example, in a 3-phase rich–lean–rich methane/air stratified flame case (which will be shown later in the model section), when the flame front passes through the leanest condition, the flame front is at the minimum value of equivalence ratios. Although the instantaneous equivalence ratio gradient is thus zero, the computed flame speed of the SF is still higher than that of HF due to memory effect that the SF propagates from rich mixtures with an excess of H_2. In stratified turbulent flames, the flame front may often experience such non-monotonic variations of equivalence ratios. In those cases, the memory effect of stratified flame makes the equivalence ratio gradient alone insufficient to describe the stratified flames. The above observation is consistent with the importance of memory effect recognized by many previous studies (Bissett and Reuss, 1986; Kang and Kyritsis, 2007; Balusamy et al., 2014; Vena et al., 2011; Sorensen, 2016).

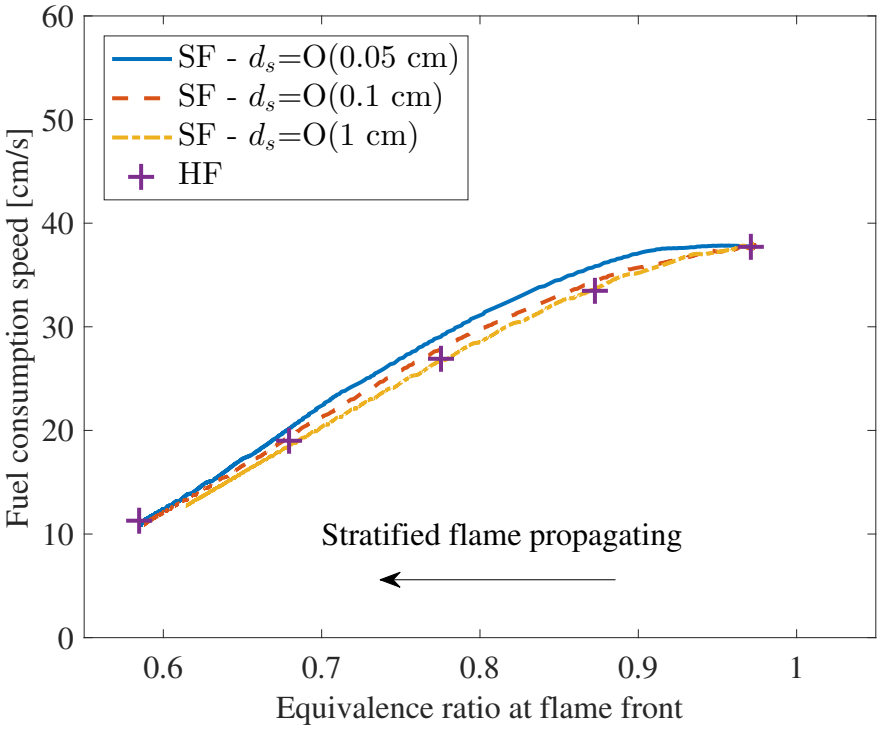

Figure 3.45: Fuel consumption speeds of the 1.0–0.6 SF with different stratification thicknesses and HF.

Model development for laminar flame speed of stratified methane/air mixtures

The goal of a stratified flame speed model is to accurately describe stratified flame speeds by distinct flame features. With a reasonably accurate flame speed model, stratified flames can be simulated without time-consuming computations of detailed chemistry and multicomponent transports. Such a model can be implemented in the G-equation method or other level-set methods, where flame speed tables are used Peters (2000). In terms of modeling methodology, there are two general approaches to incorporate the memory effect. The first approach is to calculate model variables based on information from previous flame front locations, while all the required information are taken under the current time step. For example, Kang and Kyritsis (2005) used the integral (global) characteristics of the equivalence ratio distribution and proposed a corrected overall equivalence ratio gradient to evaluate stratified flames. Although this approach is of mathematical convenience and easy to implement, it has several major disadvantages. First, the model only works qualitatively for specific situations, e.g., monotonic stratification layers. Second, it becomes very difficult to implement the model in multidimensional simulations due to the ambiguity of flame propagation direction and trajectory.

The second approach is to construct a transient model variable and solve for the corresponding modeling equation. The model variable can be then evaluated on-the-fly or

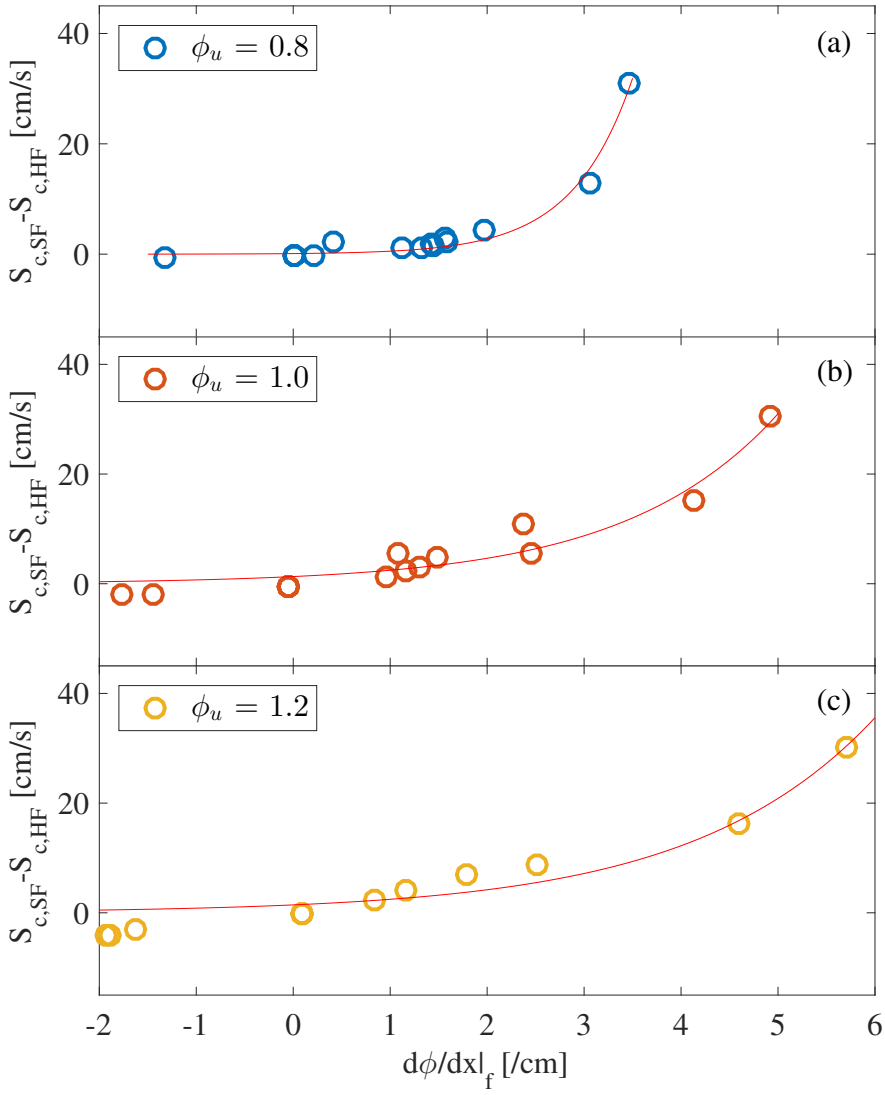

Figure 3.46: Departure of fuel consumption speeds of stratified flames compared to homogeneous flames based on instantaneous equivalence ratio gradients at flame front: (a) $\phi_u = 0.8$, (b) $\phi_u = 1.0$, (c) $\phi_u = 1.2$.

post-processed. As such, the model is able to carry the accumulated information (memory effect) when appropriately constructed. This approach is based on fluid equations and chemical processes, and can be directly implemented in multidimensional simulations. To this end, δ, defined as local stratification level (LSL), is proposed as the key variable to represent the departure of SF from HF. Specifically, the LSL at flame front, denoted by δ_f, is evaluated and correlated to the difference between fuel consumption speeds of SF and HF. There are essentially two steps involved in this modeling approach:

- Step 1: Construct and solve for a model equation of δ_f, based on global characteristics of stratified flames
- Step 2: Correlate δ_f to the difference between the flame speeds of SF and HF

During Step 1, in order to construct the model equation of δ_f, δ is assumed to relate to one or more instantaneous flame properties, such as flame temperature and concentration of certain species. Although there are many ways to relate δ to any combination of flame properties, the difference between the amounts of H_2 of SF and HF seems to be a reasonable choice based on the analysis presented above. Figure 3.47 shows the positive correlation between flame speed differences and the differences between mole fraction of H_2 on the unburnt side, i.e., $X^u_{H_2,f}$, of SF and HF. $X^u_{H_2,f}$ refers to the amount of H_2 at the location of ϕ^u_f in Fig. 3.3. The points are taken from all the computed stratified and homogeneous flames presented in this section. An overall linear correlation is observed and provides some justification that the difference in the molecular hydrogen between SF and HF is a reasonable candidate for constructing δ.

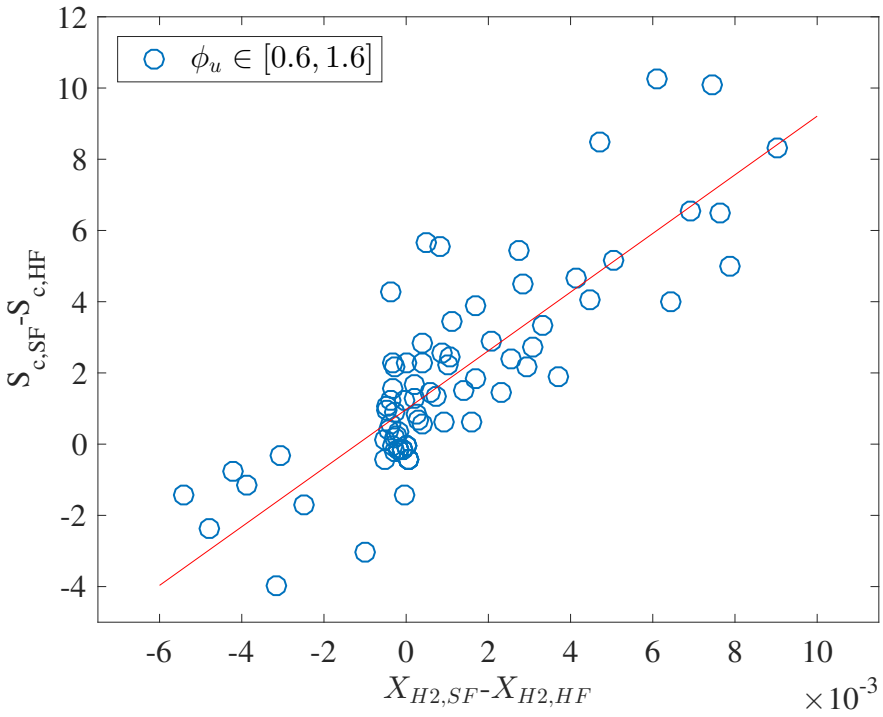

Figure 3.47: Correlation: difference between flame speeds of SF and HF, versus difference between mole fractions of H_2 on the unburnt side of SF and HF flame fronts.

A control volume surrounding δ_f is sketched in Figure 3.48. Since δ_f is the LSL at flame front, the control volume moves along with the flame implying that a flame front tracking method is required. The control volume illustrates the physical processes which drive the

change of δ_f and facilitates a simplified model. Instead of solving the entire field of δ, the change of δ_f can be simply modeled by considering 1) diffusion, 2) convection and 3) chemical reactions as described in Eq. 3.14. As H_2 is an intermediate species for methane/air flames, both its concentration and the concentration gradient on the unburnt side are assumed to be zero.

$$\frac{d\delta_f}{dt} = \mathcal{D} + \mathcal{C} + \mathcal{R} \tag{3.14}$$

The diffusion process is assumed to obey the Fick's law and the gradient of δ is correlated to local equivalence ratio and its gradient:

$$\begin{aligned}\mathcal{D} \approx D_{km} \left.\frac{d^2\delta}{dx^2}\right|_f &\approx C_{\mathcal{D}} D_{km} \frac{\left.\frac{d\delta}{dx}\right|_b - 0}{d_f} \\ &\approx C_{\mathcal{D}} \frac{D_{km}}{d_f} \left.\frac{d\delta}{dx}\right|_f \approx C_{\mathcal{D}} \frac{D_{km}}{d_f} f(\phi) \left.\frac{d\phi}{dx}\right|_f,\end{aligned} \tag{3.15}$$

where

$$\left.\frac{d\delta}{dx}\right|_f \approx f(\phi) \left.\frac{d\phi}{dx}\right|_f.$$

The subscript b denotes the quantity on the burnt side of the control volume and $f(\phi)$ denotes the transfer function from the gradient of δ to equivalence ratio gradient at flame front. The transfer function is assumed to be a function depending only on ϕ, as the local concentration of H_2 is primarily determined by local stoichiometry. The convection term can be evaluated with unburnt and burnt velocities using first-order finite difference:

$$\mathcal{C} = \left.\frac{d(\delta V)}{dx}\right|_f = C_{\mathcal{C}} \frac{0 \cdot V_u - \delta_b \cdot V_b}{d_f} \approx -C_{\mathcal{C}} \frac{V_b}{d_f} \delta_f. \tag{3.16}$$

where V_u and V_b denote the fluid velocities on the unburnt and burnt sides relative to the flame front respectively. The reaction term is approximated by the product of a rate constant and δ_f.

$$\mathcal{R} = C_{\mathcal{R}} \cdot \delta_f, \tag{3.17}$$

Here only destruction of δ_f is considered and hence $C_{\mathcal{R}}$ is negative. Since both convection and reaction terms are linear functions of δ_f, the model equation for δ_f can be simplified as

$$\frac{d\delta_f}{dt} = -C_{grad} \cdot f(\phi) \left.\frac{d\phi}{dx}\right|_f - C_{rlx} \cdot \delta_f, \tag{3.18}$$

where C_{grad} is the gradient constant and C_{rlx} the relaxation constant. The first term can be a source/sink of δ_f depending on the sign of the equivalence ratio gradient at flame front and

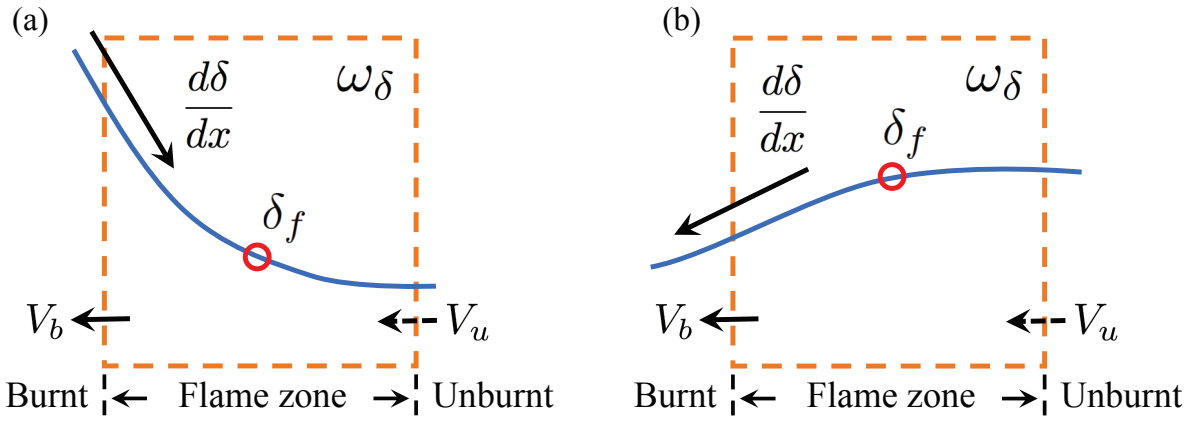

Figure 3.48: Control volume analysis of Local Stratification Level (LSL): (a) stratified flame propagation along negative equivalence ratio gradient, e.g., from rich to lean; (b) stratified flame propagation along positive equivalence ratio gradient, e.g., from lean to rich.

the second term is a relaxation term. When the equivalence ratio gradient becomes zero, δ_f will relax to zero with a characteristic time scale of C_{rlx}.

During Step 2, δ_f is translated into flame speed difference between SF and HF so that stratified flame speed can be estimated as

$$S^M_{c,SF} = S^Q_{c,HF} + F(\delta_f), \tag{3.19}$$

where $S^Q_{c,HF}$ is the flame speed of corresponding HF based on the equivalence ratio at the flame front. Figure 3.47 suggests that a roughly linear relationship between flame speed difference and H_2 mole fraction difference. In addition, a set of homogeneous flame simulations is conducted where hydrogen is added to the initial unburnt mixtures of methane/air at various equivalence ratios. The results are presented in Fig. 3.49 showing a nearly linear relationship between the amount of hydrogen in the mixture and the increase in the flame speeds. Therefore, $F(\delta_f)$ is approximated as a linear function of δ_f:

$$F(\delta_f) = C_F \cdot \delta_f, \tag{3.20}$$

where C_F is defined as a scale constant of the model.

To complete the model, $f(\phi)$, C_{grad}, C_{rlx} and C_F are to be determined. Figure 3.50(a) shows $X^u_{H_2,f}$ versus equivalence ratios at the flame front for three flames, the 1.6–0.6 SF, HF, and the 0.6–1.6 SF. In Fig. 3.50(a), for the homogeneous flames, H_2 only exists in rich flames and increases with equivalence ratio. When the stratified flame propagates from a rich mixture to a lean mixture (1.6–0.6), the amount of H_2 increases substantially. In

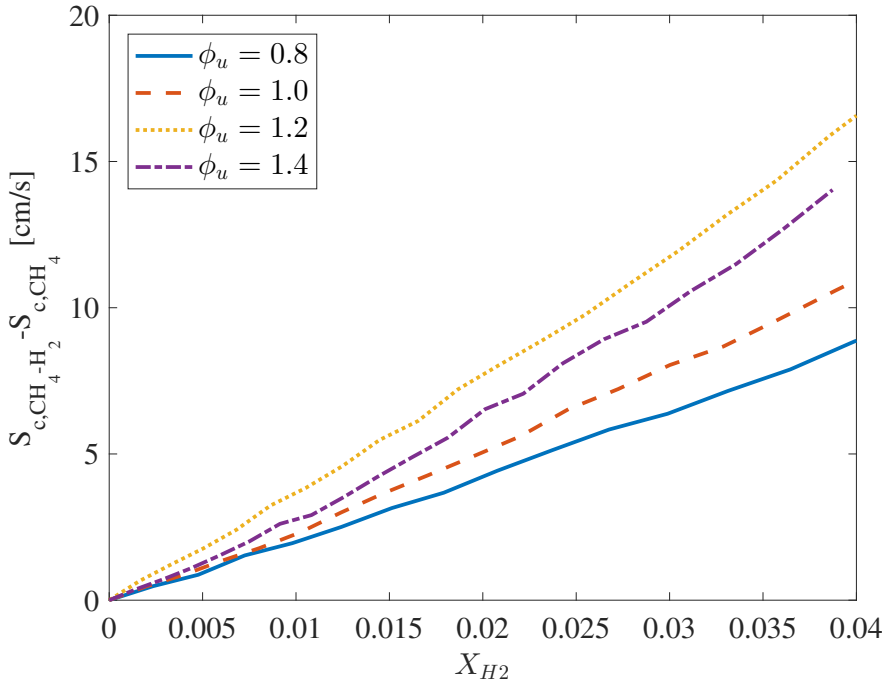

Figure 3.49: Increases of laminar flame speeds with hydrogen addition to methane/air mixtures.

contrast, the amount of H_2 in the 0.6–1.6 SF experiences a small decrease compared to HF. This trend is consistent with what has been observed in flame speeds of these three flames. There are two major reasons for the trend seen in the 0.6–1.6 SF. First, instead of receiving extra hydrogen from the burnt side, the lean–to–rich stratified flames at the flame front lose hydrogen to the burnt products. Second, since the temperature at flame front is lower than that of burnt products, the diffusion process along the direction from flame front to burnt product, e.g., in the 1.6–0.6 case, is promoted due to enhanced mass diffusivity in burnt gases, as well as due to the Soret effect. In comparison, the diffusion along the opposite direction, e.g., in the 0.6–1.6 case, is impeded.

The normalized H_2 gradient with respect to equivalence ratio is proposed as $f(\phi)$ and shown in Fig. 3.50(b), which is calculated from the HF results shown in Fig. 3.50(a). The values of C_{grad}, C_{rlx} and C_F are first estimated from simulation results of homogeneous flames. Second, to improve the accuracy of the model, these values are optimized by minimizing errors between model predictions and simulation results among all the stratified flame cases investigated in this study. The final results are shown below:

$$C_{grad} = 1.2 \times 10^3 \text{ cm} \cdot \text{s}^{-1}, \tag{3.21}$$

$$C_{rlx} = 8.0 \times 10^2 \text{ s}^{-1}, \tag{3.22}$$

$$C_F = 40 \text{ cm} \cdot \text{s}^{-1}. \tag{3.23}$$

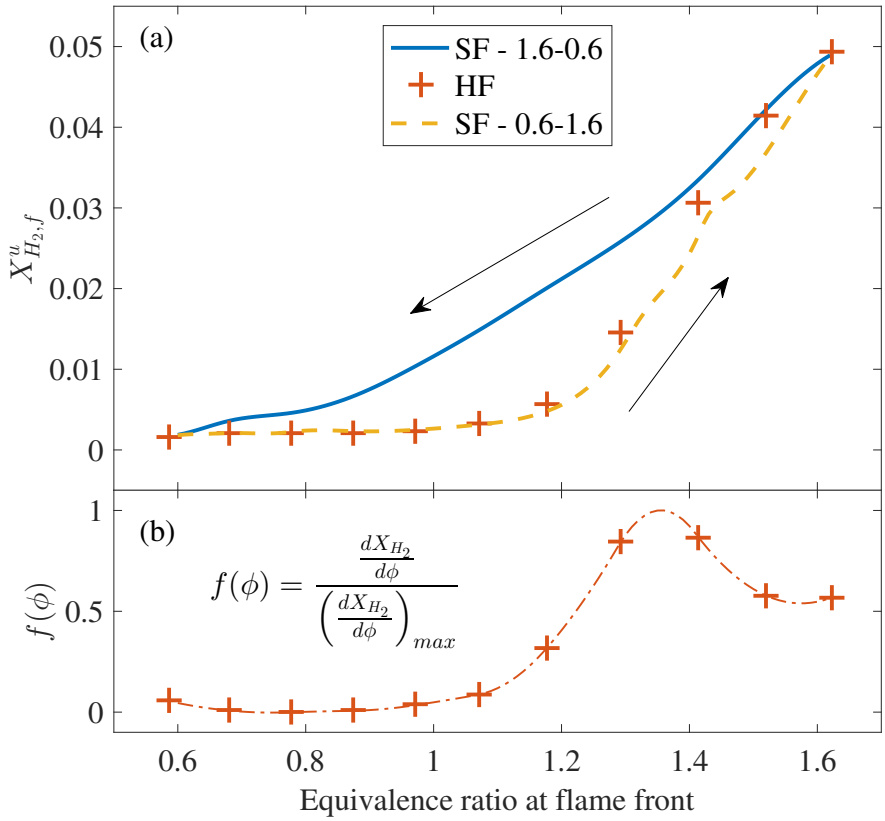

Figure 3.50: (a) Mole fraction of H_2 on the unburnt side of flame front, of the 1.6–0.6 SF, HF and the 0.6–1.6 SF. (b) Transfer function of equivalence ratio gradient based on $X^u_{H_2,f}$ in HF.

The performance of the proposed model is assessed by comparisons of results for various stratification configurations. Figure 3.51 shows three rich–to–lean SF (1.6–0.6) cases with different stratification thicknesses, while Fig. 3.52 shows lean–to–rich (0.6–1.6) case, rich–lean–rich case (1.6–0.6–1.6) and a case with an arbitrary equivalence ratio profile. Both profiles of instantaneous local equivalence ratio and equivalence ratio gradient at flame front are plotted. To evaluate the model performance, the modeled stratified flame speeds (M-Pred., $S^M_{c,SF}$) and the Quasi-HF flame speeds (Q-Pred., $S^Q_{c,HF}$) are plotted against the transient simulation results (Sim.). In the model, $F(\delta_f)$ are calculated from instantaneous equivalence ratio gradient profiles post-processed from the simulation results. Both the flame speeds and the relative errors are reported. As seen in Fig. 3.51 and Fig. 3.52, for all six cases, the model results match the simulation results quantitatively: According to the direct flame speed comparisons, .i.e, the plots in the third row of both figures, the model results are seen to follow closely to those from the simulations, while the Quasi-HF approximation sometimes deviates substantially from the simulations during and after the propagation through the stratification layers. The plots in the fourth row compare the errors revealing that most er-

rors between model predictions and simulation results are within approximately 10%, which are much improved over the Quasi-HF approximations. Moreover, large departures are observed between Quasi-HF values and simulation results at locations with a large degree of stratification. These comparisons suggest that the flame speeds of stratified mixtures are not accurately described by local equivalence ratio alone and a model, such as the LSL model, is necessary.

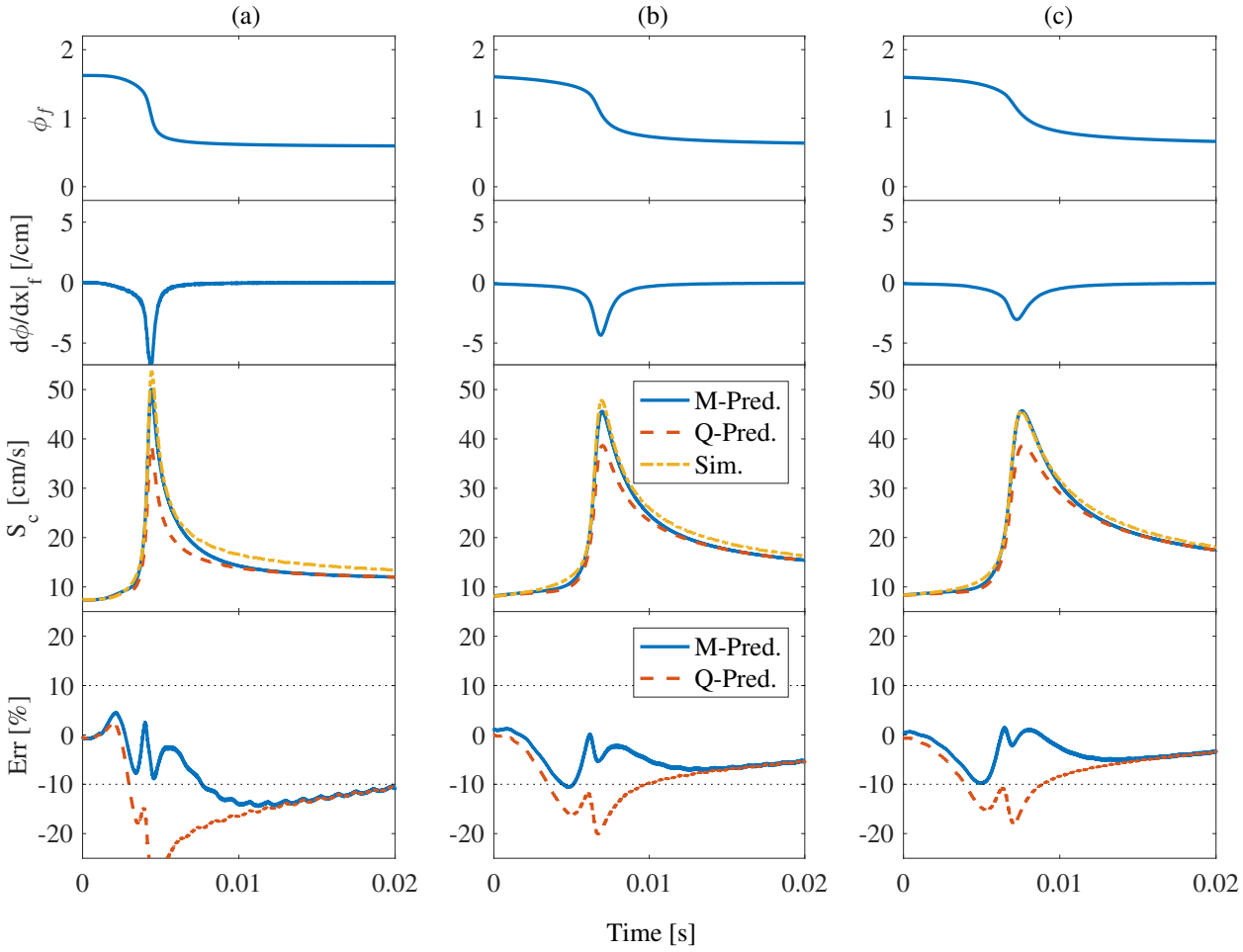

Figure 3.51: LSL model assessment – three stratification cases are tested: (a) rich–to–lean, $d_s = O(0.05$ cm), (b) rich–to–lean, $d_s = O(0.1$ cm), (c) rich–to–lean, $d_s = O(1$ cm). The results are presented versus time, from top to bottom: 1) equivalence ratio at flame front, 2) equivalence ratio gradient at flame front, 3) fuel consumption speeds of model, Quasi-HF and simulation results, and 4) percentage errors of model v.s. simulation and Quasi-HF v.s. simulation.

Alternatively, for SF cases with monotonic equivalence ratio profiles, the model assessment can be conducted by comparisons of flame speeds against local equivalence ratio. Figure 3.53 presents such a comparison for the rich–to–lean SF case with stratification thickness of

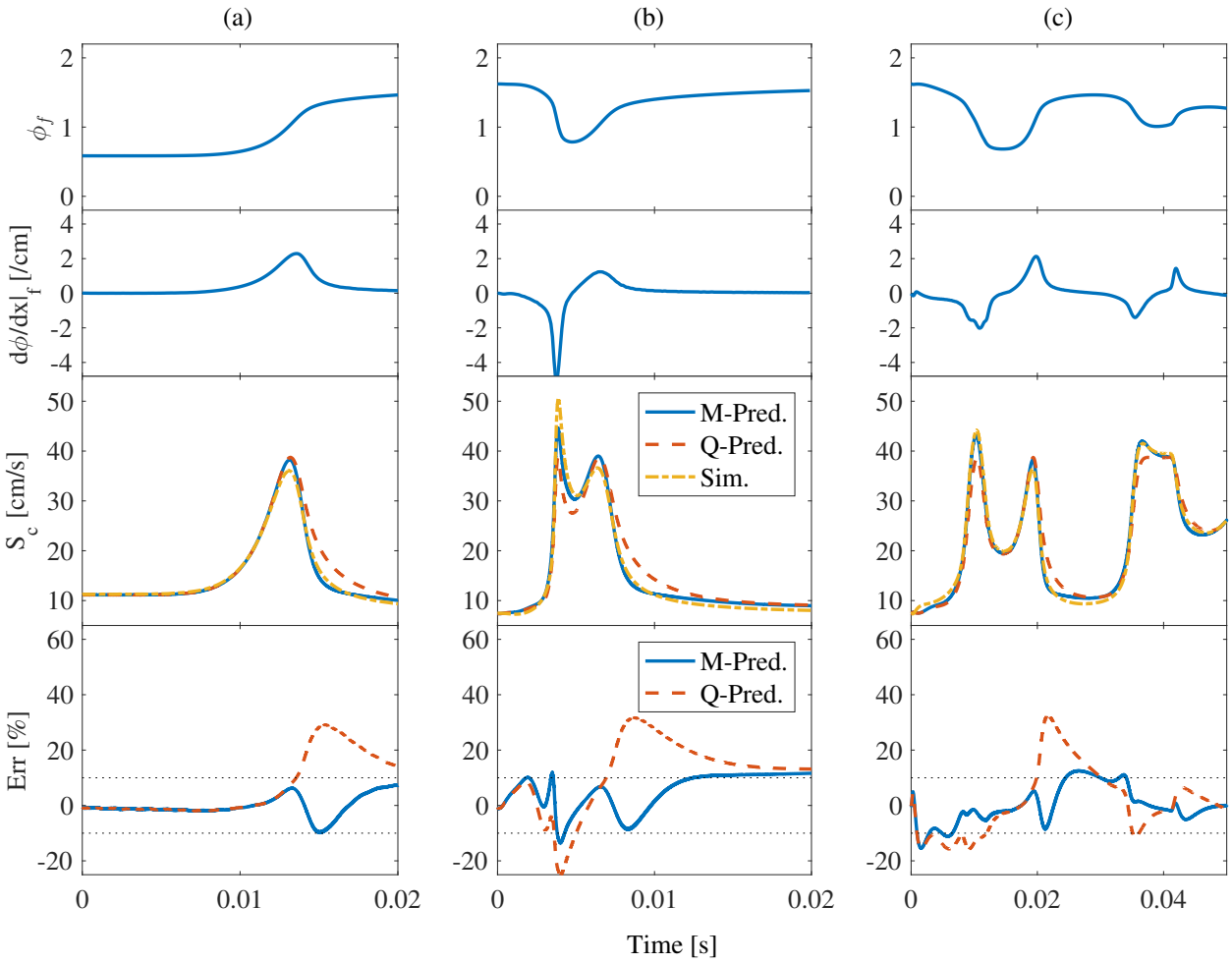

Figure 3.52: LSL model assessment – three stratification cases are tested: (a) lean–to–rich, (b) rich–lean–rich, (c) arbitrary equivalence ratio profile. The results are plotted against time, from top to bottom: 1) equivalence ratio at flame front, 2) equivalence ratio gradient at flame front, 3) fuel consumption speeds of model, Quasi-HF and simulation results, and 4) percentage errors of model v.s. simulation and Quasi-HF v.s. simulation.

0.1 cm, i.e., the same case as shown in Fig. 3.51(b). Clearly, the LSL model achieve a good agreement with the simulation results.

The LSL model certainly can be further improved in many areas. For example, there are two assumptions made in order to treat C_{grad} and C_{rlx} as constants:

1. Both constants are independent of local equivalence ratio.
2. The relation between LSL and the difference between SF and HF is linear.

Both assumptions can be relaxed by choosing variable C_{grad} and C_{rlx} based on flame prop-

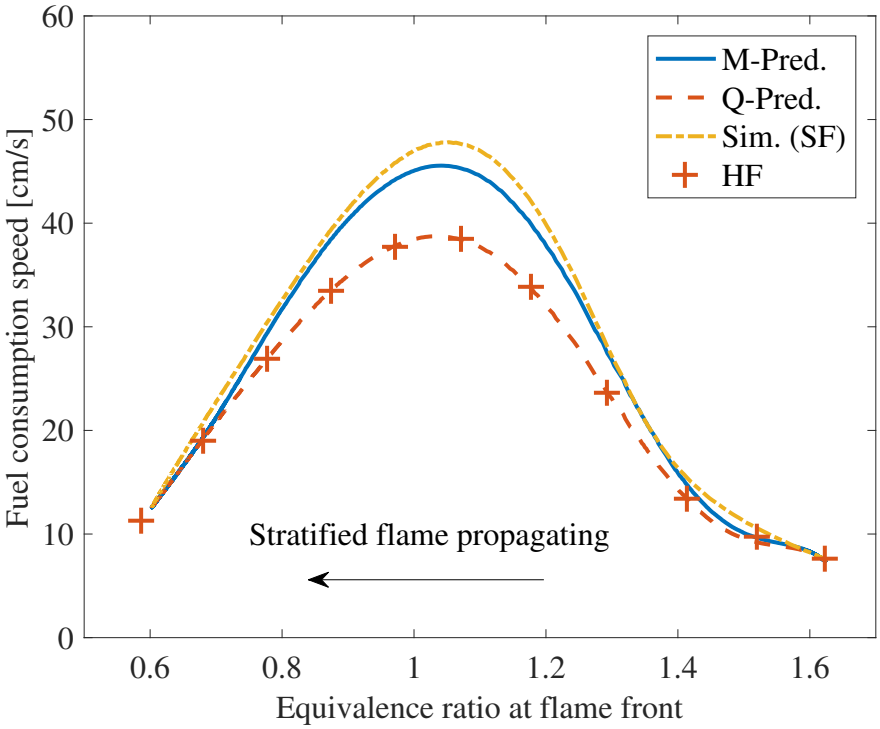

Figure 3.53: Local stratification level model assessment of the rich–to–lean stratified flame, $d_s = O(0.1 \text{ cm})$. The results are plotted against local equivalence ratio.

erties, such as flame thickness, characteristic velocities, of homogeneous flames. In addition, the flame stretching effect is not considered in the current planar one-dimensional simulations and it is a subject of future research.

Similar to the sensitivity analysis, the model methodology can also be applied to heavier fuel species or different diluent scenarios. However, rich flames of heavier hydrocarbon fuels still remain a challenge due to much more complicated chemical kinetics. Therefore, identification of dominant chemical and transport processes is a prerequisite to building such a model for heavier fuels.

Summary

Numerical simulations of various stratified methane/air flames are conducted and the results are analyzed by examining detailed flame properties to better understand the differences between laminar flame speeds of SF and HF. The following conclusions are drawn:

1. Among all methane/air stratified flames with different stratification configurations, rich–to–lean stratified flames show significant departures from homogeneous flames, where fuel consumption speeds of such stratified flames are up to 50% higher than

those of homogeneous flames. A sensitivity analysis using the assumptions of unity Lewis number reveals that preferential diffusion of molecular hydrogen as well as H and OH is mostly responsible for such departures. On one hand, excess molecular hydrogen generates radicals H, OH and increases the reaction rates within the flame zone. On the other hand, molecular hydrogen carrying excess enthalpy increases the temperature of unburnt mixtures. Furthermore, a sensitivity analysis of H_2 and H_2O diffusivity suggests that preferential diffusion of molecular hydrogen correlates with flame speed enhancement in stratified flames, while preferential diffusion of H_2O shows an opposite effect.

2. A smaller stratification thickness leads to higher degree of departure of stratified flames from homogeneous flames. Similar trends are observed with instantaneous equivalence ratio gradients in simple stratified flames. However, both of these correlations do not include the memory effect and may not be accurate to describe stratified flames with arbitrary stratification configurations.

3. A transit Local Stratification Level (LSL) model is proposed for modeling stratified flames with arbitrary stratification configurations. The local stratification level is constructed to mimic the differences in molecular hydrogen concentration within the flame zone between SF and HF. This incorporates the effect of preferential diffusion by establishing a transfer function from molecular hydrogen concentration gradient to equivalence ratio gradient at flame front. The model results agree with those from the direct simulations with relative errors less than 10%. Potential improvements of this model may be made by adopting variable coefficients incorporating flame properties.

Chapter 4

Lean Flammability Limit

In this chapter, the effect of stratification on lean flammability limit (LFL) is numerically investigated and studied. First, various definitions of LFL used by researchers in the past are reviewed. The LFL of stratified hydrogen/air mixtures is investigated by examining detailed species distribution and reaction pathway near the limit, while the LFL of stratified methane/air is studied by comparing the flame characteristics of stratified flames in different stratification configurations. Weak extensions of LFL are observed in both fuel stratified mixtures.

4.1 Definition of flammability limit

Understanding of flammability limits (FL) and limit flames in combustible mixtures is crucial, as an increasing amount of combustion devices are operating at near-limit lean conditions for optimal efficiency and emission characteristics (Shoshin and de Goey, 2010). New insights can be obtained with advanced diagnostics of flame dynamics as well as improved understanding of chemical kinetics and differential diffusion processes, especially in non-unity Lewis number mixtures. These insights can further contribute to the development of practical safety standards and the design of lean-combustion devices.

The potential of FL extension in stratified mixtures has been first recognized in experiments. Girard et al. (1979), in their soap bubble experiments, observed that the limit of flame propagation is shifted towards leaner mixtures in hydrogen/air stratified mixtures, a fact to be taken into consideration for safety problems. Kitagawa et al. (2005) experimentally investigated stratified hydrogen/air flame propagation in a constant volume chamber, where pure hydrogen was injected into a lean hydrogen/air premixed mixture charge. The flame was ignited by an electric spark in the hydrogen jet. They observed that the amount of burned hydrogen in the case of a stratified mixture was greater than that in the case of the homogeneous mixture. Kang and Kyritsis (2005, 2007) also found a significant extension of the lean flammability limits (LFL) in their convective-diffusive balanced burner and

rationalized the results in terms of the back-supported effect, i.e., heat transfer from burnt gases.

In contrast, numerical studies of LFL have always been challenging due to lack of appropriate definition of FL. Law and Egolfopoulos (1992) proposed a normalized sensitivity of variations in the dominant termination reaction to those in the dominant branching reaction, which attains unity slightly before the flammability limit is reached. Therefore, the fundamental FL can be determined directly from the transient chemical kinetic processes. Egolfopoulos et al. (2007) further numerically demonstrated that at low pressures the main branching/termination reactions are respectively H + O_2 -> OH + O and H + O_2 + M -> HO_2 + M, while at high pressures HO_2–H_2O_2 kinetics are dominant. Marzouk et al. (2000) performed reactant to product (RTP) stagnation strained flame simulations, to examine the effect of temporal composition gradients on combustion in a premixed methane/air mixture. Their results showed that equivalence ratio variations with timescales lower than 10 ms have significant effects on the burning process. The relevant feature is the establishment of a positive temperature gradient on the products side of the flame which maintains the temperature high enough and the radical concentration sufficient to sustain combustion there. Sankaran and Im (2002) exploited an unsteady opposed-flow combustion configuration (reactant to reactant, RTR) and investigated the concept of dynamic FL with time-varying composition fluctuations. Although they have demonstrated the FL of an unsteady premixed flame can be further extended to a leaner condition, the mean equivalence ratio, as well as the minimum flame temperature, have to be higher than those of steady homogeneous flames in order to sustain combustion. Zhou and Hochgreb (2013) studied counterflow RTP flames and found that stratified flames are able to propagate into mixtures beyond the premixed lean and rich flammability limits, for either positive or negative equivalence ratio gradients.

Some more explorations on the LFL extension of stratified flames are presented in the following sections. In the hydrogen/air lean stratified flames, detailed species distribution and reaction pathways of SF are compared to a reference HF at LFL. In the study of methane/air mixtures, different stratification configurations are tested and the relation between stratification and LFL extension is revealed.

4.2 Hydrogen/air lean stratified flames

According to literature, the LFL of homogeneous hydrogen/air flame under ambient temperature and atmospheric pressure is measured at equivalence ratio $\phi_u = 0.4$ (Braker and Mossman, 1980; Zabetakis, 1965). Therefore, the flame characteristics of HF at $\phi_u = 0.4$ is used as the threshold to decide the flammability limit in the following numerical study. Note that due to preferential diffusion, $\phi_u = 0.4$ is equivalent to $\phi_f = 0.356$.

A stratified flame case with mixture-average diffusivity assumption, analogous to the practical situation in direct injection engines, is performed. The stratified flame is propagat-

ing from unburnt mixture at $\phi_u = 1.0$ to $\phi_u = 0.2$ with $d_s = 0.1$ cm. The numerical setup is the same as the one shown in Fig. 3.5. A simulation of the corresponding HF at $\phi_u = 0.4$ is also performed. Figure 4.1(a) compares the major species and radical profiles of both SF and HF at lean flammability $\phi_f = 0.356$. Even though the overall concentrations of species and radicals are low as ϕ_f is at flammability limit, SF still has a relatively larger amount of H and OH radicals near the flame front as well as in the burnt gas, which can enhance the local flame burning. This conclusion can be supported by Fig. 4.1(b), showing the total heat release rate and major exothermic reaction rates of SF and HF at $\phi_f = 0.356$. SF has higher heat release rates than those of HF and major exothermic reactions are indeed related to H and OH radicals; therefore SF has not reached the LFL yet.

As SF continues to burn leaner, Figures 4.2(a) and 4.2(b) show the results of SF at $\phi_f = 0.346$ and HF at $\phi_f = 0.356$. The radical and reactant profiles near the flame front, as well as heat release profiles, match exactly with each other between SF and HF. Therefore it is reasonable to conclude that SF has reached its LFL at $\phi_f = 0.346$. The extension of lean flammability limit in SF, from $\phi_f = 0.356$ to $\phi_f = 0.346$ is achieved by local chemical effect, but relatively insignificant, i.e., only 2.8% extension. As the overall radical and reactant concentrations are quite low near flammability, the overall reactivity is so low that the local chemical effect is significantly weakened. Furthermore, since the flame is propagating really slow near the lean flammability, it gives significantly more time for the stratification layer to diffuse. When the stratified flame reaches the lean flammability limit, d_s has grown to the order of 1 cm from its original 0.1 cm.

Therefore, weak lean flammability extension is observed for hydrogen/air stratified flames, as the chemical effect is significantly weakened due to overall low reactivity and enlarged stratification thickness.

4.3 Methane/air lean stratified flames

One can argue that the reference "at-limit" HF in the hydrogen study is arbitrary and may not be representative in many practical conditions. A different approach is applied to methane/air lean stratified flames: instead of direct comparison between SF and HF, stratified flames with different stratification configurations are compared among each other. The degree of stratification is correlated with how much learner the corresponding flame can reach.

The same physical domain setup is used as shown in Fig. 3.5. As lean flammability limits are closely related to transport processes of species and radicals, and heat losses, two adjustments are made towards numerical models in order to better capture the relevant physics:

1. The multi-component diffusivity model (Dixon-Lewis, 1968) is employed instead of the original mixture-average diffusivity model.

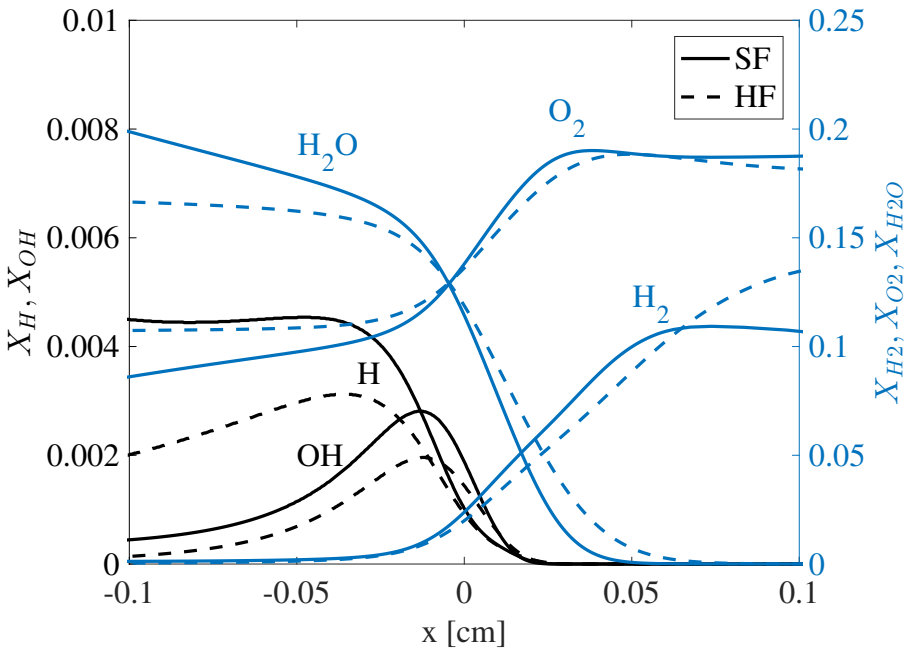

(a)

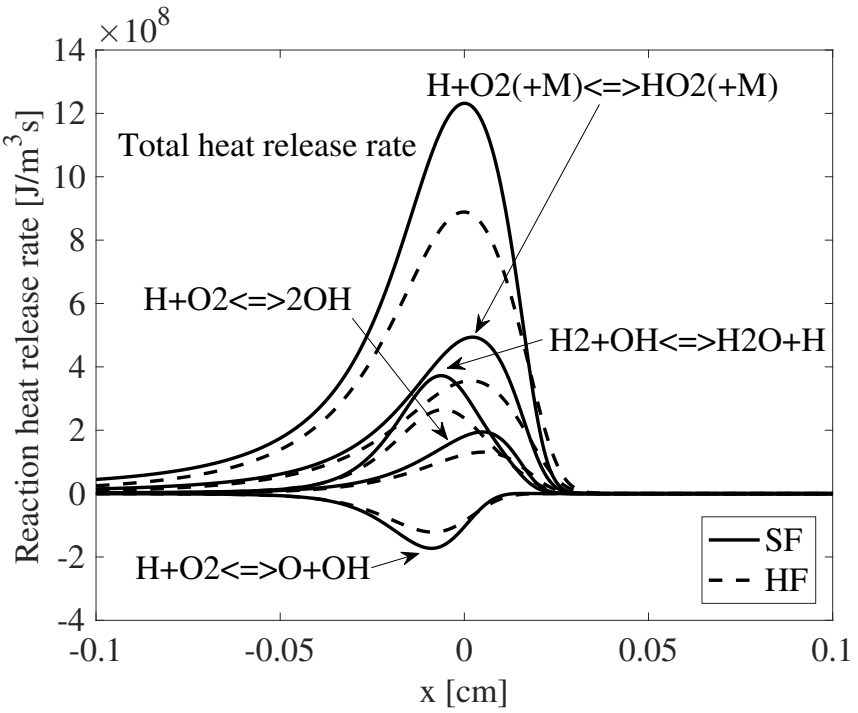

(b)

Figure 4.1: (a) Major species mole fraction and (b) heat release rate and major exothermic reaction rate profiles of SF and HF at $\phi_f = 0.356$, when SF propagates from $\phi_u = 1.0$ to $\phi_u = 0.4$, $d_s = 0.1$ cm, with mixture-average diffusivity assumption.

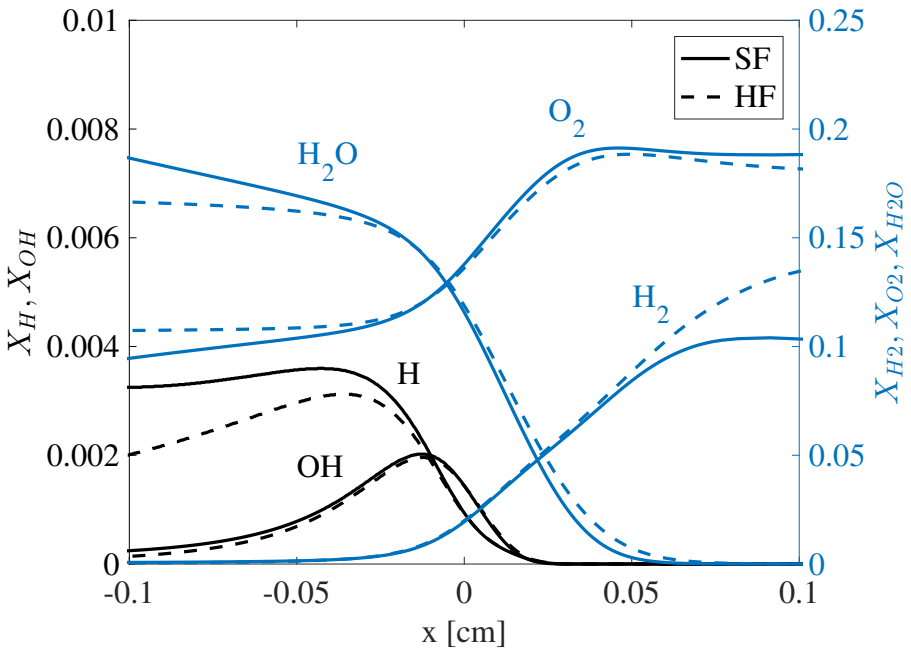

(a)

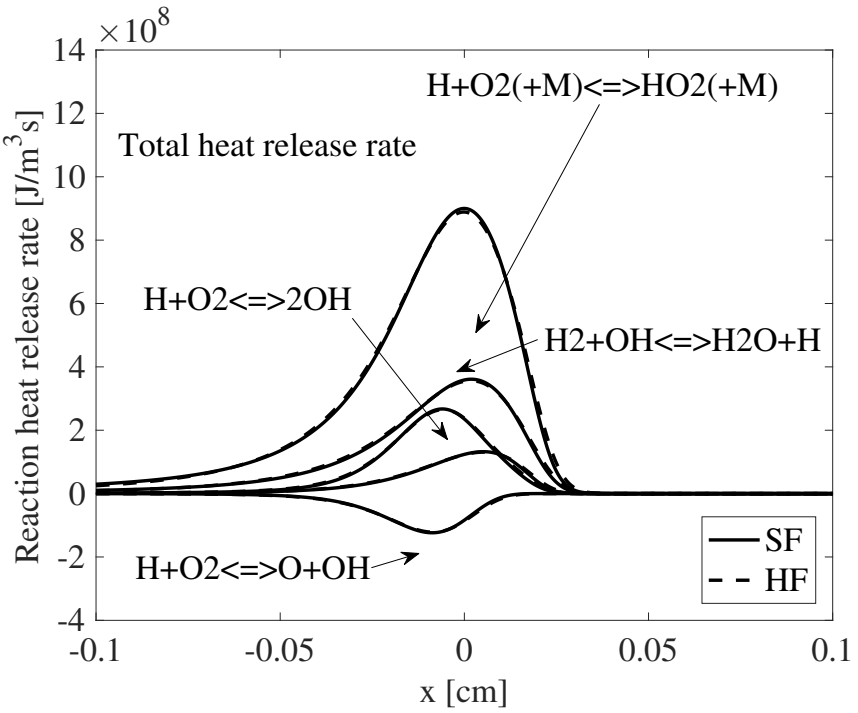

(b)

Figure 4.2: (a) Major species mole fraction and (b) heat release rate and major exothermic reaction rate profiles of HF at $\phi_f = 0.356$ and SF at $\phi_f = 0.346$, when SF propagates from ϕ_u 1.0 to 0.2, $d_s = 0.1$ cm, with mixture-average diffusivity assumption.

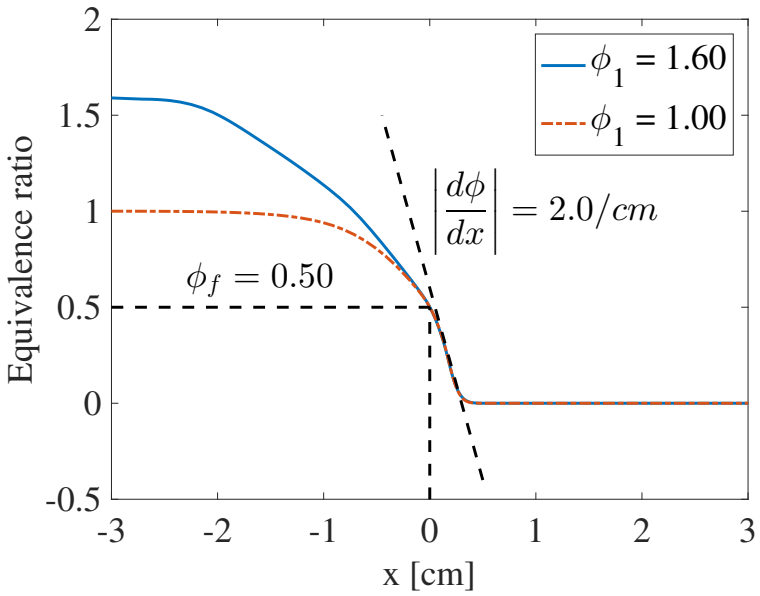

Figure 4.3: Equivalence ratio profiles of 1.6–0.0 and 1.0–0.0 SF at $\phi_f = 0.5$.

2. The optically thin radiation model (Barlow et al., 2001) is used to describe the heat loss process.

Two different cases are analyzed as the first round of exploration: 1.6–0.0 and 1.0–0.0 stratified flames. The stratification thicknesses of the two cases are adjusted so that when the flame front reaches the mixture of $\phi_f = 0.5$, the slopes of the stratification layers are the same. Figure 4.3 shows the equivalence ratio profiles around the flame front of both 1.6–0.0 and 1.0–0.0 SF at $\phi_f = 0.5$. For a reasonable comparison, the absolute magnitude of equivalence ratio gradients ahead of the flame front is 2.0 /cm for both flames. From the burnt side, the flames are seen to propagate from $\phi_f = 1.6$ and 1.0 respectively. The magnitude of equivalence ratio gradients in the burnt mixtures is smaller than those in the unburnt mixtures due to dilation of burnt gases against the left wall boundary. From this point in time history of flame propagation, the equivalence ratios at flame front of both SF are tracked in terms of time. The minimum equivalence ratio the SF reaches is regarded as the LFL.

Figure 4.4 presents the time history data of the equivalence ratios at flame front of both SF. Similar behaviors are observed, as the equivalence ratio first reaches a minimum value and then reserves back. Due to the finite-rate chemical kinetic model, chemical reactions continue to occur in the burnt gas after the flame front passes through. Therefore, the latter reverse behavior can be explained that the heat release rate at the flame front is so small that it is even smaller than that in the burnt gas. Therefore, the maximum heat release rate location remains in the burnt gas and stops propagating further in the leaner unburnt mixtures. The equivalence ratios at LFL, i.e., $\phi_{f,lfl}$ of 1.6–0.0 and 1.0–0.0 SF are seen to be

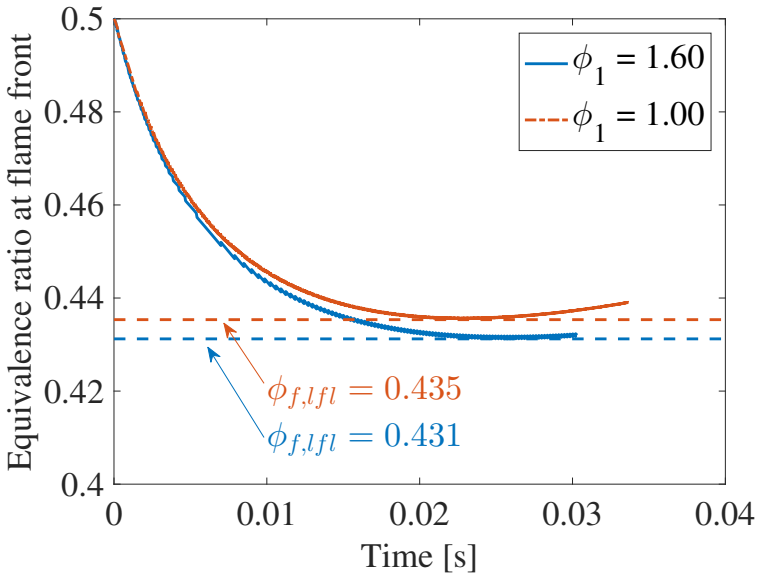

Figure 4.4: Equivalence ratio at flame front during the propagation of 1.6–0.0 and 1.0–0.0 stratified flames from $\phi_f = 0.5$ to 0.0.

0.431 and 0.435. The LFL extension introduced by rich flames is only about 1% compared to that by stoichiometric flames. Therefore, similar to hydrogen/air lean SF, very weak LFL extension is observed in methane/air lean SF.

Chapter 5

Modes of Combustion

In this chapter, the effect of stratification on modes of combustion is numerically investigated and studied. First, the Zeld'ovich reactivity gradient theory is introduced as the foundation of combustion mode studies. Ignition pockets containing gradients of temperature, equivalence ratio, and the combination of the two are studied and different modes of combustion are initiated according to the Zeld'ovich theory. Further, in a more practical setup, an energy-deposit ignition is employed in a closed chamber and different modes of the reaction front propagation introduced by the ignition and the end-gas combustion are observed. The simulated results are further analyzed from the point of view of the Zeld'ovich theory. A transient reactivity gradient method is proposed to identify the onset of detonation transition locally.

5.1 Zeld'ovich reactivity gradient theory

The increasing demand for gaseous fuel has led to a major concern about the safety issues during the processes of fuel production, carriage, storage and consumption (Heidari and Wen, 2014). If leaked gaseous fuel mixes with oxidizers and ignites, the consequent rapid combustion can result in severe destruction and losses. The degree of destruction is mainly determined by the respective combustion modes: autoignition, deflagration and detonation. In particular, detonation can lead to significant pressure rise and results in large-scale and serious damages (Petukhov et al., 2009; Dorofeev et al., 1996). A similar topic has been widely discussed in the engine knock community (Wei et al., 2014): A new engine knock mode, super knock, occurs in boosted gasoline direct injection spark ignition (DISI) engines (Willand et al., 2009; Dahnz et al., 2010; Kalghatgi and Bradley, 2012). Different from the traditional knock, the unexpected occurrence of super knock can damage engine components catastrophically due to extremely high peak pressure and severe pressure oscillations. The super knock is thought to be the result of pre-ignition events causing the end (unburnt) fuel/air mixtures to undergo a developing detonation or a deflagration to detonation transition (DDT) (Wang et al., 2014; Inoue et al., 2012).

As different modes of combustion may lead to dramatically different outcomes, understanding the classification of combustion modes and corresponding transitions is primarily necessary and fundamentally valuable. A regime classification theory was proposed by Zeldovich et al. (1970); Zeldovich (1980). By considering the following expression for the speed of reaction front

$$u_p = |\nabla \tau_i \,|^{-1} \tag{5.1}$$

where ∇ donates the spatial gradient, τ_i is the ignition delay time and u_p is defined as the reaction front propagation speed relative to unburnt gas, Zeld'ovich concluded that the propagation speed u_p derived from the spatial distribution of reactivity determines the reaction front propagation modes, including developing detonation and DDT. This theory has been successfully used in many detonation-related studies and its creditability has been well-recognized. Gu et al. (2003) adopted the Zeld'ovich theory by considering ignition delay time as a function of temperature. A dimensionless number based on critical temperature gradient at the occurrence of detonation

$$\xi = \left(\frac{\partial T_0}{\partial r}\right)\left(\frac{\partial T_0}{\partial r}\right)_c^{-1} \tag{5.2}$$

was proposed to identify different propagation modes. By specifying hot spots with different temperature gradients as ignition sources, five modes were identified by Gu et al. (2003) in a sequence of increasing initial ξ values:
1) simultaneous autoignition, $\xi = 0$,
2) supersonic autoignitive propagation, $0 < \xi \leqslant \xi_l$,
3) developing and developed detonation, $\xi_l < \xi \leqslant \xi_u$,
4) subsonic autoignitive propagation, $\xi_u < \xi \leqslant aS_L^{-1}$,
5) laminar burning deflagration (flame), $\xi > aS_L^{-1}$,
where S_L is the laminar flame speed. The fourth mode "subsonic autoignitive propagation" is also referred as "reaction-hydrodynamic wave" (Kapila et al., 2002). Since thermodynamic conditions of the mixture may change during the initial ignition delay time period due to transport processes, a range of initial ξ between ξ_l and ξ_u can lead to detonation, according to 1-D numerical simulations of stoichiometric H_2/CO/air mixtures with different initial hot spots. The values of ξ_l and ξ_u depend on the radius of the ignition hot spot r_i, local sound speed a and the excitation time of the mixture τ_e. Therefore, a second dimensionless number was introduced

$$\varepsilon = \frac{r_i}{a\tau_e}. \tag{5.3}$$

τ_e was defined as the time from the instant of 5% maximum heat release rate to that of maximum heat release rate. ε evaluates the heat release being unloaded sufficiently fast to the acoustic wave (Lutz et al., 1989). A $\xi - \varepsilon$ diagram with ξ_u and ξ_l limits was proposed to identify different combustion modes. Instead of specifying an artificial temperature gradient, i.e. hot spot, Kiverin et al. (2013) exploited coarse particle method (CPM) and numerically studied consequences of localized energy deposition into a stoichiometric H_2/O_2 mixture

leading to the ignition of different regimes of combustion. They investigated the effect of deposited energy amount, time scale, and size of the ignition spot and the corresponding results also agree with the Zeld'ovich theory.

5.2 Combustion modes of stratified mixtures

Introduction

Overall, denotation phenomena induced by temperature gradients can be well explained by the above Zeld'ovich theory. Various propagation modes were observed mainly due to the different interactions between acoustic pressure field and chemical kinetics caused by the spatial distribution of temperature field. However, as seen from engine experimental results, detonation can also be induced by other types of sources. In a real engine environment, besides temperature inhomogeneity, mixture composition inhomogeneity often exists as well. Mixture composition inhomogeneity is usually quantified by equivalence ratio distribution and mainly results from the partial mixing of fuel and air as well as intrusion of lube oil droplets.

This section aims to explore whether equivalence ratio gradients can lead to detonation phenomena. In addition, the combination of temperature and equivalence ratio gradients is also investigated. Specifically, this study aims to answer the following questions:

1. Can equivalence ratio gradients lead to detonation? If so, can the Zeld'ovich theory be extended to those scenarios with equivalence ratio gradients? Is there any difference between DDT processes triggered by temperature and equivalence ratio gradients?

2. How can reaction front propagation modes be identified when both temperature and composition gradients exist?

Several reactive mixtures of H_2/CO/air mixtures (50% H_2 and 50% CO by volume) were investigated under high temperature and pressure. Temperature and equivalence ratio gradients were specified by hot/cold and rich/lean (equivalence ratio varying) spots as sources of inhomogeneity.

Numerical Model and Setup

ASURF-Parallel is used to perform transient simulations of ignition and reaction front propagation. Finite volume method is used to capture supersonic reaction fronts.

Numerical simulations were conducted in a 1D spherical domain as shown in Fig. 5.1. Linear profiles of equivalence ratio and/or temperature with various gradients are specified within the first 5 mm domain from the center. The rest of the domain contains the stoichiometric H_2/CO/air mixture (equivalence ratio ϕ=1) at 1000 K up to 10 cm in radius.

The initial pressure is 50 atm. A reaction front is initialized at the center and propagates through the gradient layer outwardly. Reflective boundary conditions are applied to both the center and the outer boundary, analogous to closed chambers with a point source ignition at the center. The outer boundary is treated as adiabatic with no chemical reactions. The minimum grid size is 4 μm and the CFL number is set to 0.2. A 12-species skeletal chemical kinetic mechanism developed from GRI3.0 (Smith et al., 1999) was used. The computed ignition delay times agree well with results from the previous study (Gu et al., 2003). The comparison, as well as the mechanism, are included in the supplemental document.

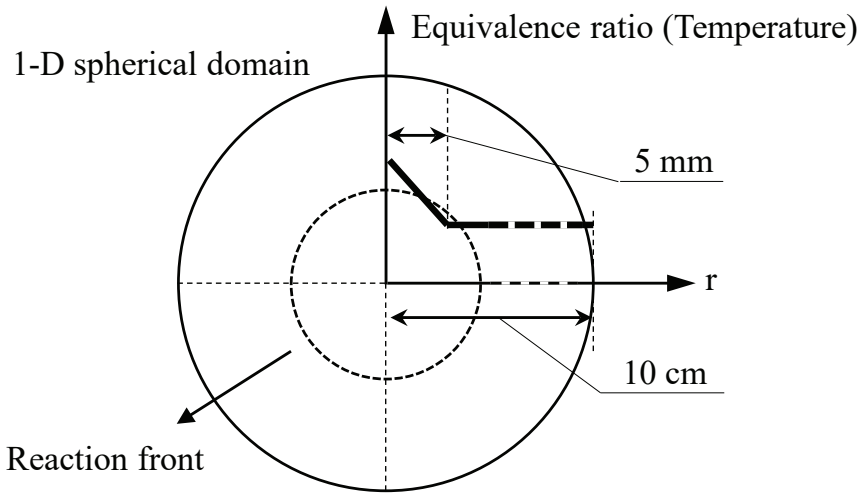

Figure 5.1: Numerical schematic in 1-D spherical coordinate with initial equivalence ratio (or temperature) profile. Note the initial gradient within 5 mm layer is not to scale.

Results and discussion

Critical equivalence ratio gradient

The computed ignition delay times of H_2/CO/air mixtures versus temperature and equivalence ratio are shown in Fig. 5.2 and 5.3 respectively. In Fig. 5.2, as equivalence ratio is set to 1, ignition delay decreases approximately linearly with increasing temperature within the small temperature range. Similarly in Fig. 5.3, as the temperature is fixed at 1000 K, ignition delay decreases with increasing equivalence ratio as well. Due to this similar trends, it is speculated that an equivalence ratio gradient might also be able to trigger different reaction front propagation modes. Note that the ignition delay time of stoichiometric H_2/CO/air mixture at 1000 K and 50 atm is 2104 μs, which is used as a reference point in calculating ξ.

Similar to the temperature gradient theory, ξ can be expressed as a function of equivalence

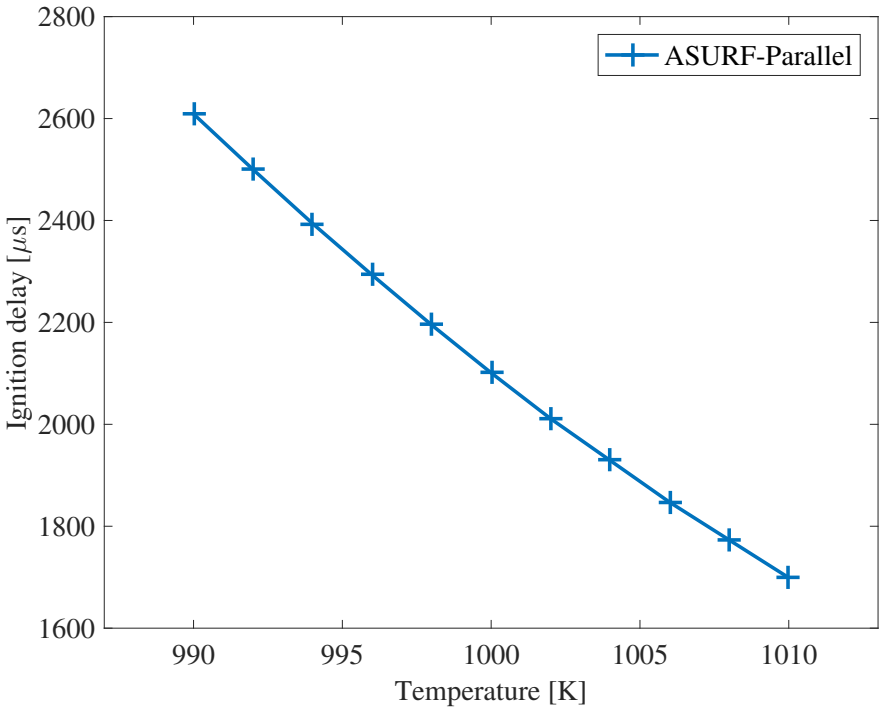

Figure 5.2: Computed ignition delay time of stoichiometric H_2/CO/air mixtures at different temperatures, P = 50 atm.

ratio instead of temperature:

$$\xi = \left(\frac{\partial \phi_0}{\partial r}\right)\left(\frac{\partial \phi_0}{\partial r}\right)_c^{-1} = \left(\frac{\partial \phi_0}{\partial r}\right) a \left(\frac{\partial \tau_i}{\partial \phi_0}\right) \tag{5.4}$$

where $\partial \tau_i / \partial \phi_0$ can be estimated according to Fig. 5.3. The sound speed can be determined as

$$a = \sqrt{\frac{kRT}{M}} \tag{5.5}$$

where k is the specific heat ratio, T is temperature and M molecular weight of the mixture. R is the universal gas constant. The sound speed of stoichiometric H_2/CO/air mixture at 1000 K and 50 atm is approximately 670 m/s, while the Chapman-Jouguet (CJ) detonation speed is approximately 1650 m/s.

Modes of reaction front propagation induced by equivalence ratio gradients

Similar to mixtures with hot or cold spots, the computed results reveal that equivalence ratio gradients can also trigger various modes of reaction front propagation. Figure 5.4 shows the development of supersonic autoignitive deflagration and thermal explosion at equivalence ratio initial condition $\xi = 1$. The initial equivalence ratio is 1.006 at the center

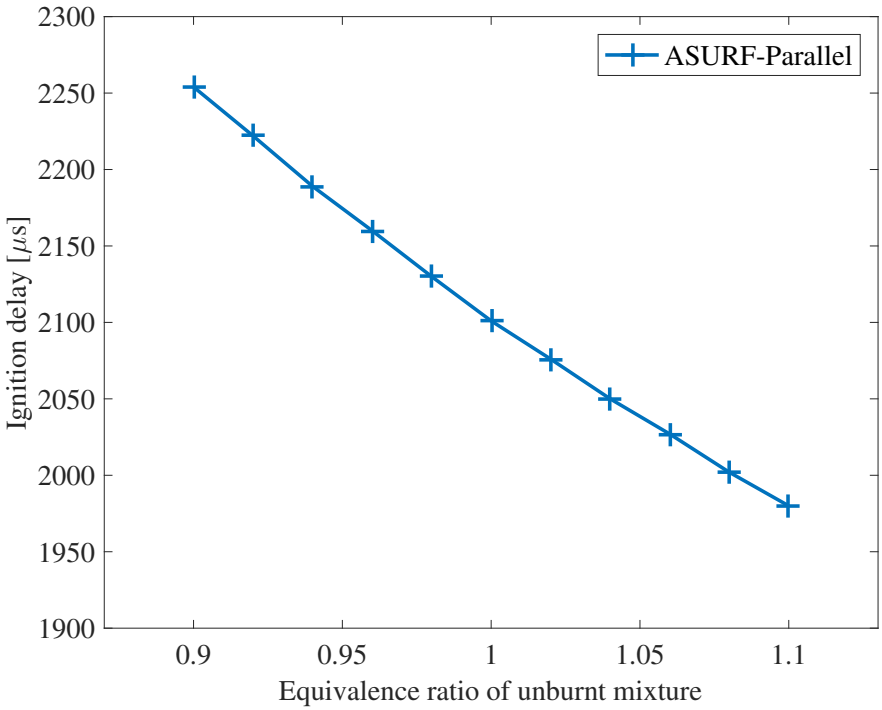

Figure 5.3: Computed ignition delay time of H_2/CO/air mixtures at 1000 K and different equivalence ratios, P = 50 atm.

and decreases linearly to 1 within 5 mm. Although ξ is equal to 1 initially, the gradient had slightly decreased due to heat conduction and species diffusion during ignition delay period. Auto-ignition occurred first at $r = 0$ due to a richer mixture, and the sequence of auto-ignition events happened at a speed, approximately 3000 m/s, greater than the CJ detonation speed. A thermal explosion followed when the rest of unburnt mixture autoignited simultaneously.

The results of $\xi = 3$ are shown in Fig. 5.5 with the initial equivalence ratio of 1.018 at $r = 0$. Right after auto-ignition at $r = 0$, the reaction front transitions into a detonation with a sharp rise in temperature, pressure and velocity. The maximum pressure was up to 350 atm, while the reaction front propagated at a speed of approximately 1600 m/s, very close to the CJ detonation speed. After 2104 μs (time sequence no. 4), a thermal explosion followed similar to the $\xi = 1$ case.

A deflagration to detonation transition case is observed when $\xi = 10$. In Fig. 5.6, the equivalence ratio at $r = 0$ is 1.06. Normal deflagration was first established after initial ignition. When the front reached around 0.6 cm, the propagation mode transitioned into detonation, where sharp pressure and velocity rises appeared. The detonation wave continued to propagate until the occurrence of a thermal explosion.

Reaction modes of thermal explosion, subsonic and normal deflagration are not shown as

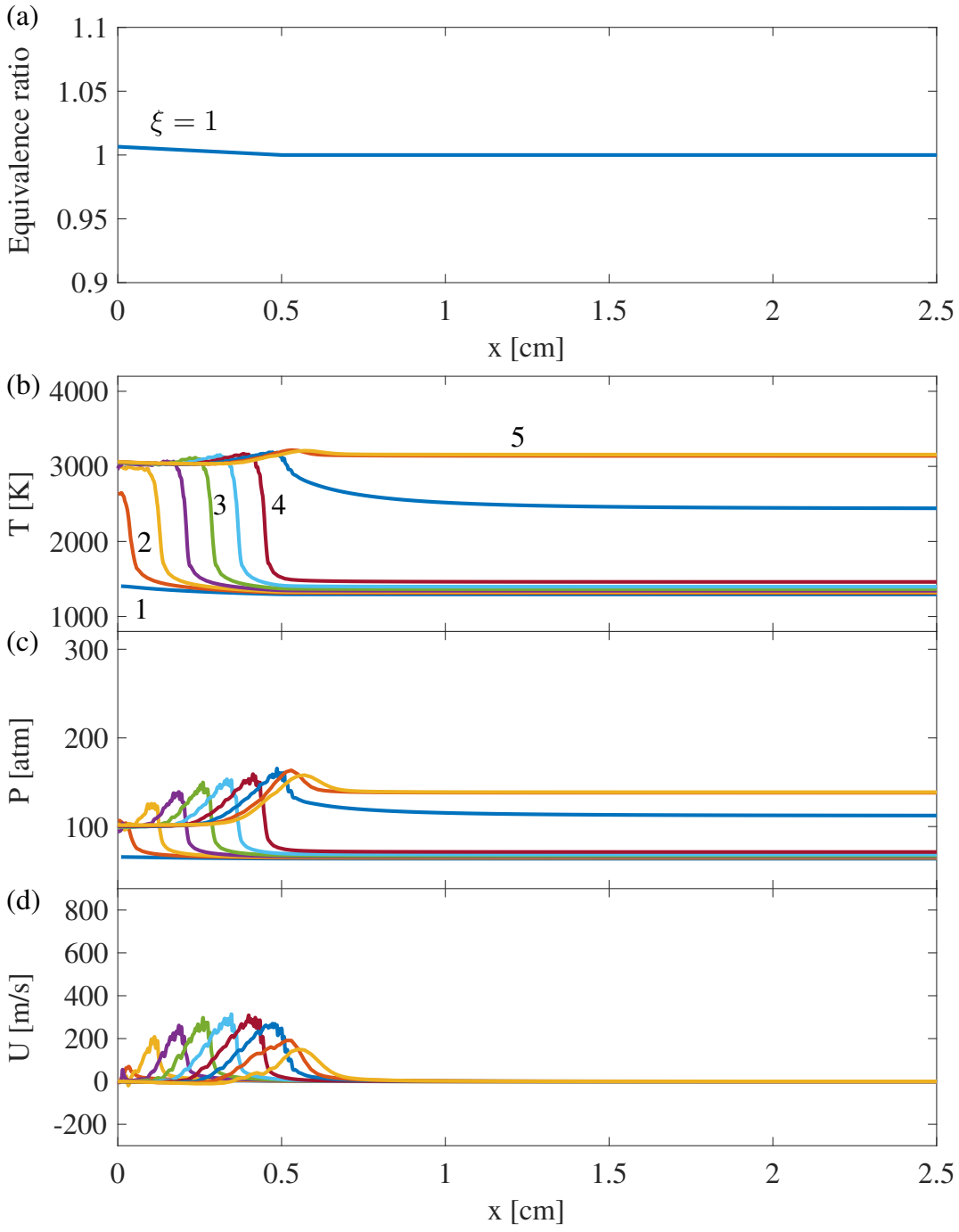

Figure 5.4: Development of a supersonic autoignitive deflagration and thermal explosion, $\xi = 1$ with a negative equivalence ratio gradient: (a) Initial condition of equivalence ratio; (b) Temperature; (c) Pressure; (d) Velocity. Time sequence (μs): 1 - 2101, 2 - 2102, 3 - 2103, 4 - 2104, 5 - 2105.

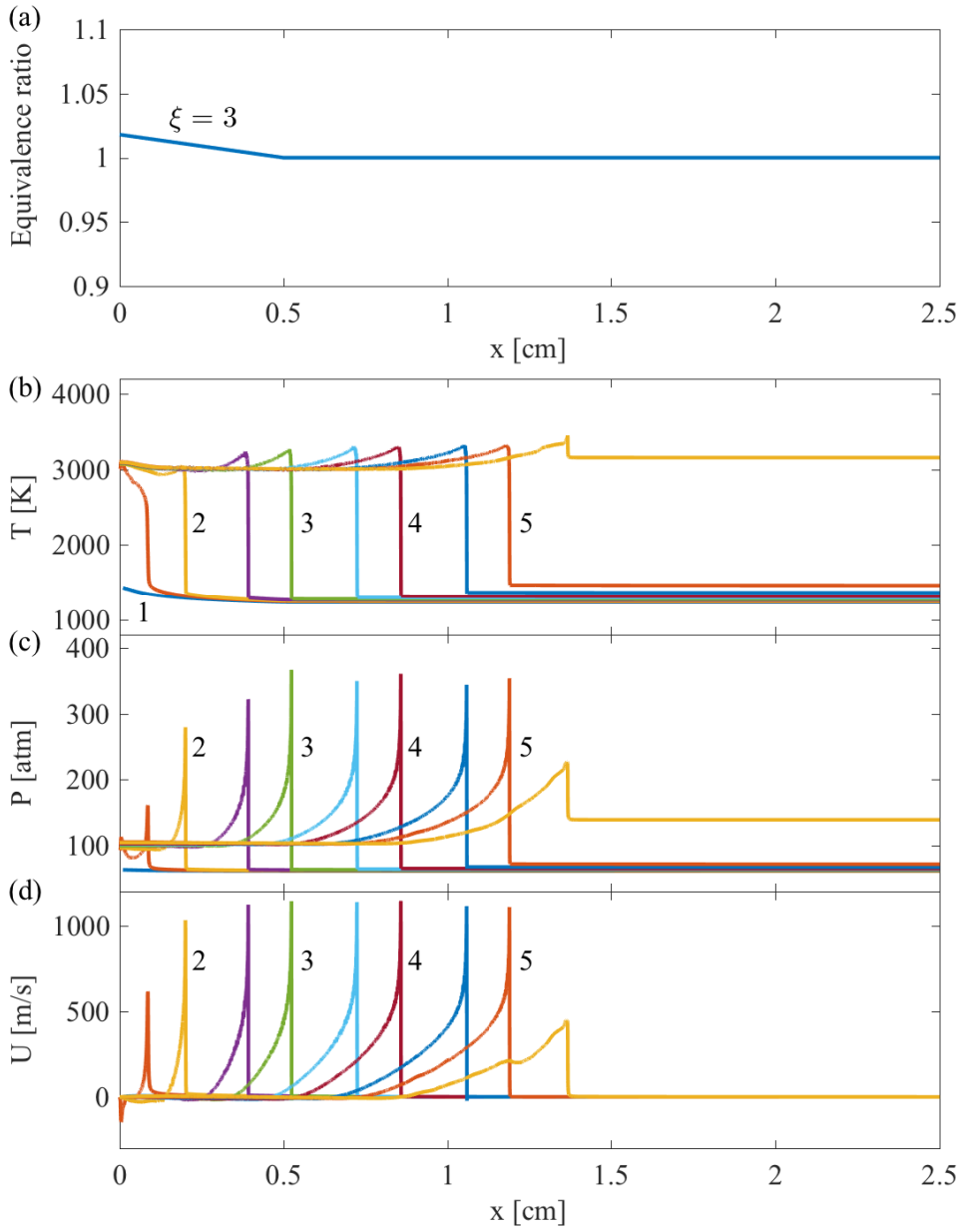

Figure 5.5: Development of a developing detonation and thermal explosion, $\xi = 3$ with a negative equivalence ratio gradient: (a) Initial condition of equivalence ratio; (b) Temperature; (c) Pressure; (d) Velocity. Time sequence (μs): 1 - 2096, 2 - 2098, 3 - 2100, 4 - 2102, 5 - 2104.

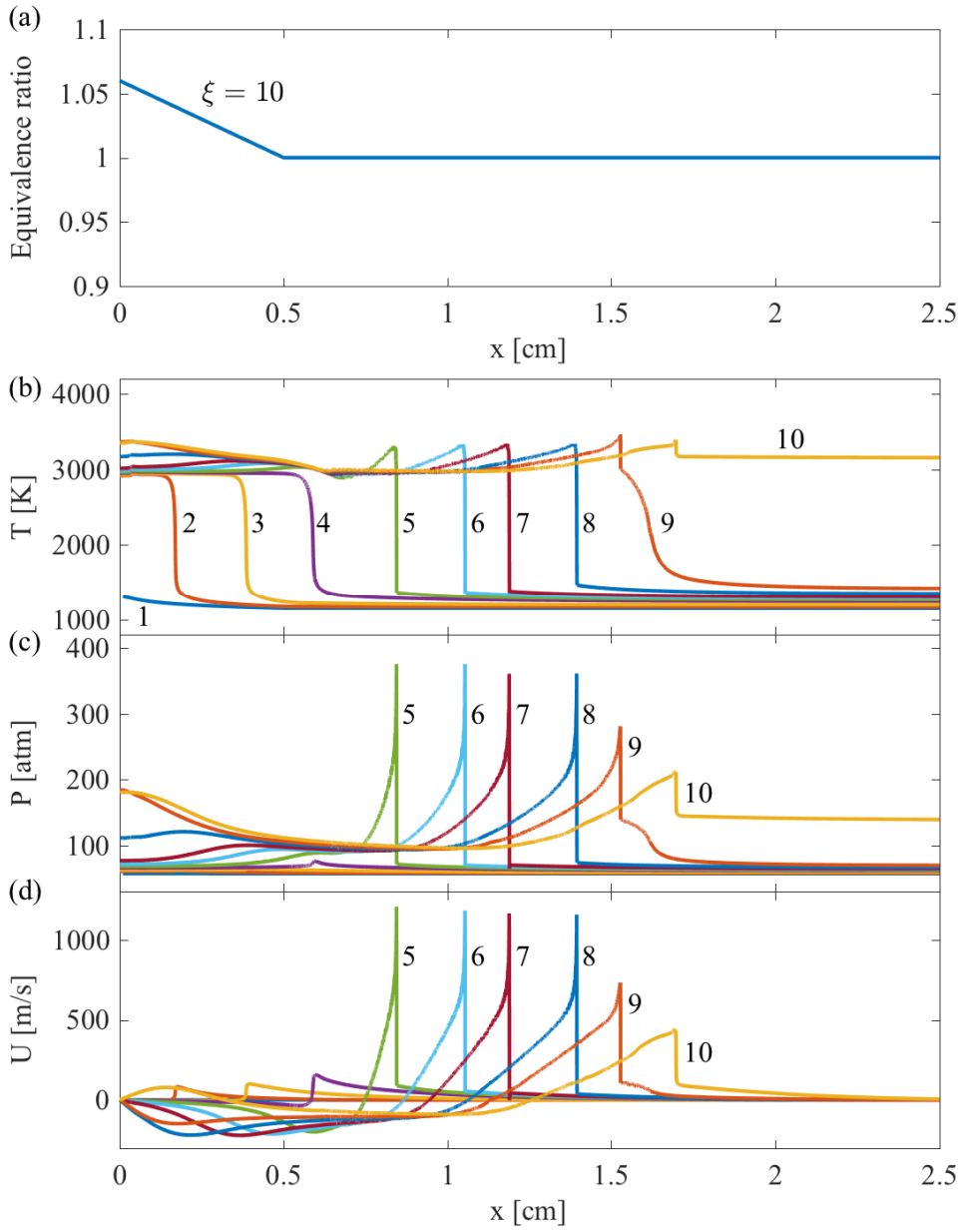

Figure 5.6: Development of a deflagration to detonation transition and thermal explosion, $\xi = 10$ with a negative equivalence ratio gradient: (a) Initial condition of equivalence ratio; (b) Temperature; (c) Pressure; (d) Velocity. Time sequence (μs): 1 - 2070, 2 - 2080, 3 - 2090, 4 - 2098, 5 - 2100, 6 - 2101, 7 - 2102, 8 - 2103, 9 - 2104, 10 - 2105.

they are relatively more common compared to the above three modes. These three modes demonstrated that equivalence ratio gradients are also able to trigger different reaction front propagation modes.

Combined temperature and equivalence ratio gradients

For comparison, Figure 5.7 shows the $\xi = 10$ case in terms of a temperature gradient, which has been conducted in Gu et al. (2003). Temperature at $r = 0$ is set to 1001.73 K based on Fig. 5.2. The entire mixture is composition-homogeneous and stoichiometric. As ignition delay is approximately a linear function with regard to either temperature or equivalence ratio when their changes are small, the ignition delay characteristics of this setup should be almost identical to the $\xi = 10$ case in terms of equivalence ratio gradients. By comparing Fig. 5.6 and Fig. 5.7, it was found that the DDT events in these two cases, including the initiation of normal deflagration, the onset of the transition and propagation speed, are almost identical. Furthermore, reaction fronts triggered by combinations of temperature and equivalence ratio gradients were simulated as well. Figure 5.8 shows the results from the combination of a negative temperature gradient and a negative equivalence ratio gradient (a hot and rich spot) with T = 1000.84 K and $\phi = 1.03$ at $r = 0$. Figure 5.9 shows the results from the combination of a positive temperature gradient and a negative equivalence ratio gradient (a cold and rich spot) with T = 998.89 K and $\phi = 1.10$ at $r = 0$. These temperature and equivalence ratio initial conditions were particularly chosen so that $\xi = 10$ in both cases. The corresponding DDT events in Fig. 5.8 and Fig. 5.9 are also found identical compared to Fig. 5.6.

Therefore, it is reasonable to conclude that as long as a specific reactivity gradient is formed, the corresponding reaction front propagation mode will develop, no matter whether the reactivity gradient is created by temperature or equivalence ratio gradients, or both. Hence, it is inadequate to consider only temperature or equivalence ratio gradients when investigating inhomogeneous mixtures in terms of both temperature and composition, such as in-cylinder fuel/air mixtures of IC engines. In such cases, according to the initial Zeld'ovich equation (Equation 5.1), the dimensionless parameter ξ can be generalized as

$$\xi = a^{-1} \left(\frac{\partial \tau_i(T, \phi)}{\partial r} \right) \tag{5.6}$$

where $\tau_i(T, \phi)$ can be calculated at specific T and ϕ, and tabulated as a function of r. Figure 5.10 plots the surface of ignition delay time of H_2/CO/air mixtures as a function of temperature and equivalence ratio at 50 atm. The right bottom corner (higher temperature and equivalence ratio) has the shortest ignition delay time and vice versa. The dashed line represents the iso-level of ignition delay at $\phi = 1$ and $T = 1000$ K. Therefore, any spatial distribution of temperature and equivalence ratio starting from a lower level compared to the dashed line could possibly lead to detonation. Arrows 1 - 4 represent the four cases shown in this study: 1 - hot spots, 2 - rich spots, 3 - hot and rich spots and 4 - cold and

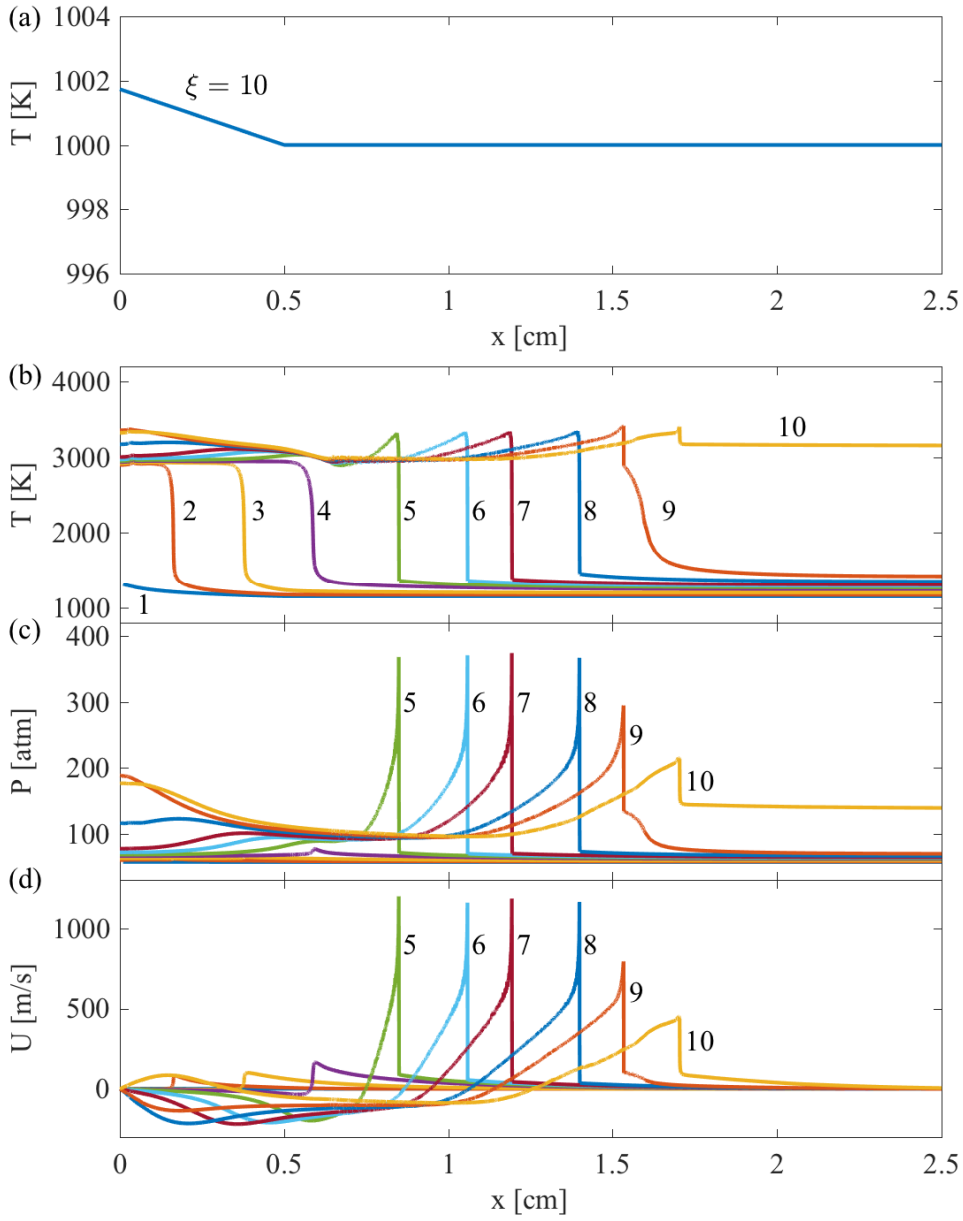

Figure 5.7: Development of a deflagration to detonation transition and thermal explosion, $\xi = 10$ with a negative temperature gradient: (a) Initial condition of equivalence ratio; (b) Temperature; (c) Pressure; (d) Velocity. Time sequence (μs): 1 - 2070, 2 - 2080, 3 - 2090, 4 - 2098, 5 - 2100, 6 - 2101, 7 - 2102, 8 - 2103, 9 - 2104, 10 - 2105.

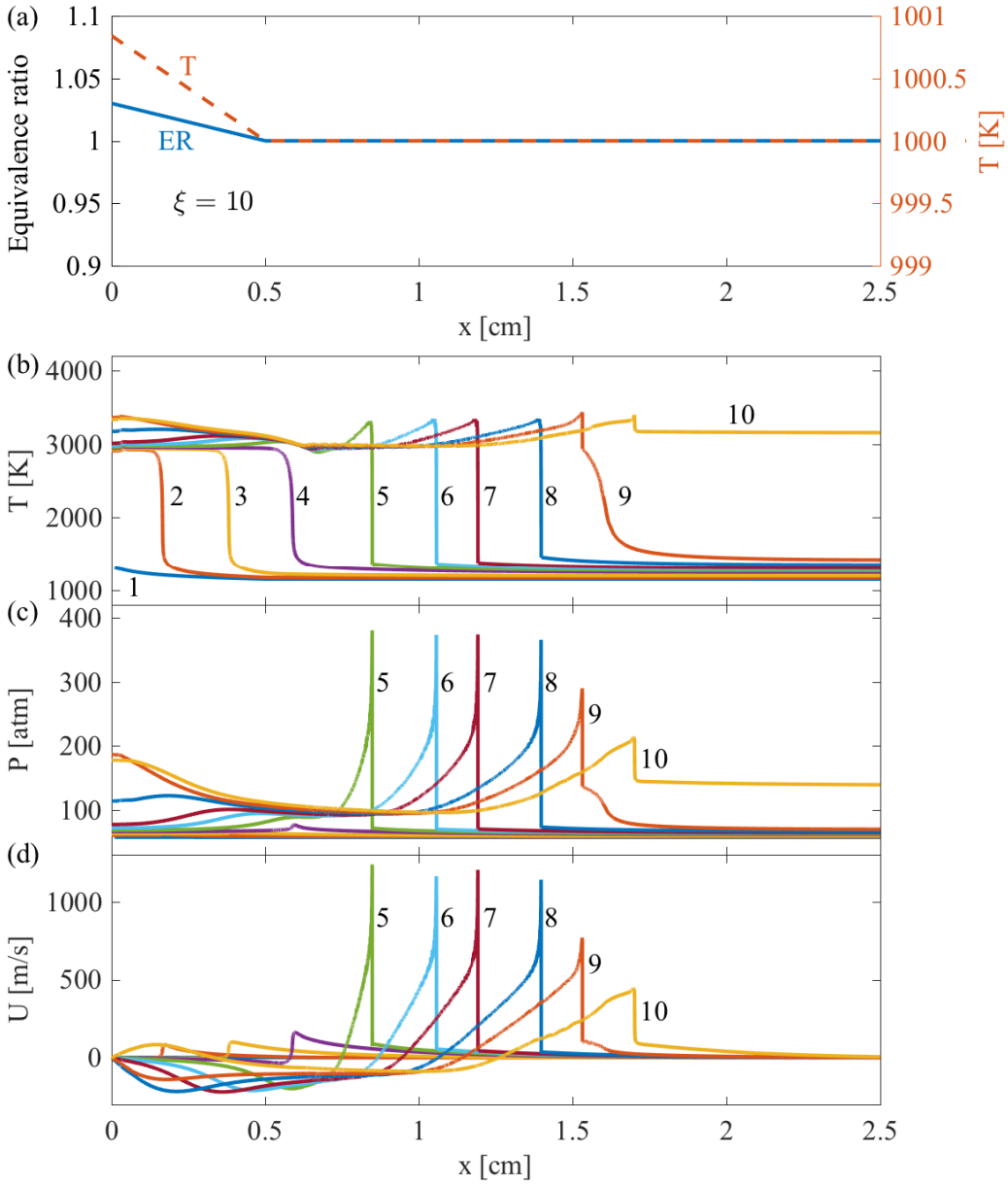

Figure 5.8: Development of a deflagration to detonation transition and thermal explosion, $\xi = 10$ with a negative temperature gradient and a negative equivalence ratio: (a) Initial condition of equivalence ratio; (b) Temperature; (c) Pressure; (d) Velocity. Time sequence (μs): 1 - 2070, 2 - 2080, 3 - 2090, 4 - 2098, 5 - 2100, 6 - 2101, 7 - 2102, 8 - 2103, 9 - 2104, 10 - 2105.

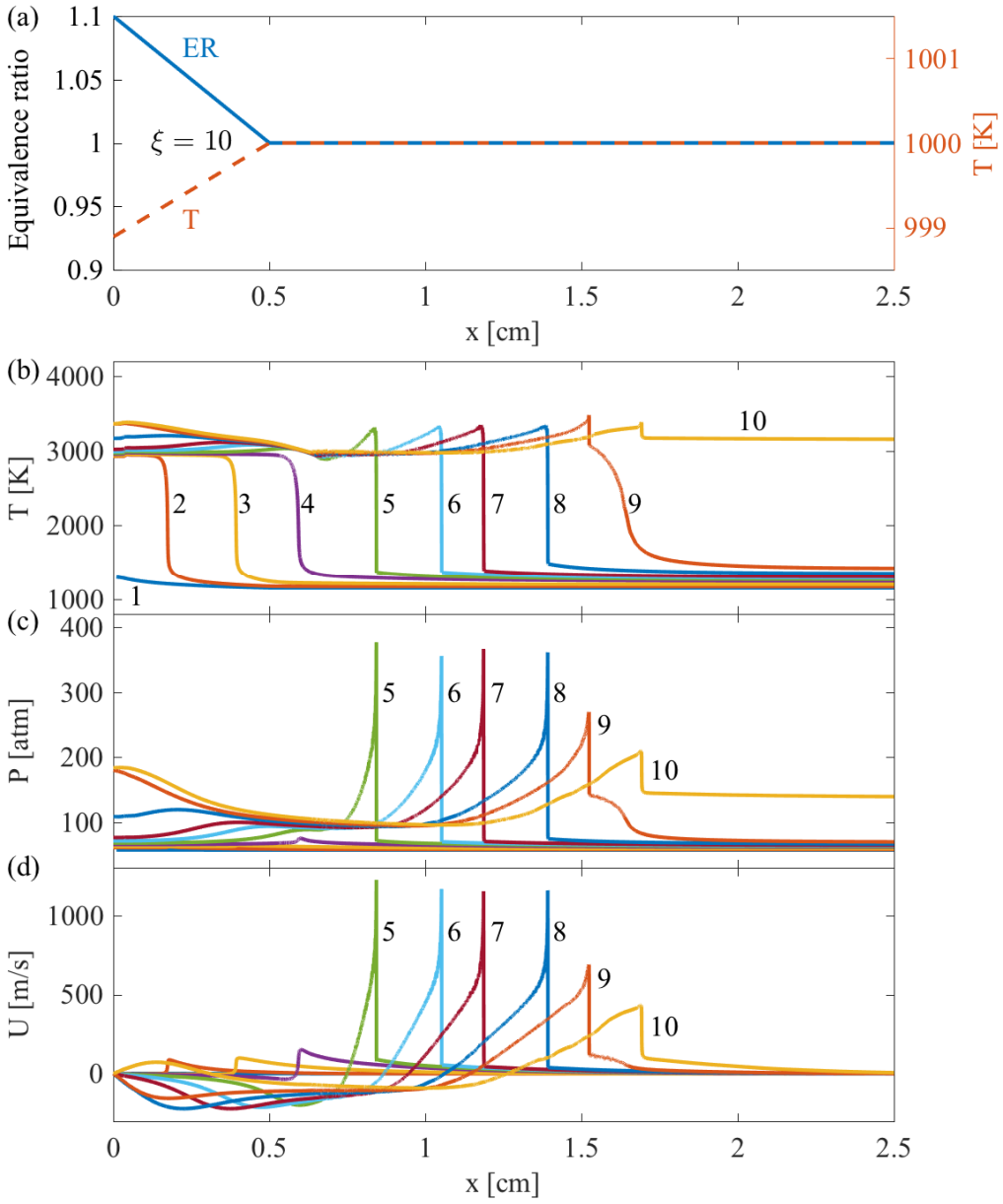

Figure 5.9: Development of a deflagration to detonation transition and thermal explosion, $\xi = 10$ with a positive temperature gradient and a negative equivalence ratio: (a) Initial condition of equivalence ratio; (b) Temperature; (c) Pressure; (d) Velocity. Time sequence (μs): 1 - 2070, 2 - 2080, 3 - 2090, 4 - 2098, 5 - 2100, 6 - 2101, 7 - 2102, 8 - 2103, 9 - 2104, 10 - 2105.

rich spots. Especially, the area enclosed by the triangle corresponds to rich mixtures with low temperatures. Oil droplets could form such mixtures and they could trigger detonation leading to a super knock under relevant engine conditions. Although different fuels may have different ignition delay surfaces, the present methodology for estimating the propensity of a mixture leading to detonation should be applicable regardless of fuel type.

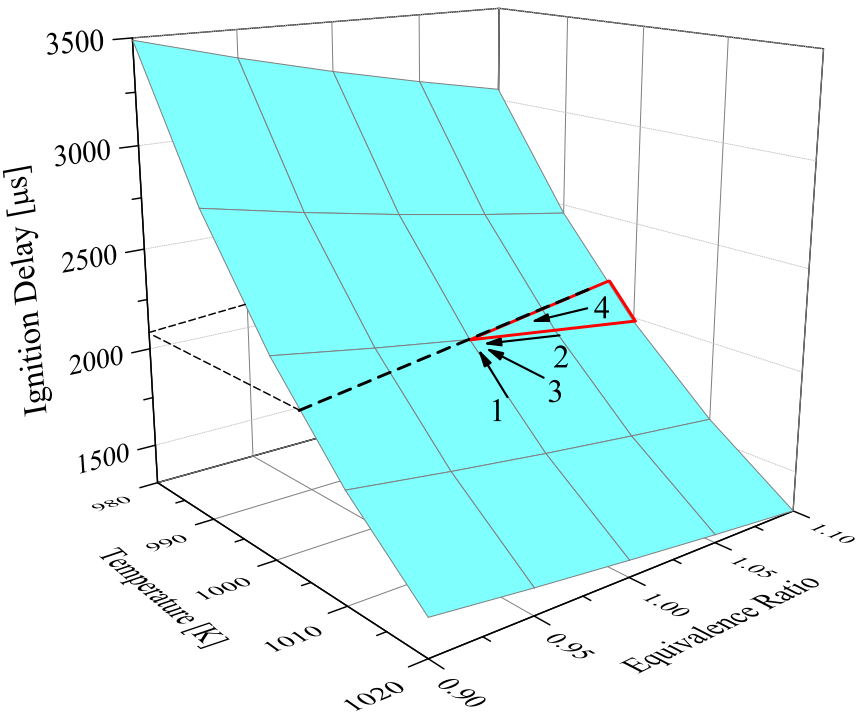

Figure 5.10: Ignition delay time of H_2/CO/air mixtures (50% H_2 and 50% CO by volume) at different temperature and equivalence ratio, P = 50 atm.

Summary

This study investigated different modes of reaction front propagation in H_2/CO/air mixtures (50% H_2 and 50% CO by volume) induced by temperature and equivalence ratio gradients. First, different reaction front propagation modes induced by equivalence ratio gradients were identified, including developing detonation and deflagration to detonation transition. The distinction among different reaction front propagation modes followed the same criterion drawn from temperature gradients in previous studies. The DDT event induced by the equivalence ratio gradient $\xi = 10$ were found identical compared to the case $\xi = 10$ with the corresponding temperature gradient. Furthermore, combinations of temperature and equivalence ratio gradients were also simulated. The same DDT mode was reproduced by either a hot/rich spot or a cold/rich spot. Therefore as long as a specific reactivity gradient

is formed, the corresponding reaction front propagation mode will develop, no matter how the reactivity gradient is created. The reactivity gradient can be estimated by considering ignition delay surface within relevant temperature and equivalence ratio range.

5.3 Modes of reaction front propagation and end-gas combustion

This section is based on the paper published in *International Journal of Hydrogen Energy* (Shi et al., 2017b).

Introduction

Note that in a confined or semi-confined environment, after ignition occurs, a corresponding pressure wave is generated and propagates towards the unburnt mixtures ahead of the ignition front, i.e., end gas. Besides the reaction front propagation introduced by the original ignition, the end gas is also possible to autoignite under certain thermodynamic conditions. There have been many experimental studies which demonstrated the possibility of end-gas combustion including detonation of hydrogen-fueled mixtures (Qi et al., 2015a; Grune et al., 2016; Qi et al., 2015b; Rudy et al., 2016, 2017; Gao et al., 2016; Li et al., 2015). For example, Qi et al. (2015a) performed combustion mode tests of H_2/O_2 mixtures in a tube-like one-dimensional constant volume chamber. They observed that a strong pressure wave can be generated from the end gas and the corresponding reaction front propagated at nearly CJ speed. In a rapid compression machine (RCM) apparatus, Qi et al. (2015b) also found that DDT was possible under the boosted engine-like conditions. The combustion images revealed that auto-ignition spots appeared near the wall, followed by the transition to detonation.

The above experimental studies demonstrate that combustion modes inside a closed chamber can be complicated due to the interaction among flame propagation, pressure wave and end-gas combustion. There have been several recent numerical studies trying to understand the interaction (Wei et al., 2014, 2015; Martz et al., 2011, 2012; Yu and Chen, 2015; Pan et al., 2016a; Wang and Wen, 2016; Gamezo et al., 2007; Ivanov et al., 2013; Liu and Liu, 2013; Taylor et al., 2013; Smirnov et al., 2015; Cai et al., 2016). Wei et al. (2014, 2015) performed 1-D incompressible simulation and observed that propagation and reflection of pressure wave in cylinder can trigger deflagration to detonation transition (DDT). Martz et al. (2011, 2012) performed 1-D transient numerical simulations of iso-octane/air mixtures, for the scenario of laminar flames propagating into highly reactive end-gas mixtures. They found that thermodynamic conditions of the end gas determined whether the reaction front propagation is transport-controlled (deflagrative) or chemistry-controlled (autoignitive). Yu and Chen (2015) and Pan et al. (2016a) performed 1-D shock-capturing simulations of hydrogen/air mixtures and identified different combustion modes of end-gas autoignition. They found that the initial pressure increase due to ignition promoted the end-gas autoignition

before laminar flame arrived. In their studies, the ignitions were either a "hot spot" with specifying a fixed temperature higher than the rest of the mixture, or a "burnt spot" with specifying burnt product profile and zero velocity field.

Different from the previous section, this study focuses on both reaction front propagation introduced by the transient energy-deposit ignition and end-gas combustion influenced by pressure waves inside the closed chamber. Instead of directly specifying hot or burnt spots, transient heat deposit is used as the ignition source. The objective aims at extending the understanding of flame-pressure-autoignition interactions by considering different initial temperatures, ignition locations and chamber sizes. Specifically,

1. 1-D unsteady, shock-capturing numerical simulations of stoichiometric hydrogen/air mixtures at elevated temperature and pressure are performed. In spite of the rare existence of highly reactive, premixed hydrogen/air mixtures. However, as an ideal numerical setup for mechanism demonstration purposes, the conclusions of this study help understand other scenarios as well.

2. Four setups with different ignition locations and chamber sizes are considered. For each setup, different levels of reactivity in terms of initial temperatures are tested.

3. An ignition model is used through increasing the mixture temperature by adding a heat source with fixed magnitude and spatial distribution. Both pressure wave and fluid velocity introduced by the ignition are captured and their significance is evaluated.

4. Effects of initial temperature, ignition location and chamber size are evaluated. In particular, when the ignition is not at the center/wall, the results can reveal more information regarding the influence of asymmetric pressure waves.

5. The simulated results are further analyzed from the point of view of the Zeld'ovich theory and the $\xi - \varepsilon$ diagram. The trends of both reaction front propagation and end-gas combustion are revealed using the $\xi - \varepsilon$ diagram, with both ξ and ε evaluated based on initial conditions. Furthermore, a transient reactivity gradient method is proposed to identify the onset of detonation transition locally.

Numerical Model and Setup

ASURF-Paralell is used to perform transient simulations of ignition, reaction front propagation and end-gas combustion. Numerical simulations are conducted in a 1D planar domain as shown in Figure 5.11. Reflective boundary conditions are applied at both sides of the domain to simulate a closed chamber. In order to resolve the acoustic wave, the finest grid size is set to be 1 μm and the time step is 5×10^{-11} s. A stoichiometric hydrogen/air mixture is simulated in this study and a 9-species detailed hydrogen kinetic model (Burke et al., 2012) is used. Both the mixture temperature and composition are initially homogeneous.

The ignition is simulated by adding a spatially normal-distributed heat source term

$$\tilde{q}(x) = \frac{\tilde{q}_m}{\sigma\sqrt{2\pi}} e^{-\frac{(x-x_i)^2}{\sigma^2}} \tag{5.7}$$

in the energy equation over a time period of 5 μs. The ignition power $\tilde{1}_m$ is 1×10^9 $W/m^3 s$ and the standard deviation σ is 0.1 cm. Therefore, the center of the ignition gains an approximately 200 K temperature rise after total heat deposit and the radius of the ignition kernel is approximately 0.3 cm. The above ignition parameters, including ignition duration, ignition power and standard deviation, are kept constant among different numerical simulation setups, while the ignition location x_i is setup-dependent. Note that if $x_i = 0$ or L cm (L is the chamber size), the heat source is added at the boundaries with only half of the total energy.

For reference, ignition delay times and flame speeds under various initial temperatures and pressures are calculated using SENKIN and PREMIX from CHEMKIN respectively.

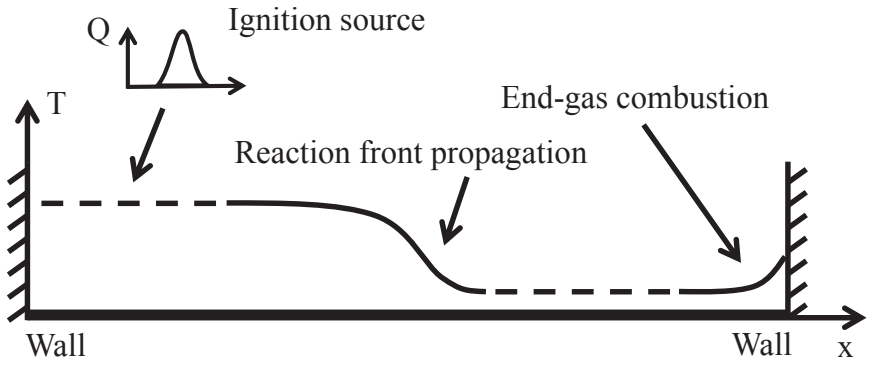

Figure 5.11: Schematic of the 1-D planar closed chamber.

It is important to recognize certain limitations of current simulations:

1. An adiabatic wall boundary condition is applied thus heat losses through walls are not considered.

2. This study focuses on flame-pressure-autoignition interactions in a 1D planar domain. Hence no 3D effect is considered, such as curvature and turbulence.

Four different setups are chosen and studied in this study, as shown in Table 5.1 and Figure 5.12. Setups 1-3 share a domain of 8 cm and ignitions are at 0, 2, 4 cm respectively. Setup 4 has a domain of 6 cm and ignition is at 0 cm. Since the ignition of Setup 3 is in the center of the 8 cm domain, it can be equivalently regarded as a setup with a domain of 4 cm

Table 5.1: Parameters of numerical simulation setups

Setup No.	1	2	3	4
Chamber Size - L	8 cm	8 cm	8 cm	6 cm
Ignition Location - x_i	0 cm	2 cm	4 cm	0 cm

and ignition at 0 cm. The effect of ignition location can be evaluated by comparing Setups 2 and 3, while the effect of chamber size can be evaluated by comparing Setups 1, 4 and 3. In order to test different levels of mixture reactivity, for each setup, stoichiometric (equivalence ratio $\phi = 1$) hydrogen/air mixture is simulated under $P_0 = 4$ atm and over a range of initial temperatures T_0 from 850 K to 1050 K at a step size of 10 K. The initial temperature and pressure conditions are picked so that the corresponding simulations are computationally-affordable and not far away from the conditions of some experimental studies (Qi et al., 2015a; Li et al., 2015).

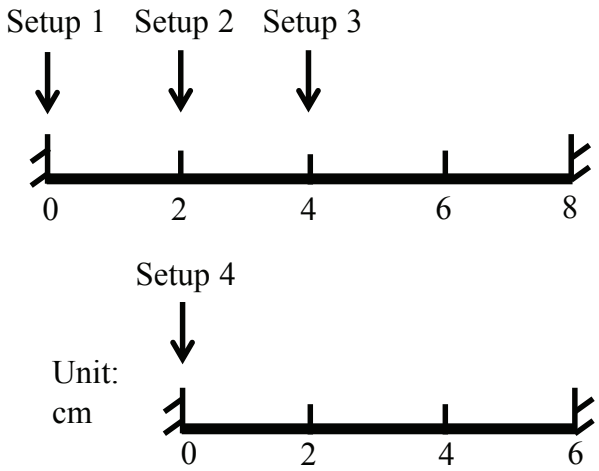

Figure 5.12: Schematic of simulation setups with different ignition locations and chamber sizes, with down arrows indicating the location of ignition.

Results and discussion

Effect of initial temperature on modes of reaction front propagation and end-gas combustion

Different combinations of reaction front propagation and end-gas combustion modes are observed with increasing initial mixture temperature: 1) deflagration without end-gas combustion (Df), 2) deflagration to end-gas autoignition (Df+AI), 3) deflagration to end-gas detonation (Df+AID), 4) developing or developed detonation (Dt). In this context, deflagration refers to reaction front propagation due to diffusion processes while detonation refers

to that due to adiabatic compression. As some of the end-gas combustion modes have been reported and discussed in details in Yu and Chen (2015) and Pan et al. (2016a), two representative cases are presented in the following sections, in terms of the temporal evolution of scalars, end-cell gas behaviors and of reaction front location, to facilitate later discussions on ignition location and chamber size.

Deflagration to end-gas detonation (Df+AID)
As mentioned in the literature review, end gas can develop its own reaction front propagation in terms of detonation. Figure 5.13 shows the temporal development of a deflagration to end-gas detonation event, in terms of temperature, pressure and fluid velocity transient profiles, under Setup 1 and $T_0 = 940$ K. For clarity, results are presented only for $x = 4.5$ to 8 cm, where x axis represents the physical location inside the closed chamber. While the deflagration front has been established and propagates towards the right wall, a detonation reaction front, indicated by the sharp front of temperature, pressure and velocity profiles, originates in the end gas and propagates from the right end towards left.

Figure 5.14 plots time against the reaction front, which is defined by the location of local maximum heat release rate. There are two local reaction fronts, in this case, namely deflagration front from initial ignition and detonation front from end gas. In order to track the much faster detonation propagation compared to deflagration, the two reaction fronts are plotted only for time after 900 μs. The deflagration front (red curve) propagates at approximately 45 m/s. In a corresponding PREMIX calculation, under the same initial temperature $T_0 = 940$ K and pressure $P_0 = 4$ atm, the laminar flame speed, S_L, is 18.6 m/s and the unburnt to burnt density ratio ρ_u/ρ_b is 2.57. Therefore, the flame front propagation speed ($S_L \cdot \rho_u/\rho_b$) is 47.8 m/s, which is in close agreement with 45 m/s from the transient ASURF-Parallel simulation. The oscillation during deflagration propagation, i.e., the wave-like behavior of the reaction front trajectory, results from the pressure wave generated by the initial ignition and the deflagration itself. The pressure wave bounces back and forth inside the closed chamber; alternatively, accelerates and decelerates the deflagration propagation. In comparison, the propagation speed of the detonation front is approximately 1900 m/s, which is compared to the CJ speed

$$S_{CJ} = a \cdot \frac{\rho_u}{\rho_b}. \tag{5.8}$$

Based on the initial condition and equilibrium calculation, sound speed of burnt mixture a is 1147 m/s and ρ_u/ρ_b is 1.69. The CJ speed is then 1944 m/s which is very close to the above ASURF-Parallel result.

Figure 5.15 presents the transient temperature and pressure of the mixture next to the right wall (end-cell gas), mimicking the data obtained by temperature and pressure transducers. Both pressure and temperature start to oscillate after the complete burning of the end gas in detonation mode, while the peak pressure is about 20 atm, while the equilibrium pressure of the domain is about 11 atm from SENKIN. Note that in Fig 5.13(b), the peak

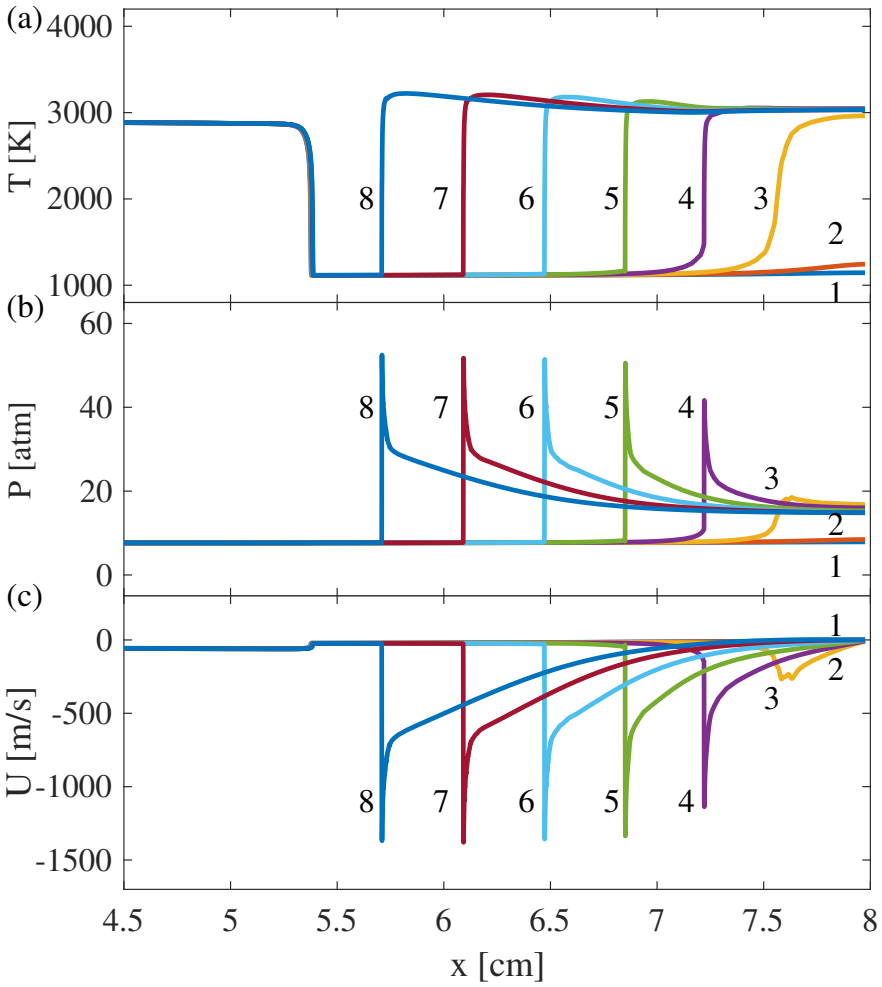

Figure 5.13: Development of deflagration to end-gas detonation, Setup 1, $T_0 = 940$ K, a) temperature b) pressure c) fluid velocity. The time sequence of number-labeled profiles: 1-1196.0 μs, 2-1198.0 μs, 3-1200.0 μs, 4-1202.0 μs, 5-1204.0 μs, 6-1206.0 μs, 7-1208.0 μs, 8-1210.0 μs

pressure at the detonation goes up to about 50 atm, higher than the peak pressure of the end-cell gas. As the detonation originates from the right wall and propagates towards left, the detonation front relaxes when it encounters the deflagration front since mixtures behind the deflagration front has already been burnt. Therefore the 50 atm front drops to 20 atm before it bounces back to the right wall.

Developing or developed detonation (Dt)

If the initial temperature is increased to $T_0 = 990$ K, a developing or developed detonation (Dt) mode without end-gas combustion is observed. Figure 5.16 shows the detailed development of Dt. During time sequence 1, 2 and 3, a reaction front propagation is established

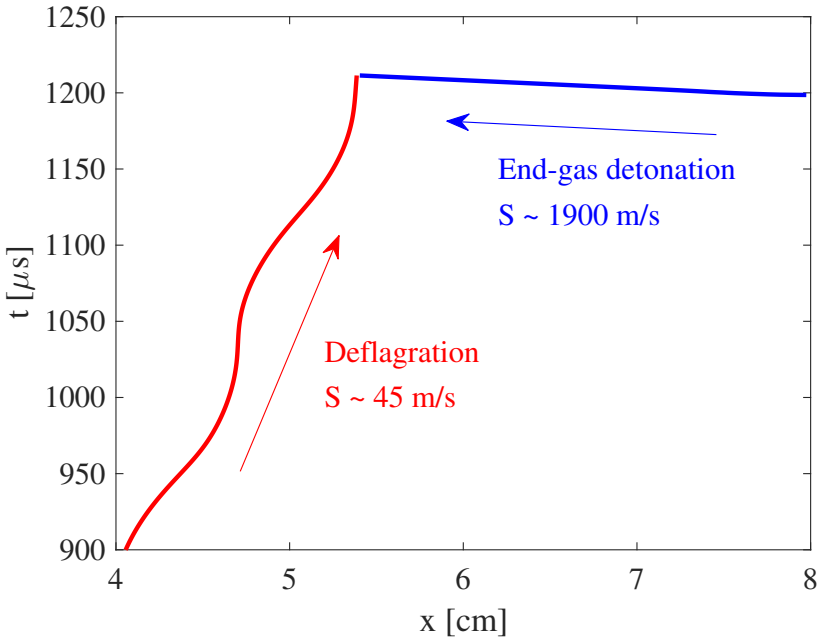

Figure 5.14: Temporal evolution of reaction front, Setup 1, $T_0 = 940$ K

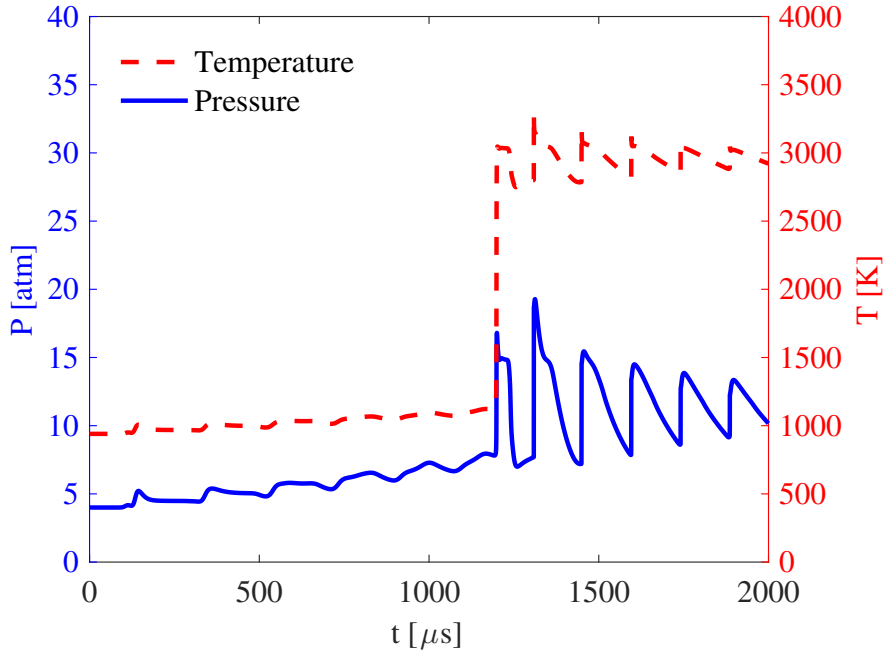

Figure 5.15: Temporal evolution of end-cell gas temperature and pressure, Setup 1, $T_0 = 940$ K

from the initial ignition. Starting from time sequence 4 - 85 μs, sharp spikes are seen in both pressure and fluid velocity profiles, indicating the start of the transition to detonation.

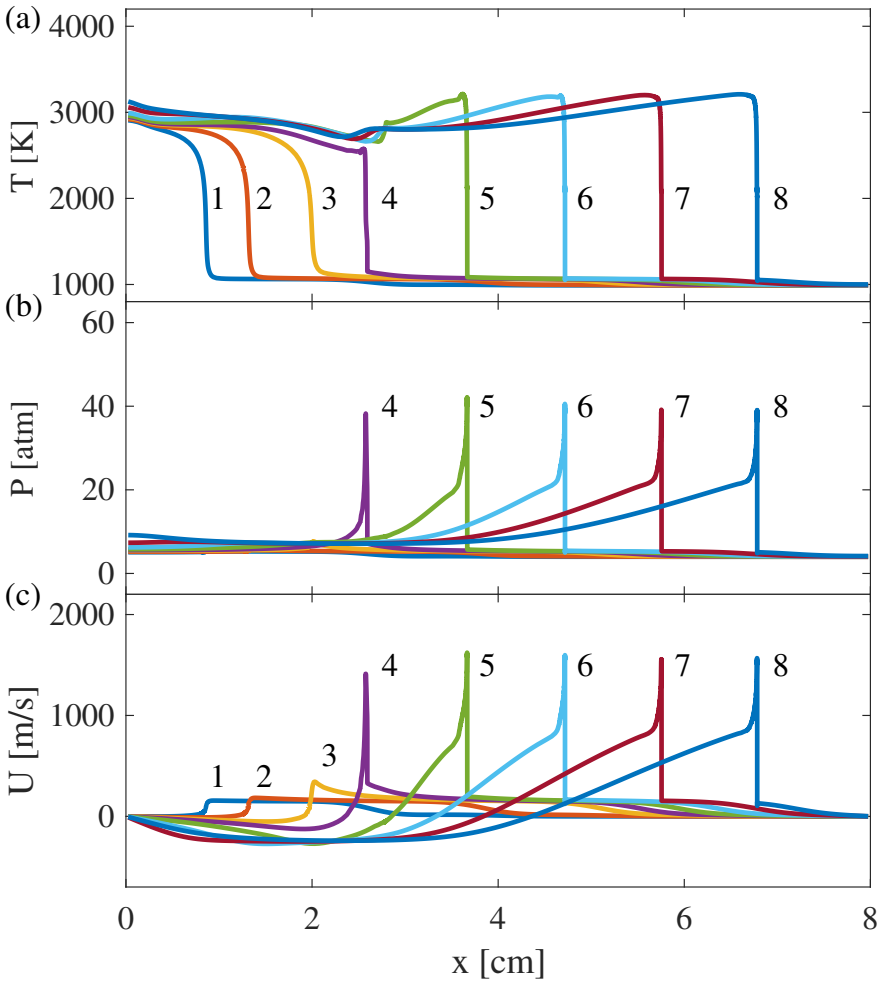

Figure 5.16: Development of deflagration to detonation transition, Setup 1, $T_0 = 990$ K, a) temperature b) pressure c) fluid velocity. The time sequence of number-labeled profiles: 1-50.0 μs, 2-65.0 μs, 3-80.0 μs, 4-85.0 μs, 5-90.0 μs, 6-95.0 μs, 7-100.0 μs, 8-105.0 μs

When tracking the speed of reaction front propagation as shown in Fig. 5.17, two distinct modes are also observed. At first, the reaction front propagates at a speed of 250 m/s then transitions into a much higher speed around 1900 m/s. The latter speed has been validated against the corresponding CJ detonation speed ($a = 1150$ m/s, $\rho_u/\rho_b = 1.69$); thus the second mode is a normal detonation propagation. However, the speed of the first mode 250 m/s is 5 times larger than the laminar flame front propagation speed 55.7 from PREMIX ($S_L = 23$ m/s, $\rho_u/\rho_b = 2.42$). The accelerated reaction front speed compared to laminar flames results from the influence of pressure wave propagation on the local convective velocity, and is, therefore, a reaction-hydrodynamic wave (Kapila et al., 2002). A further discussion on the interaction between flame front and pressure wave will be given in later sections. Compared to the previous case, the end-cell gas experiences much higher pressure, up to about 70 atm

when the detonation wave directly hit the right wall, as shown in Fig. 5.18.

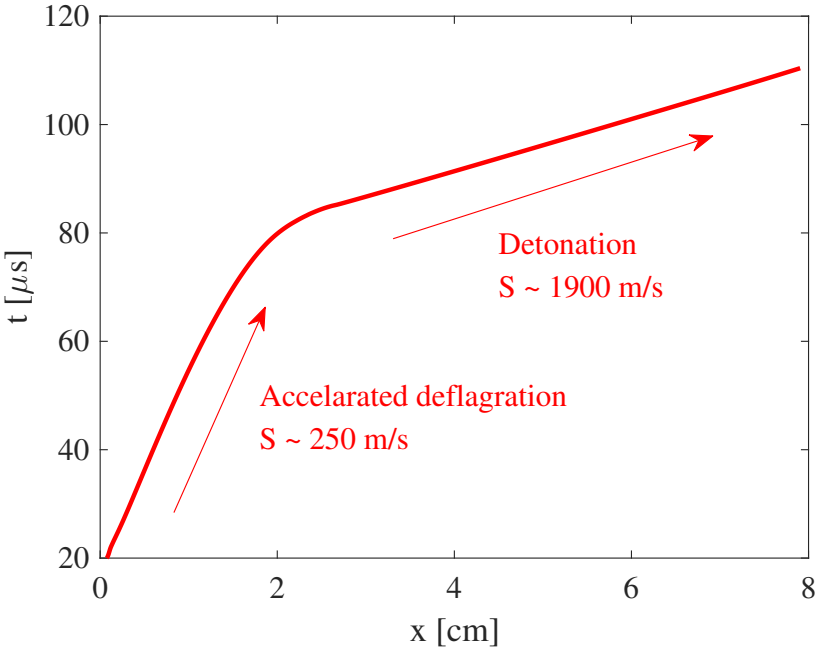

Figure 5.17: Temporal evolution of reaction front, Setup 1, $T_0 = 990$ K

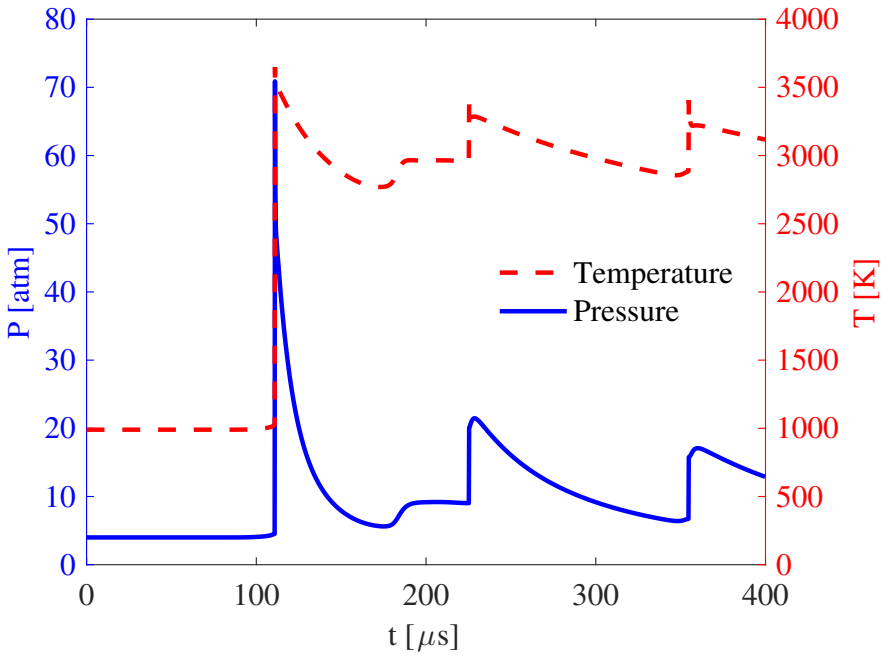

Figure 5.18: Temporal evolution of end-cell gas temperature and pressure, Setup 1, $T_0 = 990$ K

Table 5.2: Modes of reaction front propagation and end-gas combustion under initial pressure 4 atm and over a range of initial temperatures 850-1050 K

	850K	860K	870-920K	930K	940K	950K
Setup 1	Df+AI	Df+AI	Df+AI	Df+AID	Df+AID	Df+AID
Setup 2	Df+AI	Df+AI	Df+AI	Df+AID	Df+AID	Df+AID
Setup 3	Df	Df	Df+AI	Df+AI	Df+AI	Df+AID
Setup 4	Df	Df+AI	Df+AI	Df+AI	Df+AID	Df+AID

	960-970K	980K	≥990K
Setup 1	Df+AID	Df+AID	***Dt***
Setup 2	Df+AID	***Dt***	***Dt***
Setup 3	Df+AID	Df+AID	***Dt***
Setup 4	Df+AID	Df+AID	***Dt***

Table 5.2 summarizes modes of reaction front propagation and end-gas combustion of all four setups with initial temperatures ranging from 850 K to 1050 K at a step size of 10 K. The trends of the results agree well with similar studies in the literature, in terms of reaction front propagation modes (Kassoy et al., 2008; Kiverin et al., 2013) and end-gas combustion (Yu and Chen, 2015; Pan et al., 2016a). For each setup, with increasing initial temperatures, the overall combustion mode transitions in the following sequence of phases:

(Df →) Df+AI → Df+AID → Dt

Therefore, the initial thermodynamic condition plays the primary role in determining the mode of reaction front propagation and end-gas combustion.

Note that in the Df+AID mode, the end-cell gas maximum pressure reached approximately 20 atm. This pressure magnitude corresponds to a normal engine knocking cycle. In contrast, the latter mode, Dt, led to a maximum of 100 atm, similar to an engine super knock event. Therefore, it is speculated that extremely high end-cell pressure can be achieved when detonation propagates directly into the cylinder wall.

Effect of ignition location on modes of reaction front propagation and end-gas combustion

The effect of ignition location can be evaluated by comparing results from Setups 2 and 3. According to Table 5.2, the mixture under Setup 2 seems to be more reactive compared to Setup 3: the transition from Df+AI to Df+AID and that from Df+AID to Dt occur at a lower T_0 under Setup 2, compared to Setup 3. It is interesting to notice that at $T_0 = 980$ K, while Setup 3 presents a Df+AID combustion mode, Setup 2 is reactive enough to undergo the Dt mode. The difference indicates that the spatially asymmetric ignition must play a role in triggering detonation. Figure 5.19 shows the development of Dt under Setup 2 and $T_0 = 980$ K. Since the ignition occurs within the chamber instead of at walls, two reaction

fronts are initially created. Time sequences 1 and 2 represent the deflagration mode and the following sequences 3-6 describe the detonation transition on the right side of the ignition. At a later time, the unburnt mixture on the left undergoes Dt (sequences 7,8) as well.

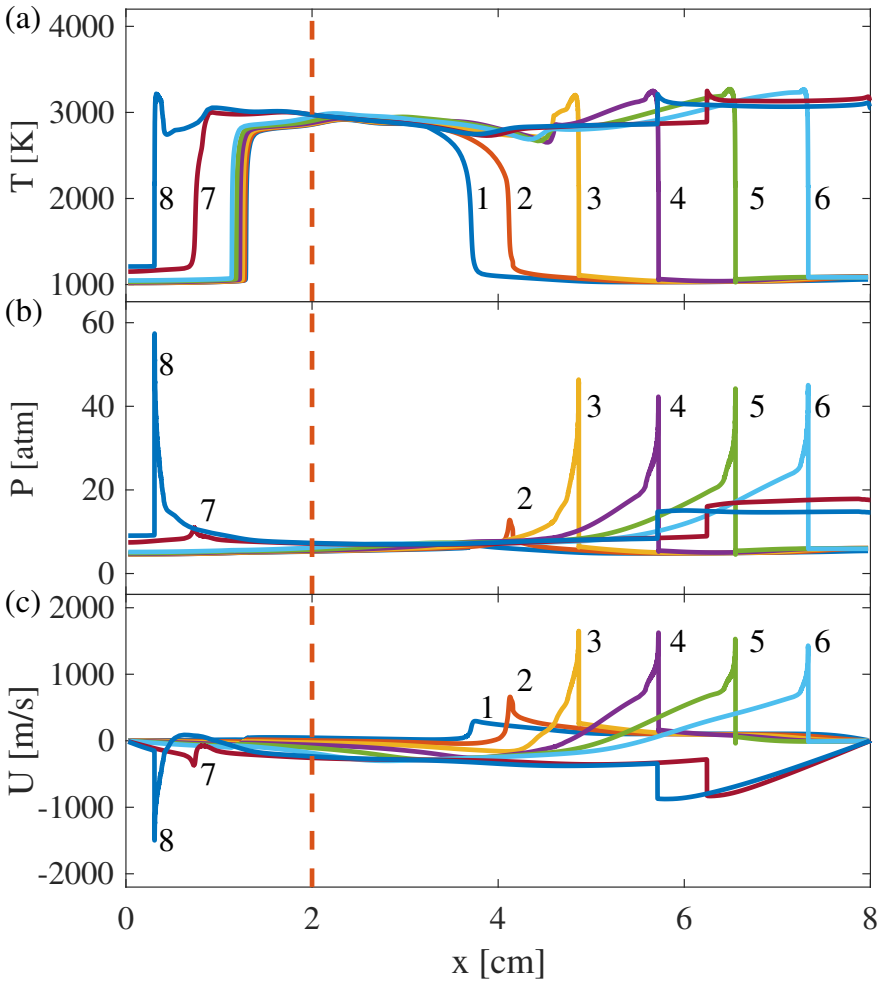

Figure 5.19: Development of deflagration to detonation transition, Setup 2, $T_0 = 980$ K, a) temperature b) pressure c) fluid velocity. The time sequence of number-labeled profiles: 1-95.0 μs, 2-100.0 μs, 3-104.0 μs, 4-108.0 μs, 5-112.0 μs, 6-116.0 μs, 7-132.0 μs, 8-135.0 μs

It is somewhat unexpected that Dt occurs at this initial temperature, also in the unburnt mixture on the right part of ignition before that on the left. To understand this, the time period during the onset of detonation transition on the right side of ignition is elaborated in Fig. 5.20, in terms of temperature, pressure and fluid velocity fields. The ignition-induced pressure wave is first generated and propagates towards both walls, shortly after which two deflagration fronts are established. They will be referred as left and right pressure waves and deflagration fronts in the following context. The left pressure wave only has 2 cm long domain to propagate into while the right pressure wave has 6 cm. Therefore, the left pressure

wave quickly reaches the left wall, as shown at time sequence 3 of Fig. 5.20. After bouncing back, the original left pressure wave propagates towards the right and encounters the left deflagration front. This causes the deflagration front becoming nearly stationary, as during time sequence 3-6 the left deflagration front barely moves forward. This nearly stationary deflagration front can be explained from two perspectives: 1) the left pressure wave creates a velocity field where unburnt mixture near the left wall starts to move towards the right. Therefore, the local fluid velocity at the left deflagration front is altered by the pressure wave and becomes approximately the same as the laminar burning speed but with opposite direction, as shown in Fig. 5.20(c). As a result, instead of burning into a static unburnt mixture, the left deflagration becomes nearly stationary where the unburnt mixture is being fed into the deflagration front. 2) After the pressure wave passes through the deflagration front, the pressure of unburnt mixtures ahead of the left deflagration front reduces and so does the temperature due to rarefaction. It can be seen that from time sequences 3 to 6, the temperature of the unburnt mixture between 0 and 1 cm keeps decreasing, reducing its tendency for detonation transition, as shown in Fig. 5.20(a). The corresponding burning speed of the left deflagration also reduces and leads to a slower propagation speed.

In contrast, when this left pressure wave propagates through the right deflagration, the unburnt mixture ahead of the right deflagration is heated up and the burning speed is enhanced. Note that the unburnt mixtures ahead of the right deflagration have already been heated up once by the original right pressure wave. The additional heating effect introduced by the original left pressure wave has made the unburnt mixture reactive enough to undergo the detonation transition. The start of detonation can be seen from time sequences 5 and 6. Therefore, the interaction of pressure waves could play an important role in detonation transition in confined spaces. Compared to Setup 3, the reactivity of unburnt mixtures under Setup 2 has the chance of being enhanced by two separate pressure waves from ignition due to the asymmetric location of ignition. Thus globally, the mixtures under Setup 2 are observed to be more reactive under this specific condition.

The temporal evolution of reaction fronts in Fig. 5.21 further confirms that Dt mode occurs first on the right side of ignition then on the left side. The deflagration speeds of both deflagration fronts are different due to the interaction of pressure waves and local fluid velocity fields. Once established, both detonation waves propagate at the CJ detonation speed around 1900 m/s. The pressure and temperature profiles of end-gas are very similar to the single Dt case previously. A maximum pressure 80 atm is achieved (not shown).

Effect of chamber size on modes of reaction front propagation and end-gas combustion

The effect of chamber size can be evaluated by comparing results from Setup 1, 4 and 3, corresponding to chamber sizes of 8, 6, and 4 cm. According to Table 5.2, all three setups transition from Df+AID to Dt at $T_0 = 990$ K. In the meanwhile, the transitions among different end-gas combustion modes, in the sequence of Df, Df+AI and Df+AID, occur at

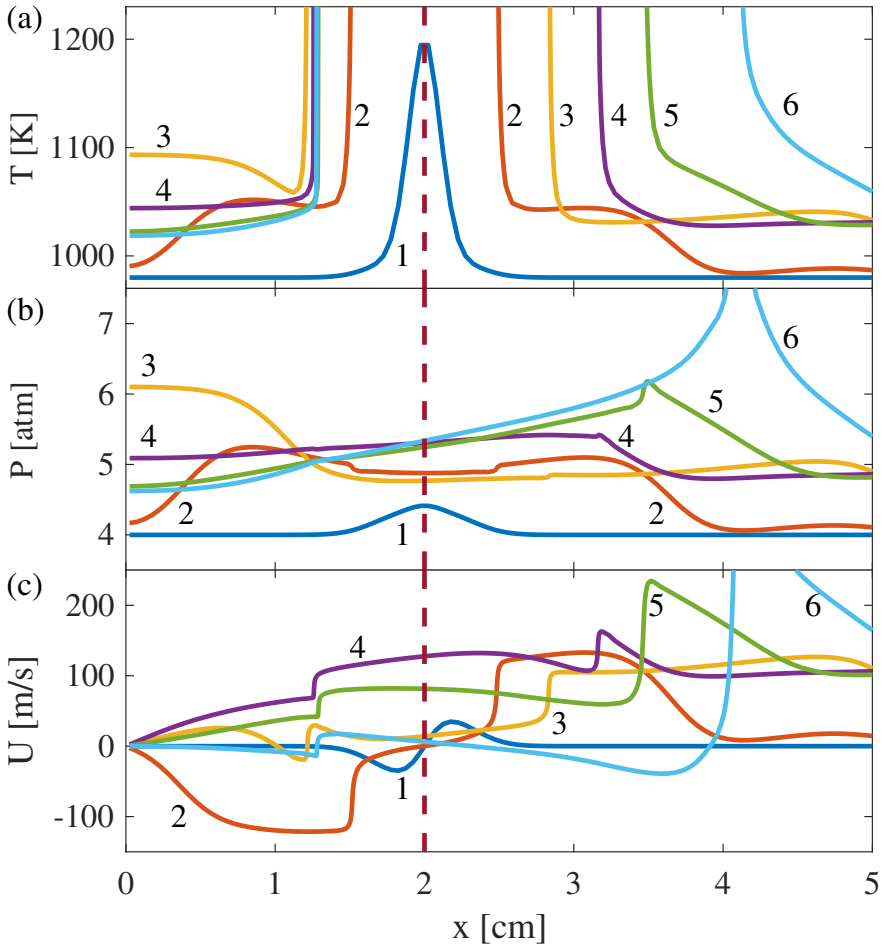

Figure 5.20: Onset of deflagration to detonation transition on the right side of ignition, Setup 2, $T_0 = 980$ K, a) temperature b) pressure. The time sequence of number-labeled profiles: 1-5.0 μs, 2-40.0 μs, 3-60.0 μs, 4-80.0 μs, 5-90.0 μs, 6-100.0 μs

a lower initial temperature, with increasing chamber sizes. Therefore, chamber size has an impact on the mode of end-gas combustion and when end gas autoignites.

In order to autoignite, the temperature of the end gas has to reach a critical temperature T_c where the ignition delay time becomes sufficiently small. The heat needed to raise the end gas temperature, from T_0 to T_c, mainly comes from the compression heating by the deflagration: the normal deflagration increases the overall pressure of the closed chamber. As a result, the pressure rise leads to the temperature rise of the end gas. Additionally, the pressure increase generated from ignition can also increase the end gas temperature when the pressure wave propagates to the end gas. However, the magnitude of temperature rise from ignition-induced pressure is much smaller compared to that from continuous deflagration heat release. Heat transfer between burnt and unburnt gases can lead to the temperature increase of the unburnt mixture as well. But this process mainly occurs around the deflagration front

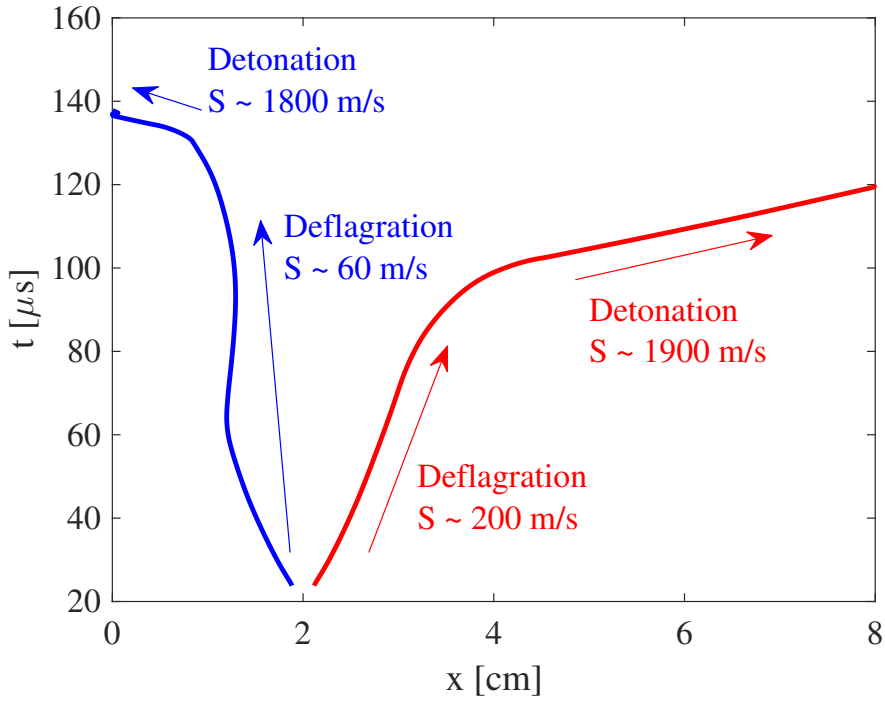

Figure 5.21: Temporal evolution of reaction fronts, Setup 2, $T_0 = 980$ K

when the temperature difference is large; thus the end gas is barely affected.

The critical ignition temperature of end gas then can be approximated by:

$$T_c = T_0 + \Delta T_f, \tag{5.9}$$

where ΔT_f is the temperature rise due to deflagration compression heating, which depends on the total amount of heat release and the total mass of the mixture. Therefore, ΔT_f can be estimated by the following

$$\Delta T_f \sim \frac{S_L t}{L}(T_f - T_0), \tag{5.10}$$

where S_L is laminar flame speed, t is time and L is the domain size. Thus the factor

$$\nu_b = \frac{S_L t}{L} \tag{5.11}$$

is proposed to quantify the overall combustion modes regardless of the chamber size. ν_b represents the volumetric ratio between burnt and total mixtures, and scales how much end gas is heated up due to deflagration heat release. Figure 5.22 presents the regime diagram for modes of reaction front propagation and end-gas combustion: ν_b of L as 8, 6, 4 cm are plotted against initial temperatures. At a given chamber size, a curve in the $\nu_b - T_0$ diagram can be drawn to separate different modes. For all three setups with different chamber sizes, the separation lines between deflagration and end-gas combustion show very good agreement

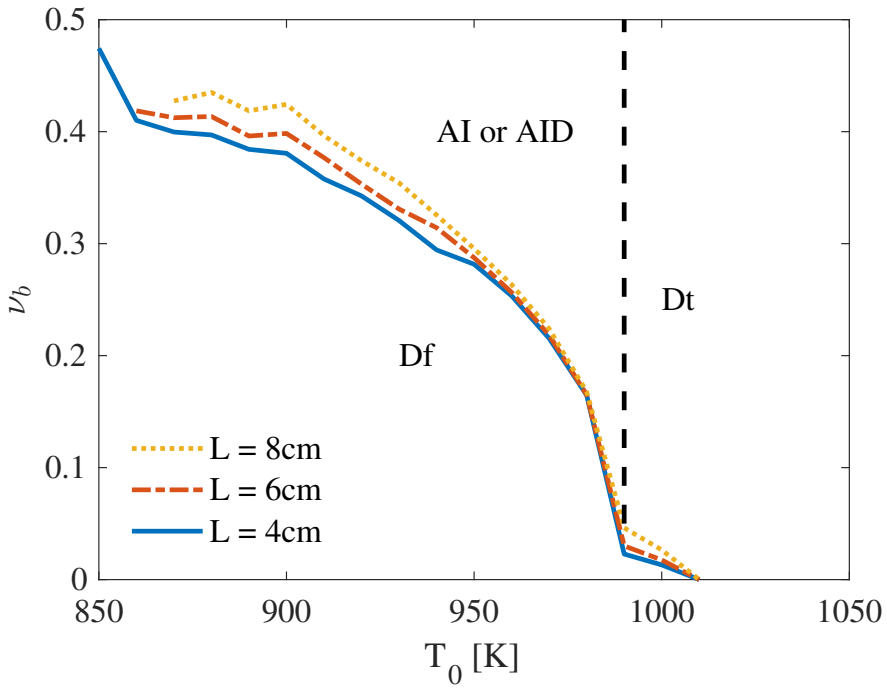

Figure 5.22: Regime diagram for modes of overall combustion, in terms of ν_b and T_0

in terms of ν_b and T_0. At lower initial temperatures, larger ν_b, in terms of either longer time or smaller domain size (or higher laminar flame speed potentially), is needed as more heating is required for end gas to reach the critical autoignition temperature. The separation between end-gas combustion and reaction front transition is mainly determined by the initial temperature with specific ignition parameters, and represented by the vertical dashed line.

Discussions on reactivity gradient theory

Figure 5.23 presents the $\xi - \varepsilon$ diagram based on the Zeld'ovich theory (Gu et al., 2003; Bates et al., 2015). The dashed lines ξ_l and ξ_u separate the regimes of deflagration, detonation and simultaneous autoignition. Compared to the above $\nu_b - T_0$ diagram, this $\xi - \varepsilon$ regime depends on constant ξ and ε values computed from initial conditions, to determine whether the detonation will develop or not, regardless of whether the detonation comes from reaction front propagation or end-gas combustion. The simulated results from Setup 1, including both modes of reaction front propagation induced by ignition (circular markers) and end-gas combustion (triangular makers), are plotted in terms of ξ and ε. ξ, as previously mentioned, can be directly calculated from its original definition

$$\xi = a\frac{\partial \tau_i}{\partial x}, \tag{5.12}$$

while ε can be approximated from Eq. 5.3.

For modes of reaction front propagation introduced by ignition, ε barely changes with different initial temperatures: the excitation time is approximately constant over the initial temperature range and at the order of 10^{-7} s, based on SENKIN calculations. The ignition size is kept constant among all simulation cases as well. The sound speed is slightly higher at higher initial temperatures. In contrast, with increasing initial temperatures, the ignition delay time reduces exponentially and the gradient of τ_i with regard to temperature reduces as well, based on ignition delay time calculations. Therefore, ξ reduces due to the decrease of $\partial\tau_i/\partial x$; and the reaction front propagation moves from the regime of deflagration to that of detonation, due to decreasing ξ.

For end-gas combustion, ξ does not change much with different initial temperatures. Since the temperature gradients in the end gas result from pressure waves induced by initial ignition, the magnitude of end-gas temperature oscillations is about 20 K regardless of initial temperatures. However, the end-gas detonation development is influenced by the space of unburnt gas between flame front and right wall. In the limiting case 850 K, even though the end-gas temperature would eventually reach critical autoignition temperature, there is only a very small portion of unburnt mixture left and detonation is not able to develop due to insufficient mixture. Therefore, the domain length of unburnt mixture when end gas reaches autoignition temperature is used as the length scale in ε for end-gas combustion. At higher initial temperatures, $T_c - T_0$ reduced. As a result, the end gas can reach the autoignition temperature in a shorter time and more unburnt mixture is left, leading to a larger ε. Therefore, modes of end-gas combustion transition from simultaneous autoignition to detonation regime, due to increasing ε. Recall that when $T_0 > 990K$, no end-gas combustion is achieved since the unburnt mixtures are completely consumed by the detonation reaction front from the original ignition. Therefore, even though cases with $T_0 > 990K$ (light-colored markers) have larger ε according to the above analysis, no end-gas combustion is observed.

Although the $\xi - \varepsilon$ diagram is able to identify combustion modes of both reaction front propagation and end-gas combustion, the approximation of ξ and ε are largely based on initial or intermediate conditions. While the diagram succeeds to indicate whether detonation will occur, it cannot tell when exactly the detonation transition takes place. A transient reactivity gradient method based on the Zeld'ovich theory is provided to identify the onset of detonation locally.

The simulated results under Setup 1 and $T_0 = 990$ K are used as an example to illustrate how the transient reactivity gradients correlate with detonation onset. Figure 5.24 presents the detailed profiles of the onset of detonation transition: besides temperature and pressure profiles, ignition delay time and ξ profiles are also calculated and presented. The ignition delay time is evaluated based on the instantaneous mixture temperature and pressure. For given temperature and pressure, the corresponding ignition delay time is interpolated from a pre-computed database of ignition delay time over various temperatures and pressures. The database is obtained from a set of SENKIN calculation and shown in Fig. 5.25. Note that the interpolated ignition delay time is only an approximation of instantaneous mixture reactivity

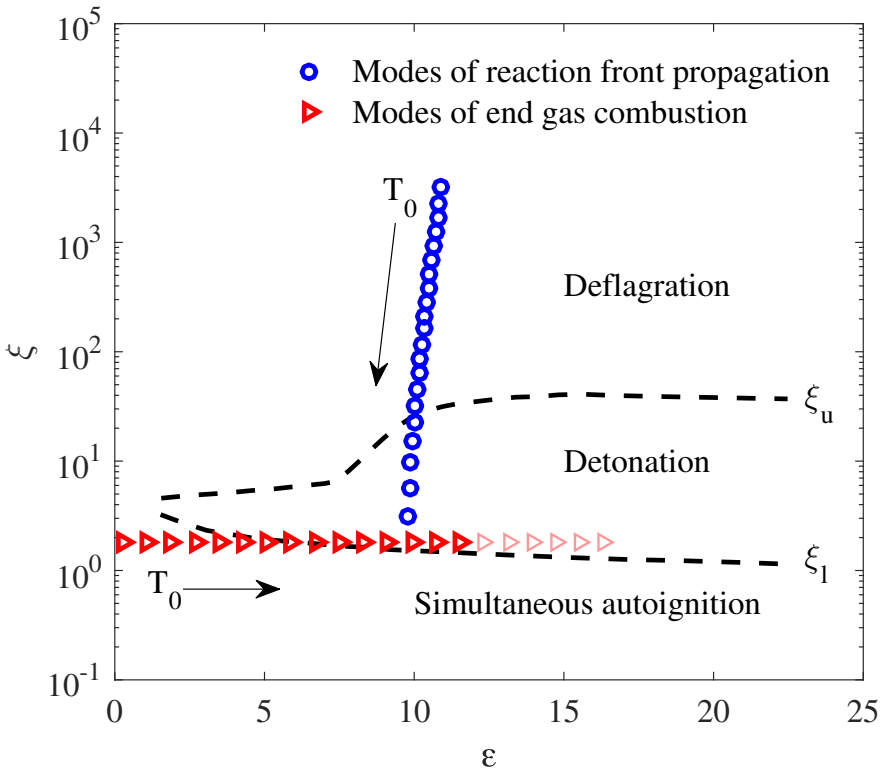

Figure 5.23: Regime diagram for modes of reaction front propagation and end-gas combustion, based on the Zeld'ovich theory

since no intermediate species are considered. The reactivity gradient dimensionless number ξ is computed directly from the ignition delay time profile. In Fig. 5.24, the calculated ξ are presented only around the reaction front area. At time 40 μs (sequence 1), a deflagration front is established while ξ at the front is in the order of 10 - 100. When the deflagration started to transition into detonation at time 70 - 75 (sequences 4, 5), as indicated by the pressure peak in Fig. 5.24(b), ξ at the reaction front also decreased to the order of 1. When $\xi = O(1)$, the reaction front is able to couple with pressure wave and develop detonation propagation. The transient reactivity gradient method based on Zeld'ovich theory is able to accurately capture the onset of detonation.

Summary

Numerical simulations are conducted to study modes of reaction front propagation and end-gas combustion for stoichiometric hydrogen/air mixtures under initial pressure 4 atm and initial temperatures ranging from 850 K to 1050 K. The following conclusions are drawn:

- With increasing initial temperatures, different combinations of reaction front propagation and end-gas combustion modes: 1) deflagration without end-gas combustion,

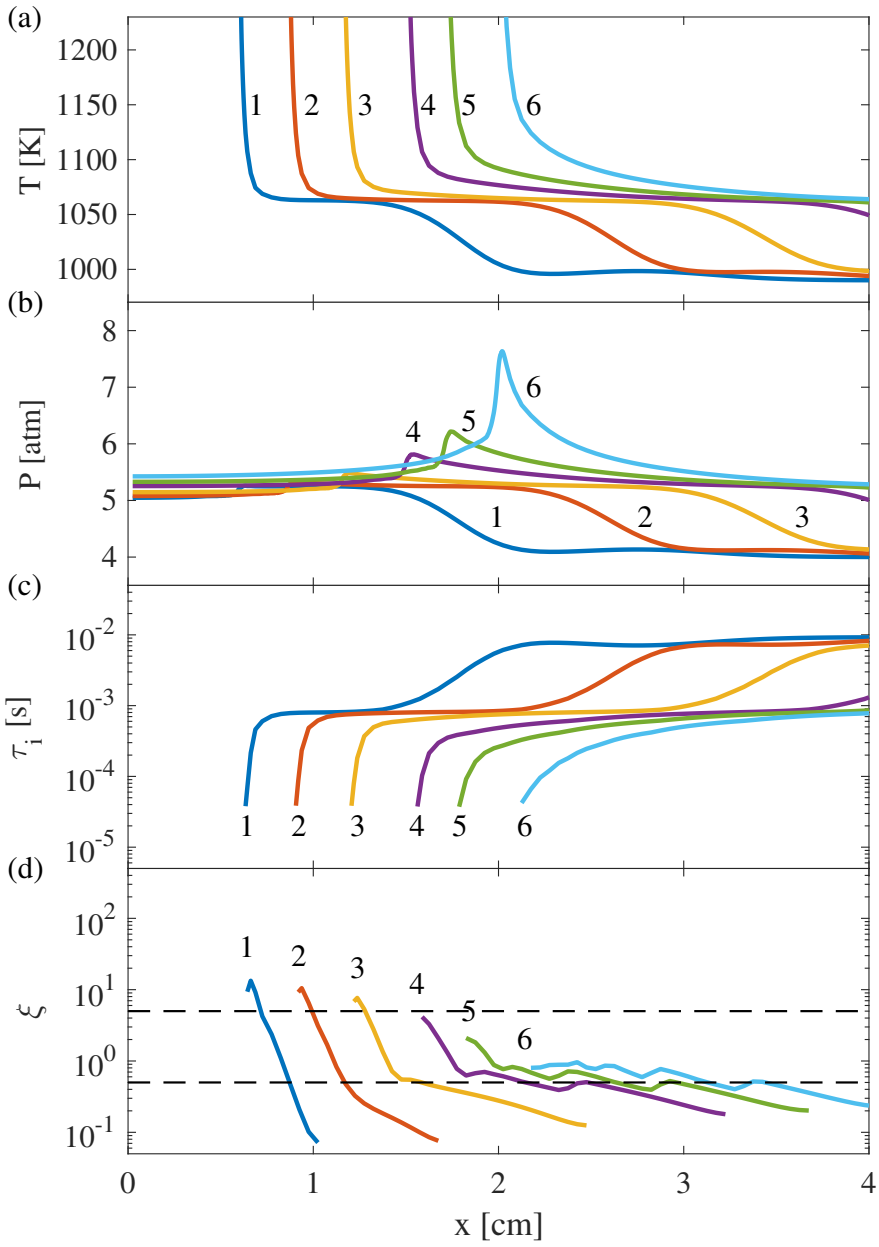

Figure 5.24: Onset of Deflagration to Detonation Transition, Setup 1, T_0 = 990 K, a) temperature b) pressure c) ignition delay (d) reactivity gradient dimensionless number. The time sequence of number-labeled profiles: 1-40.0 μs, 2-50.0 μs, 3-60.0 μs, 4-70.0 μs, 5-75.0 μs, 6-80.0 μs

2) deflagration to end-gas autoignition, 3) deflagration to end-gas detonation, 4) developing or developed detonation, are numerically obtained and analyzed. When end gas autoignites or transitions into detonation, the maximum pressure experienced at

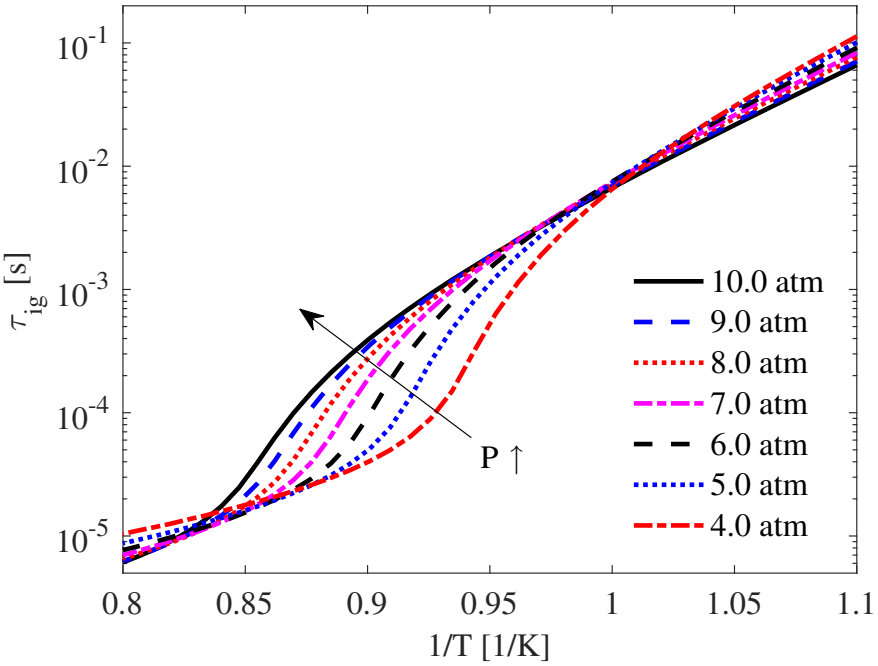

Figure 5.25: Ignition delay times of stoichiometric hydrogen/air mixtures under various initial temperatures and pressures from SENKIN

the wall is only slightly higher than the equilibrium pressure. When the detonation originates from the initial ignition and directly propagates into the wall, an extremely high pressure is observed at the wall.

- A spatially asymmetric ignition is found to promote the reactivity of unburnt mixture compared to ignitions at wall/center. Pressure waves introduced by the asymmetric ignition are able to further increase the temperature of unburnt mixture ahead of the deflagration front.

- The effect of chamber size is found important at relatively low and intermediate initial temperatures: the larger the chamber is, the later the end-gas combustion takes place. At high temperatures, the combustion modes are completely determined by initial temperature and ignition parameters. A new regime diagram is proposed in terms of ν_b and T_0. Different modes of reaction front propagation and end-gas combustion are well represented by these two parameters.

- The simulated results are analyzed using $\xi - \varepsilon$ diagram based on the Zeld'ovich theory. The modes of reaction front propagation are primarily determined by the initial temperature and the corresponding reactivity gradient from the ignition. The modes of end-gas combustion are mainly influenced by the amount of unburnt mixture left when end gas autoignites. A transient reactivity gradient method based on the instan-

taneous evolution of reactivity gradients is provided and able to capture the occurrence of detonation transition.

Chapter 6

Concluding Remarks

In this chapter, results of the presented studies and the knowledge gained from these simulations are summarized. Possible future research directions in the field of stratified combustion are also suggested.

6.1 Conclusions

Based on modern parallelization algorithms and platforms, ASURF-Parallel is developed to perform transient compressible reacting flow simulations. Using ASURF-Parallel, the effect of stratification on flame speeds, lean flammability limits and modes of combustion are identified, evaluated and analyzed. The following conclusions are drawn:

- A universal trend of enhancement in fuel consumption speeds of rich–to–lean stratified flames compared to homogeneous flames is observed in many fuel/air mixtures. For hydrogen/air mixtures, the preferential diffusion of H radical contributes to the enhancement in fuel consumption speeds, while for hydrocarbon/air flames, the preferential diffusion of molecular hydrogen plays the dominant role. The only exception occurs in rich flames of propane/air and n-heptane/air stratified mixtures, where stratified flames are slightly slower than homogeneous flames due to consumption of H and OH by intermediate hydrocarbon species in rich burnt gases.

- The difference between flame front propagation speeds, in contrast, resulted from the difference between local flame speeds due to the chemical effect as well as the hydrodynamic effect due to fluid continuity. In hydrogen/air flames, the hydrodynamic effect is comparable to the chemical effect, while in hydrocarbon/air flames, the chemical effect is dominant.

- Sensitivity analysis of transport properties in stratified methane/air flames reveals that the preferential diffusion of molecular hydrogen and H, OH radicals can be correlated with the degree of enhancement in flame speeds. The successful implementation of

the transient LSL model demonstrates that the flame speeds of stratified mixtures can be accurately described with the consideration of the chemical effect and the memory effect.

- The extension of lean flammability limits by stratification is not as nearly strong as the enhancement observed in flame speeds. Both hydrogen/air and methane/air stratified flames show a very weak extension of lean flammability limits due to reduced overall reactivity and diffusion of stratification.

- Different modes of combustion can be achieved by introducing specific reactivity gradients. Numerical results of H_2/CO/air mixtures demonstrate that the combustion modes are independent of the sources of reactivity gradients, such as temperature or mixture composition. In a practical setup, pressure waves introduced by ignition in a closed chamber can lead to different modes of reaction front propagation and end-gas combustion. The observed behaviors in the corresponding simulations of stoichiometric hydrogen/air mixtures at elevated temperature and pressure can be explained by the proposed transient reactivity gradient method.

6.2 Future work

While this dissertation has contributed to the improved understanding of stratification and its effect on flame speeds, lean flammability limits, and modes of combustion, it is insufficient to answer all questions in the field of stratified combustion. Within the scope of this dissertation, many challenges still remain undressed and future endeavours are needed. A few relevant topics are suggested:

- Stratified flame speed models for larger fuel species, such as *iso*-octane and *n*-heptane, are still challenging, due to the complexity of the corresponding chemical kinetics. Such flame speed models are very useful in large-scale simulations of combustion devices. Development of physics-based reduced chemical kinetic models is the key to facilitate these flame speed models.

- A quantitative relationship between stratification and lean flammability limit extension is still unclear, which requires a robust and reasonable identification of lean flammability limit as well as an accurate and relevant description of mixture stratification.

- While the effect of stratification on modes of combustion is relatively clear, utilization of stratification as an effective technique to achieve desired combustion modes still requires more accurate representations of practical initial and boundary conditions, such as wall heat losses and boundary layer phenomenon.

Outside the scope of the current study, a few unexplored or unmentioned topics are given:

- Some other fundamental combustion characteristics, such as turbulence and instabilities are also important in practical applications and closely coupled with stratification. Although these characteristics have been somewhat investigated in the context of stratified combustion, the understanding is not complete. For example, tests of advanced models for stratified turbulent combustion against experimental data in a wide range of substantially different conditions are still missing and required. A thorough understanding of the dependence of these characteristics on stratification will help explain experimental observations as well as provides insight into the control of these characteristics.

- Experiments where flame characteristics are "clean" and well-defined are still valuable to examine the knowledge learned from numerical simulations. Most current and past experiments are constrained, if not contaminated, by many unwanted and unavoidable conditions, such as flame stretch and buoyancy effect. Therefore, innovated experimental designs and advanced diagnostic techniques will certainly bring in possible agreement/opposition to the current understanding as well as brand-new insights.

- How to effectively transform the fundamental understanding of stratified combustion, including the findings in this dissertation, to robust and optimal combustion control strategies remains a challenging task for future combustion engineers, and needs constant and community-wide brainstorming, discussions and collaborations.

Appendix A

Plasma Assisted Combustion

A.1 Background and motivation

What is plasma? Plasma is the forth fundamental state of matter, along with solid, liquid, and gas. Unlike the other three states of matter, plasma is an ionized gas state consisting of neutral molecules, ions and electrons with no overall electric charge. Plasma exists in a wide range of conditions and environments, such as the upper atmosphere, fluorescent lamps, and nuclear fusion reactors. For combustion applications, plasma has been recognized and demonstrated as a promising technique for ignition control (Wolk et al., 2013; Casey et al., 2017), combustion stabilization (Kimura et al., 1981; Pilla et al., 2006), fuel reforming (Bromberg et al., 2000; Petitpas et al., 2007), and emission reduction (Kim et al., 2007; Starikovskii et al., 2008). A simple schematic of various plasma applications is shown in Fig. A.1. Recent advances and progress in plasma assisted combustion can be found in Starikovskaia (2006); Starikovskiy and Aleksandrov (2013); Ju and Sun (2015).

In general, there are two categories of plasma states, i.e., thermal plasma and non-thermal plasma, discussed in the context of plasma assisted combustion. Thermal plasma refers to the state where electron and other gas particles have the same temperature. It normally exists when the gas temperature or the electron number density is very high (Ju and Sun, 2015). Thermal plasma has been utilized in the industry for more than a century, such as plasma torch for welding and spark ignition systems in IC engines. In contrast, non-thermal plasma has the electron temperature much higher than the bulk gas temperature and a relatively low electron number density. The possibilities of using non-thermal plasma for ignition and combustion control have been extensively explored in the past two decades, and significant progresses have been made in understanding ion and electron dynamics, energy exchange, and plasma chemical kinetics.

Plasma influences combustion processes mainly through the following fundamental pathways:

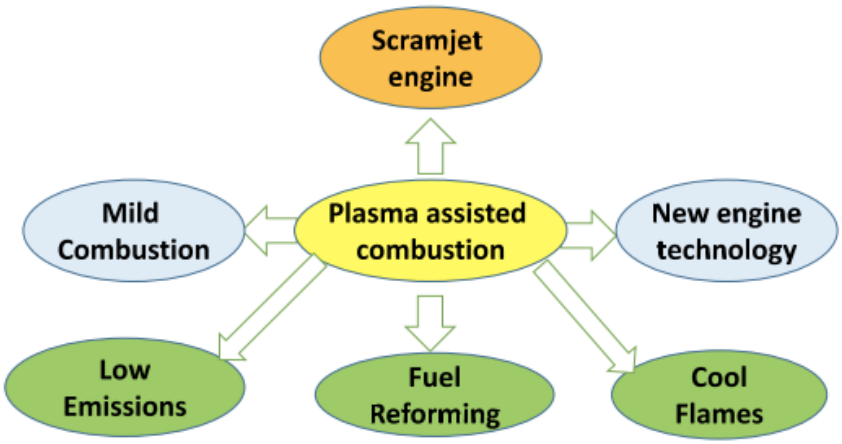

Figure A.1: Schematic of plasma assisted combustion and applications (Ju and Sun, 2015).

- Thermal effect: Energy release from plasma discharge causes bulk gas heating, resulting in higher gas temperature and consequent faster chemical reaction rates. This is the main mechanism associated with thermal plasma.
- Kinetic effect: Highly energetic electrons and ions embrace new chemical pathways for productions of radicals and other active species via various electron- and ion-impact chemical reactions.
- Transport effect: Drifting of electrons and ions under the influence of external electric fields introduces additional momentum transfer from electric source to the gas, and modifies the local gas composition due to additional fluxes of associated active particles.

In most plasma-combustion applications, two or all of the above effects are closely coupled. A simple schematic as shown in Fig. A.2 illustrates many possible interactions.

While many qualitative understanding of plasma have been achieved in the past two decades, quantitative descriptions of plasma, especially non-thermal plasma, are still very challenging. A good discussion on technical challenges of plasma research is provided in (Ju and Sun, 2015). From the perspective of numerical modeling, the multi-physical, multi-scale, non-equilibrium nature of plasma has made even one-dimensional simulations very difficult. For instance, the majority of the rates and products of electron-ion and ion-molecule reactions remain unknown. The length and time scales of plasma are vastly different from those of combustion, which poses strict restrictions on numerical grid resolution and time-stepping sizes. Therefore, improvements on chemical kinetic models and numerical schemes for plasma assisted combustion are still needed.

This appendix documents the details of plasma assisted combustion capability development inside the framework of ASURF-Parallel. The ultimate goal is to enable efficient and

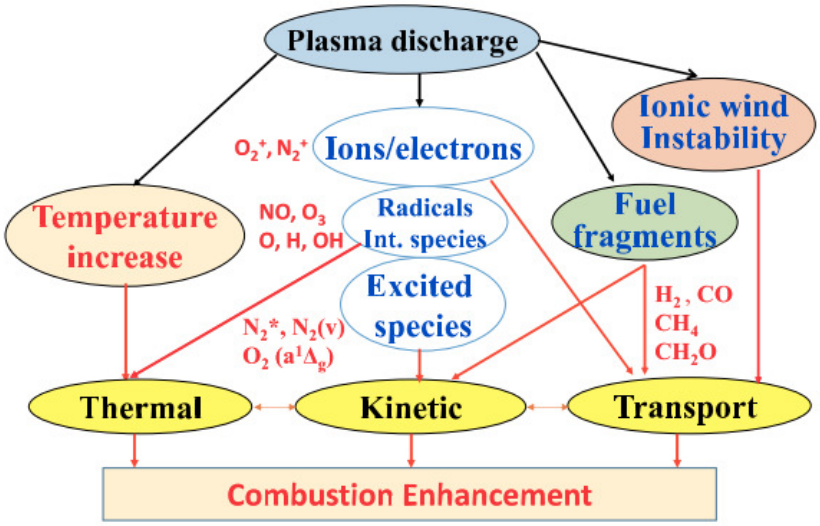

Figure A.2: Schematic of major enhancement pathways of plasma assisted combustion (Ju and Sun, 2015).

tractable plasma assisted combustion simulations, by taking advantages of ASURF-Parallel's adaptive mesh refinement and parallelization features.

A.2 Code modification

In order to account for the three effects mentioned above for plasma assisted combustion, certain adjustments were performed on the standard gas-phase reacting flow simulation framework and implemented in ASURF-Parallel.

A.2.1 Energy exchange between electrons and neutral gases

There are three main processes responsible for the total energy exchange between electrons and neutral gases: elastic collisions between electrons and gas molecules, inelastic collisions (electron-impact excitation and corresponding relaxation reactions), and electron generation (ionization reactions).

With the approximation that the electron energy distribution is Maxwellian, the elastic energy exchange can be directly written as:

$$\dot{Q}_{elas} = \frac{3m_e}{\bar{M}} n_e \nu_{elas} R_u (T_e - T_g), \tag{A.1}$$

where m_e is the electron mass, $\bar{M}$ is the mean molecular weight of mixture, n_e is the total mole of electrons, ν_{elas} is the elastic collision frequency, R_u is the universal gas constant, and

T_g, T_e are gas and electron temperatures respectively. When the electron energy distribution is treated non-Maxwellian and the electron energy distribution function (EEDF) is available, the energy exchange can then be integrated throughout the entire energy spectrum. The Boltzmann equation solver, BOLSIG+, can be used to estimate the EEDF. The details regarding BOLSIG+ can be found in Hagelaar and Pitchford (2005); Casey (2016).

For inelastic collisions, the corresponding energy exchange can be calculated by considering each of the reactions in this category:

$$\dot{Q}_{inel} = \sum_{i=1}^{N_{inelas}} \Delta H_i \dot{r}_i, \tag{A.2}$$

where ΔH_i is the enthalpy of formation and r_i is the reaction rate, of chemical reaction i. The evaluation of r_i is discussed in Section A.2.3.

For electron generation, before ionization reactions taking place, the electrons are regarded as a part of the neutral gas which stay at the gas temperature with full degree of molecular motions. After the electrons are released from gas molecules, free electrons gain certain amount of kinetic energy (translational) and reach the electron temperature. Therefore, the difference between the two stages of electron leads to the calculation of the corresponding energy exchange:

$$\dot{Q}_{elec} = \dot{\omega}_e m_e (c_{v,e} T_e - c_{p,e} T_g), \tag{A.3}$$

where $\dot{\omega}_e$ is the electron consumption rate, $c_{v,e}$ and $c_{p,e}$ are the specific heat capacities of electrons.

Therefore, the total energy exchange between electrons and neutral gases can be expressed as

$$\dot{Q}_e = \dot{Q}_{elas} + \dot{Q}_{inel} + \dot{Q}_{elec}, \tag{A.4}$$

which is added to the energy conservation equation of ASURF-Parallel as a source term.

A.2.2 Electron and ion drifting

Under the influence of electric field, ions and electrons are subject to drifting. In order to estimate the drift velocities of ions and electrons, the electric field and the mobilities of ions and electrons are required so that the drift velocity can be calculated as

$$V_{d,k} = \mu_k \mathbf{E}, \tag{A.5}$$

where $V_{d,k}$ and μ_k are the drift velocity and mobility of species k respectively. $\mathbf{E}$ is the electric field. The definition of electric potential, combined with the differential form of Gauss's law, provides a relationship between the electric potential $\mathbf{V_E}$ and the charge density ρ_c:

$$\nabla^2 \mathbf{V_E} = -\frac{\rho_c}{\varepsilon_0} \tag{A.6}$$

where $\mathbf{V_E}$, ρ_c, ε_0 are electric potential, charge density and electric constant (vacuum permittivity), respectively. Then, the electric field can be calculated:

$$\mathbf{E} = -\nabla \mathbf{V_E} \tag{A.7}$$

Mobilities of ions and electrons can be evaluated with access to the corresponding mass diffusivities and invoking the Einstein relation:

$$\mu_k = \frac{D_k}{k_B T}. \tag{A.8}$$

For neutral species at excited states, the diffusivities are assumed to be identical to those at the ground state, as data for electronic state intermolecular potentials is not available. For ions, the diffusivities are calculated using the intermolecular potential parameters from their equivalent neutral molecules. Although ions diffuse differently from neutral molecules due to their charges, some studies (Han et al., 2015) have proved that the updated transport data of ions using modified potentials has small effects on the actual ion distributions across flames. For electron, if the non-Maxwellian characteristic of electrons is considered, the electron diffusivity can be evaluated based on EEDF from BOLSIG+.

In order to solve Eq. A.6 (Poisson's equation), a modified version of HYPRE (Falgout et al., 2006) is added into the ASURF-Parallel framework and used for solving such an equation over the adaptive grid.

A.2.3 Chemical kinetics

For inelastic electron-impact reactions, once an approximation for the EEDF is obtained, the mean electron temperature can be calculated. The rates of these reactions can then be parameterized by the electron temperature in the CHEMKIN framework using the Janev et al. (1987) fit. The corresponding collision cross section data are obtained from the LXCat database (Pancheshnyi et al., 2012; DeFilippo and Chen, 2016).

A.2.4 Modified governing equations

A modified set of the governing equation terms is given, with added electron energy exchange term, drift velocity terms, and updated chemical reaction rates regarding electron-impact

reactions.

$$\mathbf{U} = \begin{pmatrix} \rho Y_1 \\ \rho Y_2 \\ \vdots \\ \rho Y_N \\ \rho u \\ E \end{pmatrix}, \qquad F(\mathbf{U}) = \begin{pmatrix} \rho u Y_1 \\ \rho u Y_2 \\ \vdots \\ \rho u Y_N \\ \rho u^2 + P \\ (E+P)u \end{pmatrix},$$
$$F_v(\mathbf{U}) = \begin{pmatrix} -\rho u Y_1 (V_1' + \boldsymbol{V_{d,1}}) \\ -\rho u Y_2 (V_2' + \boldsymbol{V_{d,2}}) \\ \vdots \\ -\rho u Y_N (V_N' + \boldsymbol{V_{d,N}}) \\ \tau \\ q + \Phi \end{pmatrix}, \qquad S_R(\mathbf{U}) = \begin{pmatrix} \boldsymbol{\dot{\omega}_1} \\ \boldsymbol{\dot{\omega}_2} \\ \vdots \\ \boldsymbol{\dot{\omega}_N} \\ 0 \\ \boldsymbol{\dot{Q}_e} \end{pmatrix}. \tag{A.9}$$

Please refer to Eq. 2.1 for the compact form of the governing equations.

Appendix B

Chemical Kinetic Models

Three reduced chemical kinetic models were developed for methane, propane, and n-heptane respectively. The development methods and model validation results are presented in this appendix.

B.1 A 16-species reduced model of methane combustion

This section provides information regarding the reduced chemical kinetic model used for methane/air combustion. The reduced model has 16 species and was developed from a short version of GRI3.0 model without NO_X chemistry, using Quasi steady-state approximation (QSSA).

Laminar flame speed results from experiments, numerical simulations with the detailed GRI3.0 model, and those with the reduced model, are first compared as shown in Fig. B.1. Fuel consumption speed is used as the reference laminar flame speed in the simulations, while experimental measurements come from various experimental setups, including counter-flow, spherical expanding and flat flames. Please refer to specific papers for more details about the experimental measurements of laminar flame speeds. Figure B.1 shows that the numerical results with both detailed and reduced models match well with the experimental observations.

In addition, mole fraction profiles of H2, H and OH at different equivalence ratios from numerical simulations with GRI 3.0 model are also compared to those with the reduced model, as these intermediate species and radicals play an important role in stratified flames. The comparison is shown in Figure S2. The results from the reduced model match very well with those from the detailed model over a wide range of equivalence ratios.

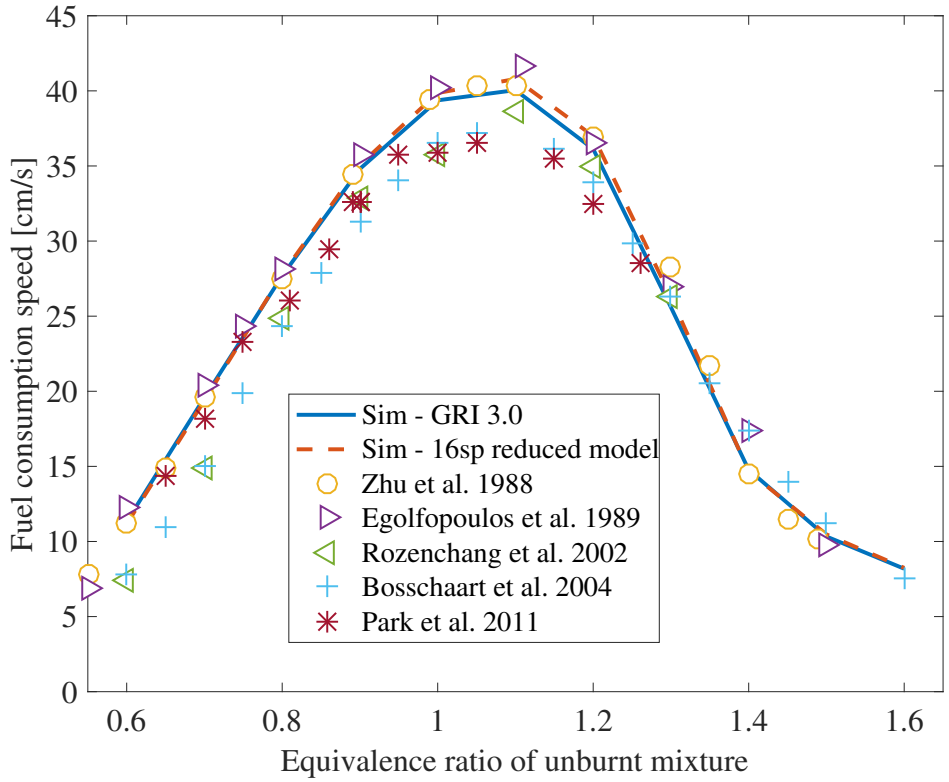

Figure B.1: Laminar flame speeds of homogeneous methane/air flames at 300 K, 1 atm.

B.2 A 24-species reduced model of propane combustion

For propane/air flames, a 50-species, 320-reaction skeletal model was first developed from 70-species, 463-reaction detailed model (Qin et al., 2000) using in-house Target Search Algorithm (TSA). A 24-species reduced model was then developed from this skeletal model using QSSA. Figure B.3 shows that the numerical results with the reduced model match well with the experimental observations.

B.3 A 32-species reduced model of *n*-heptane combustion

For *n*-heptane/air flames, a 32-species reduced model was developed from a 65-species, 315-reaction skeletal model (Smallbone et al., 2009) using QSSA. Figure B.4 shows that the numerical results with the reduced model match well with the experimental observations.

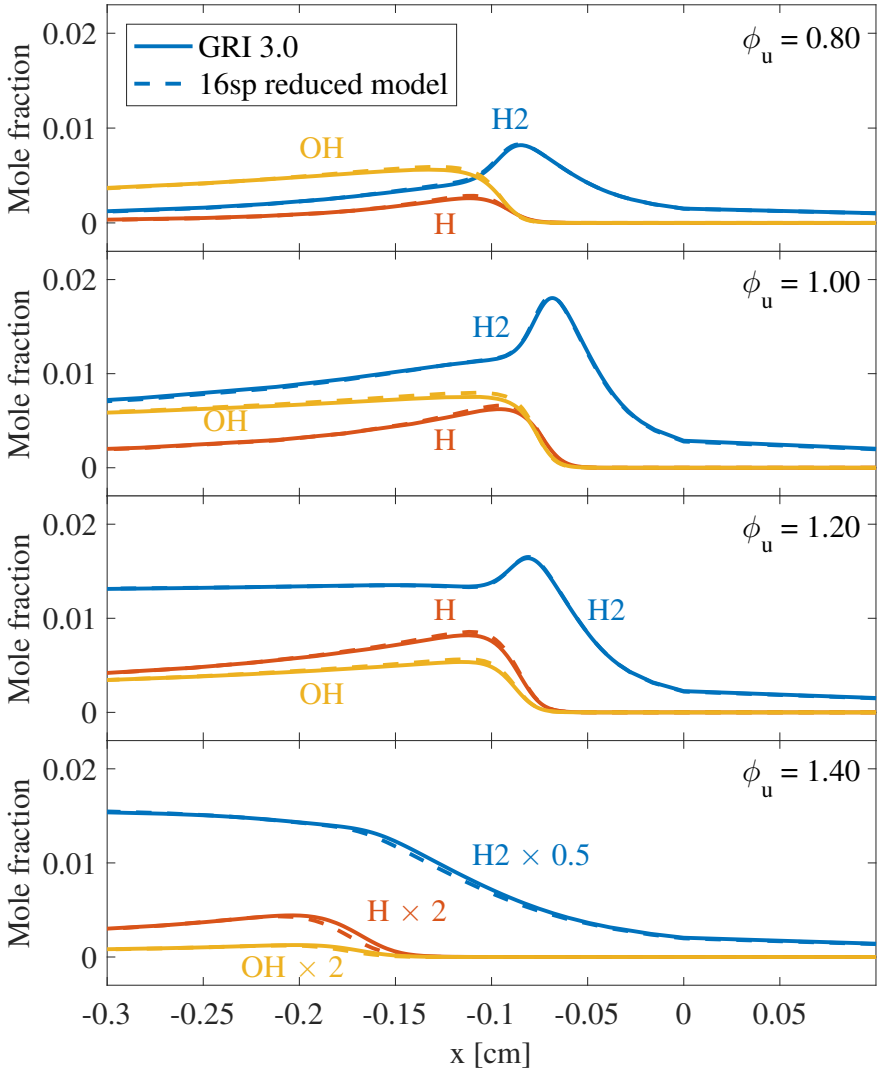

Figure B.2: Comparison between numerical results of mole fraction profiles of H2, H and OH at different equivalence ratios, with GRI3.0 model and the 16-species reduced model.

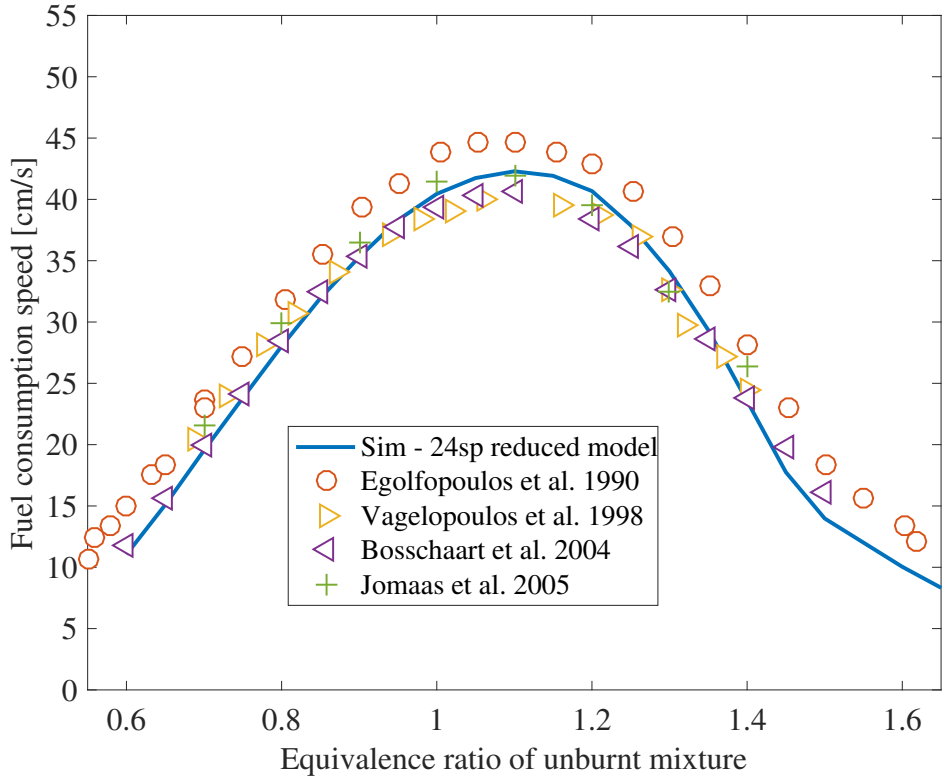

Figure B.3: Laminar flame speeds of homogeneous propane/air flames at 300 K, 1 atm.

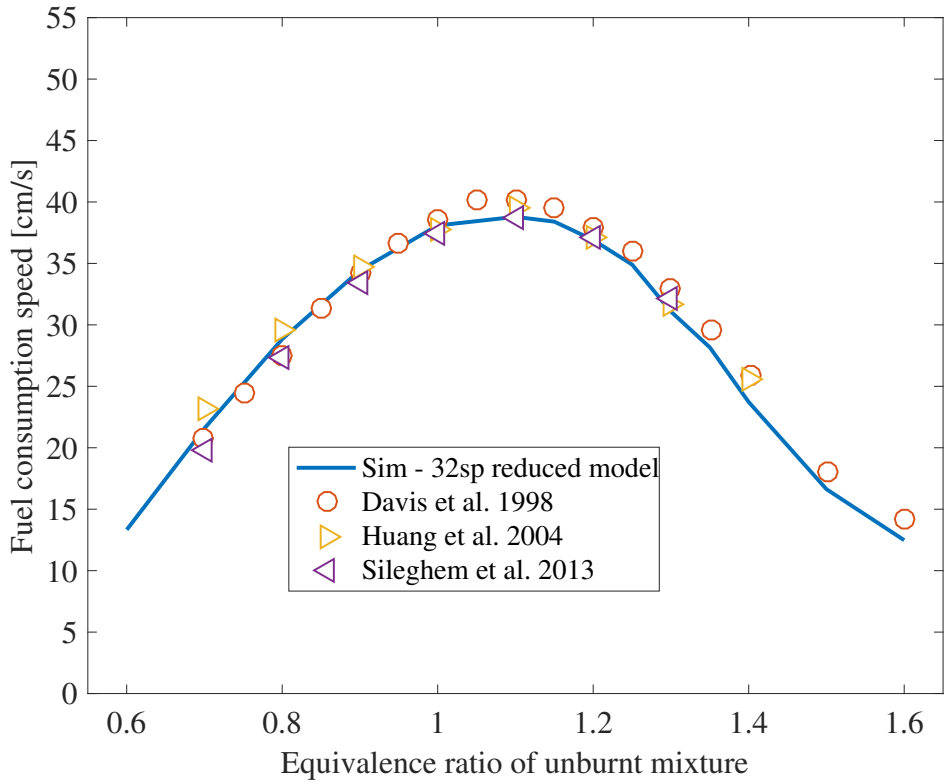

Figure B.4: Laminar flame speeds of homogeneous n-heptane/air flames at 300 K, 1 atm.

References

Alex C. Alkidas. Combustion advancements in gasoline engines. *Energy Conversion and Management*, 48:2751–2761, 2007.

Iñaki Arto, Iñigo Capellán-Pérez, Rosa Lago, Gorka Bueno, and Roberto Bermejo. The energy requirements of a developed world. *Energy for Sustainable Development*, 33:1–13, 2016.

Holger Ax and Wolfgang Meier. Experimental investigation of the response of laminar premixed flames to equivalence ratio oscillations. *Combustion and Flame*, 167:172–183, 2016.

O. Badr and G. Karim. Flame Propagation in Stratified Methane-Air Mixtures. *Journal of Fire Sciences*, 2:415–426, 1984.

Saravanan Balusamy, Armelle Cessou, and Bertrand Lecordier. Laminar propagation of lean premixed flames ignited in stratified mixture. *Combustion and Flame*, 161:427–437, 2014.

R.S. Barlow, A.N. Karpetis, J.H. Frank, and J.-Y. Chen. Scalar profiles and no formation in laminar opposed-flow partially premixed methane/air flames. *Combustion and flame*, 127:2102–2118, 2001.

Luke Bates, Derek Bradley, Günter Paczko, and Norbert Peters. Engine hot spots: Modes of auto-ignition and reaction propagation. *Combustion and Flame*, 166:80–85, 2015.

Edward J. Bissett and David L. Reuss. Analysis of a nonadiabatic flame propagation through gradients of fuel or temperature. *Symposium (International) on Combustion*, 21:531–538, 1986.

BP. BP Energy Outlook, 2017 edition, 2017.

William Braker and Allen L. Mossman. *Matheson gas data book*. Matheson East Rutherford, NJ, 1980.

L. Bromberg, D.R. Cohn, A. Rabinovich, N. Alexeev, A. Samokhin, R. Ramprasad, and S. Tamhankar. System optimization and cost analysis of plasma catalytic reforming of natural gas. *International Journal of Hydrogen Energy*, 25(12):1157–1161, 2000.

Peter N. Brown, George D. Byrne, and Alan C. Hindmarsh. VODE: A variable-coefficient ODE solver. *SIAM journal on scientific and statistical computing*, 10(5):1038–1051, 1989.

Michael P. Burke, Marcos Chaos, Yiguang Ju, Frederick L. Dryer, and Stephen J. Klippenstein. Comprehensive H2/O2 kinetic model for high-pressure combustion. *International Journal of Chemical Kinetics*, 44(7):444–474, 2012.

Thomasra Bussing and Earllm Murman. Finite-volume method for the calculation of compressible chemically reacting flows. *AIAA journal*, 26(9):1070–1078, 1988.

Xiaodong Cai, Jianhan Liang, Ralf Deiterding, Yonggang Che, and Zhiyong Lin. Adaptive mesh refinement based simulations of three-dimensional detonation combustion in supersonic combustible mixtures with a detailed reaction model. *International Journal of Hydrogen Energy*, 41(4):3222–3239, 2016.

Sébastien Candel. Combustion dynamics and control: Progress and challenges. *Proceedings of the Combustion Institute*, 29(1):1–28, 2002.

Tiernan A. Casey. *Electric field effects in combustion with non-thermal plasma*. PhD thesis, University of California, Berkeley, 2016.

Tiernan A. Casey, Jie Han, Memdouh Belhi, Paul G Arias, Fabrizio Bisetti, Hong G Im, and Jyh-Yuan Chen. Simulations of planar non-thermal plasma assisted ignition at atmospheric pressure. *Proceedings of the Combustion Institute*, 36(3):4155–4163, 2017.

David Leonard Chapman. Vi. on the rate of explosion in gases. *The London, Edinburgh, and Dublin Philosophical Magazine and Journal of Science*, 47(284):90–104, 1899.

J.-Y. Chen. A General Procedure for Constructing Reduced Reaction Mechanisms with Given Independent Relations. *Combustion Science and Technology*, 57:89–94, 1988.

Zheng Chen. *Studies on the Initiation , Propagation , and Extinction of Premixed Flames*. PhD thesis, Princeton University, 2009.

Zheng Chen. Effects of radiation and compression on propagating spherical flames of methane/air mixtures near the lean flammability limit. *Combustion and Flame*, 157: 2267–2276, 2010.

Zheng Chen. On the extraction of laminar flame speed and markstein length from outwardly propagating spherical flames. *Combustion and Flame*, 158(2):291–300, 2011.

Zheng Chen, Michael P. Burke, and Yiguang Ju. Effects of Lewis number and ignition energy on the determination of laminar flame speed using propagating spherical flames. *Proceedings of the Combustion Institute*, 32:1253–1260, 2009.

S.H. Chung. Stabilization, propagation and instability of tribrachial triple flames. *Proceedings of the Combustion Institute*, 31:877–892, 2007.

Hubert Frank Coward and George William Jones. Limits of flammability of gases and vapors. Technical report, U.S. Bureau of Mines, Washington D.C., 1952.

A. Pires Da Cruz, A.M. Dean, and J.M. Grenda. A numerical study of the laminar flame speed of stratified methane/air flames. *Proceedings of the Combustion Institute*, 28:1925–1932, 2000.

Christoph Dahnz, Kyung-man Han, Ulrich Spicher, Max Magar, Robert Schießl, and Ulrich Maas. Investigations on Pre-Ignition in Highly Supercharged SI Engines. *SAE International Journal of Engines*, 3:214–224, 2010.

A.E. Dahoe. Laminar burning velocities of hydrogen air mixtures from closed vessel gas explosions. *Journal of Loss Prevention in the Process Industries*, 18:152–166, 2005.

Peng Dai and Zheng Chen. Supersonic reaction front propagation initiated by a hot spot in n-heptane/air mixture with multistage ignition. *Combustion and Flame*, 162:4183–4193, 2015.

Anthony C. DeFilippo and Jyh-Yuan Chen. Modeling plasma-assisted methaneair ignition using pre-calculated electron impact reaction rates. *Combustion and Flame*, 172:38–48, 2016.

G. Dixon-Lewis. Flame structure and flame reaction kinetics. ii. transport phenomena in multicomponent systems. In *Proceedings of the Royal Society of London A: Mathematical, Physical and Engineering Sciences*, pages 111–135. The Royal Society, 1968.

Werner Döring. On detonation processes in gases. *Annals of Physics*, 43:421–436, 1943.

S.B. Dorofeev, V.P. Sidorov, A.E. Dvoinishnikov, and W. Breitung. Deflagration to detonation transition in large confined volume of lean hydrogen-air mixtures. *Combustion and Flame*, 104(1):95–110, 1996.

F.N. Egolfopoulos, A.T. Holley, and C.K. Law. An assessment of the lean flammability limits of CH4/air and C3H 8/air mixtures at engine-like conditions. *Proceedings of the Combustion Institute*, 31:3015–3022, 2007.

ExxonMobil. 2017 Outlook for Energy: A View to 2040, 2017.

Robert D. Falgout, Jim E. Jones, and Ulrike M. Yang. The design and implementation of hypre, a library of parallel high performance preconditioners. In *Numerical solution of partial differential equations on parallel computers*, pages 267–294. Springer, 2006.

R. M. Fristrom. Definition of Burning Velocity and a Geometric Interpretation of the Effects of Flame Curvature. *Physics of Fluids*, 8(2):273, 1965.

Vadim N. Gamezo, Takanobu Ogawa, and Elaine S. Oran. Numerical simulations of flame propagation and ddt in obstructed channels filled with hydrogen–air mixture. *Proceedings of the Combustion Institute*, 31(2):2463–2471, 2007.

Yuan Gao, Bo Zhang, Hoi Dick Ng, and John H.S. Lee. An experimental investigation of detonation limits in hydrogen–oxygen–argon mixtures. *International Journal of Hydrogen Energy*, 41(14):6076–6083, 2016.

George K. Giannakopoulos, Athanasios Gatzoulis, Christos E. Frouzakis, Moshe Matalon, and Ananias G. Tomboulides. Consistent definitions of Flame Displacement Speed and Markstein Length for premixed flame propagation. *Combustion and Flame*, 162:1249–1264, 2015.

A. Malcolm Gill, Scott L. Stephens, and Geoffrey J. Cary. The worldwide wildfire problem. *Ecological Applications*, 23(2):438–454, 2013.

P. Girard, M. Huneau, C. Rabasse, and J.C. Leyer. Flame propagation through unconfined and confined hemispherical stratified gaseous mixtures. *Symposium (International) on Combustion*, 17(1):1247–1255, 1979.

J. Grune, K. Sempert, A. Friedrich, M. Kuznetsov, and T. Jordan. Detonation wave propagation in semi-confined layers of hydrogen-air and hydrogen-oxygen mixtures. *International Journal of Hydrogen Energy*, 2016.

X.J. Gu, D.R. Emerson, and D. Bradley. Modes of reaction front propagation from hot spots. *Combustion and Flame*, 133:63–74, 2003.

Hongsheng Guo, Fengshan Liu, and Gregory J. Smallwood. A numerical study on NOx formation in laminar counterflow CH4/air triple flames. *Combustion and Flame*, 143: 282–298, 2005.

G.J.M. Hagelaar and L.C. Pitchford. Solving the boltzmann equation to obtain electron transport coefficients and rate coefficients for fluid models. *Plasma Sources Science and Technology*, 14(4):722, 2005.

Jie Han, Memdouh Belhi, Fabrizio Bisetti, and S. Mani Sarathy. Numerical modelling of ion transport in flames. *Combustion Theory and Modelling*, 19(6):744–772, 2015.

A. Heidari and J.X. Wen. Numerical simulation of flame acceleration and deflagration to detonation transition in hydrogen-air mixture. *International Journal of Hydrogen Energy*, 39(36):21317–21327, 2014.

Erjiang Hu, Zuohua Huang, Jiajia He, Chun Jin, and Jianjun Zheng. Experimental and numerical study on laminar burning characteristics of premixed methane-hydrogen-air flames. *International Journal of Hydrogen Energy*, 34:4876–4888, 2009.

P.H. Hugoniot. Mémoire sur la propagation du mouvement dans les corps et spécialement dans les gaz parfaits. première partie. *Journal de l'École Polytechnique*, 57:3–97, 1888.

H.G. Im and J.H. Chen. Structure and propagation of triple flames in partially premixed hydrogen-air mixtures. *Combustion and Flame*, 119:436–454, 1999.

Takuya Inoue, Yoshiki Inoue, and Masahiro Ishikawa. Abnormal Combustion in a Highly Boosted SI Engine - The Occurrence of Super Knock. *SAE Technical Paper 2012-01-1141*, 2012.

IPCC. Climate Change 2014: Mitigation of Climate Change., 2014.

M.F. Ivanov, A.D. Kiverin, I.S. Yakovenko, and Michael A. Liberman. Hydrogen–oxygen flame acceleration and deflagration-to-detonation transition in three-dimensional rectangular channels with no-slip walls. *International Journal of Hydrogen Energy*, 38(36):16427–16440, 2013.

Ratko K. Janev, William D. Langer, Kenneth Jr. Evans, and Douglass E. Jr. Post. *Elementary processes in hydrogen-helium plasmas: cross sections and reaction rate coefficients*, volume 4. Springer, 1987.

E. Jouguet. Sur la propagation des réactions chimiques dans les gaz. *Journal de Mathématiques Pures et Appliquées*, 1:347–425, 1905.

Yiguang Ju and Wenting Sun. Plasma assisted combustion: Dynamics and chemistry. *Progress in Energy and Combustion Science*, 48:21–83, 2015.

G.T. Kalghatgi and D. Bradley. Pre-ignition and 'super-knock' in turbo-charged spark-ignition engines. *International Journal of Engine Research*, 13:399–414, 2012.

Taekyu Kang and Dimitrios C. Kyritsis. Methane Flame Propagation in Compositionally Stratifid Gases. *Combustion Science and Technology*, 177:2191–2210, 2005.

Taekyu Kang and Dimitrios C. Kyritsis. Departure from quasi-homogeneity during laminar flame propagation in lean, compositionally stratified methane-air mixtures. *Proceedings of the Combustion Institute*, 31:1075–1083, 2007.

Taekyu Kang and Dimitrios C. Kyritsis. Theoretical investigation of flame propagation through compositionally stratified methaneair mixtures. *Combustion Theory and Modeling*, 13:705–719, 2009.

A.K. Kapila, D.W. Schwendeman, J.J. Quirk, and T. Hawa. Mechanisms of detonation formation due to a temperature gradient. *Combustion Theory and Modeling*, 6(4):553–594, 2002.

G. A. Karim and P. Tsang. Flame Propagation Through Atmospheres Involving Concentration Gradients Formed by Mass Transfer Phenomena. *Journal of Fluids Engineering*, 97: 615, 1975.

David R. Kassoy, Jeffery A. Kuehn, M.W. Nabity, and J.F. Clarke. Detonation initiation on the microsecond time scale: Ddts. *Combustion Theory and Modeling*, 12(6):1009–1047, 2008.

Robert J. Kee, J. Warnatz, and James A. Miller. A fortran computer code package for the evaluation of gas-phase viscosities, conductivities, and diffusion coefficients. *Report No. SAND83-8209*, Sandia National Laboratories, Livermore, CA, USA, 1983.

Robert J. Kee, Joseph F. Grcar, M.D. Smooke, James A. Miller, and E. Meeks. PREMIX: a Fortran program for modeling steady laminar one-dimensional premixed flames. *Report No. SAND85-8249*, Sandia National Laboratories, Livermore, CA, USA, 1985.

Robert J. Kee, Graham Dixon-Lewis, Jürgen Warnatz, Michael E. Coltrin, and James A. Miller. A fortran computer code package for the evaluation of gas-phase multicomponent transport properties. *Report No. SAND86-8246*, Sandia National Laboratories, Livermore, CA, USA, 1986.

Robert J. Kee, Fran M. Rupley, and James A. Miller. Chemkin-II: A Fortran chemical kinetics package for the analysis of gas-phase chemical kinetics. *Report No. SAND89-8009*, Sandia National Laboratories, Livermore, CA, USA, 1989.

Wookyung Kim, Hyungrok Do, M. Godfrey Mungal, and Mark A. Cappelli. Investigation of no production and flame structure in plasma enhanced premixed combustion. *Proceedings of the Combustion Institute*, 31(2):3319–3326, 2007.

Itsuro Kimura, Hiroshi Aoki, and Manabu Kato. The use of a plasma jet for flame stabilization and promotion of combustion in supersonic air flows. *Combustion and Flame*, 42: 297–305, 1981.

Toshiaki Kitagawa, Hiroyuki Kido, Nozomu Nakamura, and Masaya Aishima. Flame inertia into lean region in stratified hydrogen mixture. *International Journal of Hydrogen Energy*, 30:1457–1464, 2005.

A.D. Kiverin, D.R. Kassoy, M.F. Ivanov, and M.A. Liberman. Mechanisms of ignition by transient energy deposition: Regimes of combustion wave propagation. *Physical Review E - Statistical, Nonlinear, and Soft Matter Physics*, 87(3):1–10, 2013.

M. Kuznetsov, S. Kobelt, J. Grune, and T. Jordan. Flammability limits and laminar flame speed of hydrogen-air mixtures at sub-atmospheric pressures. *International Journal of Hydrogen Energy*, 37:17580–17588, 2012.

David S. Landes. *The unbound Prometheus: technological change and industrial development in Western Europe from 1750 to the present*. Cambridge University Press, 2003.

Chung K. Law. *Combustion physics*. Cambridge University Press, 2006.

C.K. Law and F.N. Egolfopoulos. A Unified Chain-Thermal Theory of Flammability Limits. *Symposium (International) on Combustion*, 24:137–144, 1992.

C.K. Law and C.J. Sung. Structure, aerodynamics, and geometry of premixed flamelets. *Progress in Energy and Combustion Science*, 26:459–505, 2000.

John H. Lee. *The Detonation Phenomenon*. Cambridge University Press, 2008.

Dong Li, Qi Zhang, Qiuju Ma, and Shilei Shen. Comparison of explosion characteristics between hydrogen/air and methane/air at the stoichiometric concentrations. *International Journal of Hydrogen Energy*, 40(28):8761–8768, 2015.

J. Linnett. Methods of measuring burning velocities. *Symposium (International) on Combustion*, 4:20–35, 1953.

Andrei N. Lipatnikov. Stratified turbulent flames: Recent advances in understanding the influence of mixture inhomogeneities on premixed combustion and modeling challenges. *Progress in Energy and Combustion Science*, 62:87–132, 2017.

Yintong Liu, Xian Shi, Jun Deng, Yulin Chen, Minzhang Hu, and Liguang Li. Experimental study on the characteristics of knock under di-hcci combustion mode with ethanol/gasoline mixed fuel. *SAE Technical Paper 2013-01-0544*, 2013.

Yong Liu and Xiaotian Liu. Detonation propagation characteristic of H2–O2–N2 mixture in tube and effect of various initial conditions on it. *International Journal of Hydrogen Energy*, 38(30):13471–13483, 2013.

Andrew E. Lutz, Robert J. Kee, James A. Miller, Harray A. Dwyer, and Antoni K. Oppenheim. Dynamic effects of autoignition centers for hydrogen and C1,2-hydrocarbon fuels. *Symposium (International) on Combustion*, 22:1683–1693, 1989.

Jason B. Martz, George A. Lavoie, Hong G. Im, Robert J. Middleton, Aristotelis Babajimopoulos, and Dionissios N. Assanis. The propagation of a laminar reaction front during end-gas auto-ignition. *Combustion and Flame*, 159:2077–2086, 2012.

J.B. Martz, H. Kwak, H.G. Im, G.A. Lavoie, and D.N. Assanis. Combustion regime of a reacting front propagating into an auto-igniting mixture. *Proceedings of the Combustion Institute*, 33:3001–3006, 2011.

Y.M. Marzouk, A.F. Ghoniem, and H.N. Najm. Dynamic response of strained premixed flames to equivalence ratio gradients. *Proceedings of the Combustion Institute*, 28:1859–1866, 2000.

Sara McAllister, Jyh-Yuan Chen, and Carlos Fernandez-Pello. *Fundamentals of combustion processes*. Springer Science & Business Media, 2011.

David W. Mikolaitis. The unsteady propagation of premixed flames through nonhomogeneous mixtures and thermal gradients. *Combustion and Flame*, 57:87–94, 1984.

Joshua D. Miller and Cristiano Façanha. The state of clean transport policy: a 2014 synthesis of vehicle and fuel policy developments, 2014.

Jeffrey S. Newman. Experimental evaluation of fire-induced stratification. *Combustion and Flame*, 57(1):33–39, 1984.

Jiaying Pan, Gequn Shu, Peng Zhao, Haiqiao Wei, and Zheng Chen. Interactions of flame propagation, auto-ignition and pressure wave during knocking combustion. *Combustion and Flame*, 164:319–328, 2016a.

Jiaying Pan, Haiqiao Wei, Gequn Shu, Zheng Chen, and Peng Zhao. The role of low temperature chemistry in combustion mode development under elevated pressures. *Combustion and Flame*, 174:179–193, 2016b.

S. Pancheshnyi, S. Biagi, M.C. Bordage, G.J.M. Hagelaar, W.L. Morgan, A.V. Phelps, and L.C. Pitchford. The lxcat project: Electron scattering cross sections and swarm parameters for low temperature plasma modeling. *Chemical Physics*, 398:148–153, 2012.

Cheolwoong Park, Sungdae Kim, Hongsuk Kim, and Yasuo Moriyoshi. Stratified lean combustion characteristics of a spray-guided combustion system in a gasoline direct injection engine. *Energy*, 41(1):401–407, 2012.

Norbert Peters. *Turbulent combustion*. Cambridge university press, 2000.

Guillaume Petitpas, J.-D. Rollier, A. Darmon, José Gonzalez-Aguilar, Rudolf Metkemeijer, and Laurent Fulcheri. A comparative study of non-thermal plasma assisted reforming technologies. *International Journal of Hydrogen Energy*, 32(14):2848–2867, 2007.

V.A. Petukhov, I.M. Naboko, and V.E. Fortov. Explosion hazard of hydrogen-air mixtures in the large volumes. *International Journal of Hydrogen Energy*, 34(14):5924–5931, 2009.

H. Phillips. Flame in a buoyant methane layer. *Symposium (International) on Combustion*, 10(1):1277–1283, 1965.

Guillaume Pilla, David Galley, Deanna A. Lacoste, Franois Lacas, Denis Veynante, and Christophe O. Laux. Stabilization of a turbulent premixed flame using a nanosecond repetitively pulsed plasma. *IEEE Transactions on Plasma Science*, 34(6):2471–2477, 2006.

T. Poinsot, T. Echekki, and M. G. Mungal. A Study of the Laminar Flame Tip and Implications for Premixed Turbulent Combustion. *Combustion Science and Technology*, 81: 45–73, 1992.

Thierry Poinsot and Denis Veynante. *Theoretical and numerical combustion*. RT Edwards, Inc., 2005.

Yuliang Qi, Xin He, Zhi Wang, Jianxin Wang, Huiqiang Zhang, and Yizhou Jiang. An experimental investigation of super knock combustion mode using a one-dimensional constant volume bomb. *International Journal of Hydrogen Energy*, 40:2377–2385, 2015a.

Yunliang Qi, Zhi Wang, Jianxin Wang, and Xin He. Effects of thermodynamic conditions on the end gas combustion mode associated with engine knock. *Combustion and Flame*, 162:4119–4128, 2015b.

Zhiwei Qin, Vitali V. Lissianski, Huixing Yang, William C. Gardiner, Scott G. Davis, and Hai Wang. Combustion chemistry of propane: A case study of detailed reaction mechanism optimization. *Proceedings of the Combustion Institute*, 28:1663–1669, 2000.

Youngchul Ra and Wai K. Cheng. Laminar flame propagation through a step-stratified charge. In *The fifth international symposium on diagnostics and modeling of combustion in internal engines (COMODIA 2001)*, pages 1–4, 2001.

W.J. Macquorn Rankine. On the thermodynamic theory of waves of finite longitudinal disturbance. *Philosophical Transactions of the Royal Society of London*, pages 277–288, 1870.

Rolf D. Reitz. Directions in internal combustion engine research. *Combustion and Flame*, 160(1):1–8, 2013.

Wojciech Rudy, Mateusz Zbikowski, and Andrzej Teodorczyk. Detonations in hydrogen-methane-air mixtures in semi confined flat channels. *Energy*, 116:1479–1483, 2016.

Wojciech Rudy, Karolina Dziubanii, Mateusz Zbikowski, and Andrzej Teodorczyk. Experimental determination of critical conditions for hydrogen-air detonation propagation in partially confined geometry. *International Journal of Hydrogen Energy*, 42(11):7366–7373, 2017.

Ramanan Sankaran and Hong G. Im. Dynamic flammability limits of methane/air premixed flames with mixture composition fluctuations. *Proceedings of the Combustion Institute*, 29:77–84, 2002.

Xian Shi and Jyh-Yuan Chen. Numerical analysis and model development for laminar flame speed of stratified methane/air mixtures. *Combustion and Flame*, 184:233–245, 2017.

Xian Shi, Jyh-Yuan Chen, and Zheng Chen. Numerical study of laminar flame speed of fuel-stratified hydrogen/air flames. *Combustion and Flame*, 163:394–405, 2016.

Xian Shi, Jyh-Yuan Chen, and Yulin Chen. Laminar flame speeds of stratified methane, propane, and n-heptane flames. *Combustion and Flame*, 176:38–47, 2017a.

Xian Shi, Je Ir Ryu, Jyh-Yuan Chen, and Robert W Dibble. Modes of reaction front propagation and end-gas combustion of hydrogen/air mixtures in a closed chamber. *International Journal of Hydrogen Energy*, 42(15):10501–10512, 2017b.

Y.L. Shoshin and L.P.H. de Goey. Experimental study of lean flammability limits of methane/hydrogen/air mixtures in tubes of different diameters. *Experimental Thermal and Fluid Science*, 34(3):373–380, 2010.

Magnus Sjöberg and John E. Dec. Smoothing HCCI Heat-Release Rates Using Partial Fuel Stratification with Two-Stage Ignition Fuels. *SAE Technical Paper*, 2006-01-0629, 2006.

A. Smallbone, W. Liu, C. Law, X. You, and H. Wang. Experimental and modeling study of laminar flame speed and non-premixed counterflow ignition of n-heptane. *Proceedings of the Combustion Institute*, 32:1245–1252, 2009.

N.N. Smirnov, V.F. Nikitin, L.I. Stamov, and D.I. Altoukhov. Supercomputing simulations of detonation of hydrogen-air mixtures. *International Journal of Hydrogen Energy*, 40(34): 11059–11074, 2015.

Gregory P. Smith, David M. Golden, Michael Frenklach, Nigel W. Moriarty, Boris Eiteneer, Mikhail Goldenberg, C. Thomas Bowman, Ronald K. Hanson, Soonho Song, Jr. William C. Gardiner, Vitali V. Lissianski, and Zhiwei Qin. GRI-Mech 3.0, 1999. URL `http://www.me.berkeley.edu/gri_mech`.

Caroline Sorensen. *Measurement of Flame Propagation Through Step Changes in Mixture Composition*. PhD thesis, Massachusetts Institute of Technology, 2016.

Svetlana M. Starikovskaia. Plasma assisted ignition and combustion. *Journal of Physics D: Applied Physics*, 39(16):265–299, 2006.

Andrei Y. Starikovskii, Nikolay B. Anikin, Ilya N. Kosarev, Eugeny I. Mintoussov, Maria M. Nudnova, Aleksandr E. Rakitin, Dmitry V. Roupassov, Svetlana M. Starikovskaia, and Victor P. Zhukov. Nanosecond-pulsed discharges for plasma-assisted combustion and aerodynamics. *Journal of Propulsion and Power*, 24(6):1182–1197, 2008.

Andrey Starikovskiy and Nickolay Aleksandrov. Plasma-assisted ignition and combustion. *Progress in Energy and Combustion Science*, 39:61–110, 2013.

Gilbert Strang. On the construction and comparison of difference schemes. *SIAM Journal on Numerical Analysis*, 5(3):506–517, 1968.

B.D. Taylor, D.A. Kessler, V.N. Gamezo, and E.S. Oran. Numerical simulations of hydrogen detonations with detailed chemical kinetics. *Proceedings of the Combustion Institute*, 34 (2):2009–2016, 2013.

UN. World Population Prospects: The 2017 Revision, Key Findings and Advance Tables. *Working Paper No. ESA/P/WP/248*, 2017.

UNDP. Human Development Index (HDI). `http://hdr.undp.org/en/content/human-development-index-hdi`, 2017.

Christina M. Vagelopoulos, Jonathan H. Frank, Jay Jeffries, and Friedrich Dinkelacker. An experimental and numerical study on the adequacy of CH as a flame marker in premixed methane flames. *Proceedings of the Combustion Institute*, 30:241–249, 2005.

Bram Van Leer. On the relation between the upwind-differencing schemes of godunov, engquist–osher and roe. *SIAM Journal on Scientific and Statistical Computing*, 5(1):1–20, 1984.

Emilien Varea, Joachim Beeckmann, Heinz Pitsch, Zheng Chen, and Bruno Renou. Determination of burning velocities from spherically expanding H2/air flames. *Proceedings of the Combustion Institute*, 35:711–719, 2015.

P. C. Vena, B. Deschamps, G. J. Smallwood, and M. R. Johnson. Equivalence ratio gradient effects on flame front topology in a stratified iso-octane/air turbulent V-flame. *Proceedings of the Combustion Institute*, 33:1551–1558, 2011.

J. von Neumaa. *Theory of detonation waves*. PhD thesis, Institute for Advanced Study, Princeton, NY, 1942.

C.J. Wang and Jennifer X. Wen. Numerical simulation of flame acceleration and deflagration-to-detonation transition in hydrogen-air mixtures with concentration gradients. *International Journal of Hydrogen Energy*, 2016.

Z. Wang, H. Liu, T. Song, Y. Qi, X. He, S. Shuai, and J. Wang. Relationship between super-knock and pre-ignition. *International Journal of Engine Research*, 16:166–180, 2014.

Zhi Wang, Hui Liu, Tao Song, Yunliang Qi, Xin He, Shijin Shuai, and JianXin Wang. Relationship between super-knock and pre-ignition. *International Journal of Engine Research*, 16(2):166–180, 2015.

Zhi Wang, Hui Liu, and Rolf D. Reitz. Knocking combustion in spark-ignition engines. *Progress in Energy and Combustion Science*, 61:78–112, 2017.

Haiqiao Wei, Yibao Shang, Ceyuan Chen, Dongzhi Gao, and Dengquan Feng. A numerical study on pressure wave-induced end gas auto-ignition near top dead center of a downsized spark ignition engine. *International Journal of Hydrogen Energy*, 39(36):21265–21274, 2014.

Haiqiao Wei, Yibao Shang, Ceyuan Chen, Dongzhi Gao, and Dengquan Feng. One-dimensional numerical study on pressure wave-flame interaction and flame acceleration under engine-relevant conditions. *International Journal of Hydrogen Energy*, 40:4874–4883, 2015.

Jürgen Willand, Marc Daniel, Emanuela Montefrancesco, Bernhard Geringer, Peter Hofmann, and Markus Kieberger. Limits on downsizing in spark ignition engines due to pre-ignition. *MTZ worldwide*, 70(5):56–61, May 2009.

Benjamin Wolk, Anthony DeFilippo, Jyh-Yuan Chen, Robert Dibble, Atsushi Nishiyama, and Yuji Ikeda. Enhancement of flame development by microwave-assisted spark ignition in constant volume combustion chamber. *Combustion and Flame*, 160(7):1225–1234, 2013.

Fujia Wu, Wenkai Liang, Zheng Chen, Yiguang Ju, and Chung K. Law. Uncertainty in stretch extrapolation of laminar flame speed from expanding spherical flames. *Proceedings of the Combustion Institute*, 35(1):663–670, 2014.

Hao Yu and Zheng Chen. End-gas autoignition and detonation development in a closed chamber. *Combustion and Flame*, 162:4102–4111, 2015.

Michael George Zabetakis. Flammability characteristics of combustible gases and vapors. Technical report, Bureau of Mines Washington DC, 1965.

Ya.B. Zeldovich. Regime Classification of an Exothermic Reaction With Nonuniform Initial Conditions. *Combustion and Flame*, 39:211–214, 1980.

Ya.B. Zeldovich, V.B. Librovich, G.M. Makhviladze, and G.I. Sivashinsky. On the development of detonation in a non-uniformly preheated gas. *Acta Astronautica*, 15:313–321, nov 1970.

Yakov B. Zeldovich. On the theory of propagation of detonation in gaseous systems. *Journal of Experimental and Theoretical Physics*, 10(5):542–568, 1940.

Jiacheng Zhang and John Abraham. A numerical study of laminar flames propagating in stratified mixtures. *Combustion and Flame*, 163:461–471, 2016.

Ruigang Zhou and Simone Hochgreb. The behaviour of laminar stratified methane/air flames in counterflow. *Combustion and Flame*, 160:1070–1082, 2013.